University of Pisa

Doctoral Thesis

Monostatic and Bistatic radar imaging super-resolution

Author:
Davide Cataldo

Supervisors:
Prof. Marco Martorella

Prof. Fabrizio Berizzi

A Thesis submitted in fulfillment of the requirements
for the degree of Doctor of Philosophy
in

Engineering
Remote Sensing program
Department of Information Engineering
University of Pisa

SSD ING-INF/03

June 6, 2016

Declaration of Authorship

I, Davide CATALDO, declare that this Thesis titled, 'Monostatic and Bistatic radar imaging super-resolution' and the work presented in it are my own. I confirm that:

- This work was done wholly or mainly while in candidature for a research degree at this University.
- Where any part of this Thesis has previously been submitted for a degree or any other qualification at this University or any other institution, this has been clearly stated.
- Where I have consulted the published work of others, this is always clearly attributed.
- Where I have quoted from the work of others, the source is always given. With the exception of such quotations, this Thesis is entirely my own work.
- I have acknowledged all main sources of help.
- Where the Thesis is based on work done by myself jointly with others, I have made clear exactly what was done by others and what I have contributed myself.

Signed: _____

Date: _____

UNIVERSITY OF PISA

Abstract

Doctor of Philosophy

Monostatic and Bistatic radar imaging super-resolution

by Davide CATALDO

In recent years, bistatic and multistatic radar imaging systems have become popular for several applications and have gained interest within the radar scientific community. On the other hand, super-resolution and spectral estimation algorithms are largely employed for resolution enhancement, sidelobe and artifacts suppression and speckle reduction. However, super-resolution and spectral estimation algorithms exploit the standard monostatic ISAR model and do not take into account distortion effects such as range migration. As a consequence, the applicability of super-resolution standard algorithms in case of bistatic configuration is generally not guaranteed.

This Thesis discusses the use of super-resolution techniques applied for monostatic and bistatic radar imaging. ISAR and Bistatic ISAR theory is recalled and further considerations about linear and quadratic distortions, in terms of range/Doppler migration, due to the bistatic geometry are discussed. Analytical constraints for range and Doppler migration are defined and validated by means of simulated data. Then, super-resolution is theoretically treated by exploiting the monostatic and bistatic received signal models. Novel methods for super-resolution performance analysis and a novel super-resolution based approach for bistatic distortion mitigation are proposed. Super-resolution techniques are tested and compared on real monostatic and bistatic data. Such a real data consists of a SAR image of a vessel cropped by a SAR product provided by COSMO-SkyMed (monostatic) and an ISAR image of a small aircraft from the data collected during the NATO SET-196 trials from September 29th to October 3rd, 2014 (bistatic).

Acknowledgements

The work and the results presented in this Thesis have been mostly carried out within the framework of the projects ISAR-SKY, sponsored by the Italian Ministry of Defence, and SPERI, sponsored by the European Defence Agency. Two real datasets are used in this Thesis to show the results of the work presented. The first dataset has been provided by COSMO-SkyMed, whereas the second dataset has been produced by the Radar Laboratory of the Department of Information Engineering in Pisa, within the framework of the NATO SET-196 trials. The trials were hosted by the Istituto Vallauri of the Italian Navy located in Livorno, which provided the logistic supports from September 29th to October 3rd, 2014. The real data produced have been acquired by means of two HABRA Radar systems jointly designed by Metasensing BV and the National Inter-University Consortium for Telecommunications (CNIT).

I would like to express the deepest appreciation to Professor Marco Martorella and Professor Fabrizio Berizzi for the good advice, friendship and the invaluable support on both an academic and a personal level during these three years of study and research.

I would like to thank my lab colleagues: Elisa, Daniele, Stefano, Alberto, Alessio, Sonia, Selenia, Samuele, Federica, Maria Bianca and my friends in the RaSS laboratory: Michele, Christian, Amerigo, Dario, Alessandro, Anna Lisa, Roberto, Francesco and Sabrina for their precious help and kindness, the laughs and the time spent together inside and outside the lab.

I would like to thank my friends that shared with me these years at the University of Pisa: Michele, Carlo, Pasquale, Tamara, Luca, Andrea, Leo, Dario and many others. For ten amazing years of study and work, fun and laughs, sober and not so sober moments spent together.

I would like to thank my masters Giuseppe, Antonio, Nicola and Vincenzo, all the fighters and all the fighers of the Gerace Giovannini Team for the blood, sweat and tears poured together on the parquet and the tatami working hard and supporting each other.

I would like to thank my advisors and friends at the Ohio State University and in Columbus: Professor Chris Baker, Professor Graeme Smith, Mohammed, Landon, Zach, Adam, Shirley, SeungHo Doo, Elias, Jonathan, Mike, Fabrizio and Alessandro for six awesome months spent in the USA.

Last but not least I would like to thank my parents for their support, patience and understanding, for which my mere expression of thanks does not suffice.

Contents

List of Figures

List of Tables

Abbreviations

APES	**A**mplitude and **P**hase **E**stimation of a **S**inusoid
AR	**A**uto-**R**egressive
ASR	**A**daptive **S**idelobe **R**eduction
ASC	**A**mplitude **S**pectrum **C**apon
ATR	**A**utomatic **T**arget **R**ecognition
BEF	**B**andwidth **E**xtrapolation **F**actor
BEM	**B**istatically **E**quivalent **M**onostatic
B-ISAR	**B**istatic **ISAR**
B-LoS	**B**istatic **L**ine **o**f **S**ight
BWE	**B**and**W**idth **E**xtrapolation
CDA	**C**omplex **D**ual **A**podization
CPI	**C**oherent **P**rocessing **I**nterval
CRS	**C**ross-**R**ange **S**caling
CS	**C**ompressed **S**ensing
CSIR	**C**ouncil for **S**cientific and **I**ndustrial **R**esearch
CSK	**C**OSMO **S**ky-**M**ed
DA	**D**ual **A**podization
DFT	**D**iscrete **F**ourier **T**ransform
DOA	**D**irection **O**f **A**rrival
DSTO	**D**efence **S**cience and **T**echnology **O**rganisation
DTI	**D**oppler-**T**ime-**I**ntensity
ESPRIT	**E**stimation of **S**ignal **P**arameters via **R**otational
FIR	**F**inite **I**mpulse **R**esponse
FT	**F**ourier **T**ransform
GAIC	**G**eneralized **A**kaike **I**nformation **C**riterion

GPR	**G**round **P**enetrating **R**adar
GPS	**G**lobal **P**ositioning **S**ystem
IC	**I**mage **C**ontrast
ICBA	**I**mage **C**ontrast **B**ased **A**utofocusing
IDFT	**I**nverse **D**iscrete **F**ourier **T**ransform
IE	**I**mage **E**ntropy
IFT	**I**nverse **F**ourier **T**ransform
IMP	**I**ncremental **M**ulti-**P**arameter
IMU	**I**nertial **M**easurement **U**nit
IPP	**I**mage **P**rojection **P**lane
ISAR	**Inverse S**ynthetic **A**perture **R**adar
LoS	**L**ine **o**f **S**ight
LS	**L**east **S**quares
MIMO	**M**ultiple **I**nput **M**ultiple **O**utput
ML	**M**aximum **L**ikelihood
MMSE	**M**inimum **M**ean **S**quare **E**rror
MRI	**M**agnetic **R**esonance **I**maging
MSE	**M**ean **S**quare **E**rror
MTS	**M**esosphere-**T**roposphere-**S**tratosphere
MUSIC	**MU**ltiple **SI**gnal **C**lassification
	Invariance **T**echniques
MVM	**M**inimum **V**ariance **M**ethod
PRF	**P**ulse **R**epetition **F**requency
PRI	**P**ulse **R**epetition **I**nterval
PSD	**P**ower **S**pectral **D**ensity
PSF	**P**oint **S**pread **F**unction
RCS	**R**adar **C**ross **S**ection
RD	**R**ange-**D**oppler
RIP	**R**estricted **I**sometry **P**roperty
RMSE	**R**oot **M**ean **S**quare **E**rror
RRMSE	**R**elative **R**oot **M**ean **S**quare **E**rror
RRMVM	**R**educed **R**ank **MVM**
ROI	**R**egion **O**f **I**nterest

RSE	**R**elative **S**quare **E**rror
RTK	**R**eal **T**ime **K**inematic
SAR	**S**ynthetic **A**perture **R**adar
SIR	**S**ignal to **I**nterference **R**atio
SL0	**S**moothed ℓ_0
SNR	**S**ignal to **N**oise **R**atio
SSVA	**S**uper **SVA**
SVA	**S**patially **V**ariant **A**podization
SVD	**S**ingular **V**alue **D**ecomposition
TDM	**T**ime **D**ivision **M**ultiplexing
ULA	**U**niform **L**inear **A**rray
W-CFAR	**W**COR **C**onstant **F**alse **A**larm **R**ate
WCOR	**W**avelet **COR**relator

Symbols

c	Speed of light in a vacuum	[m/s]
c_k	k^{th} AR model coefficient for BWE algorithm	
c_σ	σ decreasing factor (Compressed Sensing)	
d_i	i^{th} element of $\mathbf{D}$	
e	Euler's number	
e_b	Backward prediction error (Burg algorithm)	
e_f	Forward prediction error (Burg algorithm)	
e_n	Unmodeled noise and interference term (MVM and APES)	
f	Frequency variable	[Hz]
f_0	Carrier frequency	[Hz]
f_b	Beat frequency (Linear-FMCW signal)	[Hz]
$f_d(t_n)$	Doppler frequency	[Hz]
$f_{d,B}(t_n)$	Bistatic Doppler frequency	[Hz]
$f_{d,\max}$	Maximum non-ambiguous Doppler frequency	[Hz]
f_s	ADC sampling frequency	[Hz]
$h(n)$	Received signal support in the slow-time domain	
m	Frequency discrete variable	
n	Slow-time discrete variable	
p	Time-delay (or range) discrete variable	
p_i	i^{th} scatterer discrete delay-time coordinate	
p_{AR}	AR model order (BWE)	
q	Doppler (or cross-range) discrete variable	
q_i	i^{th} scatterer discrete Doppler coordinate	
r_G	Global cross-correlation index	
$r_{M,C}$	Complex mean mobile cross-correlation	

$r_{M,I}$	Intensity mean mobile cross-correlation	
$s_R(t_v, n)$	Received signal in the fast-time/slow-time domain	
$s_T(t_v, n)$	Transmitted signal in the fast-time/slow-time domain	
t_n	Slow-time variable	[s]
t_v	Fast-time variable	[s]
v	Target speed	[m/s]
$v_{R,\max}$	Maximum non-ambiguous radial speed	[m/s]
$w(\tau, \nu)$	ISAR Point Spread Function	
$\tilde{w}(\tau, t_n)$	Received signal support in the delay-time/slow-time domain	
w_{CoP}	Cosine-on-pedestal impulse response (SVA)	
$z_{1,0}$	Scatterer cross-range position in T_z (single scatterer target model)	[m]
$z_{1,i}$	i^{th} scatterer cross-range position in T_z	[m]
$z_{2,0}$	Scatterer range position in T_z (single scatterer target model)	[m]
$z_{2,i}$	i^{th} scatterer range position in T_z	[m]
$z_{1,\max}$	Maximum cross-range distance from the focusing center	[m]
$z_{2,\max}$	Maximum range distance from the focusing center	[m]
A	Scatterer complex reflectivity function (single scatterer target model)	
$\hat{A}_k$	k^{th} estimated scatterer complex amplitude (CLEAN)	
B	Signal frequency bandwidth	[Hz]
$\mathcal{B}$	Estimated image background area	
$\mathcal{B}(p, q)$	Square box centered on coordinate (p, q)	
B_d	Doppler bandwidth	[Hz]
$B_{d,B}$	Bistatic Doppler bandwidth	[Hz]
$D_2(\nu)$	Monostatic quadratic distortion term	
$D_{2,B}(\nu)$	Bistatic quadratic distortion term	
E_d	Cost function for the frequency PSF component estimation (CLEAN)	
E_g	Cost function for the time PSF component estimation (CLEAN)	
$F_\sigma(x)$	ℓ_0 norm approximation function (Compressed Sensing)	
H	Shannon Entropy	

$I(\tau, \nu)$	ISAR image in the delay-time/Doppler domain after Doppler compression
I_H	High-resolution SAR/ISAR image ("truth")
$\hat{I}_H$	Normalized high-resolution SAR/ISAR image
$I_{H,\lambda}$	Thresholded high-resolution SAR/ISAR image
I_S	Super-resolved SAR/ISAR image ("estimation")
$\hat{I}_S$	Normalized super-resolved SAR/ISAR image
$I_{S,\lambda}$	Thresholded super-resolved SAR/ISAR image
J	Number of elements of the σ sequence (Compressed Sensing)
J_{LS}	Cost function for LS deconvolution algorithm
J_{MMSE}	Cost function for MMSE deconvolution algorithm
J_{MVM}	Cost function for Capon's MVM
$K(t)$	Bistatic distortion term
K_0	Zero order term of $K(t)$ Taylor-Maclaurin polynomial
K_1	First order term of $K(t)$ Taylor-Maclaurin polynomial
K_2	Second order term of $K(t)$ Taylor-Maclaurin polynomial
K_f	Frequency support reduction factor
K_t	Slow-time support reduction factor
K_{zp}	Zero-padding factor
K_T	CPI reduction factor
$K_{T,crg}$	Minimum CPI reduction factor for cross-range migration mitigation
$K_{T,rng}$	Minimum CPI reduction factor for range migration mitigation
L	Number of subapertures for forward-backward covariance matrix estimation
M	Number of frequency samples
$\hat{M}$	Subaperture size along the frequency direction
M_{low}	Number of frequency samples after support reduction
$M_{\mathrm{BW},k}$	k^{th} residual image's -3dB black/white mask
N	Number of transmitted sweeps
$\hat{N}$	Subaperture size along the slow-time direction
N_{crg}	Number of "true" pixels around $M_{\mathrm{BW}}(p_k^*, q_k^*)$ along the cross-range direction

N_{loop}	Number of loops (SSVA)	
N_{low}	Number of sweeps after support reduction	
N_p	Number of detected peaks in the super-resolved image	
N_{rng}	Number of "true" pixels around $M_{\mathrm{BW}}(p_k^*, q_k^*)$ along the range direction	
N_s	Number of scatterers in the target model or detected in the ISAR image	
$N_{\mathcal{B}}$	Number of pixels in the background area	
N_{CD}	Number of correct detections (scatterer position based comparison algorithm)	
N_L	Number of iterations of the steepest ascend algorithm (Compressed Sensing)	
$N_{\mathcal{T}}$	Number of pixels in the target area	
P	Number of time-delay (or range) samples	
Q	Number of Doppler (or cross-range) samples	
R	Monostatic radar - Target distance	[m]
R'	Monostatic effective range	[m]
R_0	Distance between monostatic radar and target focusing center	[m]
R'_i	i^{th} scatterer effective range	[m]
R'_B	BEM effective range	[m]
$R_{B,0}$	BEM effective range for $n = 0$	[m]
$R_{B,1}$	BEM effective radial speed	[m/s]
$R_{B,2}$	BEM effective radial acceleration	[m/s^2]
$R_{Bi,0}$	Distance between BEM radar and target focusing center	[m]
$R_{\max}$	Maximum range distance	[m]
R_{RxTg}	Receiver - Target distance	[m]
$R_{RxTg,0}$	Distance between receiver and target focusing center	[m]
R_{TxRx}	Transmitter - Receiver (baseline) distance	[m]
R_{TxTg}	Transmitter - Target distance	[m]
$R_{TxTg,0}$	Distance between transmitter and target focusing center	[m]
$S(f, n)$	Received signal in the frequency/slow-time domain after motion compensation	
$S_R(f, n)$	Received signal in the frequency/slow-time domain	

$S'_R(\tau, n)$	Received signal in the delay-time/slow-time domain after range compression	
$\mathcal{T}$	Estimated image target area	
T_{ob}	Observation Time (CPI)	[s]
$T_{ob,L}$	Reduced observation Time (CPI)	[s]
T_x	Reference system embedded on the transmitter and centered on the transmitter	
T_z	Reference system embedded and centered on the target	
T_R	Pulse Repetition Interval	[s]
T_{SW}	FMCW waveform duration	[s]
T_ξ	Reference system embedded and centered on the target	
V	Volume occupied by the target in T_z	
$W(f, n)$	Received signal support in the frequency/slow-time domain	
$W_{\mathcal{B}}$	Square box size (mobile cross-correlation)	
W_{CoP}	Cosine-on-pedestal windowing function (SVA)	
α	Complex amplitude of a sinusoid (MVM and APES)	
β	Bistatic angle	[rad]
$\gamma(z_1, z_2)$	Projection of the target's reflectivity function onto the IPP	
$\gamma'(\mathbf{z})$	Target reflectivity function at coordinates $\mathbf{z}$	
$\gamma_B(z_1, z_2)$	Projection of the target's bistatic reflectivity function onto the IPP	
$\delta(x)$	Dirac delta function	
δ_{crg}	Cross-range resolution	[m]
$\hat{\delta}_{crg}$	Estimated mean -3dB cross-range resolution	[m]
$\delta_{crg,k}$	Estimated -3dB cross-range resolution for the k^{th} detected scatterer	[m]
$\delta_{crg,B}$	Bistatic cross-range resolution	[m]
$\delta_{i,j}$	Kronecker delta function	
δ_{rng}	Range resolution	[m]
$\hat{\delta}_{rng}$	Estimated mean -3dB range resolution	[m]
$\bar{\delta}_{rng}$	Range pixel spacing	[m]
$\delta_{rng,k}$	Estimated -3dB range resolution for the k^{th} detected scatterer	[m]
$\delta_{rng,B}$	Bistatic range resolution	[m]

δ_{srg}	Slant-range resolution	[m]
δ_ν	Doppler resolution	[Hz]
δ_τ	Delay-time resolution	[s]
δ_H	Threshold parameter for the high-resolution SAR/ISAR image	
δ_S	Threshold parameter for the super-resolved SAR/ISAR image	
$\delta_{\mathcal{T}}$	Threshold parameter for the SNR calculation	
ϵ	Arbitrary small real number	
η	Bandwidth extrapolation factor (SSVA)	
θ_i	i^{th} weighting coefficient in the sparse representation (Compressed Sensing)	
λ	Lagrange multiplier (MVM)	
λ_H	Threshold for the high-resolution SAR/ISAR image	
λ_S	Threshold for the super-resolved SAR/ISAR image	
λ_{SVD}	Threshold for SVD deconvolution algorithm	
$\lambda_{\mathcal{T}}$	Threshold for the SNR calculation	
μ	Chirp-rate	[Hz^2]
μ_H	High-resolution image amplitude mean value	
$\hat{\mu}_I$	Estimated image amplitude mean value	
μ_S	Super-resolved image amplitude mean value	
ν	Doppler frequency variable	[Hz]
ν_0	Scatterer Doppler coordinate (single scatterer target model)	[Hz]
ν_i	i^{th} scatterer Doppler coordinate	[Hz]
$\nu_{\max}$	Maximum Doppler frequency	[Hz]
σ_i	i^{th} scatterer complex reflectivity function	
σ_H	High-resolution image's amplitude standard deviation	
$\hat{\sigma}_I$	Estimated image amplitude standard deviation	
σ_S	Super-resolved image's amplitude standard deviation	
τ	Delay-time variable	[s]
τ_0	Scatterer delay-time coordinate (single scatterer target model)	[s]
τ_i	i^{th} scatterer delay-time coordinate	[s]
$\varphi(f, t_n)$	Received signal phase term	
$\varphi'(t_n)$	Received signal phase term for $f = f_0$	
φ_0	Constant phase term	

$\varphi_B(f, t_n)$	Bistatic received signal phase term	
$\varphi'_B(t_n)$	Bistatic received signal phase term for $f = f_0$	
ω	Angular frequency (pulsatance)	[rad/s]
$\omega_{M,1}$	First frequency variable in monostatic configuration (MVM and APES)	
$\omega_{M,2}$	Second frequency variable in monostatic configuration (MVM and APES)	
$\omega_{B,1}$	First frequency variable in bistatic configuration (MVM and APES)	
$\omega_{B,2}$	Second frequency variable in bistatic configuration (MVM and APES)	
Δ_1	Cross-range migration parameter due to K_1	[m]
Δ_2	Cross-range migration parameter due to K_2	[m]
Δ_{crg}	Cross-range (Doppler) migration parameter	[m]
$\Delta_{crg,0}$	Cross-range (Doppler) linear distortion parameter	[m]
$\Delta_{crg,1}$	Cross-range migration parameter due to the target rotation	[m]
$\Delta_{crg,2}$	Cross-range migration parameter due to the bistatic angle variation	[m]
Δ_{rng}	Range migration parameter	[m]
$\Delta_{rng,1}$	Range migration parameter due to the target rotation	[m]
$\Delta_{rng,2}$	Range migration parameter due to the bistatic angle variation	[m]
Δ_ν	Bistatic Doppler linear shift	[Hz]
$\bar{\Theta}_{el}$	Mean Incidence Angle	[deg]
$\mathbf{a}_P$	P-length Fourier vector (MVM and APES)	
$\mathbf{f}$	Vectorized target/scene reflectivity function	
$\mathbf{g}$	Vectorized SAR/ISAR image	
$\mathbf{h}$	Space-variant FIR filter (MVM and APES)	
$\mathbf{i}_v$	Target velocity unit vector	
$\mathbf{i}_{LoS}$	Monostatic Line of Sight	
$\mathbf{i}_{LoSBi}$	Bistatic Line of Sight	
$\mathbf{i}_{LoSRX}$	Receiver Line of Sight	
$\mathbf{i}_{LoSTX}$	Transmitter Line of Sight	
$\mathbf{i}_\Omega$	Effective angular rotation unit vector	

$\mathbf{n}$	Zero-mean white Gaussian thermal noise vector	
$\mathbf{s}$	Vectorized received signal	
$\mathbf{s}_i$	i^{th} subaperture of $\mathbf{s}$	
$\mathbf{v}$	Target velocity vector	[m/s]
$\mathbf{w}_{\text{BE}}$	Inverse filter impulse response (SSVA)	
$\mathbf{x}$	Source signal vector (Compressed Sensing)	
$\mathbf{y}$	Recorded signal vector (Compressed Sensing)	
$\mathbf{z}$	Generic scatterer position in T_z	[m]
$\mathbf{z}_i$	i^{th} scatterer position in T_z	[m]
$\hat{\mathbf{A}}_H$	Vector of the estimated complex amplitudes of the detected scatterers in the high-resolution image (scatterer position based comparison algorithm)	
$\hat{\mathbf{A}}_S$	Vector of the estimated complex amplitudes of the detected scatterers in the super-resolved image (scatterer position based comparison algorithm)	
$\mathbf{D}$	Diagonal matrix for SVD deconvolution algorithm	
$\mathbf{D}_j$	Distance vector for the j^{th} scatterer/peak (scatterer position based comparison algorithm)	
$\mathbf{H}$	Point Spread Function matrix	
$\mathbf{I}$	SAR/ISAR image matrix	
$\mathbf{I}_{CS}$	Reconstructed image (Compressed Sensing)	
$\mathbf{I}_{\text{SVA}}$	SAR/ISAR image after SVA	
$\mathbf{I}_{\text{SSVA}}$	SAR/ISAR image after SSVA	
$\mathbf{J}_P$	$P \times P$ reversal matrix	
$\mathbf{L}$	Linear operator for MMSE deconvolution algorithm	
$\mathbf{O}_P$	$P \times P$ matrix of ones	
$\mathbf{P}$	Priority vector (scatterer position based comparison algorithm)	
$\mathbf{P}_{S,crg}$	Vector of scatterers' position along the cross-range direction	
$\mathbf{P}_{S,rng}$	Vector of scatterers' position along the range direction	
$\mathbf{P}_{P,crg}$	Vector of peaks' position along the cross-range direction	
$\mathbf{P}_{P,rng}$	Vector of peaks' position along the range direction	
$\mathbf{P}_P$	Vector of the scatterers close enough to the selected peak (scatterer position based comparison algorithm)	

$\mathbf{P}_S$	Vector of the peaks close enough to the selected scatterer (scatterer position based comparison algorithm)	
$\mathbf{Q}_s$	Noise and interference Covariance matrix (APES)	
$\mathbf{R}_x$	Covariance matrix of the random variable x	
$\mathbf{R}_B$	Backward Covariance matrix	
$\mathbf{R}_F$	Forward Covariance matrix	
$\mathbf{R}_{M,C}$	Complex mobile cross-correlation map	
$\mathbf{R}_{M,I}$	Intensity mobile cross-correlation map	
$\mathbf{S}$	Received signal matrix	
$\mathbf{S}_C$	Complete source data matrix (Compressed Sensing)	
$\hat{\mathbf{S}}_C$	Reconstructed complete source data matrix (Compressed Sensing)	
$\mathbf{S}_{\text{SVA}}$	Received signal after SVA	
$\mathbf{S}_{\text{SVA-BE}}$	Received signal after SVA and Bandwidth Extrapolation	
$\mathbf{T}$	Toeplitz convolution matrix	
$\mathbf{U}$ and $\mathbf{V}$	Orthogonal matrices for SVD deconvolution algorithm	
$\mathbf{W}_{\text{BE}}$	Inverse filter (SSVA)	
$\mathbf{Y}$	Re-ordered received signal matrix (MVM and APES)	
$\boldsymbol{\Theta}$	Undercomplete Fourier matrix (Compressed Sensing)	
$\boldsymbol{\Phi}$	Sensing matrix (Compressed Sensing)	
$\boldsymbol{\Psi}$	Dictionary matrix (Compressed Sensing)	
$\boldsymbol{\Omega}_{eff}$	Effective angular rotation vector	[rad/s]
$\boldsymbol{\Omega}_{t,TX}$	Rotation vector due to the target translation with respect to the transmitter	[rad/s]
$\boldsymbol{\Omega}_{t,RX}$	Rotation vector due to the target translation with respect to the receiver	[rad/s]
$\boldsymbol{\Omega}_A$	Target angular velocity vector	[rad/s]
$\boldsymbol{\Omega}_{Bi,eff}$	Bistatic effective angular rotation vector	[rad/s]
$\boldsymbol{\Omega}_{LoS}$	Component of $\boldsymbol{\Omega}_T$ parallel to the LoS	[rad/s]
$\boldsymbol{\Omega}_{RX}$	Total angular rotation vector with respect to the receiver	[rad/s]
$\boldsymbol{\Omega}_T$	Total angular rotation vector	[rad/s]
$\boldsymbol{\Omega}_{TX}$	Total angular rotation vector with respect to the transmitter	[rad/s]

To my parents, colleagues and friends.

Chapter 1

Introduction

1.1 Historical Context

Radar is a remote sensing technology that emits electromagnetic (e.m.) waves to detect objects by sensing the e.m. echo. A radar system consists of a transmitter, a receiver, an antenna, a signal processing unit and display unit. The radar transmitter radiates an e.m. radio wave or microwave signal and the echo backscattered by the target is sensed by the receiver. Transmitter and receiver can generally be co-located (monostatic radar) or placed in different locations (bistatic radar). Then, the signal processing unit extracts the information of interest by means of opportune signal and data processing methods.

The term *RADAR* is an acronym for RAdio Detection And Ranging and was coined by the United States Navy in 1940.

The history of radar starts in the late 19th century with Guglielmo Marconi and Heinrich Hertz experiments about e.m. propagation. In 1904 Christian Hülsmeyer introduced an early shipborne warning detection system based on Hertz's apparatus [1]. However, Hülsmeyer's "Telemobiloscope" prototype [2] had no success because of its short range.

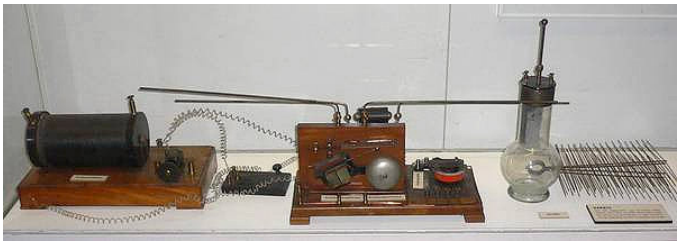

FIGURE 1.1: The *telemobiloscope*, now at the Deutsches Museum Masterpieces of Science and Technology, Munich, Germany.

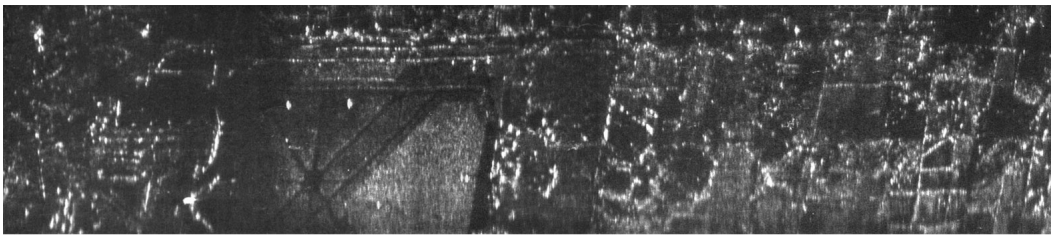

FIGURE 1.2: Willow Run Airport and vicinity, August 1957. Image courtesy University of Michigan (by https://en.wikipedia.org/wiki/Synthetic_aperture_radar).

First radar systems with improved range were made at the US Naval in the 1920s to measure the height of the ionosphere and in the 1930s for aircraft detection purposes by means of continuous-wave radar. In 1935, Sir Robert Watson-Watt patented the first radar system.

At the start of World War II, in September 1939, the US, UK, Germany, France, the Soviet Union, Japan, Italy, and the Netherlands had independently and almost simultaneously discovered and explored radar. During World War II Watson-Watt's team in the UK introduced a pulsed technique to measure the range of aircraft and, by the end of the war, radar systems were able to measure range and angle of targets. In 1938 the British turned on the first operational low frequency radar system for air defense, called the Chain Home. These radars are given credit for allowing the British to defend against the large German air attacks in 1940, the Battle of Britain [3].

Synthetic Aperture Radar (SAR) was invented in 1951 by Carl A. Wiley [4], a mathematician at Goodyear Aircraft Company in Litchfield Park, Arizona. Wiley realized that a much longer aperture can be synthesized by using the Doppler spectrum of the received signal if collected when the radar is moving along a straight path. Such a longer aperture allowed to resolve very close targets in the along-track dimension. The first experimental demonstrations was performed in 1953 by a group at the University of Illinois. An X-band radar was installed in a C-46 aircraft provided by and operated by the U.S. Air Force and used to study reflected signals from ground and sea in Key West, Florida. The first operational system (classified) was built in 1957 by the Willow Run Laboratories of the University of Michigan for the US Department of Defense. The first successful focused airborne SAR image produced with such a system is shown in Fig.1.2. The first Earth-orbiting spaceborne SAR, the SEASAT system, was launched by NASA on June 27th, 1978, for oceanographic purposes. The SEASAT system provided important results for ice and land studies also and demonstrated the importance of radar imaging for the observation of the Earth. The first documents about Inverse Synthetic Aperture Radar (ISAR) was published by Jack L. Walker [5], C.C. Chen and H.C. Andrews [6, 7] in 1980. Ausherman's publication in collaboration with Walker in 1984 [8] is worth being mentioned too.

1.2 Background and motivation

1.2.1 SAR/ISAR Radar imaging

Radar imaging is an application of radar which is used to create two-dimensional e.m. images. Finer spatial resolution is achieved by exploiting the relative motion between the radar antenna and the target/scene of interest. In such e.m. images, resolution along the slant-range direction depends on the transmitted signal frequency bandwidth, whereas resolution along the Doppler, angular, or cross-range direction depends on the antenna aperture, regardless of whether such an aperture is physical (a large antenna) or "synthetic"(a moving antenna). The synthetic aperture does not depend on the actual size of the antenna. A large synthetic aperture is achieved when a moving antenna receives the backscattered e.m. echo in different locations, i.e., when a "synthetic" antenna array is created.

Actually, the synthetic antenna aperture depends on the relative motion/rotation between radar antenna and target. Synthetic Aperture Radar (SAR) imaging is achieved when the scene illuminated by the antenna beam is stationary and the antenna is placed on a moving platform, e.g., an aircraft (airborne SAR), a satellite (spaceborne SAR) or a platform moving along a rail track (ground based SAR). In this case the geometry is perfectly known and the focused SAR image is obtained by compensating the relative motion between the antenna and the illuminated scene. Typical SAR applications are environmental monitoring, intelligence, topography, foliage penetration and even space exploration. For example, the Magellan spacecraft, also referred to as the Venus Radar Mapper, was a robotic space probe launched by NASA on May 4th, 1989 to map the surface of Venus by using synthetic aperture radar (see Fig.1.3).

Optical imagers are generally low power devices and can achieve much finer resolution than SAR. However, SAR works independently from the day/night and atmospheric conditions and is unaffected by clouds, fog, or other impairments to visibility. SAR signals can also penetrate foliage and dry ground for useful reconnaissance purposes [9]. On the other hand, when the radar antenna is stationary and the target is moving, the antenna aperture is generated by the target motion. In this case, we refer to Inverse Synthetic Aperture Radar (ISAR). Initially, the name ISAR was derived from SAR by simply considering the different radar-target dynamic where the radar platform is stationary and the target moves. However, the real difference between ISAR and SAR lies in the non-cooperation of the ISAR target. When the target is non-cooperative, the radar-target relative motion is unknown. As a consequence, the antenna aperture size and the cross-range resolution are unknown. Moreover, the radar-target distance must be compensated by means of appropriate post-processing algorithms.

FIGURE 1.3: Magellan full resolution SAR image of Lakshmi Planum and Maxwell Montes, Venus (by http://photojournal.jpl.nasa.gov/catalog/PIA00241).

ISAR imaging is a very useful radar application for surveillance, Automatic Target Recognition (ATR) and even deep space imaging of asteroids. A particularly beautiful example of this is the so-called "dog's bone" 216 Kleopatra M-class asteroid. 216 Kleopatra was discovered by Austrian astronomer Johann Palisa on April 10th, 1880 and "imaged" by means of the S-band radar system of the Arecibo Observatory in November 1999 [10] (see Fig.1.4). Furthermore, ISAR processing allows to obtain well focused images of moving targets which appear defocused in SAR imagery.

Another important aspect is the distinction between monostatic and bistatic radar systems. In monostatic radar, transmitter and receiver antennas are co-located. Bistatic radar is instead when transmitter and receiver are located in separated positions. Such a configuration brings some advantages to the radar system that extend to the radar imaging application. Typical geometrical limitations of monostatic radar imaging can be overcome by a bistatic configuration. Furthermore, different scattering mechanism in bistatic configuration can enable radar imaging of stealth targets. Bistatic (and multistatic) radar imaging is a useful tool for several applications, such as passive radar imaging [11], resolution enhancement by means of data fusion [12], 3D interferometric ISAR [13] and ATR [14]. However, bistatic/multistatic radar introduces networking and synchronization issues and distorting effects due to the bistatic geometry. Effects of the bistatic configuration on ISAR imaging are treated in [15] and [16]. Considerations about bistatic ISAR image plane and bistatic effective rotation vector and resolution are discussed in [17], whereas the effects of bistatic angle variations and synchronization errors on B-ISAR imaging have been analyzed in [18].

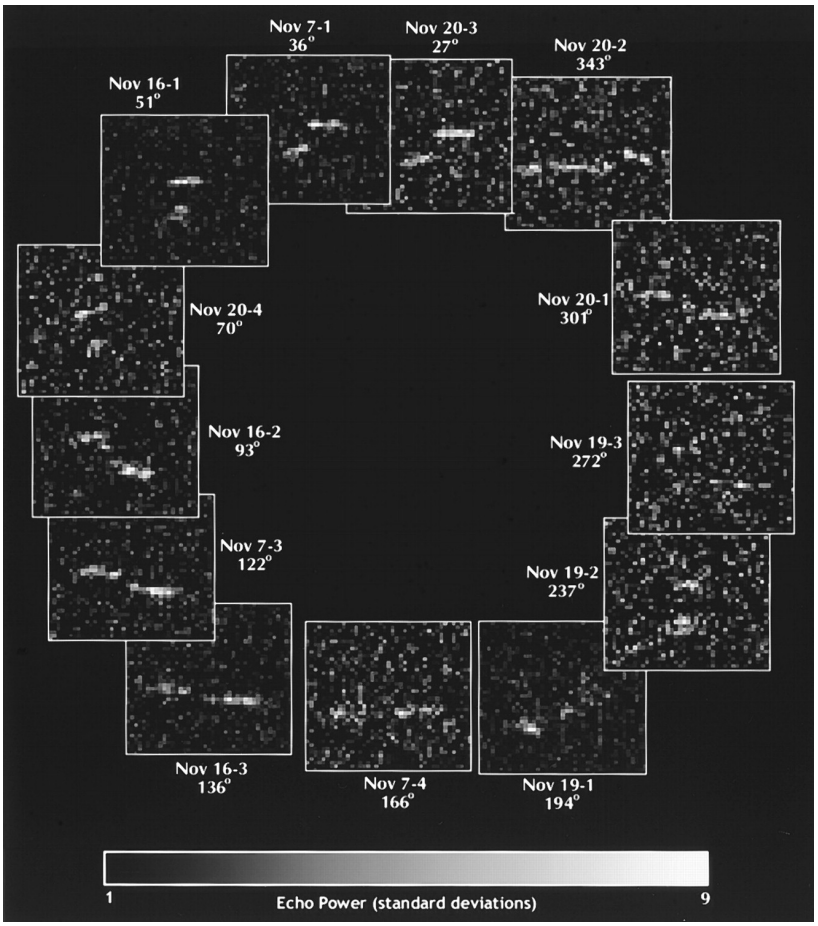

FIGURE 1.4: Radar images organized by relative rotation phase of the 216 Kleopatra asteroid, Arecibo Observatory, November 1999.

1.2.2 Super-resolution

SAR/ISAR imaging can be interpreted as a parameter estimation problem in which one seeks to estimate the e.m. signal intensity backscattered by the target/scene, i.e., an intensity image. Conventional radar imaging is performed by means of Fourier methods for estimating the target/scene reflectivity function. However, conventional Fourier methods present some limitations, which include the imaging system resolution.

"Resolution" is defined as the system capability to make different scattering sources separately observable. For example, δ_{rng} is defined as the "range resolution" if two scattering sources can be distinguished along the range direction only if the range distance between them is smaller than δ_{rng}.

In the SAR/ISAR imaging context, the image resolution in the slant-range dimension depends on the transmitted signal bandwidth. When conventional imaging is performed

$$\delta_{rng} = \frac{c}{2B} \tag{1.1}$$

where B is the transmitted signal frequency bandwidth and c is the speed of light in a vacuum. Wide band systems allows to achieve high-resolution images that can be used for several applications. For example, the PAMIR radar system is an X-band airborne SAR/MTI (Synthetic Aperture Radar/Moving Target Indication) experimental instrument by FGAN/FHR with a total signal bandwidth of about 1.8GHz and a slant-range resolution of about 10cm [19]. On the other hand, the Pi-SAR (Polarimetric and interferometric SAR), developed by the National Institute of Information and Communications Technology (NICT) and the Japan Aerospace Exploration Agency (JAXA), is a dual-frequency fully polarimetric airborne SAR system with 100MHz bandwidth in X-band and 50MHz in L-band, which means range resolution of 1.5m and 3m respectively [20].

Image resolution along the cross-range direction depends on the angular aperture of the synthetic antenna array, i.e., the total angular rotation of the target with respect to the radar point of view. In ISAR, the synthetic antenna aperture depends on the Coherent Processing Interval (CPI) and is generally unknown. In this case cross-range resolution is unknown and does not depend on the radar characteristics. Cross-range resolution can be improved by increasing the CPI, but long CPI involves several drawbacks:

1. ISAR imaging is based on the assumption that the target effective rotation vector is approximately constant during the whole CPI. If this constraint is not satisfied, a well focused ISAR image cannot be obtained. Obviously, the longer the CPI, the wider the effective rotation vector variations.

2. The longer the CPI, the larger amount of data the radar system have to store in the physical memory. A larger amount of data means that the signal processing stage will need more better-performing and expensive hardware resources. Data storage requirement could be reduced by reducing the sampling frequency at the output of the ADC in the receiver radar system, but lower sampling frequency means lower maximum non-ambiguous radial speed.

3. When a large target moves with high speed, different parts of its body could migrate from a range/Doppler resolution cell to another. This is the range/Doppler migration issue that does not allow for a well focused image to be generated. The relationship between CPI and range/Doppler migration is discussed in Chapter 2.

4. In real scenario, the target radar cross-section is not isotropic. The backscattered signal from a certain target scatterer can drastically change within few degrees depending on material, shape and interaction with other scatterers. In this case, there is no coherent integration in the Doppler compression step of the range-Doppler ISAR imaging algorithm and a well focused ISAR image cannot be obtained. This aspect effectively limits the cross-range resolution in ISAR imaging.

In this context, super-resolution and spectral estimation techniques become useful to overcome the resolution limitations in conventional range-Doppler imaging. A super-resolution technique can be interpreted either as a post-processing algorithm, which can be applied to a SAR/ISAR image, or as a substitute of the conventional range-Doppler imaging algorithm in order to exceed the resolution limitations due to the transmitted signal bandwidth and target aspect angle variation. For example, de-convolution techniques aim to invert the convolution operation with a known Point Spread Function (PSF). If the SAR/ISAR image can be modeled as the convolution between the scene/target high-resolution reflectivity function and the imaging PSF, de-convolution techniques can be considered as super-resolution algorithms. Furthermore, all techniques that aim to estimate/reconstruct the received signal beyond the available time/frequency support are super-resolution techniques.

Super-resolution and spectral estimation techniques exploit the received signal model which must be as accurate as possible. For example, the MUSIC spectral estimation technique considers a target/scene model composed by a finite number of point-like scatterers, Capon's Minimum Variance Method models the spatial frequency components of the received signal as complex sinusoids and the linear prediction based bandwidth extrapolation technique exploits an autoregressive modeling of the received signal.

In general, such signal models refer to the standard monostatic ISAR model and do not take into account distortion effects such as range migration. In bistatic/multistatic configuration, the standard monostatic received signal model is not generally accurate and the effects of the bistatic geometry must be taken into account. As a consequence, the applicability of super-resolution standard algorithms in case of bistatic geometry is not guaranteed.

In this Thesis, B-ISAR and super-resolution topics are firstly treated separately. Novel aspects about the bistatic geometry effects on radar imaging are discussed and constraints for bistatic linear and quadratic distortions are derived. After a super-resolution literature review, the most common techniques, studied and implemented during the research activity, are treated in deep and novel methods for super-resolution performance analysis and comparison are proposed. Super-resolution is then theoretically treated and validated by considering the bistatic received signal model. Furthermore, a novel super-resolution based method for bistatic distortion mitigation is proposed. Different super-resolution techniques are finally tested, evaluated and compared on simulated data for bistatic distortion mitigation purposes and on both monostatic and bistatic real data for performance comparison.

1.3 Innovative aspects

The main contributions of this Thesis are:

- Further analysis of the bistatic geometry effects in ISAR image formation. The second order approximation for the bistatic angle and the bistatic distortion term $K(t)$ is demonstrated to be fundamental to the analytical study of the bistatic quadratic distortions.
- Novel methods for super-resolution performance analysis are introduced and applied to test and compare standard super-resolution techniques on both monostatic and bistatic real data.
- Linear prediction based Bandwidth Extrapolation, Capon's MVM and APES spectral estimation, Super-SVA and Compressed Sensing based super-resolution are theoretically validated in case of bistatic configuration by exploiting the bistatic received signal model and the BEM approximation.
- A novel super-resolution based method for bistatic distortion mitigation is proposed and validated by means of simulated data. Linear prediction based Bandwidth Extrapolation, Super-SVA and Compressed Sensing are applied, evaluated and compared when used for mitigating bistatic distortions.

1.4 Thesis organization

This Thesis is organized as follows.

In Chapter 2 the B-ISAR theory is recalled. By referring to [15–17], the bistatic signal model is exploited for further analysis of the bistatic geometry effects in ISAR image formation. Bistatic quadratic distortions are analyzed in deep and constraints for bistatic range and Doppler migration are analytically derived and validated by means of simulated data.

In Chapter 3 the concept of super-resolution radar imaging is introduced and the most common super-resolution techniques are reviewed. Some of those super-resolution techniques implemented during the research activity are treated in deep in case of monostatic radar configuration.

In Chapter 4 novel super-resolution performance analysis methods are proposed. Such methods are exploited to evaluate and compare the super-resolution techniques treated in Chapter 3. Real monostatic radar data is exploited to test such techniques.

In Chapter 5 the super-resolution techniques treated in Chapter 3 are theoretically validated by considering the bistatic received signal model. A novel bistatic distortion mitigation method based on super-resolution is proposed and validated by means of simulated data. Super-resolution is then tested on real bistatic data with comprehensive performance analysis and comparison.

Chapter 6 concludes the Thesis by summarizing the findings and achievements of this study and discussing directions for future work.

1.5 List of publications

The following papers have been published during the research activities:

1. Martorella, M. ; Cataldo, D. ; Brisken, S.,
   "Bistatically equivalent monostatic approximation for bistatic ISAR",
   Radar Conference (RADAR), 2013 IEEE, 2013, Page(s): 1-5,
   Digital Object Identifier: 10.1109/RADAR.2013.6586074.

2. Stagliano', D. ; Musetti, L. ; Cataldo, D. ; Baruzzi, A. ; Martorella, M.,
   "Fast detection of maritime targets in high resolution SAR images",
   2014 IEEE Radar Conference, pages 0522-0527, May 2014,
   Digital Object Identifier: 10.1109/RADAR.2014.6875647.

Submitted:

3. Cataldo, D. ; Martorella, M.,
   "Super-resolution for bistatic distortion mitigation",
   2016 IEEE Radar Conference, pages 431-436, May 2016.

4. Bacci, A. ; Giusti, E. ; Cataldo, D. ; Tomei, S. ; Martorella, M.,
   "ISAR Resolution Enhancement via Compressive Sensing: a Comparison with state of the art SR Techniques",
   4th International Workshop on Compressed Sensing Theory and its Applications to Radar, Sonar, and Remote Sensing (CoSeRa 2016), September 2016.

Co-author in:

4. Fabrizio Berizzi, Marco Martorella, Elisa Giusti
   "Radar Imaging for Maritime Observation",
   June 6, 2016 Forthcoming by CRC Press
   Reference - 384 Pages - 220 B/W Illustrations
   ISBN 9781466580817 - CAT# K18853
   Series: Signal and Image Processing of Earth Observations

In editing:

5. Giusti, E. ; Cataldo, D. ; Bacci, A. ; Tomei, S. ; Martorella, M.,
   "Resolution Enhancement: Compressive Sensing vs State of the Art"
   To be submitted to: IEEE Transactions on Aerospace and Electronic Systems

Chapter 2

Monostatic and Bistatic ISAR

In this Chapter the ISAR signal general model, the geometry and the notation used in this Thesis are introduced and the range-Doppler (RD) imaging method for the ISAR image generation is recalled. The reference geometry and the received signal model for the most general case are introduced in Section 2.1. In Sections 2.2 and 2.3 the calculations for monostatic and bistatic ISAR image formation are recalled with exhaustive analysis regarding the range and Doppler migration effects. In Section 2.4 the bistatic distortion theoretical study is validated by means of simulated example data.

2.1 Signal Model Introduction

The acquisition geometry is shown in Fig.2.1 where two main reference systems are introduced:

- $T_z(z_1, z_2, z_3)$: Cartesian reference system embedded on the target;
- $T_\xi(\xi_1, \xi_2, \xi_3)$: Cartesian reference system embedded on the transmitter.

R_{TxTg}, R_{RxTg} and R_{TxRx} represent the transmitter-target, receiver-target and transmitter-receiver (baseline) distances respectively, β is the bistatic angle and $\mathbf{i}_{LoSBi}$ is the Bistatic Line of Sight (B-LoS) unit vector aligned with the bistatic angle bisector. This geometry represents a general model and can be used for both monostatic and bistatic radar configurations.

Assuming that the target is stationary during the transmission and reception of a sweep or a pulse (*stop & go* assumption), the slow-time can be considered a discrete variable, i.e., $t_n \doteq nT_R$ with $n = -\frac{N}{2}, \ldots, \frac{N}{2}$ where T_R denotes the Pulse Repetition Interval

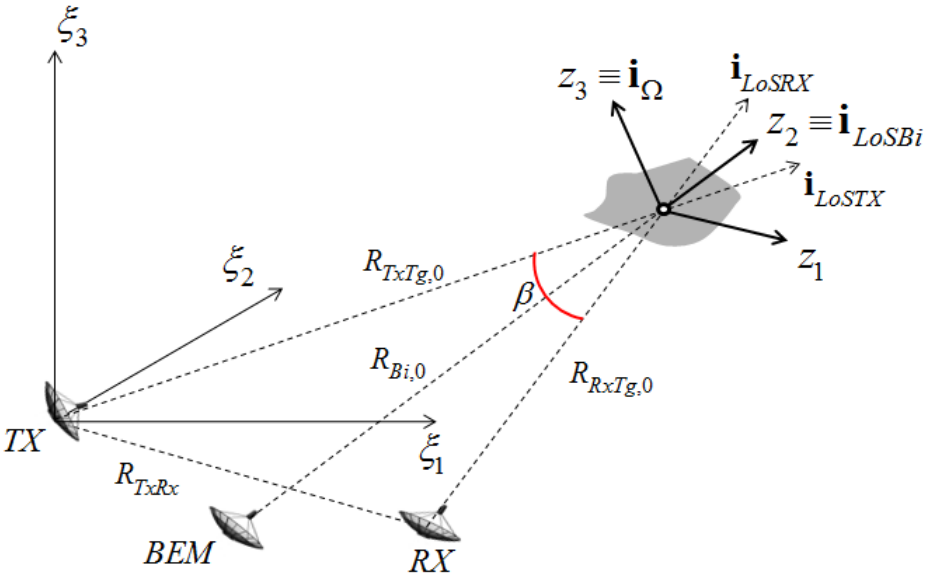

FIGURE 2.1: Bistatic geometry representation.

(PRI) and N is the number of transmitted sweeps. The product NT_R is defined as the Coherent Processing Interval (CPI) or Observation Time (T_{ob}).

Under the *far field* condition the received signal in the fast-time/slow-time domain is modeled as follows

$$s_R(t_v, n) = \int_V \gamma'(\mathbf{z})\, s_T(t_v - \tau(\mathbf{z}, n), n)\, h\,(n)\, d\mathbf{z} \tag{2.1}$$

where $s_T(t_v, n)$ is the transmitted signal within the n^{th} sweep, t_v denotes the fast-time variable and

$$\tau(\mathbf{z}, n) = \frac{R_{TxTg}(\mathbf{z}, n) + R_{RxTg}(\mathbf{z}, n)}{c} \tag{2.2}$$

is the delay-time for a point scatterer on the target with coordinates $\mathbf{z}$ in T_z at the n^{th} sweep, c is the speed of light in a vacuum and $h\,(n)$ is the signal support in the slow-time domain defined in (2.3).

$$h\,(n) = \begin{cases} 1 & \text{if } n = -\frac{N}{2}, \ldots, \frac{N}{2} \\ 0 & \text{otherwise} \end{cases} \tag{2.3}$$

$\gamma'(\mathbf{z})$ is the target reflectivity function at coordinates $\mathbf{z}$ and V is the volume occupied by the target. Actually, γ' should be dependent on n since the reflectivity function of a certain point of a real target is not isotropic. The reflectivity function of a scatterer depends on the target orientation with respect to the radar (both transmitter and receiver) and may change within few degrees. Moreover, the Radar Cross-Section (RCS) is also

a function of the incident electromagnetic (e.m.) wave frequency. However, the CPI is assumed to be small enough to make γ' essentially constant during the whole acquisition.

The received signal in (2.1) is given as input to the matched filter and the baseband output signal, after Fourier transforming along the fast-time domain, can be expressed in the frequency/slow-time domain as follows

$$S_R(f,n) = W(f,n) \int_V \gamma'(\mathbf{z}) e^{-j2\pi f \tau(\mathbf{z},n)} d\mathbf{z} \tag{2.4}$$

where f denotes the frequency, i.e., the Fourier transform variable of the fast-time t_v, and $W(f,n)$ is defined as follows

$$W(f,n) = h(n) \text{ rect} \left[\frac{f - f_0}{B} \right] \tag{2.5}$$

where f_0 is the carrier frequency of the transmitted signal, B is the frequency bandwidth and

$$\text{rect}[x] \doteq \begin{cases} 1 & \text{if } |x| \leq \frac{1}{2} \\ 0 & \text{otherwise} \end{cases} \tag{2.6}$$

2.2 Monostatic Configuration

In this Section the particular case of the monostatic configuration is considered and the method for the ISAR image formation, i.e., the RD technique, is summarized. In the monostatic case transmitter and receiver are co-located. This means that $\beta = 0$, $R_{TxTg} = R_{RxTg} = R$, $R_{TxRx} = 0$ and (2.2) can be simplified as follows

$$\tau(\mathbf{z},n) = \frac{2R(\mathbf{z},n)}{c} \tag{2.7}$$

Under the *straight iso-range approximation*, i.e., radar-target distance much greater than the target size, the delay-time $\tau(\mathbf{z},n)$ can be approximated as follows

$$\tau(\mathbf{z},n) \simeq \frac{2}{c} \left[R_0(n) + \mathbf{z} \cdot \mathbf{i}_{LoS}(n) \right] \tag{2.8}$$

where $\mathbf{i}_{LoS}(n)$ is the monostatic radar Line of Sight (LoS) unit vector, $R_0(n)$ is the distance between the monostatic radar and the target focusing center and the $\cdot$ operator denotes the scalar product. In (2.8), the radar-target distance $R_0(n)$ and the LoS unit vector depend on the discrete slow-time variable n, whereas the scatterer position $\mathbf{z}$ is assumed to be constant during the whole CPI because the target is considered as a rigid body.

The target motion with respect to the radar during the CPI is modeled as the sum of two components: a radial translational motion (with respect to the LoS) and a rotational component described by means of the total angular rotation vector $\mathbf{\Omega}_T(n)$. The radar-target distance $R_0(n)$ in (2.8) is assumed to be perfectly compensable by means of any available autofocusing technique [21, 22]. The total angular rotation vector $\mathbf{\Omega}_T(n)$ is then modeled as the sum of a component parallel to the LoS and an orthogonal one as follows

$$\mathbf{\Omega}_T(n) = \mathbf{\Omega}_{LoS}(n) + \mathbf{\Omega}_{eff}(n) = \|\mathbf{\Omega}_{LoS}(n)\|\, \mathbf{i}_{LoS}(n) + \mathbf{\Omega}_{eff}(n) \tag{2.9}$$

where $\mathbf{\Omega}_{eff}(n) \perp \mathbf{i}_{LoS}(n)$ is the *effective rotation vector* that effectively contributes to the ISAR image formation. Both $\mathbf{\Omega}_T(n)$ and $\mathbf{\Omega}_{eff}(n)$ are expressed in radiants per second [rad/s]. Assuming the effective rotation vector to be constant within the CPI, i.e., $\mathbf{\Omega}_{eff}(n) \simeq \mathbf{\Omega}_{eff}$, the resultant compensated signal can be written as follows

$$\begin{aligned} S(f,n) &= W(f,n) \int_V \gamma'(\mathbf{z}) e^{-j\frac{4\pi f}{c}[\mathbf{z}\cdot\mathbf{i}_{LoS}(n)]} d\mathbf{z} \\ &= W(f,n) \int_{z_1}\int_{z_2} \gamma(z_1,z_2) e^{-j\frac{4\pi f}{c}\left[z_1 \sin(\Omega_{eff} t_n) + z_2 \cos(\Omega_{eff} t_n)\right]} dz_1 dz_2 \end{aligned} \tag{2.10}$$

where $\gamma(z_1,z_2) \doteq \int_{z_3} \gamma'(\mathbf{z}) dz_3$ is the projection of the target reflectivity function onto the Image Projection Plane (IPP), i.e., that plane orthogonal to the effective rotation vector direction. This is because the phase term in (2.10) does not depend on z_3. The result in (2.10) is obtained by setting the reference system T_z in order to have

$$\mathbf{i}_{z_2} \equiv \mathbf{i}_{LoS}(0) \tag{2.11}$$

$$\mathbf{i}_{z_3} \equiv \mathbf{i}_{\Omega} \tag{2.12}$$

$$\mathbf{i}_{z_1} = \mathbf{i}_{z_2} \times \mathbf{i}_{z_3} \tag{2.13}$$

where $\mathbf{i}_{z_1}$, $\mathbf{i}_{z_2}$ and $\mathbf{i}_{z_3}$ are the unit vectors which define the axis of T_z and $\mathbf{i}_{\Omega}$ is the effective rotation unit vector (see Fig.2.1). As a consequence of a short CPI, the product $\Omega_{eff} t_n$ is in general $\ll 1$ and the sine and cosine functions in (2.10) can be approximated by means of the Taylor-Maclaurin polynomial. In the following, a second order approximation for the sine and cosine functions is used as shown below

$$\sin(x) \simeq x \tag{2.14}$$

$$\cos(x) \simeq 1 - \frac{x^2}{2} \tag{2.15}$$

For the sake of simplicity, consider a target composed of a single point-like scatterer with complex reflectivity function A in position $(z_{1,0}, z_{2,0})$

$$\gamma(z_1, z_2) = A\delta(z_1 - z_{1,0})\delta(z_2 - z_{2,0}) \tag{2.16}$$

where

$$A = \int_{z_1}\int_{z_2} \gamma(z_{1,0}, z_{2,0}) dz_1 dz_2 \tag{2.17}$$

and $\delta(x)$ is the Dirac delta function. Therefore, (2.10) can be approximated as follows

$$S(f, n) \simeq W(f, n)\, A\, e^{-j2\pi\varphi(f,n,z_{1,0},z_{2,0})} \tag{2.18}$$

where

$$\varphi(f, n, z_{1,0}, z_{2,0}) = \frac{2f}{c} R'(t_n, z_{1,0}, z_{2,0}) \tag{2.19}$$

is the received signal phase term and

$$R'(t_n, z_{1,0}, z_{2,0}) = \mathbf{z}\cdot \mathbf{i}_{LoS}(n) \simeq z_{1,0}\Omega_{eff} t_n + z_{2,0} - z_{2,0}\frac{\Omega_{eff}^2 t_n^2}{2} \tag{2.20}$$

is defined as the scatterer *effective range*. In the following, the ISAR image is derived by means of the RD method. To obtain the Point Spread Function (PSF) of the ISAR system, two Inverse Fourier Transforms (IFTs) are analytically calculated below.

2.2.1 Range Compression

The range compression is obtained by transforming the signal in (2.18) with respect to the frequency coordinate as follows

$$\begin{aligned} S'_R(\tau, n) &= \mathcal{FT}^{-1}_{f\to\tau}\{S(f, n)\} \\ &= \int_{-\infty}^{\infty} W(f, n)\, A\, e^{-j2\pi f \frac{2}{c} R'(t_n,z_{1,0},z_{2,0})} e^{j2\pi f\tau} df \\ &= A\,\tilde{w}\left(\tau - \frac{2}{c}R'(t_n, z_{1,0}, z_{2,0}), t_n\right) \\ &= AB\, h(n)\,\mathrm{sinc}\left\{B\left[\tau - \frac{2}{c}R'(t_n, z_{1,0}, z_{2,0})\right]\right\} e^{j2\pi f_0\left[\tau - \frac{2}{c}R'(t_n,z_{1,0},z_{2,0})\right]} \\ &= AB\, h(n)\,\mathrm{sinc}\left\{B\left[\tau - \frac{2}{c}R'(t_n, z_{1,0}, z_{2,0})\right]\right\} e^{j2\pi f_0\tau} e^{-j2\pi\varphi'(t_n,z_{1,0},z_{2,0})} \end{aligned} \tag{2.21}$$

where

$$\tilde{w}(\tau, t_n) = \mathcal{FT}^{-1}_{f\to\tau}\{W(f, n)\} = h(n)\, B\,\mathrm{sinc}(B\tau) e^{j2\pi f_0\tau} \tag{2.22}$$

$$\varphi'(t_n, z_{1,0}, z_{2,0}) = \frac{2f_0}{c} R'(t_n, z_{1,0}, z_{2,0}) = \frac{2f_0}{c}\left[z_{1,0}\Omega_{eff}t_n + z_{2,0} - z_{2,0}\frac{\Omega_{eff}^2 t_n^2}{2}\right] \quad (2.23)$$

The argument of the sinc function in (2.21) depends on the slow-time variable t_n, then range migration occurs if the total variation of $R'(t_n, z_{1,0}, z_{2,0})$ exceeds the distance of the range resolution. For the sake of simplicity, in order to determine the condition for the range migration, $R'(t_n, z_{1,0}, z_{2,0})$ is approximated by neglecting the second order term as follows

$$R'(t_n, z_{1,0}, z_{2,0}) \simeq z_{1,0}\Omega_{eff}t_n + z_{2,0} \quad (2.24)$$

Therefore, by referring to Fig.2.2, in order to avoid range migration it is important to satisfy the following condition

$$\left| R'(t_n, z_{1,0}, z_{2,0})\big|_{t_n=\frac{T_{ob}}{2}} - R'(t_n, z_{1,0}, z_{2,0})\big|_{t_n=-\frac{T_{ob}}{2}} \right| = |z_{1,0}\Omega_{eff}|\, T_{ob} < \delta_{rng} \quad (2.25)$$

where

$$\delta_{rng} = \frac{c}{2B} \text{ [m]} \quad (2.26)$$

is the image range resolution.

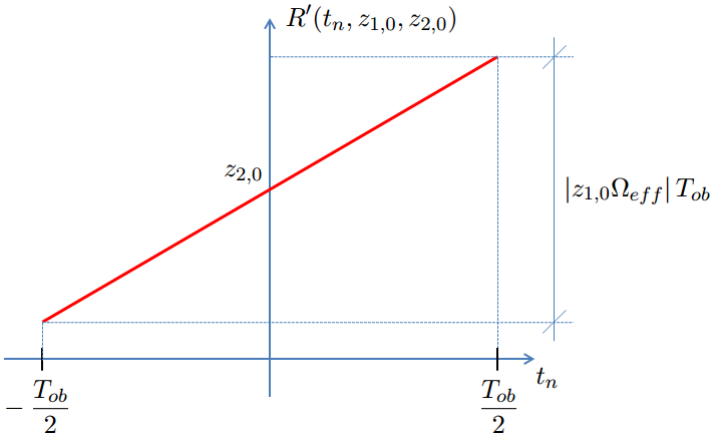

FIGURE 2.2: Range migration graphic for the monostatic configuration.

When the constraint in (2.25) is satisfied, $R'(t_n, z_{1,0}, z_{2,0})$ can be approximated equal to $z_{2,0}$ into the argument of the sinc function and (2.21) can be rewritten as follows

$$\begin{aligned} S'_R(\tau, n) &\simeq AB\, h(n)\, \text{sinc}\left\{B\left[\tau - \frac{2}{c}z_{2,0}\right]\right\} e^{j2\pi f_0 \tau} e^{-j2\pi\frac{2f_0}{c}\left[z_{1,0}\Omega_{eff}t_n + z_{2,0} - z_{2,0}\frac{\Omega_{eff}^2 t_n^2}{2}\right]} \\ &= A\,\delta\left(\tau - \frac{2}{c}z_{2,0}\right) \otimes_\tau \tilde{w}(\tau, t_n)\, e^{-j2\pi\frac{2f_0}{c}\left[z_{1,0}\Omega_{eff}t_n - z_{2,0}\frac{\Omega_{eff}^2 t_n^2}{2}\right]} \end{aligned} \quad (2.27)$$

where $\otimes_\tau$ is the convolution operator over the variable τ.

2.2.2 Doppler Image Formation

Doppler image formation is achieved by taking the IFT of the range-compressed signal in (2.27) along the time variable. The result is a complex image in the time-delay (range) and Doppler domain. The final ISAR image is calculated as follows

$$\begin{aligned} I(\tau,\nu,z_{1,0},z_{2,0}) &= \mathcal{FT}^{-1}_{t_n\to\nu}\left\{S'_R(\tau,n)\right\} \\ &= AB\,\mathrm{sinc}\left\{B\left[\tau-\frac{2}{c}z_{2,0}\right]\right\}e^{j2\pi f_0\left[\tau-\frac{2}{c}z_{2,0}\right]} \\ &\quad \int_{-\infty}^{\infty}\mathrm{rect}\left(\frac{t_n}{T_{ob}}\right)e^{-j2\pi\frac{2f_0}{c}z_{1,0}\Omega_{eff}t_n}\,e^{j2\pi\frac{2f_0}{c}z_{2,0}\frac{\Omega^2_{eff}t_n^2}{2}}\,e^{j2\pi t_n\nu}\,dt_n \\ &= AB\,\mathrm{sinc}\left\{B\left[\tau-\frac{2}{c}z_{2,0}\right]\right\}e^{j2\pi f_0\left[\tau-\frac{2}{c}z_{2,0}\right]} \\ &\quad T_{ob}\,\mathrm{sinc}\left\{T_{ob}\left[\nu-\frac{2f_0}{c}z_{1,0}\Omega_{eff}\right]\right\}\otimes_\nu\ D_2(\nu,z_{2,0}) \\ &= A\,\delta\left(\tau-\frac{2}{c}z_{2,0}\right)\delta\left(\nu-\frac{2f_0}{c}z_{1,0}\Omega_{eff}\right)\otimes_\tau\otimes_\nu w(\tau,\nu)\otimes_\nu D_2(\nu,z_{2,0}) \end{aligned} \tag{2.28}$$

where

$$D_2(\nu,z_{2,0}) = \mathcal{FT}^{-1}_{t_n\to\nu}\left\{e^{-j2\pi\frac{1}{2}\left(\frac{2f_0}{c}z_{2,0}\Omega^2_{eff}\right)t_n^2}\right\} \tag{2.29}$$

$$\begin{aligned} w(\tau,\nu) &= \mathcal{FT}^{-1}_{t_n\to\nu}\left\{\tilde{w}(\tau,t_n)\right\} \\ &= B\,\mathrm{sinc}(B\tau)\,e^{j2\pi f_0\tau}\,\mathcal{FT}^{-1}_{t_n\to\nu}\left\{\mathrm{rect}\left(\frac{t_n}{T_{ob}}\right)\right\} \\ &= B\,T_{ob}\,\mathrm{sinc}(B\tau)\,\mathrm{sinc}(T_{ob}\nu)e^{j2\pi f_0\tau} \end{aligned} \tag{2.30}$$

and $\otimes_\nu$ is the convolution operator over ν. $D_2(\nu,z_{2,0})$ in (2.29) is a chirp-like distortion term and $w(\tau,\nu)$ in (2.30) is the imaging PSF.

For the ISAR analytical calculation in (2.28) and the definition of the imaging PSF in (2.30) it has been chosen to pass from the discrete variable n to the continuous variable t_n. The $h\,(n)$ function defined in (2.3) is transformed to a rect as follows

$$t_n \doteq nT_R \Rightarrow h\,(n) = h\left(\frac{t_n}{T_R}\right) \tag{2.31}$$

$$= \begin{cases} 1 & \text{if } t_n/T_R = -\frac{N}{2},\ldots,\frac{N}{2} \Rightarrow |t_n| \le \frac{T_{ob}}{2} \\ 0 & \text{otherwise} \end{cases}$$

$$= \mathrm{rect}\left(\frac{t_n}{T_{ob}}\right) \tag{2.32}$$

In order to determine a constraint for the Doppler migration, the Doppler frequency introduced by the scatterer in position $(z_{1,0},z_{2,0})$ is calculated by differentiating the

phase term in (2.23) as shown in (2.33).

$$f_d(t_n, z_{1,0}, z_{2,0}) = \frac{\partial \varphi'(t_n, z_{1,0}, z_{2,0})}{\partial t_n} = \frac{2f_0}{c}\left[z_{1,0}\Omega_{eff} - z_{2,0}\Omega_{eff}^2 t_n\right] \tag{2.33}$$

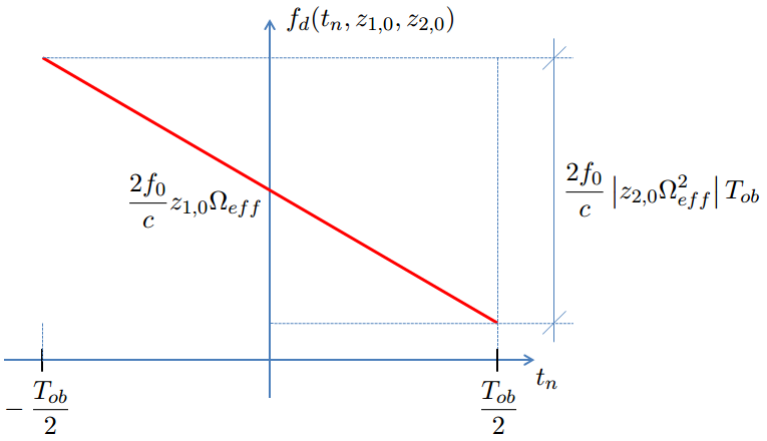

FIGURE 2.3: Doppler migration graphic for the monostatic configuration.

The Doppler frequency in (2.33) is plotted in Fig.2.3. A constraint to verify the absence of quadratic distortions can be obtained by imposing the *Doppler bandwidth* (B_d) smaller than the Doppler resolution as shown in (2.34).

$$\begin{aligned} B_d &= \left| f_d(t_n, z_{1,0}, z_{2,0})|_{t_n=\frac{T_{ob}}{2}} - f_d(t_n, z_{1,0}, z_{2,0})|_{t_n=-\frac{T_{ob}}{2}} \right| \\ &= \frac{2f_0}{c}\left|z_{2,0}\Omega_{eff}^2\right| T_{ob} < \delta_\nu \Rightarrow \left|z_{2,0}\Omega_{eff}\right| T_{ob} < \delta_{crg} \end{aligned} \tag{2.34}$$

where

$$\delta_\nu = \frac{1}{T_{ob}} \text{ [Hz]} \tag{2.35}$$

and

$$\delta_{crg} = \frac{c}{2f_0 T_{ob}\Omega_{eff}} \text{ [m]} \tag{2.36}$$

are the Doppler and cross-range resolutions of the ISAR system respectively.

If the constraint in (2.34) is satisfied, the chirp-like distortion term $D_2(\nu, z_{2,0})$ in (2.29) can be neglected. In this case the resultant ISAR image is shown in (2.37).

$$\begin{aligned} I(\tau, \nu, z_{1,0}, z_{2,0}) &= A\,\delta\left(\tau - \frac{2}{c}z_{2,0}\right)\delta\left(\nu - \frac{2f_0}{c}z_{1,0}\Omega_{eff}\right) \otimes_\tau \otimes_\nu w(\tau, \nu) \\ &= A\,B\,T_{ob}\,\text{sinc}\left[B\left(\tau - \frac{2}{c}z_{2,0}\right)\right]\text{sinc}\left[T_{ob}\left(\nu - \frac{2f_0}{c}z_{1,0}\Omega_{eff}\right)\right] e^{j2\pi f_0\left(\tau - \frac{2}{c}z_{2,0}\right)} \end{aligned} \tag{2.37}$$

Therefore, by referring to the cross-range resolution formula in (2.36), the following implication can be considered

$$z_{1,0}\Omega_{eff} = z_{1,0}\frac{c}{2f_0\delta_{crg}T_{ob}} = \frac{c}{2f_0T_{ob}}\frac{z_{1,0}}{\delta_{crg}} = \frac{c}{2f_0T_{ob}}\frac{\nu_0}{\delta_\nu} = \frac{c}{2f_0}\nu_0 \tag{2.38}$$

where ν_0 is the Doppler coordinate of the scatterer in position $(z_{1,0}, z_{2,0})$ defined as

$$\nu_0 = \frac{2f_0\Omega_{eff}}{c}z_{1,0} \tag{2.39}$$

Furthermore, by assuming

$$\tau_0 = \frac{2}{c}z_{2,0} \tag{2.40}$$

the image model in (2.37) can be written as follows

$$\begin{aligned} I(\tau,\nu,z_{1,0},z_{2,0}) &= A\,B\,T_{ob}\,\mathrm{sinc}[B\,(\tau-\tau_0)]\,\mathrm{sinc}[T_{ob}\,(\nu-\nu_0)]\,e^{j2\pi f_0(\tau-\tau_0)} \\ &= A\,\delta\,(\tau-\tau_0)\,\delta\,(\nu-\nu_0)\otimes_\tau\otimes_\nu w(\tau,\nu) \end{aligned} \tag{2.41}$$

The knowledge of the signal carrier frequency f_0 and the estimation of ν_0 make possible to estimate the product $z_{1,0}\Omega_{eff}$ even if $z_{1,0}$ and Ω_{eff} are not individually known. Therefore, the knowledge of f_0, B and the estimation of ν_0 allows for the range migration constraint in (2.25) to be evaluated. Unfortunately, the same thing cannot be said for the constraint in (2.34) which needs the knowledge/estimation of the effective rotation vector to be verified.

2.3 Bistatic Configuration

In bistatic configuration, transmitter and receiver are not co-located, i.e., $0 < \beta < \pi$, R_{TxTg} and R_{RxTg} may be different and $R_{TxRx} > 0$. In this Section the effects of the bistatic geometry on the range compression and ISAR image formation are recalled by referring to [16] and [17].

As in Section 2.2, the first step for the ISAR image formation is the simplification of the delay-time term in (2.2) by means of the straight iso-range approximation. The same approximation for the monostatic configuration in (2.8) is done for the transmitter-target and receiver-target distances as follows

$$\tau(\mathbf{z},n) \simeq \frac{2}{c}\left[\frac{R_{TxTg,0}(n)+R_{RxTg,0}(n)}{2} + \mathbf{z}\cdot\frac{\mathbf{i}_{LoSTX}(n)+\mathbf{i}_{LoSRX}(n)}{2}\right] \tag{2.42}$$

$R_{TxTg,0}(n)$ and $R_{RxTg,0}(n)$ are the distances between the target focus point and transmitter and receiver, respectively. $\mathbf{i}_{LoSTX}(n)$ and $\mathbf{i}_{LoSRX}(n)$ are the transmitter and receiver Line of Sight unit vectors (see Fig.2.1). In order to simplify the calculation, (2.42) is then rewritten as follows

$$\tau(\mathbf{z}, n) \simeq \frac{2}{c} \left[R_{Bi,0}(n) + K(n)\, \mathbf{z} \cdot \mathbf{i}_{LoSBi}(n) \right] \tag{2.43}$$

where

$$R_{Bi,0}(n) = \frac{R_{TxTg,0}(n) + R_{RxTg,0}(n)}{2} \tag{2.44}$$

$$\mathbf{i}_{LoSBi}(n) = \frac{\mathbf{i}_{LoSTX}(n) + \mathbf{i}_{LoSRX}(n)}{|\mathbf{i}_{LoSTX}(n) + \mathbf{i}_{LoSRX}(n)|} \tag{2.45}$$

$$\begin{aligned} K(n) &= \left| \frac{\mathbf{i}_{LoSTX}(n) + \mathbf{i}_{LoSRX}(n)}{2} \right| && (2.46) \\ &= \cos\left(\frac{\arccos\left(\mathbf{i}_{LoSTX}(n) \cdot \mathbf{i}_{LoSRX}(n) \right)}{2} \right) \\ &= \cos\left(\frac{\beta(n)}{2} \right) && (2.47) \end{aligned}$$

$R_{Bi,0}(n)$ and $\mathbf{i}_{LoSBi}(n)$ in (2.43) can be interpreted as the "*Bistaticaly Equivalent Monostatic*" radar-target distance and Line of Sight respectively. The direct consequence is the introduction of the Bistatically Equivalent Monostatic (BEM) approximation, which consists of introducing a virtual monostatic radar located at a distance $R_{Bi,0}(t)$ from the target along the direction of the bistatic angle bisector [17].

Therefore, the difference between the received signal model in bistatic configuration and the signal model in the monostatic case consists of:

- the bistatic reflectivity function instead of the monostatic one;
- the distortion term $K(n)$ which depends on the bistatic angle $\beta(n)$.

It is worth pointing out that, in the absence of synchronization errors, any parametric or non-parametric motion compensation technique used for monostatic ISAR is able to compensate $R_{Bi,0}(n)$ with the desired accuracy. The issue of the synchronization errors between transmitter and receiver is not discussed in this Thesis. Details about it can be found in [15, 18].

In other words, the bistatic reflectivity function and $R_{Bi,0}(n)$ do not involve any substantial change in terms of ISAR image formation. However, $K(n)$ must be carefully pointed out because it summarizes the image distortions caused by the bistatic geometry and affects the final result of the ISAR imaging.

2.3.1 Range Compression

Before starting with the analytical calculation of the Bistatic ISAR (B-ISAR) PSF, it is worth pointing out that the same assumptions introduced for the monostatic case, i.e.,

1. Transmitter-target and receiver-target distances much greater than the target size (straight iso-range approximation);
2. Target considered as a rigid body;
3. $R_{Bi,0}(n)$ perfectly compensated;
4. Constant effective rotation vector within the CPI;

are still considered valid.

Under these assumptions, the compensated received signal after radial motion compensation in bistatic configuration can be written as follows

$$S(f,n) = W(f,n) \int_{z_1} \int_{z_2} \gamma_B(z_1,z_2) e^{-j\frac{4\pi f}{c}K(n)\left[z_1 \sin(\Omega_{Bi,eff} t_n) + z_2 \cos(\Omega_{Bi,eff} t_n)\right]} dz_1 dz_2 \tag{2.48}$$

By comparing (2.48) with (2.10) three differences can be highlighted:

1. The bistatic reflectivity function $\gamma_B(z_1,z_2)$ instead of $\gamma(z_1,z_2)$;
2. The distortion term $K(n)$;
3. The bistatic effective rotation vector $\Omega_{Bi,eff}$ calculated as shown in (2.49).

$$\begin{aligned} \Omega_{Bi,eff} &\simeq \left\| \boldsymbol{\Omega}_{Bi,eff}(n) \right\|_{n=0} \\ &= \left\| \frac{(\mathbf{i}_{LoSTX}(n) \times \boldsymbol{\Omega}_{TX}(n)) + (\mathbf{i}_{LoSRX}(n) \times \boldsymbol{\Omega}_{RX}(n))}{2K(n)} \times \mathbf{i}_{LoSBi}(n) \right\|_{n=0} \end{aligned} \tag{2.49}$$

where $\boldsymbol{\Omega}_{TX}(n)$ and $\boldsymbol{\Omega}_{RX}(n)$ are the total angular rotation vectors with respect to the transmitter and receiver point of view respectively. Details about the bistatic effective rotation vector and its calculation can be found in [17].

By assuming a small variation of the bistatic angle $\beta(n)$ within the CPI, it can be approximated with the a second order Taylor-Maclaurin polynomial as follows

$$\beta(n) \simeq \beta(0) + \dot{\beta}(0) t_n + \frac{1}{2}\ddot{\beta}(0) t_n^2 \tag{2.50}$$

where $\dot{\beta}$ and $\ddot{\beta}$ are the first and second order derivatives of the bistatic angle β with respect to the slow-time variable. As a result, $K(n)$ is approximated by its second order Taylor-Maclaurin polynomial and, by using (2.46), the following equation is obtained

$$\begin{aligned} K(n) &\simeq K(0) + \dot{K}(0)t_n + \frac{1}{2}\ddot{K}(0)t_n^2 \\ &= \cos\left(\frac{\beta(0)}{2}\right) - \frac{\dot{\beta}(0)}{2}\sin\left(\frac{\beta(0)}{2}\right)t_n + \\ &\quad -\frac{1}{2}\left[\frac{\ddot{\beta}(0)}{2}\sin\left(\frac{\beta(0)}{2}\right) + \left(\frac{\dot{\beta}(0)}{2}\right)^2\cos\left(\frac{\beta(0)}{2}\right)\right]t_n^2 \\ &= K_0 + K_1 t_n + \frac{1}{2}K_2 t_n^2 \end{aligned} \tag{2.51}$$

Therefore, by considering a target composed of a single point-like scatterer and approximating the sine and cosine functions to the second order Taylor-Maclaurin polynomial, the compensated received signal in (2.48) can be approximated as follows

$$S(f,n) \simeq W(f,n)\, A\, e^{-j2\pi\varphi_B(f,n,z_{1,0},z_{2,0})} \tag{2.52}$$

where

$$\varphi_B(f,n,z_{1,0},z_{2,0}) = \frac{2f}{c}R'_B(t_n,z_{1,0},z_{2,0}) \tag{2.53}$$

is the bistatic signal phase term and

$$\begin{aligned} R'_B(t_n,z_{1,0},z_{2,0}) &= K(n)\,\mathbf{z}\cdot\mathbf{i}_{LoSBi}(n) \\ &\simeq \left[K_0 + K_1 t_n + \frac{1}{2}K_2 t_n^2\right]\left[z_{1,0}\Omega t_n + z_{2,0} - z_{2,0}\frac{\Omega^2 t_n^2}{2}\right] \\ &= K_0 z_{2,0} + (K_1 z_{2,0} + K_0 z_{1,0}\Omega)\, t_n + \\ &\quad \left(\frac{1}{2}K_2 z_{2,0} + K_1 z_{1,0}\Omega - \frac{1}{2}K_0 z_{2,0}\Omega^2\right)t_n^2 + \\ &\quad \left(\frac{1}{2}K_2 z_{1,0}\Omega - \frac{1}{2}K_1 z_{2,0}\Omega^2\right)t_n^3 + \\ &\quad \left(-\frac{1}{4}K_2 z_{2,0}\Omega^2\right)t_n^4 \\ &= R_{B,0} + R_{B,1}t_n + R_{B,2}t_n^2 + R_{B,3}t_n^3 + R_{B,4}t_n^4 \end{aligned} \tag{2.54}$$

is the *BEM effective range*. For the sake of simplicity, in (2.54) $\Omega_{Bi,eff}$ has been replaced by Ω and the dependence on $z_{1,0}$ and $z_{2,0}$ of the terms $R_{B,i}$ for $i = 0,\ldots,4$ has been omitted.

Therefore, by applying the IFT with respect to the frequency coordinate to (2.52), the bistatic range profile is obtained as shown in the following.

$$\begin{aligned} S'_R(\tau, n) &= \mathcal{FT}^{-1}_{f\to\tau}\{S(f,n)\} \\ &= \int_{-\infty}^{\infty} W(f,n)\, A\, e^{-j\frac{4\pi f}{c}R'_B(t_n,z_{1,0},z_{2,0})} e^{j2\pi f\tau} df = \\ &= AB\, h(n)\, \text{sinc}\left\{B\left[\tau - \frac{2}{c}R'_B(t_n, z_{1,0}, z_{2,0})\right]\right\} e^{j2\pi f_0\tau} e^{-j2\pi\varphi'_B(t_n,z_{1,0},z_{2,0})} \end{aligned} \tag{2.55}$$

where

$$\varphi'_B(t_n, z_{1,0}, z_{2,0}) = \frac{2f_0}{c} R'_B(t_n, z_{1,0}, z_{2,0}) \tag{2.56}$$

Range migration is then studied by approximating R'_B in the sinc argument as $R'_B(t_n, z_{1,0}, z_{2,0}) \simeq R_{B,0} + R_{B,1}t_n$ (compare with (2.24) for the monostatic configuration). By referring to Fig.2.4, range migration occurs if the total variation of R'_B exceeds the distance of the range resolution, i.e., if (2.57) is not satisfied.

$$\begin{aligned} \Delta_{rng} &\doteq \left| R'_B(t_n, z_{1,0}, z_{2,0})\big|_{t_n=\frac{T_{ob}}{2}} - R'_B(t_n, z_{1,0}, z_{2,0})\big|_{t_n=-\frac{T_{ob}}{2}} \right| \\ &= |R_{B,1}|\, T_{ob} = |K_1 z_{2,0} + K_0 z_{1,0}\Omega|\, T_{ob} < \delta_{rng} \end{aligned} \tag{2.57}$$

It is worth noting that as the radar system approaches the monostatic configuration $\beta \to 0$, $K_0 \to 1$, $K_1 \to 0$ and the constraint in (2.57) approaches the constraint in (2.25). Furthermore, the range migration term Δ_{rng} in (2.57) can be expressed as follows

$$\Delta_{rng} = |\Delta_{rng,1} + \Delta_{rng,2}| \tag{2.58}$$

where

1. $\Delta_{rng,1} \doteq K_0 z_{1,0}\Omega T_{ob}$: range migration term due to the target rotation (compare with (2.25));
2. $\Delta_{rng,2} \doteq K_1 z_{2,0} T_{ob}$: range migration term due to the bistatic angle variation.

It can be noted that $\Delta_{rng,1}$ is attenuated by the bistatic geometry, i.e., multiplied by $K_0 < 1$, whereas $\Delta_{rng,2}$ is directly proportional to K_1. Thus, if the bistatic angle is constant during the CPI, $K_1 = 0$ and the range migration effect will be mitigated with respect to the monostatic configuration.

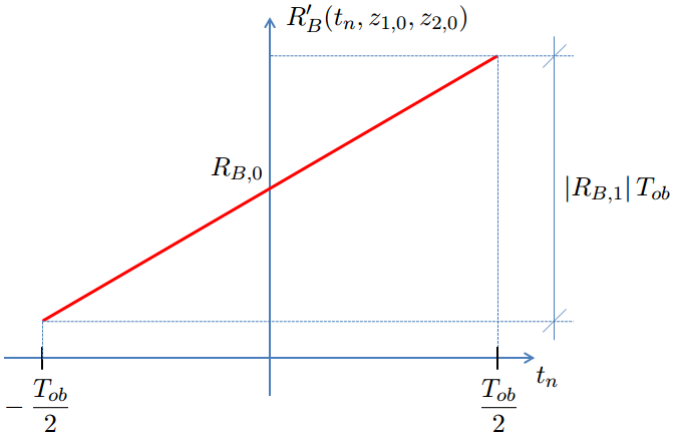

FIGURE 2.4: Range migration graphic for the bistatic configuration.

Therefore, if the constraint in (2.57) is satisfied, the range profile after motion compensation $S'_R(\tau, n)$ can be written as follows

$$\begin{aligned} S'_R(\tau,n) &\simeq AB\,h(n)\,\mathrm{sinc}\left\{B\left[\tau-\frac{2}{c}K_0 z_{2,0}\right]\right\} e^{j2\pi f_0\tau} e^{-j2\pi\varphi'_B(t_n,z_{1,0},z_{2,0})} \\ &= A\,\delta\left(\tau-\frac{2}{c}K_0 z_{2,0}\right) \otimes_\tau \tilde{w}(\tau,t_n) e^{-j2\pi\left(\varphi'_B(t_n,z_{1,0},z_{2,0})-\frac{2f_0}{c}R_{B,0}\right)} \end{aligned} \tag{2.59}$$

where $\tilde{w}(\tau, t_n)$ is defined in (2.22).

2.3.2 Doppler Image Formation

As mentioned in Section 2.2.2, the B-ISAR image is calculated by applying the IFT of the range-compressed signal $S'_R(\tau, n)$ along to the slow-time coordinate. However, before applying the IFT, for simplicity (2.59) is rewritten as follows

$$\begin{aligned} S'_R(\tau,n) &= AB\,\mathrm{sinc}\left\{B\left[\tau-\frac{2}{c}K_0 z_{2,0}\right]\right\} e^{j2\pi f_0\left[\tau-\frac{2}{c}R_{B,0}\right]} \\ &\quad \mathrm{rect}\left(\frac{t_n}{T_{ob}}\right) e^{-j2\pi\left(\varphi'_B(t_n,z_{1,0},z_{2,0})-\frac{2f_0}{c}R_{B,0}\right)} \end{aligned} \tag{2.60}$$

where the discrete variable n has been converted to the continuous variable t_n (see (2.31)). Therefore, the B-ISAR image is calculated as follows

$$\begin{aligned} I(\tau,\nu,z_{1,0},z_{2,0}) &= \mathcal{FT}^{-1}_{t_n\to\nu}\left\{S'_R(\tau,n)\right\} \\ &= AB\,\mathrm{sinc}\left\{B\left[\tau-\frac{2}{c}K_0 z_{2,0}\right]\right\} e^{j2\pi f_0\left[\tau-\frac{2}{c}R_{B,0}\right]} \\ &\quad \int_{-\infty}^{\infty} \mathrm{rect}\left(\frac{t_n}{T_{ob}}\right) e^{-j2\pi\left(\varphi'_B(t_n,z_{1,0},z_{2,0})-\frac{2f_0}{c}R_{B,0}\right)} dt_n \end{aligned} \tag{2.61}$$

The Doppler frequency shift due to the scatterer in position $(z_{1,0}, z_{2,0})$ can be obtained by calculating the derivative of the phase term in (2.61) with respect to the slow-time variable. However, before doing that, $R'_B(t_n, z_{1,0}, z_{2,0})$ is approximated to the second order polynomial as shown in (2.62).

$$R'_B(t_n, z_{1,0}, z_{2,0}) \simeq R_{B,0} + R_{B,1} t_n + R_{B,2} t_n^2 \tag{2.62}$$

Therefore

$$\begin{aligned} f_{d,B}(t_n, z_{1,0}, z_{2,0}) &= \frac{\partial}{\partial t_n}\left(\varphi'_B(t_n, z_{1,0}, z_{2,0}) - \frac{2f_0}{c} K_0 z_{2,0}\right) \\ &= \frac{\partial}{\partial t_n}\left(\frac{2f_0}{c}\left[R_{B,1} t_n + R_{B,2} t_n^2\right]\right) \\ &= \frac{2f_0}{c} R_{B,1} + \frac{4f_0}{c} R_{B,2} t_n \end{aligned} \tag{2.63}$$

In order to determine a constraint for the Doppler migration in bistatic configuration, the Doppler shift $f_{d,B}$ is then plotted in Fig.2.5 and it is imposed to have the Doppler bandwidth $B_{d,B}$ smaller than the Doppler resolution as shown in (2.64).

$$\begin{aligned} B_{d,B} &= \left| f_{d,B}(t_n, z_{1,0}, z_{2,0})\big|_{t_n = \frac{T_{ob}}{2}} - f_{d,B}(t_n, z_{1,0}, z_{2,0})\big|_{t_n = -\frac{T_{ob}}{2}} \right| \\ &= \frac{2f_0}{c} \left|2R_{B,2}\right| T_{ob} = \frac{2f_0}{c} \left|K_2 z_{2,0} + 2K_1 z_{1,0}\Omega - K_0 z_{2,0}\Omega^2\right| T_{ob} < \delta_\nu \Rightarrow \\ &\Rightarrow \Delta_{crg} \doteq \left|\frac{K_2 z_{2,0}}{\Omega} + 2K_1 z_{1,0} - K_0 z_{2,0}\Omega\right| T_{ob} < \delta_{crg} \end{aligned} \tag{2.64}$$

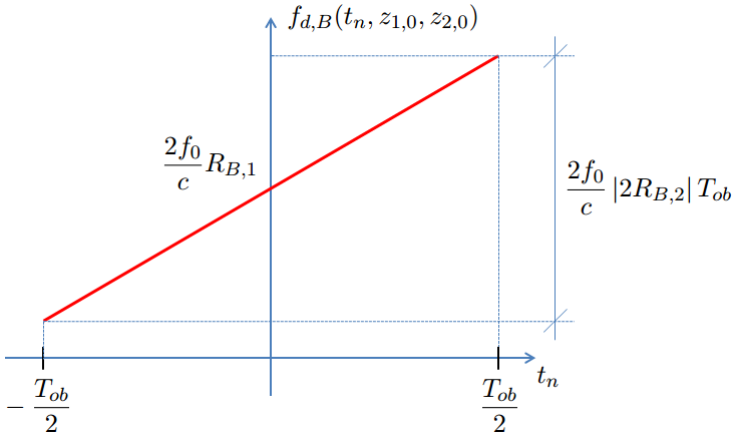

FIGURE 2.5: Doppler migration graphic for the bistatic configuration.

Even in this case, as the radar system approaches the monostatic configuration, $\beta \to 0$, $K_0 \to 1$, $K_1 \to 0$, $K_2 \to 0$ and (2.64) becomes equivalent to the constraint in (2.34).

Furthermore, also Δ_{crg} has a component caused by the target rotation

$$\Delta_{crg,1} \doteq K_0 z_{2,0} \Omega T_{ob} \tag{2.65}$$

that is mitigated by the bistatic geometry ($K_0 < 1$) and a component caused by the bistatic angle variation

$$\Delta_{crg,2} \doteq \frac{K_2 z_{2,0}}{\Omega} T_{ob} + 2K_1 z_{1,0} T_{ob} = \Delta_2 + \Delta_1 \tag{2.66}$$

where

$$\Delta_1 \doteq 2K_1 z_{1,0} T_{ob} \tag{2.67}$$

$$\Delta_2 \doteq \frac{K_2 z_{2,0}}{\Omega} T_{ob} \tag{2.68}$$

are the Doppler distortion components due to the first and second order Taylor-Maclaurin coefficients for the approximation of $K(n)$ respectively.

Therefore

$$\Delta_{crg} = |\Delta_{crg,1} - \Delta_{crg,2}| \tag{2.69}$$

If the bistatic angle is constant during the CPI, $K_1 = 0$, $K_2 = 0$ and the distortion effect will be mitigated with respect to the monostatic case. In general, K_2 is smaller than K_1 because it represents the second order coefficient of the Taylor-Maclaurin polynomial. However, in (2.64) K_2 happens to be divided by Ω which barely exceeds $1 \sim 2$ deg/s $= 0.018 \sim 0.035$ rad/s in a realistic scenario.

Therefore, even if $|K_2| \ll |K_1|$, Δ_2 cannot be neglected and sometimes can even become dominant with respect to Δ_1. This is why $K(n)$ is approximated to the second order Taylor-Maclaurin polynomial in (2.51) as the sine and cosine functions in (2.18).

If the condition in (2.64) is satisfied, the Doppler migration effect can be neglected and (2.63) can be approximated as follows

$$f_{d,B}(t_n, z_{1,0}, z_{2,0}) \simeq \frac{2f_0}{c} R_{B,1} = \frac{2f_0}{c} \left[K_1 z_{2,0} + K_0 z_{1,0} \Omega\right] \tag{2.70}$$

whereas the phase term in (2.56) is written as

$$\varphi'_B(t_n, z_{1,0}, z_{2,0}) = \frac{2f_0}{c} K_0 z_{2,0} + \frac{2f_0}{c} \left[K_1 z_{2,0} + K_0 z_{1,0} \Omega\right] t_n \tag{2.71}$$

As a consequence, (2.61) can be solved as follows

$$\begin{aligned} I(\tau,\nu,z_{1,0},z_{2,0}) &= AB\,\mathrm{sinc}\left\{B\left[\tau-\frac{2}{c}K_0 z_{2,0}\right]\right\} e^{j2\pi f_0\left[\tau-\frac{2}{c}K_0 z_{2,0}\right]} \\ &\quad \int_{-\infty}^{\infty}\mathrm{rect}\left(\frac{t_n}{T_{ob}}\right) e^{-j2\pi\frac{2f_0}{c}[K_1 z_{2,0}+K_0 z_{1,0}\Omega]t_n}dt_n = \\ &= A\,B\,T_{ob}\,\mathrm{sinc}\left[B\left(\tau-\frac{2}{c}K_0 z_{2,0}\right)\right] \\ &\quad \mathrm{sinc}\left[T_{ob}\left(\nu-\frac{2f_0}{c}K_0 z_{1,0}\Omega-\Delta_\nu\right)\right] e^{j2\pi f_0\left(\tau-\frac{2}{c}K_0 z_{2,0}\right)} \\ &= A\,\delta\left(\tau-\frac{2}{c}K_0 z_{2,0}\right)\delta\left(\nu-\frac{2f_0}{c}K_0 z_{1,0}\Omega-\Delta_\nu\right)\otimes_\tau\otimes_\nu w(\tau,\nu) \end{aligned} \tag{2.72}$$

where $w(\tau,\nu)$ is defined in (2.30) and

$$\Delta_\nu = \frac{2f_0}{c}K_1 z_{2,0} \tag{2.73}$$

is the *linear distortion* term, i.e., a shift term along the Doppler coordinate introduced by the bistatic angle change rate parameter K_1 and proportional to the scatterer position along the range coordinate. It is worth noting that if the bistatic geometry is known for every slow-time sample, i.e., the target trajectory and the transmitter and receiver position are known, the bistatic angle $\beta(n)$ and consequently the K_1 parameter can be estimated. In this case such a distortion can be estimated and eventually compensated. Anyway, in order to have negligible linear distortion, it can be imposed to have the maximum value of $|\Delta_\nu|$ smaller than the Doppler resolution δ_ν as shown in (2.74).

$$|\Delta_\nu| = \left|\frac{2f_0}{c}K_1 z_{2,0}\right| < \frac{1}{T_{ob}} \Rightarrow |\Delta_{crg,0}| < \frac{c}{2f_0\Omega T_{ob}} = \delta_{crg} \tag{2.74}$$

where

$$\Delta_{crg,0} \doteq \frac{K_1 z_{2,0}}{\Omega} \tag{2.75}$$

If the constraint in (2.74) is satisfied, the linear distortion term Δ_ν can be neglected too and $I(\tau,\nu,z_{1,0},z_{2,0})$ can be written as follows

$$\begin{aligned} I(\tau,\nu,z_{1,0},z_{2,0}) &= A\,B\,T_{ob}\,\mathrm{sinc}\left[B\left(\tau-\frac{2}{c}K_0 z_{2,0}\right)\right] \\ &\quad \mathrm{sinc}\left[T_{ob}\left(\nu-\frac{2f_0}{c}K_0 z_{1,0}\Omega\right)\right] e^{j2\pi f_0\left(\tau-\frac{2}{c}K_0 z_{2,0}\right)} \\ &= A\,\delta\left(\tau-\frac{2}{c}K_0 z_{2,0}\right)\delta\left(\nu-\frac{2f_0}{c}K_0 z_{1,0}\Omega\right)\otimes_\tau\otimes_\nu w(\tau,\nu) \end{aligned} \tag{2.76}$$

By considering (2.38) and the definition in (2.40), (2.76) can then be simplified as follows

$$\begin{aligned} I(\tau,\nu,z_{1,0},z_{2,0}) &= A\,B\,T_{ob}\,\mathrm{sinc}[B\,(\tau-K_0\tau_0)]\,\mathrm{sinc}[T_{ob}\,(\nu-K_0\nu_0)]\,e^{j2\pi f_0(\tau-K_0\tau_0)} \\ &= A\,\delta\,(\tau-K_0\tau_0)\,\delta\,(\nu-K_0\nu_0)\otimes_\tau\otimes_\nu w(\tau,\nu) \end{aligned} \tag{2.77}$$

By comparing (2.76) and (2.77) with (2.37) and (2.41) for the monostatic case, it can be stated that, in absence of distortions caused by the bistatic geometry, the B-ISAR image is a scaled version of the monostatic ISAR by a factor K_0. The mechanism with which the B-ISAR image is formed is the same as that of the monostatic. The only differences are a scaling effect and a different physical scattering mechanism because in (2.48) the bistatic reflectivity function $\gamma_B(z_1,z_2)$ replaces the monostatic one $\gamma(z_1,z_2)$.

The space-invariant characteristic of the PSF makes sure that the resolution properties remain constant in any region of the image. This characteristic is desirable as the target image shape is not altered, which is often a requirement for classification and recognition purposes.

As a consequence of the scaling factor K_0, the bistatic geometry generates a resolution loss. The resultant formulas for the range and cross-range resolutions for the bistatic configuration are reported in (2.78) and (2.79) respectively.

$$\delta_{rng,B} = \frac{c}{2K_0B} \geq \delta_{rng} \tag{2.78}$$

$$\delta_{crg,B} = \frac{c}{2f_0K_0\Omega T_{ob}} \geq \delta_{crg} \tag{2.79}$$

Such a distortion loss does not consist of a blurring in the final image or a widening of the PSF, but in a simple approaching of the image scatterers to the focusing center.

However, in the conditions regarding the range and Doppler migration effects ((2.57) and (2.64) respectively) it has been chosen to write a constraint as a function of the monostatic range (δ_{rng}) and cross-range resolutions (δ_{crg}).

The introduction of a bistatic geometry does not change the fact that the product $z_{1,0}\Omega_{Bi,eff}$ can be estimated even if $z_{1,0}$ and $\Omega_{Bi,eff}$ are not individually known (see (2.38)). However, in this case also the estimation of the parameters K_0 and K_1, i.e., the bistatic geometry and target trajectory, becomes necessary. On the other hand, even in this case the Doppler migration constraint evaluation needs the estimation/knowledge of the effective rotation vector besides the estimation of K_0, K_1 and K_2.

R_{TxTg}	1000 m
R_{RxTg}	1000 m
β	$\pi/4$
v	50 m/s
$\mathbf{\Omega}_T$	$[0, 0, 0.0175]$ rad/s
T_{ob}	1 s
f_0	60 GHz
B	1 GHz
PRF	300 Hz

TABLE 2.1: Simulation set-up example: parameters of interest.

On the other hand, if both linear and quadratic distortions cannot be neglected, the final distorted image is written as follows

$$\begin{aligned} I(\tau,\nu,z_{1,0},z_{2,0}) &= A\,\delta\left(\tau-\frac{2}{c}K_0 z_{2,0}\right)\delta\left(\nu-\frac{2f_0}{c}K_0 z_{1,0}\Omega_{eff}-\Delta_\nu\right)\otimes_\tau\otimes_\nu \\ & \quad w(\tau,\nu)\otimes_\nu D_{2,B}(\nu,z_{1,0},z_{2,0}) \end{aligned} \tag{2.80}$$

where

$$\begin{aligned} D_{2,B}(\nu,z_{1,0},z_{2,0}) &= \mathcal{FT}^{-1}_{t_n\to\nu}\left\{e^{-j2\pi\frac{2f_0}{c}R_{B,2}t_n^2}\right\} \\ &= \mathcal{FT}^{-1}_{t_n\to\nu}\left\{e^{-j2\pi\frac{1}{2}\left(\frac{2f_0}{c}K_2 z_{2,0}+\frac{2f_0}{c}2K_1 z_{1,0}\Omega-\frac{2f_0}{c}K_0 z_{2,0}\Omega^2\right)t_n^2}\right\} \end{aligned} \tag{2.81}$$

is the bistatic chirp-distortion term (compare with (2.29)).

2.4 Distortion analysis on simulated data

In this Section simulated data is used to validate the analytical results above and the second order polynomial approximation for $K(n)$. A rotating rigid target is placed in the simulation scenario depicted in Fig.2.6b in a reference system $T_x(x_1, x_2, x_3)$, which is a translated version of T_ξ. Such a target is shown in Fig.2.6a and is composed of five point-like scatterers. One scatterer is in position $\mathbf{z}_1 = [0, 0, 0]$, whereas the other four describe a rectangle of size 8×16 m. The target is both rotating counterclockwise with constant rotation speed around the central scatterer and moving along the bistatic angle bisector, approaching the bistatic baseline with speed v. This is in order to create the "worst case scenario" where the bistatic angle variation speed in maximized [16]. Other information of interest is summarized in Table 2.1.

For these target and scenario the ISAR image is simulated by using four different models for the received signal.

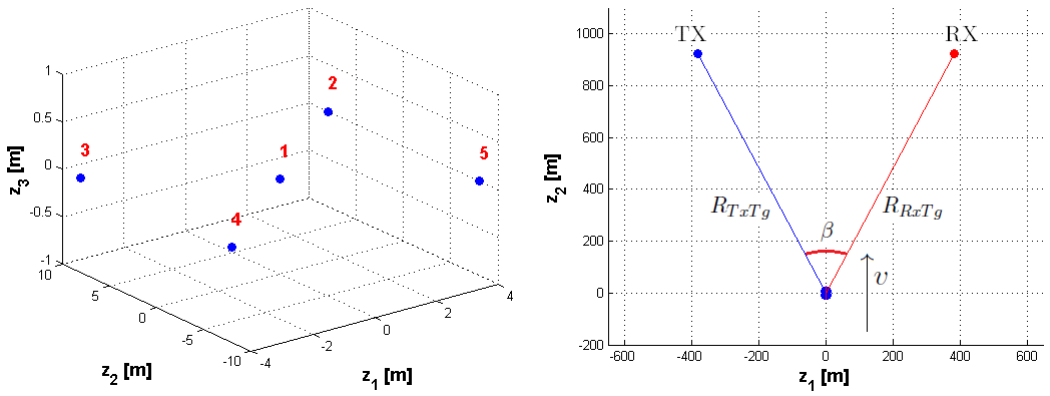

(a) (b)

FIGURE 2.6: Simulation set-up example: simulated target (a) and scenario (b).

1. The most general model with the actual $\tau(\mathbf{z}, n)$ in (2.2):

$$S(f,n) = \sum_{i=1}^{N_s} \sigma_i \, e^{-j2\pi f \frac{R_{TxTg}(\mathbf{z}_i,n)+R_{RxTg}(\mathbf{z}_i,n)}{c}} \tag{2.82}$$

   where $N_s = 5$ is the number of scatterers which compose the simulated target, $\sigma_i = e^{j2\pi\varphi_i}$ is the complex reflectivity function of the i^{th} scatterer, $\varphi_i \in \mathcal{U}[0, 2\pi]$ and $\mathbf{z}_i = [z_{1,i}, z_{2,i}, z_{3,i}]$ is the position in the T_z reference system.

2. The model obtained by exploiting the straight iso-range approximation, the second order polynomial approximation for the sine and cosine functions and the actual $K(n) = \cos(\beta(n)/2)$:

$$S(f,n) = \sum_{i=1}^{N_s} \sigma_i \, e^{-j\frac{4\pi f}{c}K(n)\left[z_{1,0}\Omega t_n + z_{2,0} - z_{2,0}\frac{\Omega^2 t_n^2}{2}\right]} \tag{2.83}$$

3. The model in (2.83) with $K(n) = K_0 + K_1 t_n$.

4. The model in (2.83) with $K(n) = K_0 + K_1 t_n + \frac{1}{2}K_2 t_n^2$.

The ISAR image obtained by using the first model in (2.82) is shown in Fig.2.7 with the five scatterers labeled with the relative numbers, whereas Fig.2.8 shows a zoom on scatterer #3 for the four models. Simulated ISAR images in Fig.2.7, Fig.2.8 and all the following in this Section are displayed after a 10× zero-padding and in dB scale for illustration purposes.

Images in Fig.2.8 show that

$$R'_B(t_n, z_{1,i}, z_{2,i}) \simeq K(n)\left[z_{1,i}\Omega t_n + z_{2,i} - \frac{1}{2}z_{2,i}\Omega^2 t_n^2\right] \tag{2.84}$$

K_0	0.9239
K_1	-0.0073
K_2	-0.0010
δ_{rng}	0.15 m
δ_{crg}	0.1432 m
δ_{ν}	1 Hz

TABLE 2.2: Simulation example: K parameters and resolution.

is a valid approximation of the BEM effective range (compare Fig.2.8a with Fig.2.8b). The same can be stated for the fourth model when the second order polynomial approximation for $K(n)$ is used, (see Fig.2.8d). The first order polynomial for $K(n)$ (the third model) appears instead to be not a good approximation (see Fig.2.8c).

By the way, by looking at Fig.2.7 and Fig.2.8, a strong distortion on the resultant image appears evident. In order to analyze such a distortion, the estimated K parameters and the calculated resolution values are summarized in Table 2.2, whereas the calculated distortion terms are shown in Table 2.3.

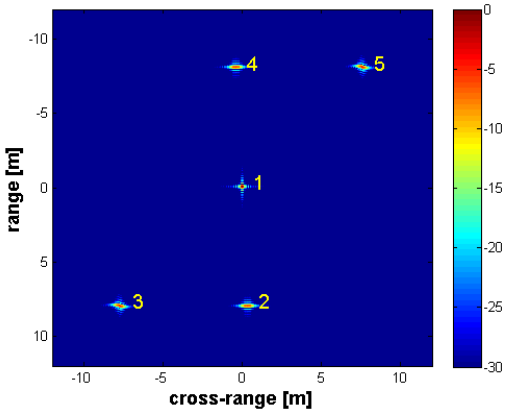

FIGURE 2.7: Simulation set-up example: ISAR image for the model in (2.82) with the five scatterers labeled.

By analyzing the results in Table 2.3 the following considerations can be discussed. The first scatterer coincides with the focusing center and does not present any distortion. By comparing the Δ_{rng} parameters with the range resolution in Table 2.2, it appears that all the scatterers satisfy the constraint in (2.57) and no-one presents range migration. However, range migration is not an "on-off" effect. In fact, for scatterers #3 and #5, it cannot be neglected even though $\Delta_{rng} < \delta_{rng}$ and a distortion effect along the range direction can be clearly seen in Fig.2.7 and Fig.2.8. This is because for scatterers #3 and #5 the distortion term due to the target rotation ($\Delta_{rng,1}$) and the distortion term due to the bistatic angle variation ($\Delta_{rng,2}$) have the same sign, whereas for scatterers #2 and #4 they have opposite signs (see (2.58)). This means that the bistatic geometry causes a mitigation effect on the range migration for scatterers #2 and #4, but a distortion

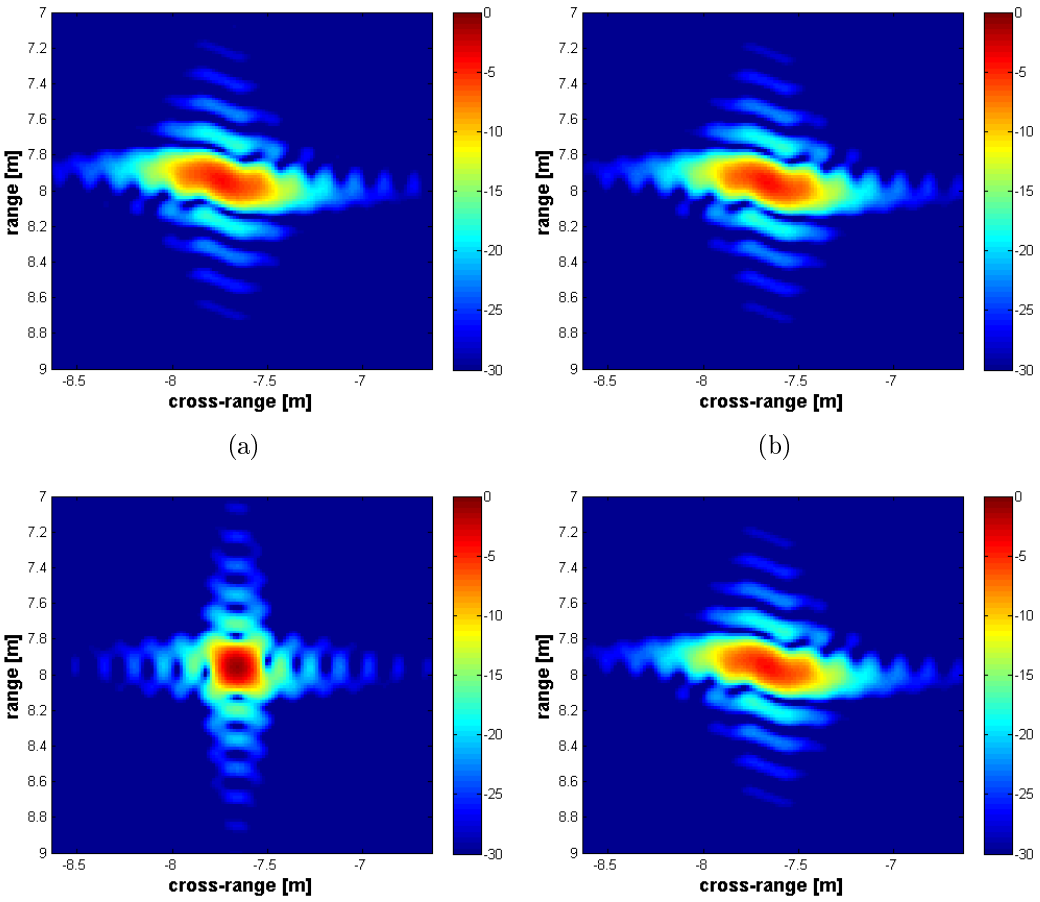

FIGURE 2.8: Simulation set-up example: zoom on scatterer #3 for the first (a), second (b), third (c) and fourth (d) signal model.

Scatterer	**#1**	**#2**	**#3**	**#4**	**#5**
$z_{1,i}$	0	4	-4	-4	4
$z_{2,i}$	0	8	8	-8	-8
$z_{3,i}$	0	0	0	0	0
Δ_{rng}	0.0000	0.0059	0.1231	0.0059	0.1231
$\Delta_{rng,1}$	0.0000	-0.0586	-0.0586	0.0586	0.0586
$\Delta_{rng,2}$	0.0000	0.0645	-0.0645	-0.0645	0.0645
Δ_{crg}	0.0000	0.6535	0.5362	0.6535	0.5362
$\Delta_{crg,0}$	0.0000	-3.3597	-3.3597	3.3597	3.3597
$\Delta_{crg,1}$	0.0000	0.1290	0.1290	-0.1290	-0.1290
$\Delta_{crg,2}$	0.0000	-0.5245	-0.4072	0.5245	0.4072
Δ_1	0.0000	-0.0586	0.0586	0.0586	-0.0586
Δ_2	0.0000	-0.4658	-0.4658	0.4658	0.4658

TABLE 2.3: Simulation example: Range and Doppler distortion terms.

enhancement for scatterers #3 and #5. Such a distortion enhancement is clearly visible in Fig.2.7 and highlighted in Fig.2.9, where the ISAR image is zoomed on scatterers #2 and #3.

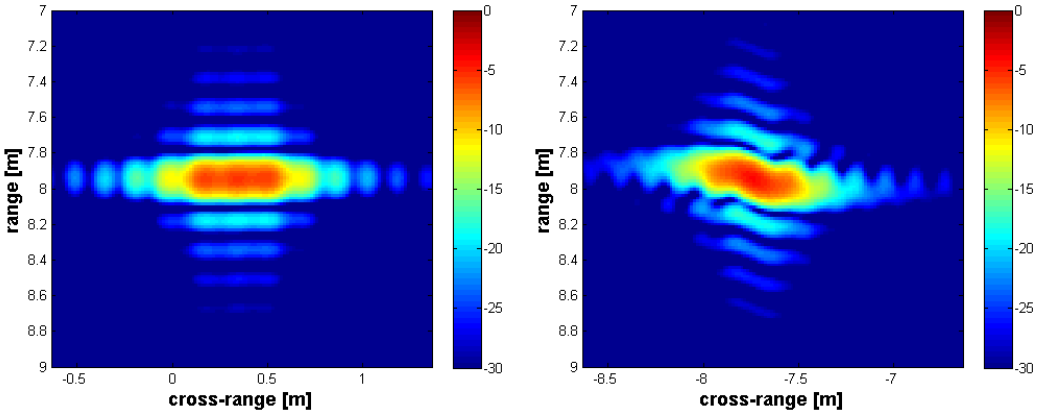

(a) (b)

FIGURE 2.9: Simulation set-up example: zoom on scatterer #2 (a) and #3 (b) for the signal model in (2.82).

On the other hand, by looking at Fig.2.7, Fig.2.9 and the results in Table 2.2, all the four external scatterers present a strong Doppler migration effect. For all the four scatterers, $\Delta_{crg,1}$ and $\Delta_{crg,2}$ have opposite signs and, for (2.69), the bistatic geometry causes a significant distortion enhancement. Moreover, it appears that $|\Delta_2|$ is significantly greater than $|\Delta_1|$ even if $|K_2| < |K_1|$. This means that the most of the Doppler migration effect is due to the second order approximation term of $K(n)$ rather than K_1.

In all cases the linear distortion term $\Delta_{crg,0}$ appears to be much greater than δ_{crg}. This is why the ISAR image in Fig.2.7 appears with a parallelepipedal shape rather than a rectangle and all the external scatterers are shifted by 3.3597m along the cross-range.

In the final ISAR image, a "range migration window" and a "cross-range migration window" can be defined. In Fig.2.10a the ISAR image is shown and the region where range migration occurs is highlighted. The cross-range migration window is shown in Fig.2.10b. In Fig.2.11 the ISAR image and the "range migration window" are shown in the range/-Doppler domain. Such a window in the range/Doppler domain can be calculated by combining (2.57) and (2.38) with the following result

$$\Delta_{rng} = \left| K_1 z_{2,0} + K_0 \frac{c}{2f_0} \nu_0 \right| T_{ob} < \delta_{rng} \tag{2.85}$$

Δ_{rng} can be estimated even if the cross-range resolution is unknown, i.e., without effective rotation vector estimation and cross-range scaling. However, the image focusing center is required to be estimated.

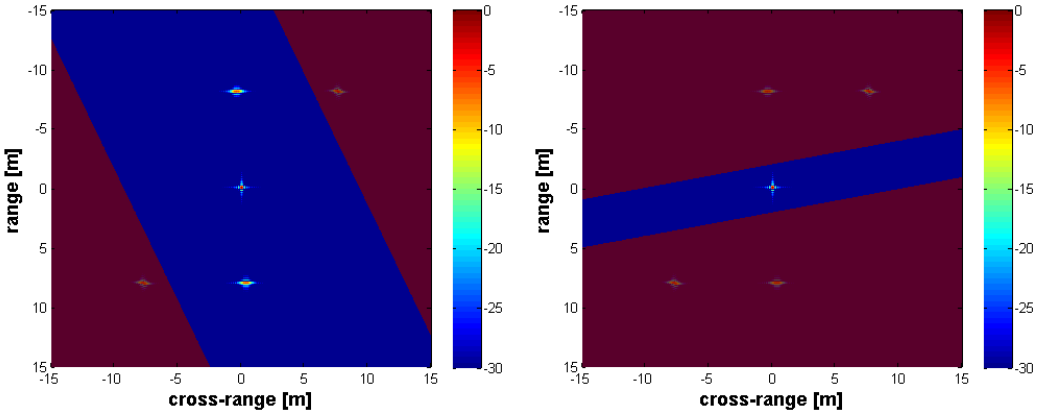

(a) (b)

FIGURE 2.10: ISAR image in Fig.2.7 with the range migration window (a) and cross-range migration window (b) superimposed in the range/cross-range domain.

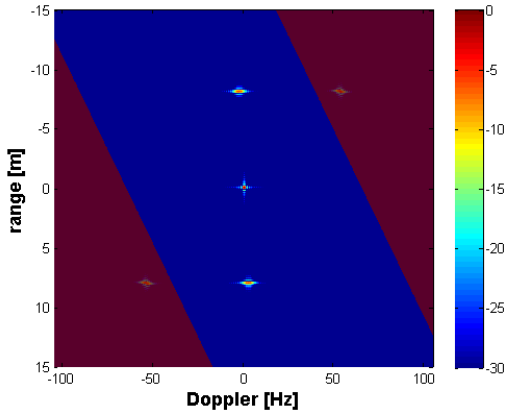

FIGURE 2.11: ISAR image in Fig.2.7 with the range migration window superimposed in the range/Doppler domain.

Assume now to have both the conditions in (2.57) and (2.64) unsatisfied, i.e., presence of distortions in the B-ISAR image caused by range and Doppler migration. Then assume to reduce the observation time by a factor K_T defined as follows

$$K_T \doteq \frac{T_{ob,L}}{T_{ob}} \tag{2.86}$$

where $0 \leq K_T \leq 1$ and $T_{ob,L}$ is the new value for the CPI in order to mitigate both the migration effects. In fact, both Δ_{rng} and Δ_{crg} are directly proportional to T_{ob} since K_0, K_1, K_2, the scatterer position and Ω do not depend on it. Therefore, in order to satisfy the constraint in (2.57), the following condition for K_T is obtained

$$\Delta_{rng} K_T < \delta_{rng} \Rightarrow K_T < \frac{\delta_{rng}}{\Delta_{rng}} = \frac{\delta_{rng}}{|K_1 z_{2,0} + K_0 z_{1,0} \Omega| T_{ob}} = \frac{c}{2B |K_1 z_{2,0} + K_0 z_{1,0} \Omega| T_{ob}} \tag{2.87}$$

For the Doppler migration it has to be also considered that $\delta_{crg} \propto \frac{1}{T_{ob}}$. As a consequence

$$\Delta_{crg} K_T < \frac{\delta_{crg}}{K_T} \Rightarrow K_T^2 < \frac{\delta_{crg}}{\Delta_{crg}} = \frac{\delta_{crg}}{\left|\frac{K_2 z_{2,0}}{\Omega} + 2K_1 z_{1,0} - K_0 z_{2,0}\Omega\right| T_{ob}} = \frac{c}{2f_0 \left|K_2 z_{2,0} + 2K_1 z_{1,0}\Omega - K_0 z_{2,0}\Omega^2\right| T_{ob}^2} \tag{2.88}$$

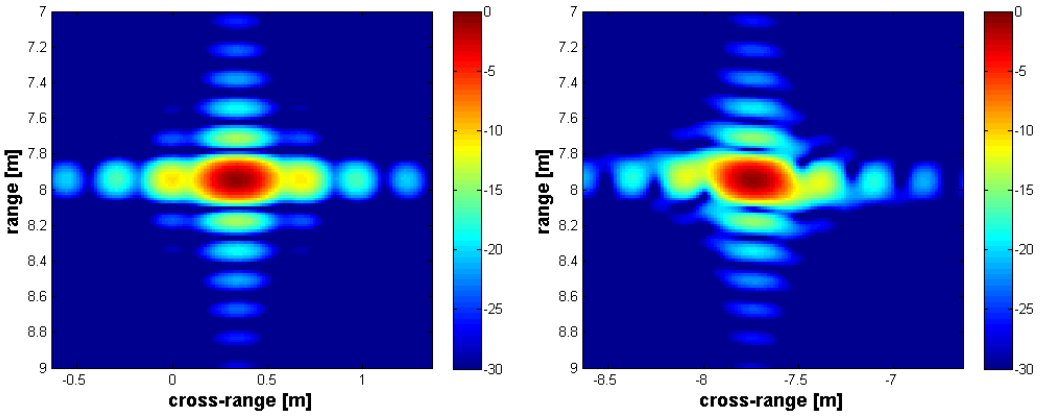

(a) (b)

FIGURE 2.12: Simulation set-up example: zoom on scatterer #2 (a) and #3 (b) after the CPI reduction by $K_T = 0.6$.

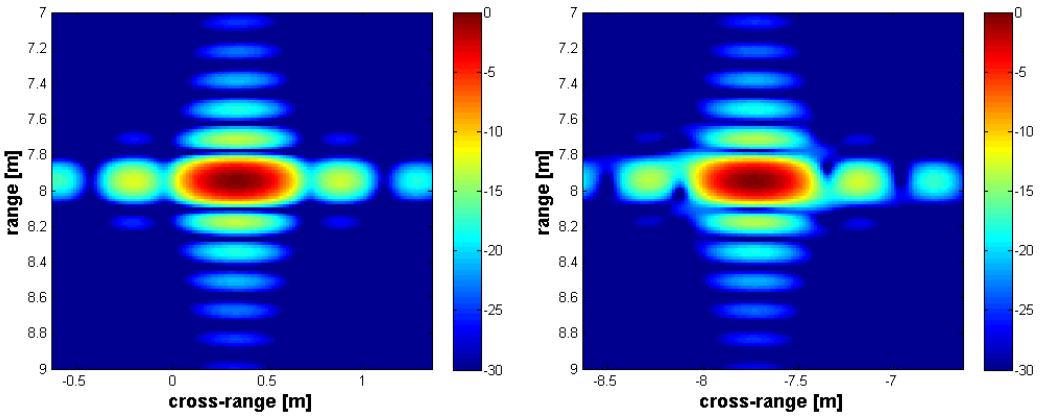

(a) (b)

FIGURE 2.13: Simulation set-up example: zoom on scatterer #2 (a) and #3 (b) after the CPI reduction by $K_T = 0.4$.

Consider now the "five scatterers" example shown above. In this case, for scatterers #2 and #4

$$\delta_{rng}/\Delta_{rng} = 25.4237 > 1 \tag{2.89}$$

whereas for the #3 and #5

$$\delta_{rng}/\Delta_{rng} = 1.2185 > 1 \tag{2.90}$$

As a consequence, the reduction of the CPI for the range migration distortion attenuation is not needed. On the other hand

$$\delta_{crg}/\Delta_{crg} = 0.2192 < 1 \tag{2.91}$$

for scatterers #2 and #4 and 0.2671 for scatterers #3 and #5. Therefore, in order to delete the Doppler migration effect, it is needed a reduction of the CPI by a factor

$$K_T < \sqrt{0.2192} = 0.4682 \tag{2.92}$$

In order to validate such a result, the effect of the CPI reduction on scatterers #2 (Fig.2.12a and Fig.2.13a) and #3 (Fig.2.12b and Fig.2.13b) for $K_T = 0.6$ and 0.4 are shown in Fig.2.12 and Fig.2.13 respectively. Fig.2.12a shows that the sinc-like shape has been recovered along the range direction. This result can be compared to that shown in Fig.2.9a. In fact, the value of Δ_{rng} is very small compared to the range resolution for scatterer #2. The same cannot be stated for scatterer #2 along the cross-range. However, the distortion mitigation is evident in Fig.2.12a with respect to Fig.2.9a even though the sinc-like shape is not recovered along the cross-range. For scatterer #3 in Fig.2.12b the situation is even worse. Images in Fig.2.13a and Fig.2.13b show instead a more sinc-like shape even if a small distortion is still visible along the cross-range direction in Fig.2.13b. However, the price to pay for recovering the sinc-like shape is a strong resolution loss.

In conclusion, the reduction of the CPI allows for the range and Doppler migration effects to be mitigated, but it obviously causes a resolution loss along the cross-range (see (2.36)). However, it is worth supposing that the application of a super-resolution technique could be useful to restore the original cross-range resolution but not the distortions caused by the migration effects. Such super-resolution techniques are introduced in Chapter 3 and applied for bistatic distortion mitigation in Chapter 5.

Chapter 3

Super-Resolution techniques review

In this Chapter the concept of super-resolution applied for SAR/ISAR imaging is introduced. A general summary and theoretical description of the most common super-resolution techniques is given in Section 3.1. Some of the techniques described are theoretically analyzed in deep and their properties and advantages for SAR/ISAR imaging are discussed in Sections 3.2 to 3.6.

3.1 General Overview

"Resolution" is defined as the system capability to make different input sources separately observable at the output of the system itself. It depends generally on the system PSF. In radar imaging, "resolution" is defined as the capability of the imaging system to distinguish different scattering sources.

A super-resolution technique can be interpreted either as a post-processing algorithm, which can be applied to a SAR/ISAR image, or as a substitute of the RD imaging algorithm in order to exceed the resolution limitations due to the transmitted signal bandwidth and target aspect angle variation within the CPI. The category of the super-resolution techniques includes several areas, i.e., algorithms designed for purposes of bandwidth extrapolation, deconvolution, "Direction of Arrival" (DOA) estimation and estimation of sinusoidal parameters (spectral estimation). Such areas are summarized below.

1. The SAR/ISAR image PSF depends on the frequency/slow-time support (see (2.30)). Bandwidth extrapolation consists of estimating the received signal beyond the available frequency-time support by means of prediction methods or non-linear filtering. As a result, it allows for a narrower PSF in the image domain.

2. As shown in (2.37) for the monostatic case and in (2.76) for the bistatic case, in the absence of distortions, the RD image can be seen as the convolution between the high-resolution reflectivity function of the scene of interest (SAR) or target (ISAR) and the PSF of the imaging system. Therefore, all those methods which aim to invert such a convolution operation, i.e., deconvolution algorithms, can be considered as super-resolution algorithms.

3. In remote sensing and communication systems, array of antennas are frequently used. From an antenna theory point of view, it is known that weights can be applied to the signal received at each antenna in order to modify the beam pattern of the whole array system. This is thanks to the Fourier relationship between the beam pattern and the excitation at the array. One particular application of antenna theory is the DOA estimation which consists of estimating the direction of arrival of the incident e.m. wave. When the angles of arrival of the incident e.m. wave from two different signal sources fall within the main lobe of a uniform linear array (ULA), such sources can not be resolved using conventional beamforming. However, a super-resolution DOA estimator, e.g. MUSIC, can able to separate the two contributors.

4. From the Radar imaging theory it is known that the Fourier transform of an ISAR image relative to an ideal point target is a complex sinusoid with a real-part frequency that depends on the position of the target. From (2.18), (2.21) and (2.28)

$$I(\tau, \nu, z_{1,0}, z_{2,0}) = \mathcal{FT}^{-1}_{t_n \to \nu} \left\{ \mathcal{FT}^{-1}_{f \to \tau} \{S(f, n)\} \right\} \tag{3.1}$$

that implies

$$\mathcal{FT}^{2} \{I(\tau, \nu, z_{1,0}, z_{2,0})\} = S(f, n) = W(f, n)\, A\, e^{-j2\pi f \tau(z_{1,0}, z_{2,0}, n)} \tag{3.2}$$

Therefore, any method that aims to estimate the parameters of multiple sinusoids closely spaced in frequency can be considered to be super-resolution.

In general, super-resolution techniques can be classified in two classes depending on the signal model used:

1. Parametric techniques where the scene is modeled as a collection of a finite number of point scatterers which their position and amplitude have to be estimated.

2. Non-parametric techniques where the scene is assumed as a continuously varying high-resolution function blurred by the imaging PSF. The imaging PSF have to be conveniently altered in order to reduce the blurring effect and improve the capability to distinguish different scattering sources.

Parametric and non-parametric techniques can also be denominated "Point-source" and "Distributed-source" respectively [23].

Parametric or point-source techniques allow for a better modeling and estimation of amplitude and position of major isolated scatters. The drawback is that the final result consists of a linear superposition of perfect point scatters and could be not sufficiently accurate to describe the target of interest. Moreover, the number of scatterers which compose the signal model must be estimated before estimating their position and amplitude. Such a number is an important parameter because, if too small, the final result will not properly describe the high-resolution scene/target reflectivity function and, if too large, it could generate a large number of "false scatterers" (artifacts). Moreover, in many cases, the number of scatterers is calculated by estimating and analyzing the signal covariance matrix that could require a large computational power and amount of memory to be estimated and used for calculations. Most of the super-resolution techniques originally designed for DOA estimation belong to this category.

Non-parametric or distributed-source techniques allow for a better modeling of extended targets and the number of scatterers does not need to be estimated. The high-resolution reflectivity function is modeled as a set of samples on a regular grid and the "number of scatterers" is fixed according to the number of samples in such a grid. However, if an isolated strong scatterer is not positioned on a scene grid point, it may not be estimated accurately. Most of the deconvolution and spectral estimation algorithms belong to this category.

In the following, some of the most commonly used parametric and non-parametric super-resolution techniques are summarized.

3.1.1 Parametric super-resolution techniques

One of the most studied and popular techniques in the point-source class is the Multiple Signal Classification (MUSIC) algorithm by Schmidt [24]. The MUSIC algorithm has been introduced for DOA estimation and consists of modeling the measured data as a combination of a signal subspace and an orthogonal noise subspace. Such subspaces are estimated by means of the analysis of eigen-values and eigen-vectors of the signal covariance matrix. The number of scatterers is estimated by analyzing the eigen-values of the covariance matrix. This technique allows for a good estimation of the position of each scattering center (or sources direction), but it does not allow for the scatterers complex amplitude to be estimated, which remain a separate task. Details about the application of the MUSIC technique for 2D SAR/ISAR imaging can be found in [25].

Another parametric technique is the ESPRIT by Richard Roy [26]. Also ESPRIT has been introduced for DOA estimation and exploits the concept of signal and noise subspaces. ESPRIT is similar to MUSIC but introduces significant advantages in terms of computation and storage requirements. ESPRIT does not require detailed knowledge of the array geometry and element characteristics and is manifestly more robust, i.e., less sensitive with respect to array imperfections than MUSIC. Furthermore, ESPRIT allows for the number of sources, i.e. DOAs, to be simultaneously estimated, unlike MUSIC.

Another technique is the Linear Prediction based Bandwidth Extrapolation (BWE) where the received complex signal is modeled as an auto-regressive (AR) process and extrapolated beyond the frequency/slow-time support by means of a linear prediction based algorithm. The AR model order depends on the number of scatterers and the AR coefficients are estimated by means of appropriated techniques, such as those due to Pisarenko, Prony or Burg. The BWE technique is treated in Section 3.2.

Other techniques such as CLEAN or RELAX can be included in this category since their final result depends on the defined number of scatterers. Such techniques aim to detect the dominant scatterers in the SAR/ISAR image and do not allow for two or more scatterers in the same main beam to be resolved. For this reason they can no longer be said to be real super-resolution techniques. The CLEAN was introduced by Jan Högbom in 1974 [27] to reduce sidelobes and induced artifacts in radio astronomy and appears for the first time in radar imaging in [28] by Tsao and Steinberg.

This technique consists of the following basic steps:

1. Selection of the highest peak of the image assumed as related to the strongest point source in the scene;
2. Measurement of the complex amplitude and position;
3. Estimation of the PSF related to the selected scatterer;
4. Subtraction of the estimated PSF from the image in order to leave a residual;
5. Repeat the steps above on the residual from the previous iteration until a certain constraint, for example related to the residual energy, is satisfied or until a fixed number of scatterers are detected.

The CLEAN technique is treated in Chapter 4. The main disadvantage is that once a scatterer has been detected and its position and amplitude estimated, such estimations are fixed. As a consequence, it may happen that spurious low-power targets can be created near the main scatterer to compensate for estimation errors.

For this reason the RELAX algorithm was proposed for spectral estimation purposes by Jim Li and Stoica in [29] as an improvement of the CLEAN, whereby at each iteration the estimated parameters of all the previously discovered targets are re-estimated in an iterative loop. Thus, target parameters are more accurately estimated. Furthermore, a generalized Akaike information criterion (GAIC) is proposed to automatically determine the number of scatterers instead using a fixed number.

The Incremental Multi-Parameter (IMP) algorithm iteratively removes detected signals from the data and then searches the residual for further signals [30]. Unlike CLEAN and RELAX, the IMP works by calculating the subspace spanned by the calibration vectors corresponding to the latest estimates at each iteration. Rather than subtracting the effect of the detected scatterer, the data is projected onto the orthogonal subspace. Similarly to the RELAX, the IMP algorithm refines the estimated parameters of the previously detected signals at each iteration. The subspace formulation of IMP is reminiscent of MUSIC, but IMP is capable of resolving uncorrelated signals at Signal to Noise Ratio (SNR) lower than required by MUSIC.

3.1.2 Non-parametric super-resolution techniques

Some of the most basic non-parametric approaches for super-resolution consist of the application of deconvolution algorithms, e.g., the Least Squares (LS), the Minimum Mean Square Error (MMSE) and the Singular Value Decomposition (SVD) methods. Deconvolution algorithms work by assuming the imaging PSF known and the range-Doppler compression process equivalent to the convolution between the imaging 2D PSF and the high-resolution reflectivity function of the target/scene $\gamma(\mathbf{z})$. In this case, the imaging process is mathematically described as follows

$$\mathbf{g} = \mathbf{T}\mathbf{f} + \mathbf{n} \tag{3.3}$$

where $\mathbf{g}$ is the vectorized SAR/ISAR image

$$\begin{aligned} \mathbf{g} &= \text{vec}\,(\mathbf{I}) = \text{vec}\left(\begin{bmatrix} I(\tau_1,\nu_1) & I(\tau_1,\nu_2) & \cdots & I(\tau_1,\nu_N) \\ I(\tau_2,\nu_1) & I(\tau_2,\nu_2) & \cdots & I(\tau_2,\nu_N) \\ \vdots & \vdots & \ddots & \vdots \\ I(\tau_M,\nu_1) & I(\tau_M,\nu_2) & \cdots & I(\tau_M,\nu_N) \end{bmatrix}\right) = \\ &= [I(\tau_1,\nu_1),\cdots,I(\tau_M,\nu_1),I(\tau_1,\nu_2),\cdots,I(\tau_M,\nu_{N-1}),I(\tau_1,\nu_N),\cdots,I(\tau_M,\nu_N)]^T \end{aligned} \tag{3.4}$$

$\mathbf{f}$ is the vectorized target/scene reflectivity function, $\mathbf{n}$ is the additive zero-mean white Gaussian thermal noise with diagonal covariance matrix $\mathbf{R}_n$ and $\mathbf{T}$ is the $MN \times MN$ Toeplitz convolution matrix that applies the effect of the PSF

$$\mathbf{T} = \begin{bmatrix} \mathbf{T}_c & \mathbf{T}_{c-1} & \cdots & \mathbf{T}_2 & \mathbf{T}_1 & 0 & \cdots & 0 & 0 \\ \mathbf{T}_{c+1} & \mathbf{T}_c & \cdots & \mathbf{T}_3 & \mathbf{T}_2 & \mathbf{T}_1 & \cdots & 0 & 0 \\ \vdots & \vdots & \ddots & \vdots & \vdots & \vdots & \ddots & \vdots & \vdots \\ \mathbf{T}_{M-1} & \mathbf{T}_{M-2} & \cdots & \mathbf{T}_c & \mathbf{T}_{c-1} & \mathbf{T}_{c-2} & \cdots & \mathbf{T}_1 & 0 \\ \mathbf{T}_M & \mathbf{T}_{M-1} & \cdots & \mathbf{T}_{c+1} & \mathbf{T}_c & \mathbf{T}_{c-1} & \cdots & \mathbf{T}_2 & \mathbf{T}_1 \\ 0 & \mathbf{T}_M & \cdots & \mathbf{T}_{c+2} & \mathbf{T}_{c+1} & \mathbf{T}_c & \cdots & \mathbf{T}_3 & \mathbf{T}_2 \\ \vdots & \vdots & \ddots & \vdots & \vdots & \vdots & \ddots & \vdots & \vdots \\ 0 & 0 & \cdots & \mathbf{T}_M & \mathbf{T}_{M-1} & \mathbf{T}_{M-2} & \cdots & \mathbf{T}_c & \mathbf{T}_{c-1} \\ 0 & 0 & \cdots & 0 & \mathbf{T}_M & \mathbf{T}_{M-1} & \cdots & \mathbf{T}_{c+1} & \mathbf{T}_c \end{bmatrix} \tag{3.5}$$

where $\mathbf{T}_i$ is the $N \times N$ convolution matrix determined from the i^{th} column of the 2D PSF matrix $\mathbf{H}$ with central coordinates (d, c) defined by

$$\mathbf{H} = \begin{bmatrix} h_{1,1} & h_{1,2} & \cdots & h_{1,c} & \cdots & h_{1,M-1} & h_{1,M} \\ h_{2,1} & h_{2,2} & \cdots & h_{2,c} & \cdots & h_{2,M-1} & h_{2,M} \\ \vdots & \vdots & \ddots & \vdots & \ddots & \vdots & \vdots \\ h_{d,1} & h_{d,2} & \cdots & h_{d,c} & \cdots & h_{d,M-1} & h_{d,M} \\ \vdots & \vdots & \ddots & \vdots & \ddots & \vdots & \vdots \\ h_{N-1,1} & h_{N-1,2} & \cdots & h_{N-1,c} & \cdots & h_{N-1,M-1} & h_{N-1,M} \\ h_{N,1} & h_{N,2} & \cdots & h_{N,c} & \cdots & h_{N,M-1} & h_{N,M} \end{bmatrix} \tag{3.6}$$

the superscript T in (3.4) denotes the transpose operator.

Actually, the model above does not take into account effects like multiple reflections between different parts of the target, shadowing, non-linear components of the radar, distortions due to range and/or Doppler migration, etc. Therefore, any super-resolution technique based on this model does not take them into account.

Given the image model in (3.3), deconvolution techniques aim to estimate $\mathbf{f}$ by minimizing a certain cost function J.

The LS approach aims to minimize the square difference between the generated image from the scene estimation and the measured one. The cost function for the LS approach is defined as follows

$$J_{\text{LS}} = \|\mathbf{g} - \mathbf{T}\mathbf{f}\|^2 \tag{3.7}$$

In order to estimate $\mathbf{f}$, the cost function in (3.7) is derived with the following result

$$\hat{\mathbf{f}}_{\text{LS}} = \mathbf{T}^{\dagger}\mathbf{g} = \left(\mathbf{T}^H\mathbf{T}\right)^{-1}\mathbf{T}^H\mathbf{g} \tag{3.8}$$

where the superscript H denotes the Hermitian transpose operator and $\mathbf{T}^{\dagger}$ is the Moore-Penrose pseudoinverse matrix of $\mathbf{T}$.

However, the LS approach is unstable with respect to data perturbations, i.e., small changes in the measured data results in very large changes in the final result. The most popular approach to stabilize the problem is the Tikhonov regularization or diagonal loading. The main effect of the Tikhonov regularization method is an additional quadratic term that mitigates peaks and effects of noise amplification, i.e., a smoothing effect in the final result. Furthermore, this regularization method does not involve any further computational loading.

The MMSE approach is similar to LS but the solution is achieved by using a Bayesian formulation and Gaussian statistics. The MMSE approach is very popular and there is a large variety of implementations, such as the MMSE-T and MMSE-A treated and tested in [23]. The basic form of MMSE super-resolution is known as Wiener deconvolution and needs the knowledge/estimation of the scene and noise covariance matrices. The MMSE aims to apply a linear operator $\mathbf{L}$ in order to minimize the expected square norm of the reconstruction error, i.e., the following cost function

$$J_{\text{MMSE}} = \mathbb{E}\left\{\|\mathbf{Lg} - \mathbf{f}\|^2\right\} \tag{3.9}$$

where $\mathbb{E}\{\cdot\}$ is the expectation operator. As a result, the reflectivity function estimation $\hat{\mathbf{f}}_{\text{MMSE}}$ is calculated as follows [31]

$$\hat{\mathbf{f}}_{\text{MMSE}} = \mathbf{Lg} = \mathbf{R}_f\mathbf{T}^H\left(\mathbf{T}\mathbf{R}_f\mathbf{T}^H + \mathbf{R}_n\right)^{-1}\mathbf{g} \tag{3.10}$$

where $\mathbf{R}_f$ is the covariance matrix of the a priori statistical distribution of $\mathbf{f}$. The problem is that $\mathbf{R}_f$ is generally not known and have to be estimated from the available measured data [32].

In the SVD super-resolution the same cost function of the LS is used and the PSF matrix $\mathbf{T}$ is decomposed as follows

$$\mathbf{T} = \mathbf{UDV}^H \tag{3.11}$$

where $\mathbf{U}$ and $\mathbf{V}$ are orthogonal matrices and $\mathbf{D}$ is a diagonal matrix composed of the "Singular Values" d_i. Those singular values below a certain threshold λ_{SVD} are set to zero and the inverse of the PSF matrix is calculated as follows

$$\mathbf{T}^{-1}_{\text{SVD}} = \mathbf{V}\mathbf{D}^{-1}\mathbf{U}^H \tag{3.12}$$

where the elements of $\mathbf{D}^{-1}$ are set as

$$\left\{\mathbf{D}^{-1}\right\}_{i,j} = \begin{cases} 1/d_i & \text{if} \quad i = j \quad \text{and} \quad d_i \geq \lambda_{\text{SVD}} \\ 0 & \text{if} \quad i = j \quad \text{and} \quad d_i < \lambda_{\text{SVD}} \\ 0 & \text{if} \quad i \neq j \end{cases} \tag{3.13}$$

Therefore, the SVD estimates the high-resolution reflectivity function as follows

$$\hat{\mathbf{f}}_{\mathrm{SVD}} = \mathbf{T}_{\mathrm{SVD}}^{-1}\mathbf{g} \tag{3.14}$$

If $d_i \geq \lambda_{\mathrm{SVD}}\, \forall i = 1, \ldots, MN$, the SVD algorithm is equivalent to the LS and $\mathbf{T}_{\mathrm{SVD}}^{-1} = \mathbf{T}^{\dagger}$.

The cancellation of small singular values results in higher SNR in the final image. This is because small singular values cause the condition number of the matrix to increase and, as a consequence, amplification of noise. However, if too many values are removed, some useful signal components may be canceled, resulting in a biased estimate. λ_{SVD} has to be carefully chosen since it is not defined in the basic algorithm and depends on the specific application. In [33] this approach is used for data fusion and super-resolution.

Other non-parametric super-resolution techniques such as the Capon's Minimum Variance Method (MVM) [34] and the Amplitude and Phase Estimation of a Sinusoid (APES) [35] belong to the power spectrum estimation and adaptive beamforming category.

Capon's MVM is one of the most known super-resolution approaches. It has been implemented in several variations for several applications ans is based on a bank of adaptive band-pass FIR filters. In radar imaging application, Capon's MVM aims to estimate the Radar Cross Section (RCS) for each pixel location.

One of the most popular variations of the MVM is the APES technique. Unlike Capon's MVM, both noise and interference are estimated in the covariance matrix and, as a consequence, APES is a matched filter that allows for more accurate spectral estimates by reducing the amount of noise that leaks through the filter.

Capon's MVM and APES are analyzed in deep in Section 3.3 and 3.4 respectively.

Another commonly used and studied distributed-source super-resolution technique is the Super-SVA (SSVA) [36], which iteratively exploits the non-linear properties of the Spatially Variant Apodization (SVA) technique. SVA was introduced by Stankwitz for spectral estimation and adaptive beamforming and is based on a bank of adaptive FIR filters [37]. It is a powerful technique used to eliminate sidelobes. However, rather than Capon's MVM and APES, SVA is not a super-resolution technique since it does not allow to exceed the resolution limitations of the RD imaging algorithm. The super-resolution effect can be achieved by exploiting the fact that SVA is based on a non-linear adaptive filtering and, as a consequence, it causes a bandwidth widening at its output. Such a bandwidth widening is iteratively exploited in order to make a controlled extrapolation of the complex signal along both the frequency and slow-time directions and, as a consequence, the image resolution along both the range and Doppler directions can be enhanced. Details about SSVA can be found in Section 3.5.

Another non-parametric super-resolution approach is based on the concept of Compressed Sensing (CS). The CS theory is based on the principle that, through optimization, the sparsity of a signal can be exploited to recover the signal itself from a smaller number of samples than required by the Shannon-Nyquist sampling theorem and it is used for several applications.

The CS theory can be exploited for Radar imaging super-resolution by reconstructing the received signal over a larger bandwidth or a longer CPI and, as a consequence, enhance the resolution in the image domain. The main difference between the CS-based super-resolution and the other extrapolation methods, parametric spectral estimation techniques and adaptive beamforming algorithms is that the CS is a probabilistic approach, which refers to the capability of CS to reconstruct the signal with a certain probability. CS application for super-resolution is treated in Section 3.6.

In conclusion, the reader is referred to [38], where Pastina *et al.* give a review of several algorithms with several useful references, and to [39] where De Graaf extensively discusses the use of several spectral estimation algorithms for SAR imaging with comprehensive comparison and performance analysis.

3.2 Linear Prediction based Bandwidth Extrapolation

The Linear Prediction based Bandwidth Extrapolation (BWE) is a parametric super-resolution technique where the received signal is modeled as the summation of a finite number of contributions from a finite number of scatterers. An autoregressive (AR) time-series model is used to extrapolate the spectral bandwidth of the uncompressed signal. This AR approach was investigated by S. B. Bowling of Lincoln Laboratory in 1977 as a means of improving resolution for Doppler-Time-Intensity (DTI) analysis [40]. In [41] K.M. Cuomo discusses it to improve the slant range resolution of the pulse compression process.

By referring to [42], the exploited signal model is shown in (3.15).

$$S(f,n) = \sum_{i=1}^{N_s} \sigma_i(f,n)\, e^{-j2\pi f \frac{2}{c} R'_i(n)} \tag{3.15}$$

where N_s is the number of scatterers which composes the signal model, $\sigma_i(f,n)$ is the complex reflectivity function of the i^{th} scatterer and $R'_i(n)$ its effective range as in (2.20) and (3.16).

$$R'_i(n) = \mathbf{z}_i \cdot \mathbf{i}_{LoS}(n) = [z_{1,i}, z_{2,i}, z_{3,i}] \cdot \mathbf{i}_{LoS}(n) \tag{3.16}$$

As written in Section 2.1, the reflectivity function can be assumed as constant with respect to both frequency and slow-time for all the scatterers. Therefore, it can be assumed $\sigma_i(f,n) \simeq \sigma_i$. Furthermore, it is assumed a uniformly sampled frequency spectrum

$$f = f_0 + m\delta_f \tag{3.17}$$

where δ_f is the frequency sampling spacing and f_0 the carrier frequency of the transmitted signal. As a consequence, the frequency variable in (3.15) can be discretized and the signal model can be rewritten as follows

$$S(m,n) = \sum_{i=1}^{N_s} \sigma_i \, e^{-j\frac{4\pi(f_0+m\delta_f)}{c}R_i'(n)} \tag{3.18}$$

Given the signal model in (3.18), after motion compensation the BWE algorithm works in two steps:

1. Frequency bandwidth extrapolation;
2. Aperture extrapolation.

In the first step, the frequency response in (3.18) is approximated by a linear-prediction all-pole model. For a uniformly sampled frequency spectrum, such a model states that the samples must meet the following condition

$$s_n[m] = \begin{cases} -\sum_{k=1}^{p_{\mathrm{AR}}} c_k \, s_n[m-k] & \text{forward} \\ -\sum_{k=1}^{p_{\mathrm{AR}}} c_k^* \, s_n[m+k] & \text{backward} \end{cases} \tag{3.19}$$

where $(\cdot)^*$ denotes the complex conjugate operator, c_k are the model coefficients, p_{AR} is the model order, given by the number of scattering centers, and

$$s_n[m] \doteq S(m,n) \tag{3.20}$$

The relationship in (3.19) holds assuming the number of scatterers known and the exact model coefficients. The first step consists of estimating the AR coefficients c_k from the measured data by means of appropriated techniques. Several methods have been proposed, such as techniques due to Pisarenko, Prony and Burg mentioned in Section 3.1.1. In this Thesis the Burg's algorithm is treated since it is computationally efficient and offers advantages over the others in terms of performance and stability, i.e., it avoids exponentially growing signals at the linear-prediction filter output.

Burg's algorithm [43] is an iterative procedure that aims to minimize the sum of the prediction error over the entire data set. The prediction error is defined in (3.21) in the forward and in (3.22) in the backward direction.

$$e_f = s_n[m] + \sum_{k=1}^{p_{\mathrm{AR}}} c_k \, s_n[m-k] \tag{3.21}$$

$$e_b = s_n[m-p_{\mathrm{AR}}] + \sum_{k=1}^{p_{\mathrm{AR}}} c_k^* \, s_n[m-p_{\mathrm{AR}}+k] \tag{3.22}$$

By referring to [44], Burg's method in its basic form is shown below.

1. Initialization:

$$i = 0 \tag{3.23}$$

$$\mathbf{e}'_{f,0} = \mathbf{e}'_{b,0} = [s_n[0],\, s_n[1],\, \ldots,\, s_n[M-1]]^T \tag{3.24}$$

   where M is the number of frequency samples.

2. The first element of $\mathbf{e}'_{f,i}$ and the last of $\mathbf{e}'_{b,i}$ are removed:

$$\mathbf{e}_{f,i} = \mathbf{e}'_{f,i}(1 : M-i-1) \tag{3.25}$$

$$\mathbf{e}_{b,i} = \mathbf{e}'_{b,i}(0 : M-i-2) \tag{3.26}$$

3. The i^{th} model coefficient is calculated as follows

$$c_i = -\frac{2\mathbf{e}_{b,i}^H \mathbf{e}_{f,i}}{\mathbf{e}_{f,i}^H \mathbf{e}_{f,i} + \mathbf{e}_{b,i}^H \mathbf{e}_{b,i}} \tag{3.27}$$

4. If $i = p_{\mathrm{AR}}$ all the coefficients have been calculated and the algorithm is finished. Otherwise go on with the following steps.

5. The prediction errors are updated as follows

$$\mathbf{e}'_{f,i+1} = \mathbf{e}_{f,i} + c_i \mathbf{e}_{b,i} \tag{3.28}$$

$$\mathbf{e}'_{b,i+1} = \mathbf{e}_{b,i} + c_i^* \mathbf{e}_{f,i} \tag{3.29}$$

6. $i = i + 1$ and back to the step (2).

Once the Burg's algorithm is applied to estimate the linear-prediction model coefficients from the measured data, (3.19) is used to extend the data outside the measured spectrum.

The expanded data is then weighted and compressed via the Fourier transform. The weighting process is used to reduce the influence of the extrapolated data and mitigate prediction errors. Important features that contribute to the success of BWE are

1. The retention of measured data and the phase coherency of the resulting range profile;
2. The use of conventional pulse compression after the data extrapolation;

The Aperture extrapolation step is performed by applying the same as before fixing the frequency and varying the slow-time index as follows

$$s_m[n] = \begin{cases} -\sum_{k=1}^{p_{\mathrm{AR}}} c_k \, s_m[n-k] & \text{forward} \\ -\sum_{k=1}^{p_{\mathrm{AR}}} c_k^* \, s_m[n+k] & \text{backward} \end{cases} \tag{3.30}$$

where

$$s_m[n] \doteq S(m,n) \tag{3.31}$$

This is to extrapolate the measured data along the aspect angle dimension and leads to better resolution in the cross-range direction.

The primary difference between aperture extrapolation and bandwidth extrapolation is that phase may be not linear in n even if the scatterers reflectivity function σ_i is assumed to be independent on the slow-time/aspect angle variable, i.e., the total aperture angle is supposed small enough to approximate $\sigma_i(f,n) \simeq \sigma_i$. This is because even a simple rotating target causes the range terms $R_i'(n)$ to have a sinusoidal dependence on n (see (2.10) and (2.48) for the monostatic and bistatic configuration respectively). Therefore, the aperture extrapolation can be efficaciously applied if the angle change is small enough to approximate the sine and cosine functions with a first order Taylor-Maclaurin polynomial and no range/cross-range migration effects occur. When the phase dependence on n is linear, then the analysis proceeds exactly as in the bandwidth extrapolation case. Obviously the coefficients c_k have to be estimated again for the aperture extrapolation.

BWE can also be applied for data interpolation when the SAR/ISAR image is degraded by frequency gaps or missing pulses. BWE can be used to reconstruct missing signal components by extrapolating two (or more) different signal portions separately. Then, the interpolated synthetic data can be produced from a weighted sum of the multiple extrapolated data. For better understanding the reader is referred to Fig.3.1 where such a procedure is illustrated. In Fig.3.1 n represents the discrete frequency index, $\mathrm{v_L[n]}$ and

$v_H[n]$ refer to the available low-frequency and high-frequency data portions respectively and $\hat{v}[n]$ is the reconstructed data calculated as

$$\hat{v}[n] = \frac{E - n}{E - B}\,\hat{v}_L[n] + \frac{n - B}{E - B}\,\hat{v}_H[n] \tag{3.32}$$

where $\hat{v}_L[n]$ and $\hat{v}_H[n]$ are the high-frequency and low-frequency extrapolated data within the frequency notch respectively and $B \leq E$. Fig.3.1 is borrowed from [42].

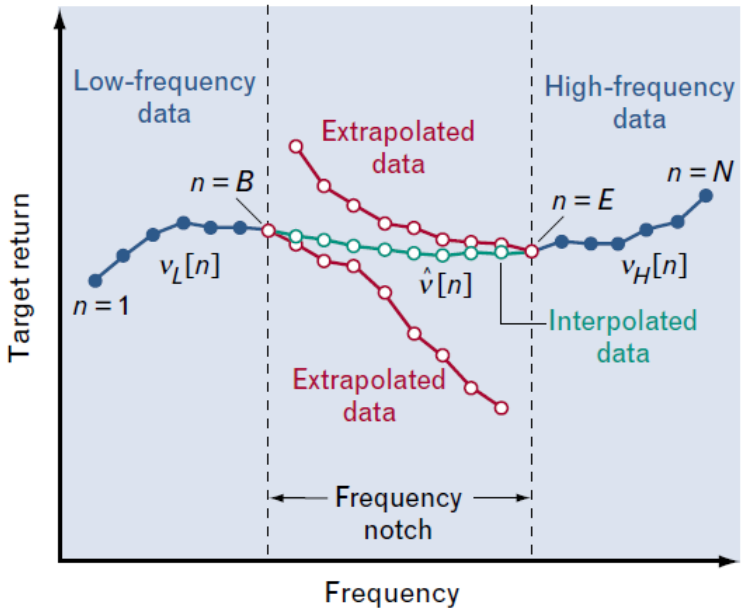

FIGURE 3.1: Signal interpolation based on linear prediction BWE: illustration for 1D gapped signal.

Further details and discussion about the BWE algorithm for super-resolution can be found in [42], whereas in [44] Koen Vos proposes a fast implementation for Burg's algorithm.

3.3 Capon's Minimum Variance Method

Capon's Minimum Variance Method was proposed by J. Capon in 1969 for array beamforming and DOA estimation [34]. Nowadays it is a very popular spectral estimation technique and, for example, is one of the preferred for vertically pointed Mesosphere-Troposphere-Stratosphere (MST) imaging radars [45] and is also used for non-parametric beamforming in SAR tomography [46]. Actually, Capon's MVM does not aim to minimize the variance of the estimate, but evaluates a different linear combination of the signal history samples, i.e., an adaptive FIR filtering, in order to maximize the expected Signal to Interference Ratio (SIR) satisfying the unit gain constraint.

Mathematically, given the measured data samples arranged in the vector $\mathbf{s}$, the linear combination $\mathbf{h}^H(\omega)\,\mathbf{s}$ is performed, where $\mathbf{h}(\omega)$ is the complex space-variant weighting vector for the frequency sample ω. Both $\mathbf{s}$ and $\mathbf{h}(\omega)$ are assumed as column vectors.

For frequency ω, the n^{th} element of $\mathbf{s}$ is modeled as follows

$$s_n = \alpha(\omega)e^{jn\omega} + e_n(\omega) \tag{3.33}$$

where $\alpha(\omega)$ denotes the complex amplitude of a sinusoid with frequency ω which has to be estimated and $e_n(\omega)$ is the unmodeled noise and interference at frequency ω for the n^{th} element of $\mathbf{s}$. MVM maximizes the SIR by selecting $\mathbf{h}(\omega)$ for each ω to minimize the expected output energy

$$\mathbb{E}\left\{\left\|\mathbf{h}^H(\omega)\mathbf{s}\right\|^2\right\} = \mathbf{h}^H(\omega)\,\mathbf{R}_s\,\mathbf{h}(\omega) \tag{3.34}$$

whereas the unit gain constraint is insured by setting

$$\mathbf{h}^H(\omega)\mathbf{a}(\omega) = 1 \tag{3.35}$$

where the elements of $\mathbf{a}(\omega)$ are the samples of the complex 2D unit sinusoid that corresponds to the scattering from a point target at frequency ω. In particular, for arbitrary integer P, the Fourier vector $\mathbf{a}_P(\omega)$ is defined as follows

$$\mathbf{a}_P(\omega) = \left[1\,,\, e^{j\omega}\,,\, e^{j2\omega}\,,\, \cdots\,,\, e^{j(P-1)\omega}\right]^T \in \mathbb{C}^{P\times 1} \tag{3.36}$$

If the length parameter is not specified, such as in (3.35), it is assumed with the same length of the vector it multiplies. Capon's MVM solves the optimization problem in (3.34) by applying the method of Lagrange multipliers, which consists of minimizing the following cost function

$$J_{\text{MVM}} = \mathbf{h}^H(\omega)\,\mathbf{R}_s\,\mathbf{h}(\omega) - \lambda\left(\mathbf{h}^H(\omega)\mathbf{a}(\omega) - 1\right) \tag{3.37}$$

Such a problem is solved in two steps

1. Calculate the partial derivative with respect to $\mathbf{h}(\omega)$ and solve as follows

$$\frac{\partial J_{\text{MVM}}}{\partial \mathbf{h}(\omega)} = \mathbf{h}^H(\omega)\,\mathbf{R}_s - \lambda\mathbf{a}^H(\omega) = \mathbf{0}^T \Rightarrow \mathbf{h}^H(\omega) = \lambda\mathbf{a}^H(\omega)\mathbf{R}_s^{-1} \tag{3.38}$$

2. Choose λ to ensure the solution meets the constraint in (3.35)

$$\mathbf{h}^H(\omega)\mathbf{a}(\omega) = 1 \Rightarrow \left(\lambda\mathbf{a}^H(\omega)\mathbf{R}_s^{-1}\right)\mathbf{a}(\omega) = 1 \Rightarrow \lambda = \frac{1}{\mathbf{a}^H(\omega)\mathbf{R}_s^{-1}\mathbf{a}(\omega)} \tag{3.39}$$

As a consequence, the optimal filter results as follows

$$\mathbf{h}_{\mathrm{MVM}}(\omega) = \frac{\mathbf{R}_s^{-1}\mathbf{a}(\omega)}{\mathbf{a}^H(\omega)\mathbf{R}_s^{-1}\mathbf{a}(\omega)} \tag{3.40}$$

In the equations above, $\mathbf{R}_s$ is the signal history covariance matrix. Theoretically

$$\mathbf{R}_s = \mathbb{E}\left\{\mathbf{s}\mathbf{s}^H\right\} \tag{3.41}$$

but in real applications it is unknown and have to be estimated. Moreover, in (3.40) $\mathbf{R}_s$ needs to be inverted. Consequently, in order to calculate the Capon's optimal filter, a full-rank, non-singular covariance matrix estimate is required.

If a set of N_r realizations of a signal vector $\mathbf{s}$ is available, the most simple way to estimate the covariance matrix is

$$\hat{\mathbf{R}}_s = \frac{1}{N_r}\sum_{n=1}^{N_r}\mathbf{s}_n\mathbf{s}_n^* \tag{3.42}$$

where $\mathbf{s}_n$ is the n^{th} realization of $\mathbf{s}$. However, in radar imaging this approach can be only used if multi-look measurements are available, e.g., in multi-look polarimetric SAR imaging [47]. Most commonly, in radar imaging applications, only one look is available and this approach cannot be used.

In case of single look measurements, there are several ways to estimate the signal covariance matrix, but the most common is the forward-backward method [48]. Such a method consists of averaging different estimated covariance matrices from different subapertures of the whole available data along both the "forward" and "backward" directions.

Referring to Fig.3.2, consider the 1D signal $\mathbf{s} \in \mathbb{C}^{N\times 1}$ and the subaperture $\mathbf{s}_i$ defined as follows

$$\mathbf{s}_i = \left[\mathbf{s}(i), \mathbf{s}(i+1), \ldots, \mathbf{s}(i+\hat{N})\right]^T \in \mathbb{C}^{\hat{N}\times 1} \tag{3.43}$$

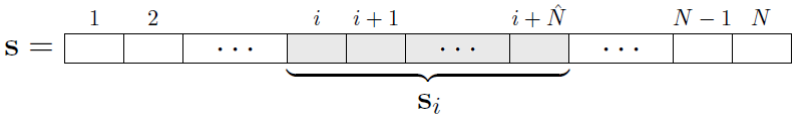

FIGURE 3.2: Subaperture selection for the 1D signal vector $\mathbf{s}$.

Therefore, $L = N - \hat{N} + 1$ overlapping subapertures are available and the forward covariance matrix $\mathbf{R}_F$ is calculated as follows

$$\mathbf{R}_F = \frac{1}{L}\sum_{i=i}^{L}\mathbf{s}_i\mathbf{s}_i^H \tag{3.44}$$

whereas the backward covariance matrix $\mathbf{R}_B$

$$\mathbf{R}_B = \frac{1}{L}\sum_{i=i}^{L} \mathbf{J}_{\hat{N}} \left(\mathbf{s}_i \mathbf{s}_i^H\right)^T \mathbf{J}_{\hat{N}} = \frac{1}{L}\sum_{i=i}^{L} \mathbf{J}_{\hat{N}} \mathbf{s}_i^* \mathbf{s}_i^T \mathbf{J}_{\hat{N}} = \mathbf{J}_{\hat{N}} \mathbf{R}_F^T \mathbf{J}_{\hat{N}} \tag{3.45}$$

where $\mathbf{J}_P$ denotes the $P \times P$ reversal matrix, i.e., a matrix with ones on its anti-diagonal and zeros everywhere else

$$\mathbf{J}_P = \begin{bmatrix} 0 & 0 & \cdots & 0 & 1 \\ 0 & 0 & \cdots & 1 & 0 \\ \vdots & \vdots & \iddots & \vdots & \vdots \\ 0 & 1 & \cdots & 0 & 0 \\ 1 & 0 & \cdots & 0 & 0 \end{bmatrix} \tag{3.46}$$

The forward-backward estimation covariance matrix of $\mathbf{s}$ is calculated by averaging $\mathbf{R}_F$ and $\mathbf{R}_B$ as shown below.

$$\hat{\mathbf{R}}_s = \frac{1}{2}\left(\mathbf{R}_F + \mathbf{R}_B\right) = \frac{1}{2}\left(\mathbf{R}_F + \mathbf{J}_{\hat{N}} \mathbf{R}_F^T \mathbf{J}_{\hat{N}}\right) \in \mathbb{C}^{\hat{N} \times \hat{N}} \tag{3.47}$$

The idea of forward-backward averaging comes from the fact that a complex sinusoid evolves in one spatial direction in the same manner as the conjugate sinusoid evolves in the opposite spatial direction. On the other hand, conjugating and reversing the clutter/noise contribution yields an independent realization. As a consequence forward-backward averaging results in doubling the actual averaging operations.

Covariance matrix estimation is a keystone of the whole Capon's MVM and the most of spectral estimation algorithms. The final result is strictly correlated with it and in case of forward-backward estimation the Capon's filter size depends on the covariance matrix size, i.e., the subaperture length $\hat{N}$. Typically the longer the filter length, the more increased the spectral resolution, but the statistical stability of the spectral estimates can be compromised. This is because, since $L = N - \hat{N} + 1$, a larger filter is obtained by reducing the number of subapertures, i.e., amount of averaging operations.

If the estimated covariance matrix is too large and not enough averaging operations are performed, $\hat{\mathbf{R}}_s$ could result ill-conditioned, i.e., condition number results increased and noise at the output of the Capon's filter amplified. Thus, the aperture size must be chosen as a compromise between spectral resolution and SNR.

In case of a bidimensional signal, i.e., SAR/ISAR application, the signal vector $\mathbf{s}$ is modeled as follows

$$\mathbf{s} = \text{vec}\left(\mathbf{S}\right) = \text{vec}\left(\begin{bmatrix} S(1,1) & S(1,2) & \cdots & S(1,N) \\ S(2,1) & S(2,2) & \cdots & S(2,N) \\ \vdots & \vdots & \ddots & \vdots \\ S(M,1) & S(M,2) & \cdots & S(M,N) \end{bmatrix}\right) \tag{3.48}$$

where

$$S(m,n) = \alpha(\omega_1,\omega_2)e^{j(m\omega_1+n\omega_2)} + e_{m,n}(\omega_1,\omega_2) \tag{3.49}$$

Compare (3.49) with (3.33).

In this case, the signal vector length becomes MN and the covariance matrix have to be estimated from the 2D signal matrix $\mathbf{S}$. Consequently, assuming $L_1 = M - \hat{M} + 1$ and $L_2 = N - \hat{N} + 1$, the forward-backward algorithm works by extracting $L_1 L_2$ bidimensional $\hat{M} \times \hat{N}$ subapertures

$$\mathbf{S}_{l_1,l_2} = \begin{bmatrix} S(l_1,l_2) & S(l_1,l_2+1) & \cdots & S(l_1,l_2+\hat{N}) \\ S(l_1+1,l_2) & S(l_1+1,l_2+1) & \cdots & S(l_1+1,l_2+\hat{N}) \\ \vdots & \vdots & \ddots & \vdots \\ S(l_1+\hat{M},l_2) & S(l_1+\hat{M},l_2+1) & \cdots & S(l_1+\hat{M},l_2+\hat{N}) \end{bmatrix} \tag{3.50}$$

Therefore, the forward covariance matrix can be calculated as follows

$$\mathbf{R}_F = \frac{1}{L_1 L_2}\sum_{l_1=1}^{L_1}\sum_{l_2=1}^{L_2}\mathbf{s}_{l_1,l_2}\mathbf{s}_{l_1,l_2}^H = \frac{\mathbf{Y}\mathbf{Y}^H}{L_1 L_2} \tag{3.51}$$

where

$$\mathbf{s}_{l_1,l_2} = \text{vec}\left(\mathbf{S}_{l_1,l_2}\right) \in \mathbb{C}^{\hat{M}\hat{N}\times 1} \tag{3.52}$$

and

$$\mathbf{Y} = [\mathbf{s}_{1,1}\,,\,\mathbf{s}_{2,1}\,,\,\cdots\,,\,\mathbf{s}_{L_1,1}\,,\,\mathbf{s}_{1,2}\,,\,\cdots\,,\,\mathbf{s}_{L_1,2}\,,\,\cdots\,,\,\mathbf{s}_{L_1,L_2}] \in \mathbb{C}^{\hat{M}\hat{N}\times L_1 L_2} \tag{3.53}$$

For the bidimensional case, the forward-backward sample covariance matrix is then calculated as shown below.

$$\hat{\mathbf{R}}_s = \frac{1}{2}\left(\mathbf{R}_F + \mathbf{J}_{\hat{M}\hat{N}}\mathbf{R}_F^T\mathbf{J}_{\hat{M}\hat{N}}\right) \in \mathbb{C}^{\hat{M}\hat{N}\times\hat{M}\hat{N}} \tag{3.54}$$

For 2D SAR/ISAR, subaperture sizes of $40-50\%$ generally give good results for the most of the methods that exploit the covariance matrix, such as MVM or MUSIC [39].

Once the covariance matrix is estimated, the 2D Fourier vector $\mathbf{a}_{P_1,P_2}(\omega_1,\omega_2)$ for arbitrary integers P_1 and P_2 is calculated as follows

$$\mathbf{a}_{P_1,P_2}(\omega_1,\omega_2) = \mathbf{a}_{P_1}(\omega_1) \otimes \mathbf{a}_{P_2}(\omega_2) \in \mathbb{C}^{P_1P_2\times 1} \tag{3.55}$$

where the 1D Fourier vectors $\mathbf{a}_{P_1}(\omega_1)$ and $\mathbf{a}_{P_2}(\omega_2)$ are calculated by means of (3.36), $\otimes$ denotes the Kronecker product and

$$\begin{aligned} \omega_1 &= 2\pi p/P \quad \text{for} \quad p = 0,\, 1,\, \cdots,\, P-1 \\ \omega_2 &= 2\pi q/Q \quad \text{for} \quad q = 0,\, 1,\, \cdots,\, Q-1 \end{aligned} \tag{3.56}$$

whereas the 2D Fourier transform $\bar{\mathbf{g}}(\omega_1,\omega_2)$ is defined as follows

$$\begin{aligned} \bar{\mathbf{g}}(\omega_1,\omega_2) &= \frac{1}{L_1L_2}\sum_{l_1=1}^{L_1}\sum_{l_2=1}^{L_2}\mathbf{s}_{l_1,l_2}e^{-j(\omega_1(l_1-1)+\omega_2(l_2-1))} \\ &= \frac{1}{L_1L_2}\mathbf{Y}\mathbf{a}_{L_1,L_2}(-\omega_1,-\omega_2) \in \mathbb{C}^{\hat{M}\hat{N}\times 1} \end{aligned} \tag{3.57}$$

Therefore, once $\mathbf{a}_{\hat{M},\hat{N}}(\omega_1,\omega_2)$, $\hat{\mathbf{R}}_s$ and $\bar{\mathbf{g}}(\omega_1,\omega_2)$ are defined, it is possible to apply the Amplitude Spectrum Capon (ASC) estimator as follows

$$\hat{\alpha}_{\text{CAPON}}(\omega_1,\omega_2) = \frac{\mathbf{a}^H_{\hat{M},\hat{N}}(\omega_1,\omega_2)\,\hat{\mathbf{R}}_s^{-1}\,\bar{\mathbf{g}}(\omega_1,\omega_2)}{\mathbf{a}^H_{\hat{M},\hat{N}}(\omega_1,\omega_2)\,\hat{\mathbf{R}}_s^{-1}\,\mathbf{a}_{\hat{M},\hat{N}}(\omega_1,\omega_2)} \tag{3.58}$$

Typically the estimated spectrum is evaluated on a fine uniform frequency grid of size $P \times Q$. High values of P and Q allow for a better modeling of strong isolated scatterers but increase the computational load and do not imply a significant resolution enhancement. Moreover, direct implementation of the above is computationally very demanding. In general, all of the methods that require estimation, inversion, or eigen-decomposition of a full-rank covariance matrix, e.g., MVM, APES, MUSIC, MMSE, etc. are computationally intensive. In typical SAR application the scene of interest can be very wide and the SAR image can be very big in terms of number of samples. Considering for example a 1000×1000 pixel SAR/ISAR image (without zero-padding), assuming a subaperture size of 40%, the resultant covariance matrix will be of 160000×160000 elements. Therefore, to apply these algorithms to typical SAR scenes, it is necessary to employ a "decimation and mosaicing" strategy briefly illustrated below [39, 49]:

1. The signal history is downsampled (decimated) and a series of small overlapping subimages, or Regions Of Interest (ROI), within the entire SAR scene are obtained. The size of these subimages (or image chips) depends primarily on the available computing resources.

2. MVM (or other algorithms) is applied on each subimage serially or in parallel.

3. The chip images after the super-resolution algorithm performing are re-combined into a single image (mosaicing).

Moreover, the forward-backward algorithm can be not enough to guarantee a non-singular invertible covariance matrix compromising the algorithm stability. For this reason, several approaches and variations of the basic MVM have been proposed, e.g., the Reduced Rank MVM (RRMVM) [39], the Rank-Deficient Robust Capon Filter [50], the "Loaded Capon" [51], etc. Further discussion about Capon's MVM can be found in [39].

3.4 Amplitude and Phase Estimation of a Sinusoid

The Amplitude and Phase Estimation of a Sinusoid (APES) is an adaptive filtering approach introduced by Jian Li and Petre Stoica in [35]. APES is closely related to Capon's MVM but estimates both noise and interference in the covariance matrix, i.e., is a matched filter and allows for more accurate spectral estimates by reducing the amount of noise that leaks through the filter. MVM usually gives higher resolution and less biased peak locations than APES, but also higher spectral amplitude bias and Mean Square Error (MSE), i.e., APES gives more accurate spectral estimates at the true peak locations than MVM [49].

In the bidimensional case, assuming the same signal model used for MVM (see (3.49)), the 2D-APES filter is defined as follows

$$\mathbf{h}_{\text{APES}}(\omega_1,\omega_2) = \frac{\mathbf{Q}_s^{-1}(\omega_1,\omega_2)\mathbf{a}(\omega_1,\omega_2)}{\mathbf{a}^H(\omega_1,\omega_2)\mathbf{Q}_s^{-1}(\omega_1,\omega_2)\mathbf{a}(\omega_1,\omega_2)} \tag{3.59}$$

and, the APES estimator is defined by (3.60).

$$\hat{\alpha}_{\text{APES}}(\omega_1,\omega_2) = \frac{\mathbf{a}^H_{\hat{M},\hat{N}}(\omega_1,\omega_2)\,\hat{\mathbf{Q}}_s^{-1}(\omega_1,\omega_2)\,\bar{\mathbf{g}}(\omega_1,\omega_2)}{\mathbf{a}^H_{\hat{M},\hat{N}}(\omega_1,\omega_2)\,\hat{\mathbf{Q}}_s^{-1}(\omega_1,\omega_2)\,\mathbf{a}_{\hat{M},\hat{N}}(\omega_1,\omega_2)} \tag{3.60}$$

where

$$\hat{\mathbf{Q}}_s(\omega_1,\omega_2) = \hat{\mathbf{R}}_s - \frac{1}{2}\begin{bmatrix} \bar{\mathbf{g}}(\omega_1,\omega_2) & \tilde{\mathbf{g}}(\omega_1,\omega_2) \end{bmatrix}\begin{bmatrix} \bar{\mathbf{g}}^*(\omega_1,\omega_2) \\ \tilde{\mathbf{g}}^*(\omega_1,\omega_2) \end{bmatrix} \tag{3.61}$$

$$\tilde{\mathbf{g}}(\omega_1,\omega_2) = \frac{1}{L_1L_2}\tilde{\mathbf{Y}}\mathbf{a}_{L_1,L_2}(-\omega_1,-\omega_2) \tag{3.62}$$

$$\tilde{\mathbf{Y}} = \mathbf{J}_{\hat{M}\hat{N}}\mathbf{Y}^*\mathbf{J}_{L_1L_2} \tag{3.63}$$

$\hat{\mathbf{R}}_s$ is the forward-backward estimated covariance matrix of the signal vector $\mathbf{s}$, $\mathbf{a}_{\hat{M},\hat{N}}(\omega_1,\omega_2)$ and $\bar{\mathbf{g}}(\omega_1,\omega_2)$ are calculated as in (3.55) and (3.57) respectively and the $\mathbf{J}$s are the reversal matrices as in (3.46). Equations (3.59) and (3.60) are analytically demonstrated in [35].

By assuming the noise and interference in $\bar{\mathbf{s}}_{m,n} = \mathbf{s}_{m,n}$ (see (3.52)) and $\tilde{\mathbf{s}}_{m,n} = \mathbf{J}_{MN}\,\mathbf{s}^*_{m,n}$ as independently and identically distributed zero-mean Gaussian random vectors with arbitrary covariance matrix, the $\hat{\alpha}_{\text{APES}}(\omega_1,\omega_2)$ obtained by means of (3.60) is the maximum likelihood (ML) estimate of $\alpha(\omega_1,\omega_2)$. However, this is not exactly true because the $\mathbf{s}_{m,n}$ vectors are overlapping. The noise vectors, i.e., those vectors containing the elements $e_{m,n}(\omega_1,\omega_2)$ (see the 3.49), cannot be considered independent.

Furthermore, $\hat{\mathbf{Q}}_s(\omega_1,\omega_2)$ is an estimate of the noise and interference covariance matrix. This is why $\mathbf{h}_{\text{APES}}$ in (3.59) is a matched filter.

The reader may refer to [35] and [49] for further details about the APES super-resolution technique. In both [52] by Larsson and Stoica and [53] by Zheng-She Liu *et al.* faster and more efficient variants of both MVM and APES are proposed.

3.5 Super Spatially Variant Apodization

Super-SVA is a super-resolution technique introduced by Stankwitz and Kosek in [36]. It exploits the non-linear properties of the Spatially Variant Apodization (SVA) [37] technique in order to enhance the image resolution by extrapolating the signal support. The term "apodization" is borrowed from Hecht's Optics [54] and refers to the suppression of diffraction sidelobes.

In conventional SAR/ISAR imaging, when no weighting is applied, a point target observed in the scene is associated with a 2D sinc-like PSF (see (2.37) for the monostatic case and (2.72) for the bistatic case). For the sinc-like impulse response, the first sidelobe is -13.5dB below the peak and the sidelobe envelope decreases 6dB per octave beyond that. Since SAR/ISAR imagery can have a dynamic range of 50dB or higher, sidelobes for a strong scatterer can easily interfere or obscure nearby weaker targets. Traditionally, sidelobes are reduced by applying an amplitude weighting function to the data, such as the Hamming, Hanning and Kaiser windows. The effect of such weighting functions is a sidelobe reduction but also a mainlobe expansion, i.e., a resolution loss. The Hanning mainlobe for example is twice as wide (null-to-null) as the sinc function. In general, all linear weighting functions are a compromise between a narrow mainlobe (resolution) and low sidelobes and result in a spatially invariant PSF, i.e., the same for every location in the image. The reader may refer to [55] for further details about linear weighting.

The SVA is a special case of Adaptive Sidelobe Reduction (ASR) [56] based on cosine-on-pedestal weighting that allows to suppress sidelobes while preserving the mainlobe width. Rather than Hamming, Hanning or other weighting functions, SVA is a non-linear technique which results in a spatially variant PSF, i.e., a different weighting function for every pixel in the image.

In particular, SVA is based on the multi apodization concept summarized below:

1. Compute different versions of the image by using different weighting functions, such as uniform and Hanning (see Fig.3.3a in blue and red respectively);
2. Select the value with minimum module from the different images for each spatial location (see Fig.3.3b).

In case of complex images the second step is performed by selecting the complex value whose magnitude is minimum. However, in the most of cases the real (I or in-phase) and imaginary (Q or quadrature) parts are elaborated separately. In case of two images this procedure is called Dual Apodization (DA).

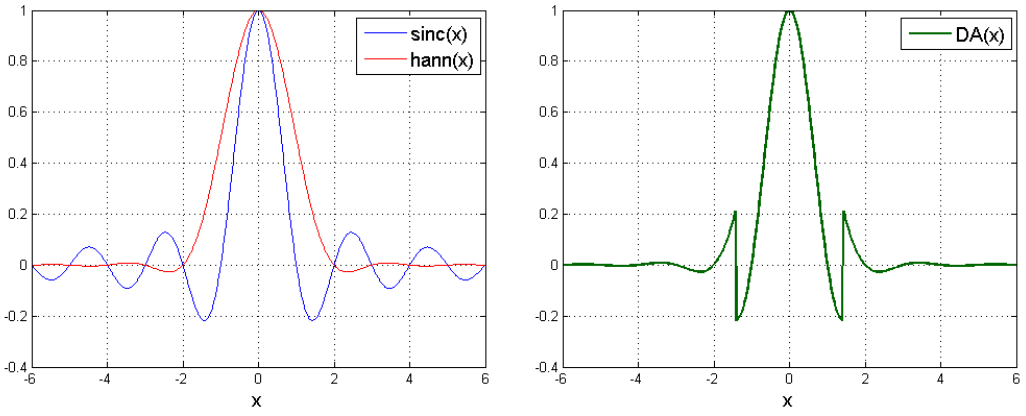

(a) (b)

FIGURE 3.3: Illustration of the uniform (in blue) and Hanning (in red) point spread functions (a) and Dual Apodization result (b).

Another version of this procedure exploits the fact that, for those points for which the uniform and Hanning PSFs have different sign, there must be some intermediate weighting function for which the value of the component is zero. Exploiting the sign change is a way to effectively exploit a family of weighting windows while only having to compute two images.

The algorithm which makes use of this principle is called Complex DA (CDA) and works in the following steps:

1. Compute two versions of the image of interest (real part) by using uniform and Hanning weightings (see Fig.3.4a in blue and red respectively);

2. If the real components of the two images have the same sign then select the one which has the smaller absolute value, otherwise select the value zero (see Fig.3.4b).

Then do the same for the imaginary part. CDA is especially powerful because the sidelobes for the uniform and Hanning windows are opposite in sign. The result for a single bright point is simply the mainlobe of the sinc function (see Fig.3.4b). However, for 2D images the CDA is less effective if the PSF sidelobes are not along the cardinal axes. In [57] a variation of the SVA for squinted images is proposed.

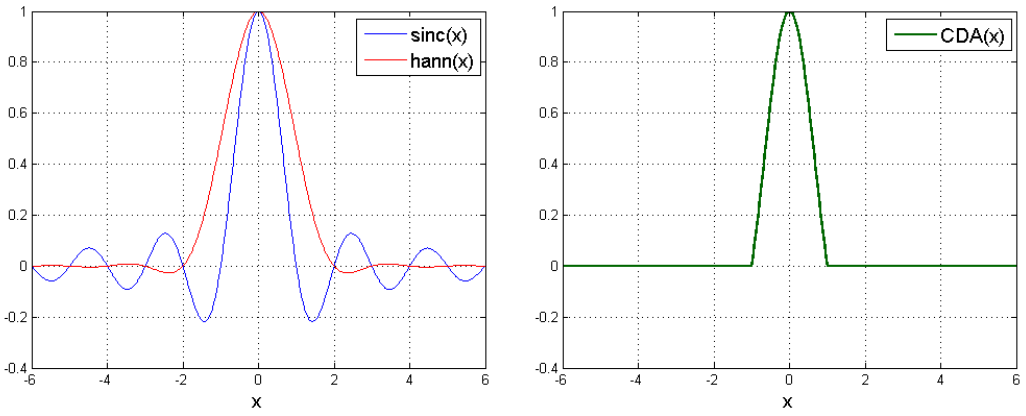

(a) (b)

FIGURE 3.4: Illustration of the uniform (in blue) and Hanning (in red) point spread functions (a) and Complex Dual Apodization result (b).

SVA is based on this concept and effectively eliminates finite-aperture induced sidelobes from uniformly weighted SAR/ISAR images while retaining the mainlobe resolution.

The family of the cosine-on-pedestal weighting functions is given by

$$W_{\mathrm{CoP}}(n) = 1 + 2w\cos\left(2\pi n/N\right) \tag{3.64}$$

where N is the window length and w identifies the particular window of the family ($w = 0$ for the uniform, $w = 0.43$ for the Hamming, $w = 0.5$ for the Hanning, etc.).

Therefore, by taking the N-length discrete Fourier transform of a cosine-on-pedestal weighting function, the Nyquist-sampled impulse response is given by

$$w_{\mathrm{CoP}}(i) = w\delta_{i,-1} + \delta_{i,0} + w\delta_{i,1} \tag{3.65}$$

where $\delta_{i,j}$ denotes the Kronecker delta function

$$\delta_{i,j} = \begin{cases} 1 & \text{if} \quad i = j \\ 0 & \text{if} \quad i \neq j \end{cases} \tag{3.66}$$

The cosine-on-pedestal weighting functions can then be implemented by using a 3-point convolver that makes the SVA extremely simple computationally. In [37] the SVA is proposed in two approaches:

1. I and Q Jointly which is the most natural extension of DA;
2. I and Q Separately which is computationally simpler and yields even greater side-lobe suppression in presence of clutter.

In the following the "I and Q Separately" approach is briefly summarized for the monodimensional case.

Let $g(i)$ be the samples of either the real (in-phase) or imaginary (quadrature) component of a uniformly weighted Nyquist-sampled image. The output from the 3-point convolver in (3.65) is given by

$$g_{\text{SVA}}(i) = w(i)g(i-1) + g(i) + w(i)g(i+1) \tag{3.67}$$

where $w(i)$ varies from 0 (uniform weighting) to 1/2 (Hanning weighting). Therefore, the $w(i)$ which minimizes $|g_{\text{SVA}}(i)|^2$ by setting

$$\frac{\partial}{\partial w(i)} |g_{\text{SVA}}(i)|^2 = 0 \tag{3.68}$$

have to be found. As a result, the unconstrained $w(i)$ that gives the minimum

$$w_u(i) = \frac{-g(i)}{g(i-1) + g(i+1)} \Rightarrow g_{\text{SVA}}(i) = 0 \tag{3.69}$$

However, $w(i)$ must be imposed to be ≥ 0 and $\leq 1/2$, that implies

$$g_{\text{SVA}}(i) = \begin{cases} g(i) & \text{if} \quad w_u(i) < 0 \\ 0 & \text{if} \quad 0 \leq w_u(i) \leq 1/2 \\ g(i) + \frac{1}{2}\left[g(i-1) + g(i+1)\right] & \text{if} \quad w_u(i) > 1/2 \end{cases} \tag{3.70}$$

that is performed on the in-phase and quadrature values independently. Integer Nyquist sample rates are easily handled by applying $g(i-k)+g(i+k)$ instead of $g(i-1)+g(i+1)$ in (3.67) and (3.70) for a sample rate k times Nyquist. Non-integer Nyquist sample rates

need instead some variations to the basic algorithm [58]. For the I and Q Jointly the reader may refer to [37].

In case of bidimensional signals the SVA can be implemented in two ways:

1. Two Dimensions Sequentially: the SVA is implemented for each dimension sequentially, i.e., first along the horizontal and then along the vertical direction;
2. Two Dimensions Simultaneously: the SVA is implemented by means of a bidimensional version of the FIR filter in (3.65).

Both of them can be implemented via the "I and Q Jointly" and "I and Q Separately" approaches.

In the "Two Dimensions Simultaneously" case, the following 2D FIR filter is employed

$$\mathbf{w}_{\text{CoP}}(p,q) = \begin{bmatrix} w_p w_q & w_q & w_p w_q \\ w_p & 1 & w_p \\ w_p w_q & w_q & w_p w_q \end{bmatrix} \tag{3.71}$$

where both w_p and w_q depend on (p,q). Now let

$$Q_p = I(p-1,q) + I(p+1,q) \tag{3.72}$$

$$Q_q = I(p,q-1) + I(p,q+1) \tag{3.73}$$

$$P_{p,q} = I(p-1,q-1) + I(p-1,q+1) + I(p+1,q-1) + I(p+1,q+1) \tag{3.74}$$

Then, the convolution between the image $\mathbf{I}$ and the filter $\mathbf{w}_{\text{CoP}}$ in (3.71) at pixel (p,q)

$$\begin{aligned} I_{\text{SVA}}(p,q) &= I(p,q) + w_p w_q P_{p,q} + w_p Q_p + w_q Q_q \\ &= I(p,q) + [w_q P_{p,q} + Q_p]\, w_p + w_q Q_q \end{aligned} \tag{3.75}$$

By looking at (3.75), it appears that for any given w_q, $I_{\text{SVA}}(p,q)$ is a linear function of w_p and vice versa. It follows that both the maximum and minimum values of $I_{\text{SVA}}(p,q)$ can be found at the four corners of the box $\left[0, \frac{1}{2}\right] \times \left[0, \frac{1}{2}\right]$, i.e., at $(w_p, w_q) = (0,0)$, $(0, \frac{1}{2})$, $(\frac{1}{2}, 0)$, or $(\frac{1}{2}, \frac{1}{2})$. Furthermore, since $I_{\text{SVA}}(p,q)$ is monotonic in w_p and w_q, it goes through zero within the box interval if and only if it changes sign within the interval. As a consequence, for SVA only those four corners need to be checked [37]. Therefore, the 2D SVA is implemented as follows

1. Define

$$\mathbf{w}_{0,\frac{1}{2}} = \begin{bmatrix} 0 & \frac{1}{2} & 0 \\ 0 & 1 & 0 \\ 0 & \frac{1}{2} & 0 \end{bmatrix} \tag{3.76}$$

$$\mathbf{w}_{\frac{1}{2},0} = \begin{bmatrix} 0 & 0 & 0 \\ \frac{1}{2} & 1 & \frac{1}{2} \\ 0 & 0 & 0 \end{bmatrix} \tag{3.77}$$

$$\mathbf{w}_{\frac{1}{2},\frac{1}{2}} = \begin{bmatrix} \frac{1}{4} & \frac{1}{2} & \frac{1}{4} \\ \frac{1}{2} & 1 & \frac{1}{2} \\ \frac{1}{4} & \frac{1}{2} & \frac{1}{4} \end{bmatrix} \tag{3.78}$$

2. Compute

$$\begin{aligned} \mathbf{I}_{\text{SVA},1} &= \mathbf{I} && \text{for} \quad (w_p, w_q) = (0,0) \\ \mathbf{I}_{\text{SVA},2} &= \mathbf{I} \otimes \mathbf{w}_{0,\frac{1}{2}} && \text{for} \quad (w_p, w_q) = (0,\tfrac{1}{2}) \\ \mathbf{I}_{\text{SVA},3} &= \mathbf{I} \otimes \mathbf{w}_{\frac{1}{2},0} && \text{for} \quad (w_p, w_q) = (\tfrac{1}{2},0) \\ \mathbf{I}_{\text{SVA},4} &= \mathbf{I} \otimes \mathbf{w}_{\frac{1}{2},\frac{1}{2}} && \text{for} \quad (w_p, w_q) = (\tfrac{1}{2},\tfrac{1}{2}) \end{aligned} \tag{3.79}$$

3. For each (p,q), if any of the $I_{\text{SVA},i}(p,q)$ for $i = 1,2,3,4$ have sign opposite that of $I(p,q)$, then set $I_{\text{SVA}}(p,q) = 0$.

4. Otherwise, $I_{\text{SVA}}(p,q) = I_{\text{SVA},i}(p,q)$ where i selects the one with minimum magnitude.

In [37] the algorithm is analytically tested for both a single and multiple sinc functions, effects of noise and phase errors are analyzed and the different approaches are treated in deep. In [59] Thomas *et al.* propose a variant of the SVA based on the Kaiser window. Furthermore, in [60] Pastina *et al.* analyze the effect of apodization on the statistical properties of SAR images.

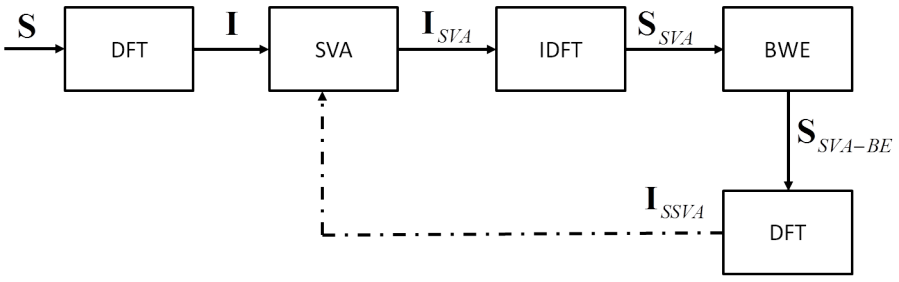

FIGURE 3.5: Super-SVA: algorithm flow chart.

As written in Section 3.1, the non-linearity of the SVA causes a bandwidth widening that can be exploited in order to perform a controlled extrapolation of the complex signal and

enhance the image resolution. The Super-SVA is based on a bandwidth extrapolation (BWE) step performed by an inverse filtering on the SVA result. The process is depicted in Fig.3.5 and can be explained as follows. Let

1. $\mathbf{I}(p,q)$ be the matrix of either the real or imaginary part of the uniformly weighted k-Nyquist-sampled input image;
2. $\mathbf{S}(m,n) = \text{IDFT}\{\mathbf{I}(p,q)\}$ assumed as band-limited;
3. $\mathbf{I}_{\text{SVA}}(p,q)$ be the result of the SVA process;
4. $\mathbf{S}_{\text{SVA}}(m,n) = \text{IDFT}\{\mathbf{I}_{\text{SVA}}(p,q)\}$;
5. $\mathbf{S}_{\text{SVA-BE}}(m,n)$ be the result of the bandwidth extrapolation step;
6. $\mathbf{I}_{\text{SSVA}}(p,q) = \text{DFT}\{\mathbf{S}_{\text{SVA-BE}}(m,n)\}$.

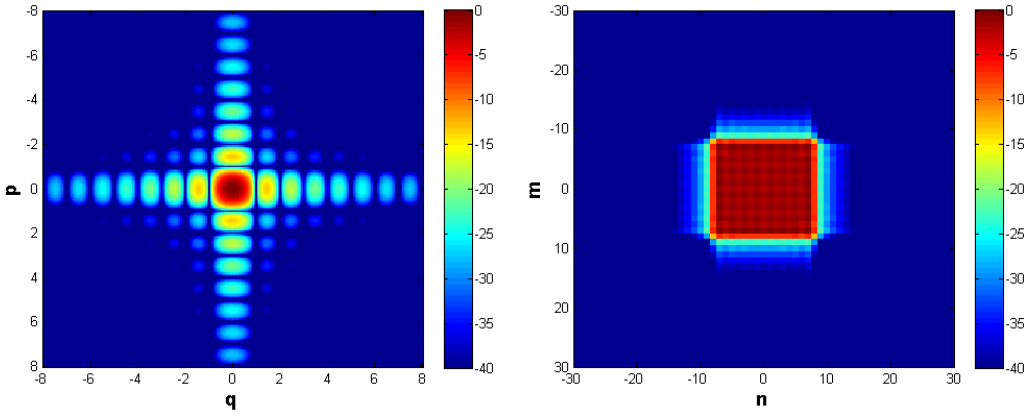

(a) (b)

FIGURE 3.6: Super-SVA first loop example: $\mathbf{I}(p,q)$ (a) and $\mathbf{S}(m,n)$ (b).

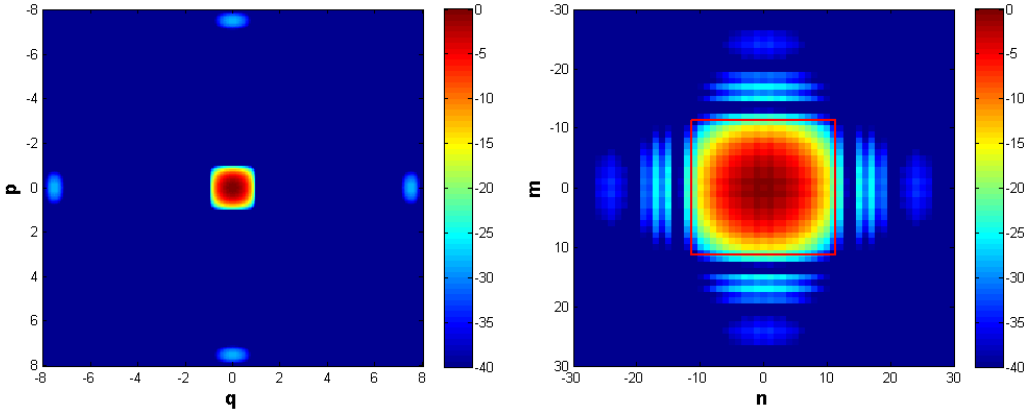

(a) (b)

FIGURE 3.7: Super-SVA first loop example: $\mathbf{I}_{\text{SVA}}(p,q)$ (a) and $\mathbf{S}_{\text{SVA}}(m,n)$ (b).

Consider the sinc-like image in Fig.3.6a as an example for $\mathbf{I}(p,q)$ and its relative $\mathbf{S}(m,n)$ zoomed in Fig.3.6b. Since SVA is a non-linear operation, $\mathbf{S}_{\text{SVA}}(m,n)$ shown in Fig.3.7b is no longer band-limited and has larger extent in the frequency domain than $\mathbf{S}(m,n)$. $\mathbf{I}_{\text{SVA}}(p,q)$ is instead depicted in Fig.3.7a. Images in Fig.3.6, 3.7 and all the following are shown in dB scale for illustration purposes.

The bandwidth extrapolation is then performed in two steps:

1. Inverse filtering to equalize the magnitude taper over an aperture within the first nulls of $\mathbf{S}_{\text{SVA}}(m,n)$ in Fig.3.7b in order to avoid singularities over the extrapolated aperture;
2. Replacing of the filtered signal portion within the original bandwidth with the original complex signal.

The inverse filter is created by defining a 2D sinc function with its sidelobes forced to zero as follows

$$\mathbf{W}_{\text{BE}}(p,q) = \begin{cases} \text{sinc}\,(\mathbf{p})^T \,\text{sinc}\,(\mathbf{q}) & \text{if} \quad |\mathbf{q} \leq 1| \quad \text{and} \quad |\mathbf{p} \leq 1| \\ 0 & \text{otherwise} \end{cases} \tag{3.80}$$

A 2D-IDFT is then performed in order to generate the inverse filter $\mathbf{w}_{\text{BE}}(m,n)$

$$\mathbf{w}_{\text{BE}}(m,n) = \text{IDFT}\{\mathbf{W}_{\text{BE}}(p,q)\} \tag{3.81}$$

where

$$\mathbf{q} = \left[-\frac{N}{2}\,,\, -\frac{N}{2}+\Delta n\,,\, \cdots\,,\, -\Delta n\,,\, 0\,,\, \Delta n\,,\, 2\Delta n\,,\, \cdots\,,\, \frac{N}{2}-1-\Delta n\,,\, \frac{N}{2}-1\right]$$

$$\mathbf{p} = \left[-\frac{M}{2}\,,\, -\frac{M}{2}+\Delta m\,,\, \cdots\,,\, -\Delta m\,,\, 0\,,\, \Delta m\,,\, 2\Delta m\,,\, \cdots\,,\, \frac{M}{2}-1-\Delta m\,,\, \frac{M}{2}-1\right]$$

and where N and M denote the size of the complex signal $\mathbf{S}(m,n)$ along the horizontal and vertical coordinates respectively (before any zero-padding). Δn and Δm are calculated as the ratio between the original and the zero-padded signal size along the same coordinates. The magnitude tapering effect of the SVA in then inverted as follows

$$\mathbf{S}_{\text{SVA-BE}}(m,n) = \begin{cases} \frac{\mathbf{S}_{\text{SVA}}(m,n)}{|\mathbf{w}_{\text{BE}}(m,n)|} & \text{if} \quad (m,n) \in \mathcal{R} \\ 0 & \text{otherwise} \end{cases} \tag{3.82}$$

where $\mathcal{R}$ is the domain contained within the first nulls of the inverse filter magnitude along both the horizontal and vertical coordinates. Such a domain is set to be wider than the original signal bandwidth by a factor $\eta > 1$ named "Bandwidth Extrapolation Factor" (BEF) and is highlighted in red in Fig.3.7b for $\eta = \sqrt{2}$. The result of this first step is shown in Fig.3.8a.

The second step of the bandwidth extrapolation is then performed by replacing the original complex signal within its original bandwidth:

$$\mathbf{S}_{\text{SVA-BE}}(m,n) = \begin{cases} \mathbf{S}_{\text{SVA}}(m,n) & \text{if} \quad (m,n) \in \mathcal{B} \\ \mathbf{S}_{\text{SVA-BE}}(m,n) & \text{otherwise} \end{cases} \tag{3.83}$$

where $\mathcal{B}$ is the supporting frequency domain of the original signal. The final result of the bandwidth extrapolation in shown in Fig.3.8b.

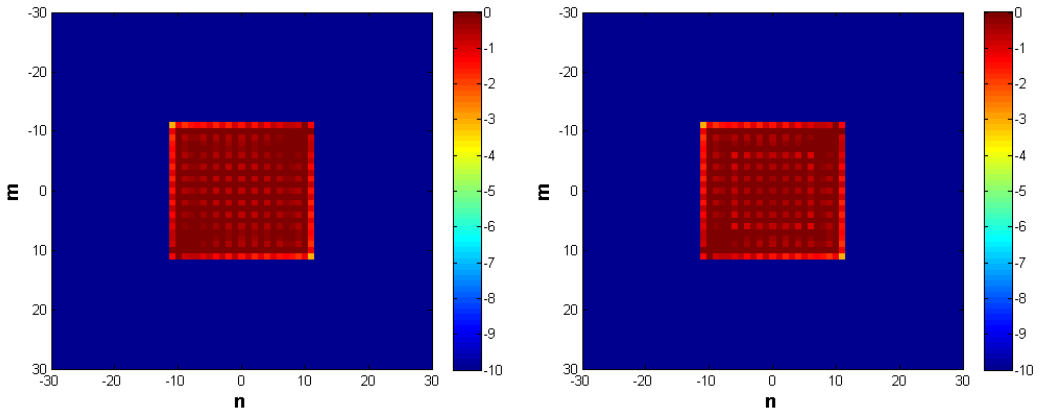

(a) (b)

FIGURE 3.8: Super-SVA first loop example: $\mathbf{S}_{\text{SVA-BE}}(m,n)$ before (a) and after (b) the substitution step.

In the end a 2D-DFT is applied to $\mathbf{S}_{\text{SVA-BE}}(m,n)$ to obtain $\mathbf{I}_{\text{SSVA}}(p,q)$ shown in Fig.3.9a.

The sequence SVA →IDFT →BWE →DFT can be iterated to reach the desired value of resolution. In particular, Fig.3.9b shows the SSVA result after the fourth loop. It is worth highlighting that, by defining Δp and Δq as the first-null resolution of the sinc-like function in Fig.3.6a along the p and q directions respectively, at each SSVA iteration they decrease through the following law

$$\Delta p_i = \Delta p\, \eta_p^i \tag{3.84}$$

$$\Delta q_i = \Delta q\, \eta_q^i \tag{3.85}$$

where i denotes the i^{th} iteration. η_p and η_q highlight the fact that the BEF does not need to be the same for both the horizontal and vertical directions. If the resolution is wanted to be enhanced by a factor K_p and K_q along the p and q directions respectively, the SSVA is needed to be run in

$$N_{loop} = \max\left\{ \left\lceil \log_{\eta_p}(K_p) \right\rceil \,,\, \left\lceil \log_{\eta_q}(K_q) \right\rceil \right\} \tag{3.86}$$

loops.

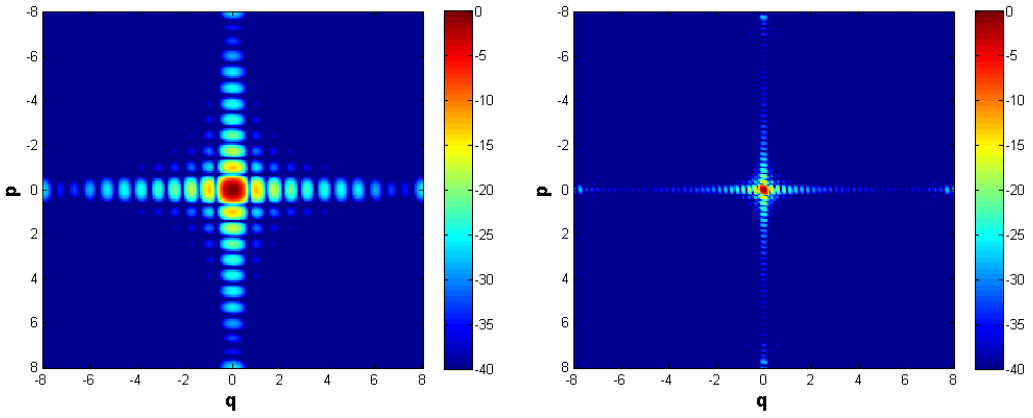

(a) (b)

FIGURE 3.9: Super-SVA example: $\mathbf{I}_{\mathrm{SSVA}}(p,q)$ at the first (a) and fourth (b) SSVA loop.

SSVA is particularly effective for isolated point scatterers where the convolutional model is accurate and can be used for sparse aperture filling [61]. It is important to specify that, to apply the SSVA for super-resolution to SAR/ISAR images, it is needed a sinc-like PSF, i.e., any linear weighting window needs to be inverted before. Moreover, any zero-padding needs to be known since the SVA needs to know the sampling rate in the image domain. For (3.84) it is also worth pointing out that, even if the input image $\mathbf{I}(p,q)$ has integer Nyquist sample rate, this is not guaranteed after the first SSVA iteration. Thus, it is recommended to use the generalized SVA for non-integer Nyquist sampling rates proposed in [58]. In [62] a variant of the SSVA based on a 5-taps SVA is proposed.

3.6 Super-Resolution via Compressed Sensing

The theory of Compressed Sensing (CS) is based on the following concept:

> The Nyquist-Shannon sampling theorem states that a certain minimum number of samples is required in order to perfectly capture an arbitrary bandlimited signal, but when the signal is sparse in a known basis we can vastly reduce the number of measurement that need to be stored. Consequently, when sensing sparse signals we might be able to do better than suggested by classical results.

by [63].

Compressed Sensing theory is based on the concept of "sparsity", i.e., the possibility to represent a signal in a domain where it can be written as a linear combination of a small number of elements.

By assuming the source signal vector $\mathbf{x} \in \mathbb{R}^{N\times 1}$, if a "sparsity basis" $\{\psi_i\}$ exists, a K-sparse representation of $\mathbf{x}$ can be stated as a linear combination of K basis vectors as follows

$$\mathbf{x} = \sum_{i=1}^{N} \theta_i \psi_i = \sum_{k=1}^{K} \theta_{i_k} \psi_{i_k} \tag{3.87}$$

where $\{i_k\}$ are the indexes of those vectors and $\{\theta_i\}$ the weighting coefficients. In (3.87) θ_i is a scalar number, $\{\psi_i\}$ is a N-length column vector and θ_{i_k} are the K non-zero weighting coefficients of the sparse representation. Therefore, by stacking the basis vectors in the $N \times N$ basis matrix $\mathbf{\Psi} = [\psi_1, \ldots, \psi_N]$, the following matrix notation can be used

$$\mathbf{x} = \mathbf{\Psi}\theta \tag{3.88}$$

where θ is the N-length column vector of the weighting coefficients. $\mathbf{\Psi}$ is also named the "dictionary" matrix.

Now, consider to measure $M < N$ linear projections of the signal on a second set of vectors $\{\phi_m\}$. In this case the M-length measured signal $\mathbf{y}$ can be written as

$$\mathbf{y} = \mathbf{\Phi}\mathbf{x} \tag{3.89}$$

where $\mathbf{\Phi} = [\phi_1, \ldots, \phi_M]^T$ is the $M \times N$ "sensing" matrix.

CS theory allows to recover the K largest elements of θ from this set of $M = \mathcal{O}\left(K \log(N/K)\right)$ measurements [64], i.e., to recover a sparse signal from the incomplete measurement with high probability by solving a sparsity-driven optimization problem.

In radar imaging applications, SAR/ISAR images can be considered as composed of a small number of strong point-like scatterers with respect to the total number of pixels. Then, SAR/ISAR images can be considered sparse and reconstructed from incomplete data through CS. However, the sparsity of the SAR/ISAR image is not the only condition for the successful image reconstruction. Another key point is the Restricted Isometry Property (RIP) condition, i.e., the incoherence between the dictionary and the sensing matrices, and an effective algorithm for the optimization problem.

Consider the signal model in (2.10) and suppose the target/scene as a set of point-like scatterers (samples) in a regular grid and its reflectivity function writable as follows

$$\gamma(z_1, z_2) = \sum_{i=1}^{P}\sum_{j=1}^{Q} \sigma_{i,j}\, \delta\left(z_1 - z_{1,j}\right) \delta\left(z_2 - z_{2,i}\right) \tag{3.90}$$

where $\sigma_{i,j}$ is the complex reflectivity function of the scene in the $(i,j)^{\text{th}}$ grid sample. By approximating the sine and cosine functions with their first order Taylor-Maclaurin

polynomial, the received signal after motion compensation can then be written as

$$\begin{aligned} S(f,n) &= W(f,n)\int_{z_1}\int_{z_2}\gamma(z_1,z_2)\,e^{-j\frac{4\pi f}{c}\left[\Omega_{eff}t_n z_{1,j}+z_{2,i}\right]}dz_1dz_2 \qquad (3.91)\\ &= W(f,n)\sum_{i=1}^{P}\sum_{j=1}^{Q}\sigma_{i,j}\int_{z_1}\int_{z_2}\delta\left(z_1-z_{1,j}\right)\delta\left(z_2-z_{2,i}\right)e^{-j\frac{4\pi f}{c}\left[\Omega_{eff}t_n z_{1,j}+z_{2,i}\right]}dz_1dz_2\\ &= W(f,n)\sum_{i=1}^{P}\sum_{j=1}^{Q}\sigma_{i,j}\,e^{-j\frac{4\pi f}{c}\left[\Omega_{eff}t_n z_{1,j}+z_{2,i}\right]}\\ &= W(f,n)\sum_{i=1}^{P}\sum_{j=1}^{Q}\sigma_{i,j}\,e^{-j2\pi(\tau_i f+\nu_j t_n)} \end{aligned}$$

where

$$\tau_i = \frac{2z_{2,i}}{c} \qquad (3.92)$$

$$\nu_j = \frac{2f\Omega_{eff}z_{1,j}}{c} \simeq \frac{2f_0\Omega_{eff}z_{1,j}}{c} \qquad (3.93)$$

denote the delay-time and the Doppler frequency for the $(i,j)^{\text{th}}$ scatterer. The frequency variable f in (3.93) is approximated by the carrier frequency f_0 for the *rectangular domain approximation* of the sample grid in the Fourier domain. However, in a real scenario, both the variables in the signal domain (f,n) and in the image domain (τ,ν) have to be discretized. Therefore, the signal in (3.91) have to be written as function of the following discrete variables:

$$m \;:\; f = f_0 + m\delta_f \qquad (3.94)$$

$$n \;:\; t_n = nT_R \qquad (3.95)$$

$$p \;:\; \tau = p\delta\tau \qquad (3.96)$$

$$q \;:\; \nu = q\delta\nu \qquad (3.97)$$

for $m = 1,\ldots,M$, $n = 1,\ldots,N$, $p = 1,\ldots,P$ and $q = 1,\ldots,Q$ where δ_f is the frequency sampling spacing (see Section 3.2), $\delta\tau$ is the delay-time pixel spacing in (3.98) and $\delta\nu$ is the Doppler frequency pixel spacing in (3.99).

$$\delta\tau = \frac{1}{B} = \frac{1}{P\delta_f} \qquad (3.98)$$

$$\delta\nu = \frac{1}{T_{ob}} = \frac{1}{QT_R} \qquad (3.99)$$

Therefore

$$\tau_i f = \frac{p_i}{P\delta_f}\,(f_0 + m\delta_f) = \frac{mp_i}{P} + \frac{f_0}{B}p_i \qquad (3.100)$$

$$\nu_j t_n = \frac{q_j}{QT_R} nT_R = \frac{nq_j}{Q} \tag{3.101}$$

and the signal model in (3.91) can be rewritten as follows

$$S(m,n) = W(m,n) \sum_{i=1}^{P} \sum_{j=1}^{Q} \sigma_{i,j}\, e^{-j2\pi \frac{f_0}{B} p_i}\, e^{-j2\pi \frac{mp_i}{P}}\, e^{-j2\pi \frac{nq_j}{Q}} \tag{3.102}$$

where $W(m,n)$ represents the signal support in the discrete frequency/slow-time domain. Therefore, by applying the inverse Fourier transform on (3.102), the ISAR image can be expressed as follows

$$I(p,q) = \sum_{i=1}^{P} \sum_{j=1}^{Q} \sigma_{i,j}\, w(p-p_i, q-q_j)\, e^{-j2\pi \frac{f_0}{B} p_i} \tag{3.103}$$

where $w(p,q)$ is the discretized version of the imaging PSF in (2.30). Consider now the matrices $\mathbf{S}_C \in \mathbb{C}^{M\times N}$ and $\mathbf{I} \in \mathbb{C}^{P\times Q}$ to represent the signal in (3.102) and the image in (3.103) respectively. With this notation (3.102) can be written as

$$\mathbf{S}_C = \mathbf{\Psi}_y \mathbf{I} \mathbf{\Psi}_x^T \tag{3.104}$$

where $\mathbf{\Psi}_y \in \mathbb{C}^{M\times P}$ and $\mathbf{\Psi}_x \in \mathbb{C}^{N\times Q}$ are the "Fourier dictionaries" in which $P = M$ and $Q = N$ that perform the range and cross-range compression respectively:

$$[\mathbf{\Psi}_y]_{m,p} = e^{-j2\pi \frac{mp}{P}} \tag{3.105}$$

$$[\mathbf{\Psi}_x]_{n,q} = e^{-j2\pi \frac{nq}{Q}} \tag{3.106}$$

Consider now $\mathbf{S}_C$ in (3.104) as the complete source data matrix from which the full-resolution ISAR image $\mathbf{I}$ is obtained. Then assume $\mathbf{S}$ as a partial signal acquired because of data loss due to hardware malfunctioning or compression requirements. In these cases, the acquired signal $\mathbf{S}$ is assumed to be obtained from the signal in (3.104) after a sensing process

$$\mathbf{S} = \mathbf{\Phi}_y \mathbf{\Psi}_y \mathbf{I} \mathbf{\Psi}_x^T \mathbf{\Phi}_x^T = \mathbf{\Theta}_y \mathbf{I} \mathbf{\Theta}_x^T \tag{3.107}$$

where

$$\begin{aligned} \mathbf{S} &\in \mathbb{C}^{M'\times N'} \\ \mathbf{\Phi}_y &\in \mathbb{C}^{M'\times M} \\ \mathbf{\Phi}_x &\in \mathbb{C}^{N'\times N} \\ \mathbf{\Theta}_y &\in \mathbb{C}^{M'\times P} \\ \mathbf{\Theta}_x &\in \mathbb{C}^{N'\times Q} \end{aligned}$$

where $M' < M$ and $N' < N$. $\mathbf{\Phi}_y$ and $\mathbf{\Phi}_x$ in (3.107) represent the sensing matrices which perform the random selection of samples in the frequency/slow-time domain respectively, whereas $\mathbf{\Theta}_y$ and $\mathbf{\Theta}_x$ are the "undercomplete Fourier matrices" which satisfy the RIP constraint and provide stronger non-coherence than the Gaussian matrix [63, 65]. In [66], the authors introduce a method based on eigenvalue statistics to prove that such an undercomplete Fourier dictionary satisfy the RIP. $\mathbf{\Theta}_y$ and $\mathbf{\Theta}_x$ are defined by considering the indexes of the pulses and frequency bins selected by the sensing process. In particular,

$$[\mathbf{\Theta}_y]_{i,p} = e^{-j2\pi \frac{pm_i}{P}} \tag{3.108}$$

$$[\mathbf{\Theta}_x]_{j,q} = e^{-j2\pi \frac{qn_j}{Q}} \tag{3.109}$$

where $\{m_i\}_{i=1}^{M'}$ and $\{n_j\}_{j=1}^{N'}$ are the frequency and slow-time indexes respectively. The reconstruction of $\mathbf{I}$ from the measurement $\mathbf{S}$ is then achieved by means of the following minimization problem [63]

$$\hat{\mathbf{I}} = \min_{\mathbf{I}} \|\mathbf{I}\|_0 \quad : \quad \left\|\mathbf{S} - \mathbf{\Theta}_y \mathbf{I} \mathbf{\Theta}_x^T\right\|_F^2 \leq \epsilon \tag{3.110}$$

where ϵ is an arbitrary small real number. $\|\cdot\|_F$ and $\|\cdot\|_0$ denote the Frobenius norm and the ℓ_0-norm respectively:

$$\|\mathbf{A}\|_F \doteq \sqrt{\sum_{m=1}^{M}\sum_{n=1}^{N} |a_{m,n}|^2} = \sqrt{\text{trace}\left(\mathbf{A}^H\mathbf{A}\right)} \tag{3.111}$$

$$\|\mathbf{x}\|_0 \doteq |\text{supp}(\mathbf{x})| \tag{3.112}$$

where $a_{m,n}$ is the element in position (m,n) of the generic $M \times N$ size matrix $\mathbf{A}$ in position (m,n), $\text{supp}(\mathbf{x}) = \{i : x_i \neq 0\}$ is the support of the generic vector $\mathbf{x}$ and $|\text{supp}(\mathbf{x})|$ denotes the cardinality of $\text{supp}(\mathbf{x})$, i.e., the number of non-zero components of $\mathbf{x}$. The minimization problem in (3.110) can then be solved by the Smoothed ℓ_0 Norm based sparse decomposition algorithm (SL0) proposed by Hosein Mohimani *et al.* in [67] (see also [68]). The main idea behind the SL0 algorithm is to approximate the ℓ_0 norm, which is a discontinuous function, with a smoothed and continuous function and solve the minimization problem by means of a steepest descend method. The continuous function which approximate the ℓ_0 norm is made with a parameter σ which determines the quality of the approximation. Consider the (one-variable) family of functions

$$f_\sigma(x) = \exp\left\{\frac{-x^2}{2\sigma}\right\} \tag{3.113}$$

for which

$$\lim_{\sigma\to 0} f_\sigma(x) = \begin{cases} 1 & \text{if } x = 0 \\ 0 & \text{if } x \neq 0 \end{cases} \quad \Rightarrow \quad f_\sigma(x) \approx \begin{cases} 1 & \text{if } |x| \ll \sigma \\ 0 & \text{if } |x| \gg \sigma \end{cases} \tag{3.114}$$

Consider now the generic P-dimensional vector $\mathbf{x}$ and the function $F_\sigma(\mathbf{x})$ defined as

$$F_\sigma(\mathbf{x}) = \sum_{i=1}^{P} f_\sigma(x_i) \tag{3.115}$$

Therefore, from (3.114) and (3.115), for small values of σ, the ℓ_0 norm of $\mathbf{x}$ can be approximated as

$$\|\mathbf{x}\|_0 \approx N - F_\sigma(\mathbf{x}) \tag{3.116}$$

The ℓ_0 norm minimization problem can be solved by maximizing $F_\sigma(\mathbf{x})$ for a small value of σ. The value of σ determines the smoothness of F_σ. If σ is large, F_σ will be smoother but a worse approximation of the ℓ_0 norm. On the other hand, if σ is small, F_σ will be a better approximation of $\|\mathbf{x}\|_0$ but the maximization procedure will be more difficult. This is because for small values of σ, F_σ is highly non-smooth and contains a lot of local maxima. The idea is then to use a decreasing sequence of σ and maximize F_σ for each σ_i. The initial value for the maximization algorithm for the generic σ_i is given by the result of the maximization for σ_{i-1}. If σ is gradually decreased, for each σ_i the maximization algorithm starts with an initial solution near to the actual maximizer of F_σ and hence the algorithm will likely escaping from getting trapped into local maxima. Consider now the following linear noiseless model

$$\mathbf{y} = \mathbf{\Phi}\mathbf{x} \tag{3.117}$$

where $\mathbf{y} \in \mathbb{C}^{[M'\times 1]}$ is the recorded signal vector, $\mathbf{x} \in \mathbb{C}^{[P\times 1]}$ is the source signal vector to be estimated and $\mathbf{\Phi} \in \mathbb{C}^{[M'\times P]}$ is the sensing matrix. In [67] is then proven that "for sufficiently large values of σ, the maximizer of $F_\sigma(\mathbf{x})$ subject to $\mathbf{\Phi}\mathbf{x} = \mathbf{y}$ is the minimum ℓ^2 norm solution of $\mathbf{\Phi}\mathbf{x} = \mathbf{y}$, i.e., the solution given by the pseudo-inverse of $\mathbf{\Phi}$". Therefore, the algorithm is initialized with a first solution given by

$$\hat{\mathbf{x}}_0 = \mathbf{\Phi}^\dagger \mathbf{y} \tag{3.118}$$

i.e., the minimum ℓ^2 norm solution which corresponds to $\sigma \to +\infty$. In general, the next value for σ, i.e., the first one of the decreasing sequence, is chosen about two or four times the maximum absolute value of $\hat{\mathbf{x}}_0$. On the other hand, the last (smallest) element of the sequence depends on the desired estimation accuracy. In applications where the inactive elements of $\mathbf{x}$ are exactly zero, σ can be decreased to arbitrarily small values. If

inactive elements of $\mathbf{x}$ are instead small but not exactly zero (in case of noise), i.e.,

$$\mathbf{y} = \mathbf{\Phi x} + \mathbf{n} \tag{3.119}$$

where $\mathbf{n} \in \mathcal{N}(0, \sigma_n^2)$ is the additive noise term, the smallest should be about one to two times the standard deviation of such a noise (σ_n). This is because, while is in this range, the cost function $f_\sigma(x)$ treats small (noisy) samples as zeros, i.e., $f_\sigma(x_i) \approx 1$. Below this range, the algorithm tries to "learn" these undesired noisy values. Intermediate values can be calculated by means of a certain decreasing factor c_σ usually chosen between 0.5 and 1. The sequence of the σ parameters can then be calculated as follows

$$\sigma_j = c_\sigma \, \sigma_{j-1} = c_\sigma^{j-1} \, \sigma_1 = c_\sigma^{j-1} \, 2 \max\left(|\hat{\mathbf{x}}_0|\right) \tag{3.120}$$

for $j = 1, 2 \ \ldots, J$, where J depends on the chosen last value for the sequence:

$$c_\sigma^{J-1} \, \sigma_1 \leq 2\sigma_n \Rightarrow J = 1 + \left\lceil \log_{c_\sigma} \left(\frac{\sigma_n}{\max\left(|\hat{\mathbf{x}}_0|\right)} \right) \right\rceil \tag{3.121}$$

The first estimation $\hat{\mathbf{x}}_0$ and the sequence $[\sigma_1, \sigma_2, \ldots, \sigma_J]$ are then given as input to the following iterative algorithm for $j = 1, \ldots, J$

1. Let $\sigma = \sigma_j$;
2. Let $\mathbf{x} = \hat{\mathbf{x}}_{j-i}$;
3. For $l = 1, \ldots, N_L$ (loop N_L times);
   (a) Let $\mathbf{\Delta} \doteq \left[x_1 \exp\left(\frac{-x_1^2}{2\sigma}\right), \, x_2 \exp\left(\frac{-x_2^2}{2\sigma}\right), \, \ldots, \, x_P \exp\left(\frac{-x_P^2}{2\sigma}\right) \right]^T$;
   (b) Let $\mathbf{x} \leftarrow \mathbf{x} - \mu\mathbf{\Delta}$ where μ is a small positive constant;
   (c) Project $\mathbf{x}$ into a feasible set $\mathcal{S} = \{\mathbf{x} \mid \mathbf{\Phi x} = \mathbf{y}\}$:

$$\mathbf{x} \leftarrow \mathbf{x} - \mathbf{\Phi}^\dagger \left(\mathbf{\Phi x} - \mathbf{y}\right)$$

4. Set $\hat{\mathbf{x}}_j = \mathbf{x}$

where steps 2 and 3 perform an approximate maximization of $F_\sigma(\mathbf{x})$ on the feasible set $\mathcal{S}$ using a fixed number of N_L iterations of the steepest ascend algorithm followed by the projection onto $\mathcal{S}$. The maximization is only approximated because, at each step, it is only needed to enter the region near the (global) maximizer of F_σ for escaping from its local maximizers. In the end $\hat{\mathbf{x}} = \hat{\mathbf{x}}_J$. Further details about this algorithm with theoretical analysis and experimental results can be found in [67].

For SAR/ISAR imaging, the model in (3.117) is replaced by (3.107), i.e., $\mathbf{x}$ is replaced by $\mathbf{I}$ and $\mathbf{y}$ by $\mathbf{S}$. In this case the algorithm is initialized by setting

$$\hat{\mathbf{I}}_0 = \boldsymbol{\Theta}_y^{\dagger} \mathbf{S} \boldsymbol{\Theta}_x^{\dagger T} \tag{3.122}$$

In this case $\boldsymbol{\Delta}$ becomes a $P \times Q$ matrix

$$[\boldsymbol{\Delta}]_{p,q} = I(p,q)\, e^{-\frac{I(p,q)^2}{2\sigma}} \tag{3.123}$$

where $I(p,q)$ is the (p,q) entry of the matrix $\mathbf{I}$ and the step 3(c) is performed as follows

$$\mathbf{I} \leftarrow \mathbf{I} - \boldsymbol{\Theta}_y^{\dagger} \left(\boldsymbol{\Theta}_y \mathbf{I} \boldsymbol{\Theta}_x^T - \mathbf{S} \right) \boldsymbol{\Theta}_x^{\dagger T} \tag{3.124}$$

In the end $\hat{\mathbf{I}} = \hat{\mathbf{I}}_J$.

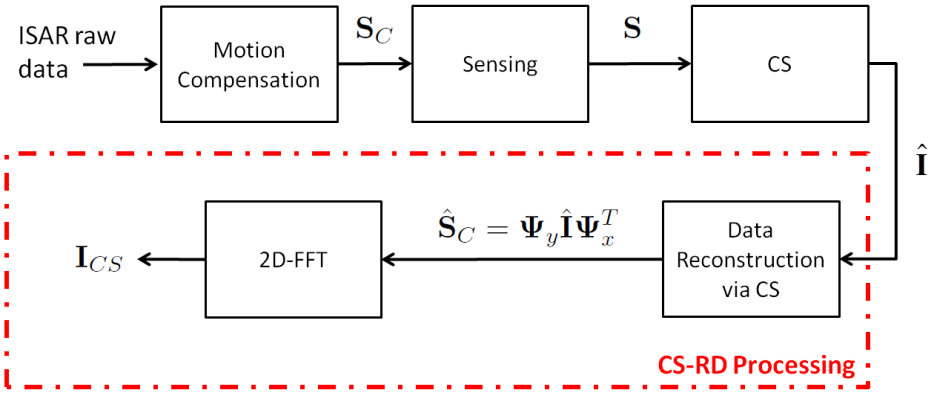

FIGURE 3.10: Sensing and CS reconstruction block diagram.

However, the image at the output of the SL0 algorithm cannot be directly compared with the image at the output of the RD algorithm, because the pixel size does not correspond to the spatial resolution $\delta_{rng} \times \delta_{crg}$ (see (2.26) and (2.36) respectively). For this reason, as shown in Fig.3.10, the raw data is first reconstructed from the CS image by means of the Fourier dictionaries

$$\hat{\mathbf{S}}_C = \boldsymbol{\Psi}_y \hat{\mathbf{I}} \boldsymbol{\Psi}_x^T \tag{3.125}$$

and the ISAR image is then obtained by means of the conventional RD algorithm

$$\mathbf{I}_{CS} = \text{2D-DFT} \left\{ \hat{\mathbf{S}}_C \right\} \tag{3.126}$$

This is how the CS theory is exploited in order to recover from incomplete data, but the same principle can be used to reconstruct the received signal beyond the available bandwidth and CPI for resolution enhancement [65, 69]. The idea is to assume the available signal samples as part of a reduced domain, i.e., the result of a sensing operation over a larger frequency/slow-time support. Then the CS reconstruction algorithm is

applied to this "sensed" signal in order to reconstruct it over a larger bandwidth and a longer observation time, which leads to a finer resolution (see Fig.3.11). The same principle can be applied for other applications, e.g., 3D-ISAR [13, 70], passive radar imaging [71, 72], Ground Penetrating Radar imaging (GPR) [73–75], Multiple Input Multiple Output (MIMO) radar imaging [76–78] and Magnetic Resonance Imaging (MRI) [79]. The theory of CS is treated in deep in [63].

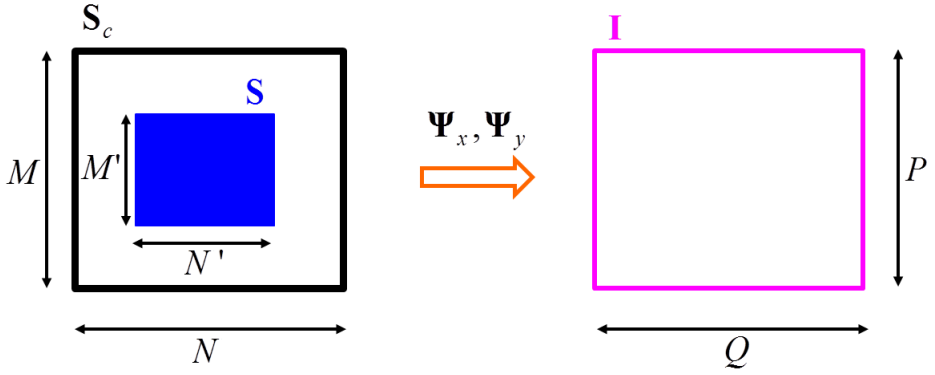

FIGURE 3.11: CS-based resolution enhancement concept.

Chapter 4

Super-Resolution: Performance Analysis

In this Chapter the topic of performance analysis for super-resolution techniques is treated.

It is important to define one or more methods to analyze the proposed super-resolution techniques and, in general, any super-resolution technique to give measurable parameters and provide comparable indexes of performance. This is because a simple image assessment by visual inspection is not sufficient to provide a valid performance evaluation.

Even if a super-resolution technique allows for the imaging system resolution to improve, it is not guaranteed that such a resolution improvement is equivalent to a better image quality for a particular application, such as Automatic Target Recognition (ATR). If the super-resolution technique allows for a good resolution enhancement but introduces strong distortions, the image quality could even deteriorate. The SSVA, for example, consists of iteratively applying and inverting a non-linear filtering which may generate distortions and artifacts.

In the following, two approaches for performance analysis are proposed:

1. Truth Based performance analysis methods;
2. Quality Index Based performance analysis methods.

Truth Based performance analysis methods consist of comparing the super-resolved image under test with a "truth", i.e., another image with the same size and resolution of the super-resolved one which is considered as an "estimation". Such methods aim to measure the distortion introduced by a generic super-resolution technique.

Quality Index Based performance analysis methods are in principle simpler than Truth Based and consist of measuring standard quality metrics, e.g., image contrast or entropy. Such methods return one (or more) performance metric index which only depends on the image at the output of the super-resolution algorithm and do not give any evaluation of the distortion introduced. However, they can be useful to compare different super-resolution techniques in terms of resolution enhancement and SNR gain.

In Section 4.1 the CLEAN technique for scattering center detection is treated, since it is needed for the performance analysis algorithms introduced in this Chapter. The proposed Truth Based and Quality Index Based methods are described in Section 4.2 and 4.3 respectively. In Section 4.4, the super-resolution techniques described in Chapter 3 are tested on COSMO-SkyMed data and compared by means of the proposed performance analysis methods.

4.1 CLEAN

As mentioned in Chapter 3, the CLEAN technique does not allow for two or more scatterers in the same main beam to be resolved. In this Thesis, the CLEAN is not used for super-resolution, but to detect the dominant scatterers in the SAR/ISAR images of interest. Some comparison algorithms between "truth" and "estimation" proposed in Section 4.2 (Truth Based performance analysis) are based on the scatterers position and amplitude. Such scatterers are detected by means of the CLEAN. This is the reason why the CLEAN algorithm is treated in this Chapter and not in Chapter 3.

As a parametric technique, the CLEAN assumes the received signal as a linear combination of a finite number of contributes and the target/scene is assumed as a set of N_s point-like scatterers.

Consider the received signal model in (2.4), the time-frequency window function defined in (2.5) and the range/delay-time approximation in (2.7). By considering the slow-time as a continuous variable

$$t_n = nT_R \to t \tag{4.1}$$

the signal model can be written as follows

$$S_R(f,t) = \text{rect}\left[\frac{f-f_0}{B}\right] \text{rect}\left[\frac{t}{T_{ob}}\right] e^{-j\frac{4\pi f}{c}R_0(t)} \int_V \gamma'(\mathbf{z}) e^{-j\frac{4\pi f}{c}\mathbf{z}\cdot\mathbf{i}_{LoS}(t)} d\mathbf{z} \tag{4.2}$$

After motion compensation the ISAR image $I(\tau,\nu)$ in the range/Doppler domain is obtained by means of 2D Fourier transform, i.e., the RD imaging method which consists of considering a rectangular support for the received signal in the Fourier domain. Such

an approximation leads to the separation of the domain in two independent time and frequency domains. The received signal, relative to a single point-like scatterer, is then approximated as the product of a time and a frequency component as follows

$$S_R(f,t) \simeq s_1(t)\, s_2(f) \tag{4.3}$$

where

$$s_1(t) = \tilde{B}\ \mathrm{rect}\left[\frac{t}{T_{ob}}\right] \exp\left\{j2\pi\left(\varphi_0 + f_d t + \frac{\mu}{2}t^2\right)\right\} \tag{4.4}$$

$$s_2(f) = \tilde{C}\ \mathrm{rect}\left[\frac{f-f_0}{B}\right] \exp\left\{j2\pi f \tau_0\right\} \tag{4.5}$$

where the product $A = \tilde{B}\tilde{C}$ is the scatterer complex reflectivity function, τ_0 is the time-delay associated with the point-like scatterer, f_d is the Doppler frequency and μ is the chirp rate which accounts for a quadratic radial motion, i.e., Doppler acceleration.[1]

Consider now the SAR/ISAR image of interest in the delay-time/Doppler domain $I(\tau,\nu)$ and $I_1(\tau,\nu) = I(\tau,\nu)$. The CLEAN technique at the generic k^{th} iteration can be briefly summarized as follows:

1. The brightest spot in the image is located

$$(\tau_k^*, \nu_k^*) = \arg\max_{(\tau,\nu)} \{|I_k(\tau,\nu)|\} \tag{4.6}$$

   and assumed as related to the strongest point source in the scene;

2. The selected scatterer complex amplitude and the scattering PSF are estimated;

3. The estimated system response is subtracted from $I_k(\tau,\nu)$ to leave a residual;

4. The process is iteratively repeated until a certain stop condition is not satisfied.

The estimation of the PSF is performed by minimizing the image energy after scattering center removal and exploiting the signal approximation in (4.3). By referring to (4.4), f_d and μ are the parameters to be estimated, whereas φ_0 can be neglected because it is a constant that does not affect the shape of the PSF (see the 2.30). The cost function is then defined as follows

$$E_d(f_d, \mu, B) = \int |d(\nu)|^2\, d\nu \tag{4.7}$$

where

$$d(\nu) = |I_k(\tau_k^*, \nu)| - |S_1(\nu)| \tag{4.8}$$

[1] μ is not the transmitted chirp rate if any is employed.

$S_1(\nu)$ is the Fourier transform of $s_1(t)$ and $B = |\tilde{B}|$. E_d in (4.7) is the energy remaining in the range bin after scattering center deletion. Therefore, the following optimization problem is solved

$$\left\{\hat{f}_d, \hat{\mu}, \hat{B}\right\} = \arg \min_{(f_d,\mu,B)} \{E_d(f_d, \mu, B)\} \tag{4.9}$$

A similar procedure follows to estimate the frequency component of the PSF. τ_0 and $C = |\tilde{C}|$ are jointly estimated as follows

$$\left\{\hat{\tau}_0, \hat{C}\right\} = \arg \min_{(\tau_0,C)} \{E_g(\tau_0, C)\} \tag{4.10}$$

where

$$E_g(\tau_0, C) = \int |g(\tau)|^2 \, d\tau \tag{4.11}$$

$$g(\tau) = |I_k(\tau, \nu_k^*)| - |S_2(\tau)| \tag{4.12}$$

and $S_2(\tau)$ is the inverse Fourier transform of $s_2(f)$.

The ISAR PSF for the selected brightest scatterer is then obtained by calculating the two-dimensional Fourier transform of the product of the estimated time and frequency components. However, only its amplitude is considered. The phase term is extracted from the SAR/ISAR image as shown below

$$I_{PSF}(\tau, \nu) = \left|\mathcal{F}^2 \left\{\hat{s}_1(t) \, \hat{s}_2(f)\right\}\right| e^{j\angle(I_k(\tau,\nu))} \tag{4.13}$$

This is why only the magnitude of B and C are estimated in (4.9) and (4.10). Then, the k^{th} scatterer reflectivity function is estimated as

$$\hat{A}_k = \hat{B}\hat{C} \, e^{j\angle\left(I_k(\tau_k^*, \nu_k^*)\right)} \tag{4.14}$$

and the selected scattering center is subtracted from the image in order to extract the next brightest scatterer as in (4.15).

$$I_{k+1}(\tau, \nu) = I_k(\tau, \nu) - I_{PSF}(\tau, \nu) \tag{4.15}$$

The image PSF is re-estimated for every iteration because, in real images, it actually could vary in different image regions even if it theoretically should not. The stop condition can be set depending on the measured complex amplitude or the residual image energy and a defined threshold. Otherwise, the number of scatterers N_s can be pre-estimated or arbitrarily pre-defined.

The final result is a vector containing the position of the detected scatterers τ_k^* and ν_k^* and another one containing their estimated complex amplitude $\hat{A}_k$. The output image

$R_0(n)\|_{n=0}$	800m
v	22 m/s
T_{ob}	0.3 s
f_0	60 GHz
B	0.5 GHz
PRF	400 Hz
NoS	120

TABLE 4.1: Simulation set-up example: parameters of interest.

can then be built as a linear combination of the detected scattering sources

$$I_{\text{CLEAN}}(\tau,\nu) = \sum_{i=1}^{N_s} \hat{A}_k \, \delta\left(\tau - \tau_k^*\right) \delta\left(\nu - \nu_k^*\right) \otimes_\tau \otimes_\nu w(\tau,\nu) \tag{4.16}$$

where $w(\tau,\nu)$ is defined in (2.30). It is worth pointing out that the knowledge of the signal bandwidth, carrier frequency and CPI is necessary for the success of the CLEAN technique. Further details about the CLEAN technique applied for Radar imaging can be found in [80] and [28].

4.2 Truth Based performance analysis methods

Truth Based performance analysis methods consist of comparing two images: the original SAR/ISAR image and the super-resolution result. By referring to Fig.4.1 the basic algorithm works in four steps:

1. Possible post-processing compensation (windowing, zero-padding, etc.);
2. Generation of a low-resolution image by means of signal support reduction along both the frequency and slow-time dimensions;
3. Application of the super-resolution technique under test in order to create the super-resolved image;
4. Comparison between the original high-resolution image after the post-processing compensation ("truth") and the super-resolved one ("estimation").

For illustration purposes consider the simulation scenario shown in Fig.4.2. Fig.4.2a shows a point-like target model composed of 32 scatterers which draws the shape of a small airliner.As shown in Fig.4.2b, this aircraft moves with constant speed v along a linear trajectory $\mathbf{i}_v = [1,0,0]$ orthogonal to the Radar LoS $\mathbf{i}_{LoS}(0) = [0,-1,0]$ in the reference system T_x.

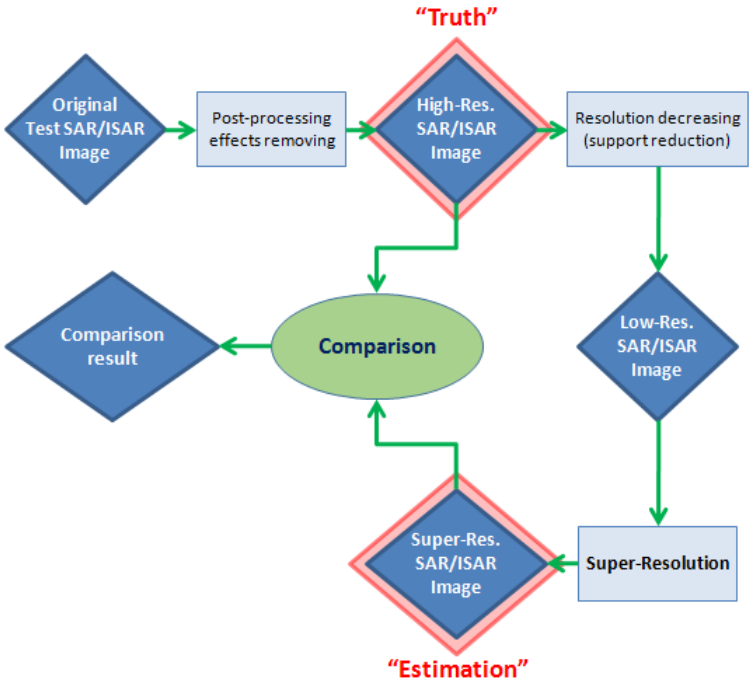

FIGURE 4.1: Truth Based performance analysis: basic flow chart.

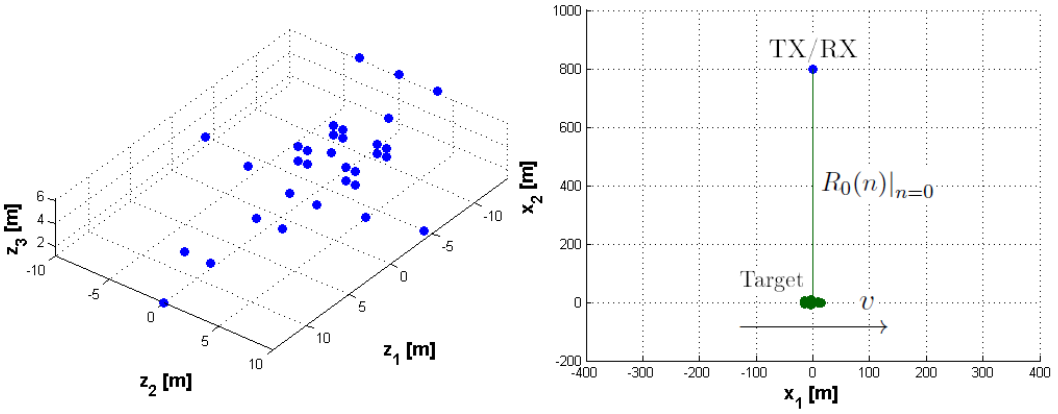

(a) (b)

FIGURE 4.2: Truth Based performance analysis: example target model (a) and scenario (b).

The (monostatic) Radar is drawn as a blue point in Fig.4.2b and its specifics are summarized in Table 4.1 with together other information of interest, e.g., target speed v and the number of frequency samples (NoS) set equal to the number of slow-time pulses $N = T_{ob}\, PRF$.

By exploiting the same signal model for point-like targets in (2.82) used in Section 2.2.2, the monostatic full-resolution ISAR image is simulated as shown in Fig.4.3a, whereas in Fig.4.3b it is shown the complex raw signal in the frequency/slow-time domain.

The simulated aircraft moves along a straight trajectory. The total rotation vector with respect to the Radar only depends on the translational motion and is calculated as follows

$$\mathbf{\Omega}_T = \frac{\mathbf{i}_{LoS}(0) \times \mathbf{v}(0)}{R_0(n)|_{n=0}} = [0\,,\, 0\,,\, 0.0275]\,\text{rad/s} \tag{4.17}$$

where $\mathbf{v}$ is the target velocity vector and $\times$ denotes the cross product operator. Therefore, the effective rotation vector

$$\mathbf{\Omega}_T \perp \mathbf{i}_{LoS}(0) \Rightarrow \mathbf{\Omega}_{eff} = \mathbf{\Omega}_T \tag{4.18}$$

and the image resolution

$$\delta_{rng} = 0.300 \text{ m} \tag{4.19}$$

$$\delta_{crg} = 0.303 \text{ m} \tag{4.20}$$

The ISAR image shown in Fig.4.3a is not further processed, windowed and no zero-padding is applied, thus the first step of the basic algorithm in in Fig.4.1 is not necessary. The ISAR image in Fig.4.3a is the "Truth" of the Truth Based performance analysis algorithm.

As in Fig.4.1, the next step consists of reducing the signal support along the frequency direction, slow-time direction or both. The high-resolution signal support in Fig.4.3b is reduced by a factor K_f along the vertical and K_t along the horizontal direction, i.e., the central $M_{low} \times N_{low}$ portion of the complex signal is retained. The size of such a portion is calculated as follows

$$M_{low} = \left\lfloor \frac{M}{K_f} \right\rfloor \qquad N_{low} = \left\lfloor \frac{N}{K_t} \right\rfloor \tag{4.21}$$

where $M \times N$ is the signal matrix size. The "Resolution Decreasing" output is shown in Fig.4.4 for $K_f = K_t = 2$.

The formed low-resolution ISAR image can then be given as input to the super-resolution algorithm. The output of the third step is shown in Fig.4.5. SSVA is performed on the ISAR image in Fig.4.4a for $\eta = \sqrt[4]{2}$ (bandwidth extrapolation factor) and in four loops (see Section 3.5). The resultant ISAR image in Fig.4.5a is the "estimation" that is compared with the "truth" in Fig.4.3a in order to evaluate the distortion introduced by the super-resolution technique.

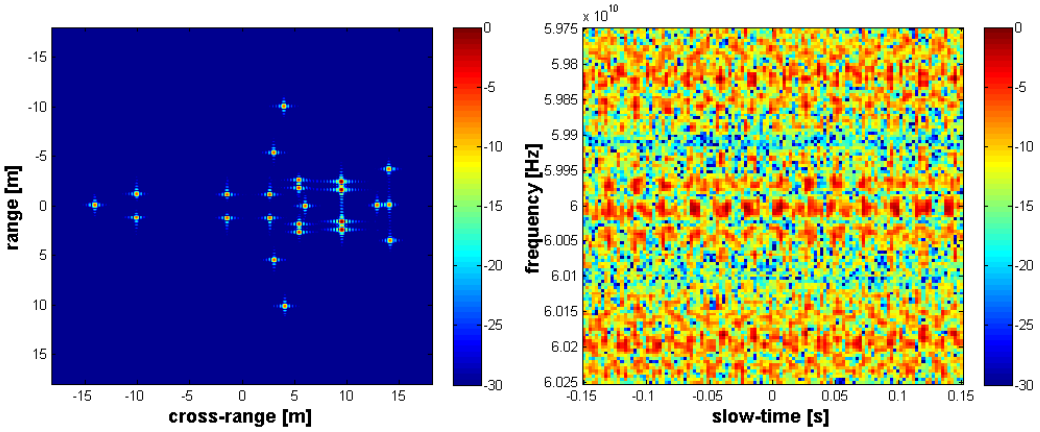

(a) (b)

FIGURE 4.3: Simulated high-resolution ISAR image (a) and relative complex raw signal (b).

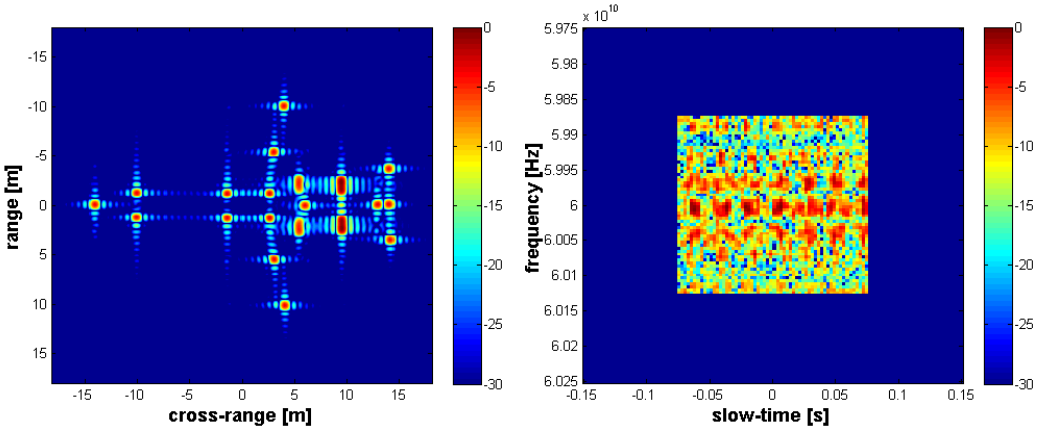

(a) (b)

FIGURE 4.4: Low-resolution ISAR image (a) and relative complex raw signal (b) after the "Resolution Decreasing" step.

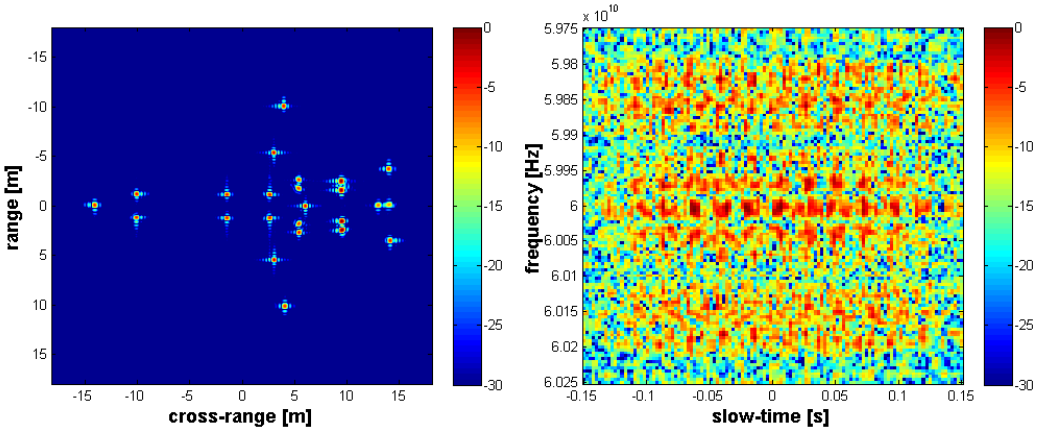

(a) (b)

FIGURE 4.5: SSVA super-resolution output image (a) and relative complex raw signal (b).

Different approaches can be used to compare "truth" and "estimation", such as calculating the normalized Global Correlation Index

$$r_G = \frac{\sum_{p=1}^{P}\sum_{q=1}^{Q}\left(|I_H(p,q)| - \overline{|I_H|}\right)\left(|I_S(p,q)| - \overline{|I_S|}\right)}{\sqrt{\left(\sum_{p=1}^{P}\sum_{q=1}^{Q}\left(|I_H(p,q)| - \overline{|I_H|}\right)^2\right)\left(\sum_{p=1}^{P}\sum_{q=1}^{Q}\left(|I_S(p,q)| - \overline{|I_S|}\right)^2\right)}} \tag{4.22}$$

or the Root Mean Square Error

$$\text{RMSE} = \sqrt{\frac{1}{PQ}\sum_{p=1}^{P}\sum_{q=1}^{Q}\left(|\hat{I}_H(p,q)| - |\hat{I}_S(p,q)|\right)^2} \tag{4.23}$$

where $I_H(p,q)$ and $I_S(p,q)$ denote the $P \times Q$ high-resolution and super-resolved images in position (p,q) respectively, $\overline{|I_H|}$ and $\overline{|I_S|}$ are the mean values of the high-resolution and super-resolved ISAR images magnitude and $\hat{I}_H$ and $\hat{I}_S$ are the images normalized as follows

$$\hat{I}_H = \frac{I_H}{\sqrt{\frac{1}{PQ}\sum_{p=1}^{P}\sum_{q=1}^{Q}|I_H(p,q)|^2}} \tag{4.24}$$

$$\hat{I}_S = \frac{I_S}{\sqrt{\frac{1}{PQ}\sum_{p=1}^{P}\sum_{q=1}^{Q}|I_S(p,q)|^2}} \tag{4.25}$$

In MatLab, r_G in (4.22) can be calculated by means of the `corr2` function. In the following, two novel comparison methods are proposed for further performance analysis: the Scatterer Position based comparison algorithm and the Mobile Cross-Correlation based comparison algorithm.

1. The first one is based on detecting the strong peaks/scatterers in both the high-resolution and super-resolved images, comparing the results of such a detection and return a result in terms of number of correctly reconstructed scatterers (correct detections), scatterers which are lost during the performance analysis chain (missed detections) and artifacts introduced by the super-resolution technique (false alarms).

2. The second approach consists of applying a cross-correlation measurement within a small moving window in order to highlight areas where the high-resolution image has been well or badly estimated.

The Truth Based performance analysis methods can be extended to a larger dataset of homogeneous images, i.e., generated by the same Radar imaging system in the same configuration, in order to return statistic performance metrics.

4.2.1 Scatterer Position based comparison algorithm

The Scatterer Position based comparison approach consists of detecting the strong peaks/scatterers in both the high-resolution and super-resolved images and compare the results of such a detection. For simplicity, in this Section the word "scatterers" indicates the peaks in the high-resolution original image and the word "peaks" is used for the super-resolved image. The distortion introduced by the super-resolution technique is then analyzed in terms of

1. False alarms: a peak is generated in the super-resolved image at a position where no scatterers are present in the "truth";
2. Missed detections: no peak is present in the "estimation" at a position where a scatterer is detected in the high-resolution image;
3. Amplitude estimation errors: the peak position is well estimated and the error in the complex amplitude estimation is considered.

A missed detection may occur if two scatters in the high-resolution image are merged during the support reduction stage (compare Fig.4.3a with Fig.4.4a) and the super-resolution technique is not able to separate them again; if the super-resolution technique causes a signal to noise ratio deterioration (e.g., Capon's MVM if the estimated covariance matrix is ill-conditioned) or if some scatterers are attenuated below the noise level. For example, one disadvantage of the SSVA is the weak signal suppression effect, i.e., weak peaks in the neighborhood of a stronger one may occur to be attenuated.

False alarms may instead occur if some artifacts or "false scatterers" are introduced, for example if a too large number of scatterers is estimated in case of parametric super-resolution (see Section 3.1), or some noise peaks are excessively enhanced.

Scatterers and peaks detection is performed by using the CLEAN (see Section 4.1). The CLEAN output on the ISAR images in Fig.4.3a ("truth") and Fig.4.5a ("estimation"), i.e., the estimated τ_k^* and ν_k^* for $k = 1, \ldots, 24$ in the range/cross-range domain, are depicted in Fig.4.6a and Fig.4.6b respectively. In this case both the scatter-plots show the same number of scatterers and peaks, but in general this is not guaranteed. Consider then N_s as the number of detected scatterers and N_p as the number of detected peaks.

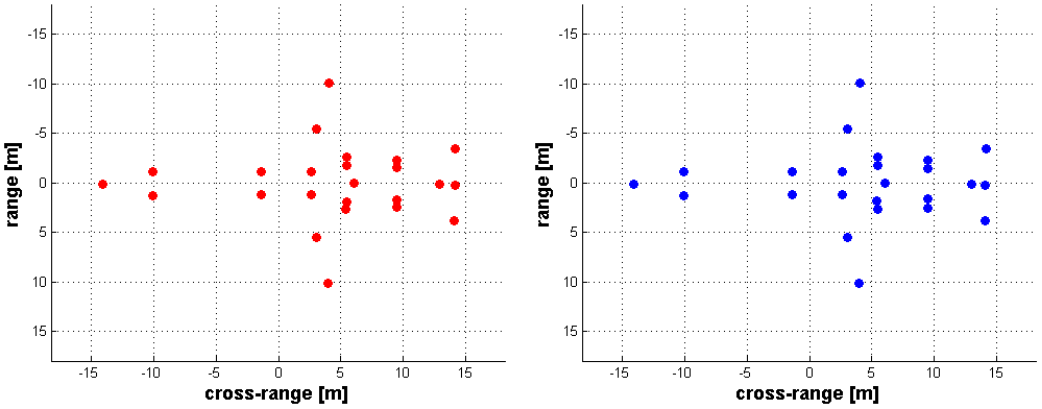

(a) (b)

FIGURE 4.6: Detected scatterers position for the high-resolution image (a) and the super-resolved one (b) in the range/cross-range domain (using CLEAN).

Once scatterers position for both high-resolution and super-resolved images are estimated, the comparison algorithm continues in two steps:

1. Scatterers-Peaks association;
2. Amplitude estimation error evaluation.

The association step aims to evaluate the number or "correct detections", "missed detections" and "false alarms" and basically consists of filling an "Association" vector. The association vector $(1 \times N_s)$ is built to contain in the i^{th} element the indexes of those peaks which are associated with the i^{th} scatterer. Two cell-arrays are firstly defined:

`near_peaks_P` : the i^{th} element of such a vector contains the indexes of the scatterers which are close enough to the i^{th} peak;

`near_peaks_S` : the i^{th} element of such a vector contains the indexes of the peaks which are close enough to the i^{th} scatterer.

In order to build `near_peaks_P` for the i^{th} detected peak, the distances between it and all the scatterers along both range and cross-range are calculated. Those scatterers whose distance along the range direction is smaller than the range resolution and whose distance along the cross-range direction is smaller than the cross-range resolution are selected as "close enough". The indexes of such scatterers fill the i^{th} element of `near_peaks_P`. To explain it mathematically, consider the following vectors:

- $\mathbf{P}_{S,crg}$: scatterers position along the cross-range direction $(1 \times N_s)$;
- $\mathbf{P}_{S,rng}$: scatterers position along the range direction $(1 \times N_s)$;
- $\mathbf{P}_{P,crg}$: peaks position along the cross-range direction $(1 \times N_p)$;
- $\mathbf{P}_{P,rng}$: peaks position along the range direction $(1 \times N_p)$;

The distance vectors for the i^{th} peak along the cross-range ($\mathbf{\Delta}_{crg}$) and range ($\mathbf{\Delta}_{rng}$) directions are calculated as follows

$$\mathbf{\Delta}_{crg} = |\mathbf{P}_{S,crg} - \mathbf{P}_{P,crg}(i)| \in \mathbb{R}_{+}^{[1\times N_s]} \tag{4.26}$$

$$\mathbf{\Delta}_{rng} = |\mathbf{P}_{S,rng} - \mathbf{P}_{P,rng}(i)| \in \mathbb{R}_{+}^{[1\times N_s]} \tag{4.27}$$

and the i^{th} element of `near_peaks_P` is built to contain those indexes j such that

$$(\mathbf{\Delta}_{crg}(j) < \delta_{crg}) \wedge (\mathbf{\Delta}_{rng}(j) < \delta_{rng}) \tag{4.28}$$

where $\wedge$ denotes the `and` operator.

In MatLab:

```
near_peaks_P = cell(1,Np);
for i = 1:Np
    dist_crg = abs(pos_P(1,i)-pos_S(1,:));
    dist_rng = abs(pos_P(2,i)-pos_S(2,:));
    near_peaks_P{i} = find((dist_crg<dCrg) & (dist_rng<dRng));
end
```

where `pos_P` is the $2 \times N_p$ matrix which contains the position of all the detected peaks in cross-range and range, `pos_S` is a $2 \times N_s$ matrix containing the position of the scatterers in the high-resolution image, `dRng` is the range resolution and `dCrg` is the cross-range resolution. `near_peaks_S` is built in the same way by swapping peaks and scatterers.

If the i^{th} element of `near_peaks_P` remains empty, the i^{th} peak will be a false alarm. If the i^{th} element of `near_peaks_S` remains empty, the i^{th} scatterer will be associated to a missed detection.

Nevertheless, there are anomalous cases that need to be considered. If two scatterers are "close" to one peak, their relative elements of `near_peaks_S` will not be empty, even if one of them should be classified as a missed detection. Once `near_peaks_P` and `near_peaks_S` are defined, the Association vector is built as shown in Fig.4.7.

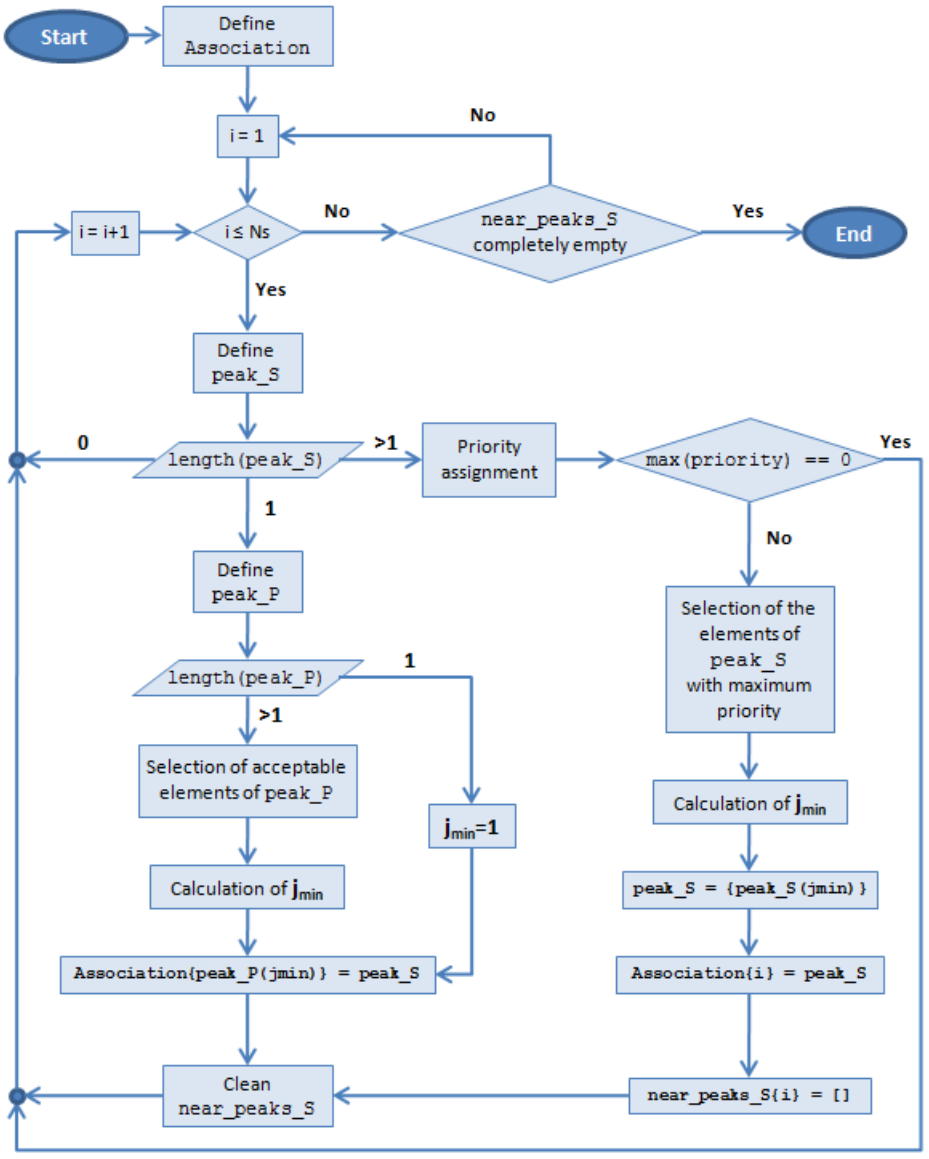

FIGURE 4.7: Scatterer Position based comparison algorithm flow chart.

Firstly the Association vector is initialized as

```
Association = cell(1,Ns);
```

and the algorithm goes on by filling it while emptying `near_peaks_S` in a for-cycle. This cycle is repeated until `near_peaks_S` is completely emptied.

The first step in the for-cycle consists of defining `peak_S` ($\mathbf{P}_S$) as

```
peak_S = near_peaks_S{i};
```

Then three events may occur:

1. $\mathbf{P}_S$ is empty;
2. $\mathbf{P}_S$ is a scalar;
3. $\mathbf{P}_S$ contains more than one element.

In the first case the i^{th} scatterer does not have any peak in its neighborhood, or those peaks have been already assigned to other scatterers. The i^{th} element of `Association` remains empty and the i^{th} scatterer is classified as missed detection.

If $\mathbf{P}_S$ is a scalar, the i^{th} scatterer has one peak in its neighborhood (or one peak left unassigned). In this case the "best" scatterer is associated to this peak. Thus, the vector `peak_P` ($\mathbf{P}_P$) is calculated as

```
peak_P = near_peaks_P{peak_S};
```

to contain the indexes of those scatterers in the neighborhood of such a peak. If $\mathbf{P}_P$ is a scalar too, there is a one-to-one correspondence and the association will be automatic:

```
Association{peak_P} = peak_S;
```

Otherwise, there are more than one scatterer in the neighborhood of the peak and the algorithm proceeds to find out the "best" one in three steps:

1. The acceptable elements of $\mathbf{P}_P$ are selected.

   Only those scatterers (elements of $\mathbf{P}_P$) with only one peak in their neighborhood are considered. This is to avoid "false missed detections" and "false false alarms".

2. The closest acceptable scatterer is selected

$$j_{\min} = \arg\min_j \{\mathbf{D}_j\} \tag{4.29}$$

   where

$$\mathbf{D}_j = \sqrt{(\mathbf{D}_{crg,j})^2 + (\mathbf{D}_{rng,j})^2} \tag{4.30}$$

$$\mathbf{D}_{crg,j} = \mathbf{P}_{S,crg}(\mathbf{P}_P(j)) - \mathbf{P}_{P,crg}(\mathbf{P}_S) \tag{4.31}$$

$$\mathbf{D}_{rng,j} = \mathbf{P}_{S,rng}(\mathbf{P}_P(j)) - \mathbf{P}_{P,rng}(\mathbf{P}_S) \tag{4.32}$$

   and the relative element of `Association` is filled

```
Association{peak_P(jmin)} = peak_S;
```

3. `near_peaks_S` is cleaned.

   Once the peak-scatterer association is done, the peak can no longer be associated with other scatterers. Each peak of the super-resolved image have to be associated with no more than one scatterer of the high-resolution image. In order to guarantee this, all the references to the selected peak in `near_peaks_S` have to be deleted:

```
for j = 1:Ns
    near_peaks_S{j}(near_peaks_S{j}==peak_S) = [];
end
```

   On the other hand, it can be chosen to allow associations between one scatterer and more than one peak (this is why `Association` is defined as a cell-array and not as a simple array). This step is also performed if $\mathbf{P}_P$ is scalar, i.e., in case of one-to-one correspondence (see Fig.4.7 if `length(peak_P)=1`).

For a better understanding, consider the example shown in Fig.4.8 where the high-resolution image scatterers (in red) have to be associated with the peaks of the super-resolved (in blue). At first $i = 1$ and $\mathbf{P}_S = [1]$ is a scalar (only blue peak #1 is close enough to red scatterer #1). Then $\mathbf{P}_P = [1, 2]$ (in the neighborhood of blue peak #1 there are both red scatterers #1 and #2).

FIGURE 4.8: Association example.

Assume now to skip the step 1 (the acceptable elements of $\mathbf{P}_P$ selection). In this case red scatterer #2 is the closest one to blue peak #1 and they are associated. Thus, scatterer #1 is classified as missed-detection and peak #2 as false-alarm (see Fig.4.9).

FIGURE 4.9: Association example result if the acceptable scatterers selection is skipped.

If the step 1 is performed, for each element of $\mathbf{P}_P$ the peaks in the neighborhood are firstly counted: red scatterer #1 has only one blue peak (#1) nearby, whereas red scatterer #2 has two blue peaks (#1 and #2). The second element of $\mathbf{P}_P$ is then discarded

$$\mathbf{P}_P = [1]$$

Therefore, a one-to-one correspondence occurs, $\mathbf{D}_1$ is a scalar and

$$j_{\min} = 1$$

Therefore, red scatterer #1 and blue peak #1 are associated

```
Association{1} = 1
```

Then `near_peaks_S` is cleaned as shown in Fig.4.10.

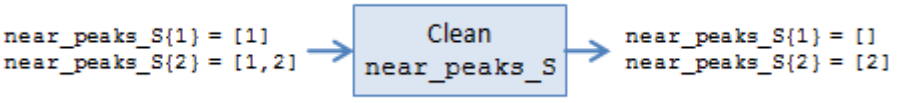

FIGURE 4.10: Association example: cleaning of `near_peaks_S` at loop 1.

In the next for-cycle iteration ($i = 2$) there is a one-to-one correspondence, the association is made

```
Association{2} = 2
```

and the second element of `near_peaks_S` is emptied. The final result is shown in Fig.4.11.

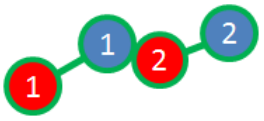

FIGURE 4.11: Association example: final result.

If $\mathbf{P}_S$ is a vector with more than one element, there are more than one peak the neighborhood of the i^{th} scatterer. As in Fig.4.7 the algorithm proceeds to find out the "best" peak to be associated with the scatterer by means of a priority-based sub-routine as in Fig.4.12. In order to avoid "false false alarms" and "false missed detections", a priority level is assigned to each peak. For each j^{th} peak, a priority vector $\mathbf{P}_{P,j}$ is defined as

```
peak_P = near_peaks_P{peak_S(j)};
peak_P = peak_P(peak_P~=i);
```

i.e., as before but without the reference to the i^{th} scatterer. Then, the priority level is assigned to the j^{th} peak as a function of $\mathbf{P}_{P,j}$:

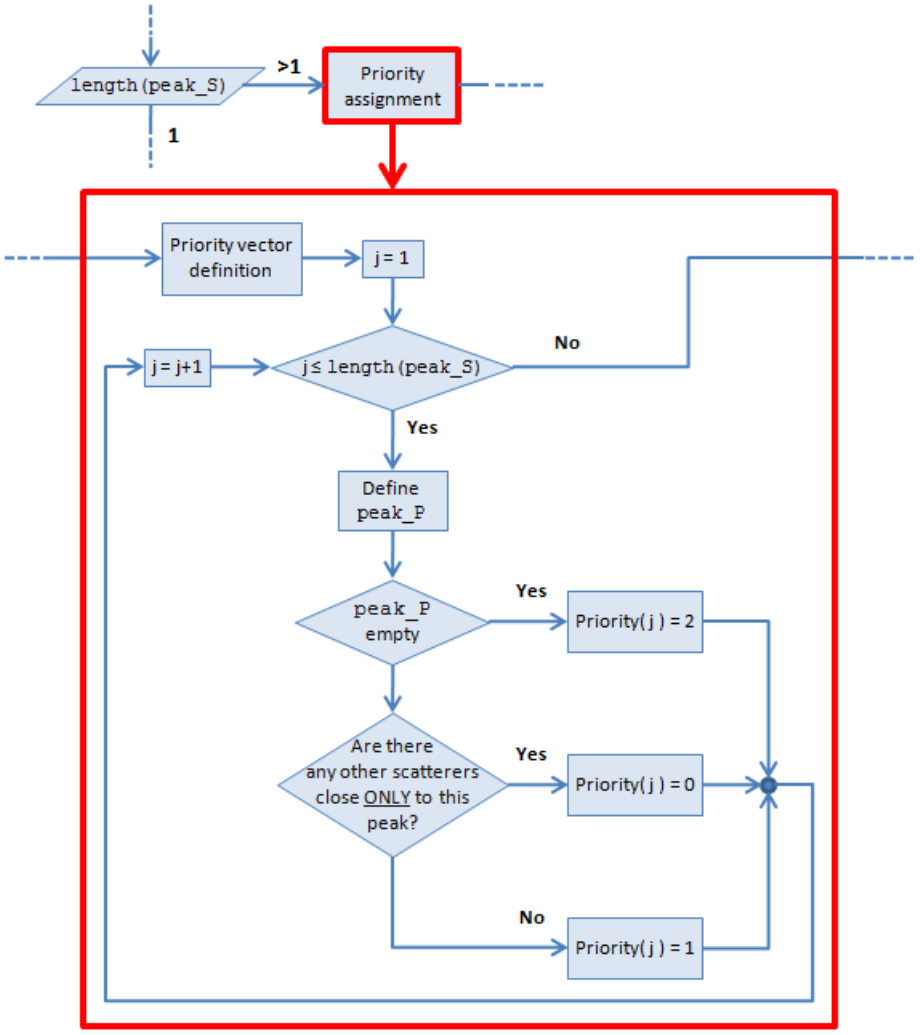

FIGURE 4.12: Priority-based sub-algorithm flow chart.

- If $\mathbf{P}_{P,j}$ is empty, priority level 2 is assigned to the j^{th} peak. The maximum priority level is given to those peaks which have only the i^{th} scatterer in their neighborhood and would be classified as false alarms if they were not associated with it.

- If $\mathbf{P}_{P,j}$ is not empty, all the pointed scatterers are analyzed. If at least one scatterer is only close to the j^{th} peak, then priority level 0 will be given to such a peak. This is because if the i^{th} scatterer and the j^{th} peak were associated, the other scatterer only close to such a peak would be labeled as a "missed detection".

- If all the scatterers are also close to other peaks, then priority level 1 is given to the j^{th} peak. In this case there is no risk to have "false missed detections".

A priority level (0, 1 or 2) is then assigned to all the elements of $\mathbf{P}_S$. If all the priority levels are 0, the i^{th} scatterer will be labeled as a missed detection. Otherwise, those peaks with maximum priority level are selected.

$j_{\min}$ is calculated as in (4.33) and the closest peak is associated with the i^{th} scatterer.

$$j_{\min} = \arg\min_{j} \{\mathbf{D}_j\} \tag{4.33}$$

where

$$\mathbf{D}_j = \sqrt{(\mathbf{D}_{crg,j})^2 + (\mathbf{D}_{rng,j})^2} \tag{4.34}$$

$$\mathbf{D}_{crg,j} = \mathbf{P}_{P,crg}\left(\mathbf{P}_S(j)\right) - \mathbf{P}_{S,crg}\left(i\right) \tag{4.35}$$

$$\mathbf{D}_{rng,j} = \mathbf{P}_{P,rng}\left(\mathbf{P}_S(j)\right) - \mathbf{P}_{S,rng}\left(i\right) \tag{4.36}$$

This is if only one-to-one associations are allowed. Otherwise, if associations between one scatterer and more than one peak are allowed, all the peaks with maximum priority can be associated with the i^{th} scatterer. In MatLab environment it can be written as

```
peak_S = peak_S(Priority==max(Priority));
if only_one_to_one
    Dcrg = pos_P(1,peak_S) - repmat(pos_S(1,i),1,length(peak_S));
    Drng = pos_P(2,peak_S) - repmat(pos_S(2,i),1,length(peak_S));
    D = sqrt(Dcrg.^2 + Dcrg.^2)
    [~,jmin] = min(D);
    peak_S = peak_S(jmin);
end
Association{i} = peak_S;
```

where `Priority` denotes the priority vector and `only_one_to_one` is a boolean parameter set as "true" if only one-to-one associations are allowed. In the end the `near_peaks_S` cleaning step is performed as before, but in this case the whole i^{th} element of `near_peaks_S` have to be cleared first. This is because if $\mathbf{P}_S$ has more than one element and one of them is associated with the i^{th} scatterer, the others will never be associated to any scatterer, `near_peaks_S` will never be completely cleaned and the algorithm outer loop will never end as in Fig.4.7. This is the reason of the block

```
near_peaks_S{i} = [];
```

in the lower-right corner in Fig.4.7. Once `near_peaks_S` is completely emptied, those peaks which do not appear in any element of the `Association` vector are classified as false alarms, whereas those scatterers which refer to an empty entry of `Association` are classified as missed detections. For a better understanding of this "priority game", consider the example in Fig.4.13.

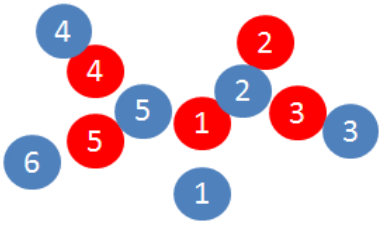

FIGURE 4.13: Association example for non-scalar $\mathbf{P}_S$.

Starting with $i = 1$, in the neighborhood of scatterer #1 there are blue peaks #1, #2 and #5. Then $\mathbf{P}_S = [1, 2, 5]$ and the priority vector is initialized as $\mathbf{P} = [0, 0, 0]$.

- $j = 1$: $\mathbf{P}_{P,1}$ is empty because only red scatterer #1 is close enough to peak #1. Therefore, $\mathbf{P}(1) = 2$.
- $j = 2$: $\mathbf{P}_{P,2} = [2, 3]$ because both scatterers #2 and #3 are close to peak #2. Then they are checked:
  - Scatterer #2: only peak #2 is in the neighborhood;
  - Scatterer #3: peaks #2 and #3 are in the neighborhood.

  Then the priority level is set to zero: $\mathbf{P}(2) = 0$.
- $j = 5$: $\mathbf{P}_{P,5} = [4, 5]$. $\mathbf{P}(3) = 1$ because both scatterers #4 and #5 have at least another blue peak in their neighborhood (the #4 and #6).

Then the priority vector $\mathbf{P} = [2, 0, 1]$ and the peak with the maximum priority level is associated with red scatterer #1. After running all loops of the for-cycle, the `Association` vector is then filled as follows

```
Association{1} = 1
Association{2} = 2
Association{3} = 3
Association{4} = 4
Association{5} = 5
```

and blue peak #6 is classified as false alarm. Assume now to skip the priority assignment:

- $i = 1$, $\mathbf{P}_S = [1, 2, 5]$: blue peak #2 is the closest one to red scatterer #1 and they are associated;
- $i = 2$, $\mathbf{P}_S = [\ ]$: scatterer #2 is classified as missed detection;
- $i = 3$, $\mathbf{P}_S = [3]$: one-to-one correspondence between scatterer #3 and peak #3;

- $i = 4$, $\mathbf{P}_S = [4, 5]$: blue peak #4 is the closest one to red scatterer #4 and they are associated;
- $i = 5$, $\mathbf{P}_S = [5, 6]$: blue peak #5 is the closest one to red scatterer #5 and they are associated.

Then:

```
Association{1} = 2
Association{2} = [] => Missed detection
Association{3} = 3
Association{4} = 4
Association{5} = 5
```

Red scatterer #2 is classified as missed detection and blue peaks #1 and #6 are false alarms.

Considering the example of the simulated airliner, scatterers in Fig.4.6a and peaks in Fig.4.6b are then associated by means of the algorithm above and the final result is shown in Fig.4.14. This is a simple case where all the scatterers and peaks are associated and no false alarms or missed detections occur.

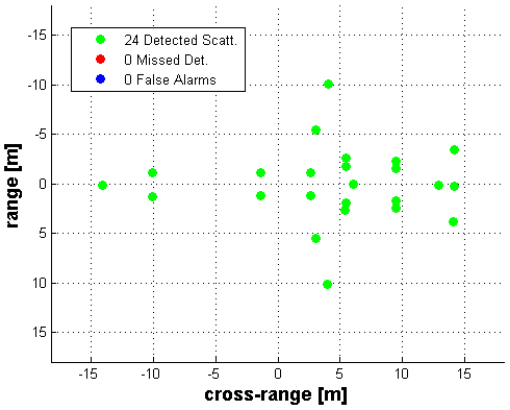

FIGURE 4.14: Association result for scatterers and peaks in Fig.4.6.

The same experiment is then performed for $K_f = K_t = 4$. The low-resolution and SSVA super-resolved images are depicted in Fig.4.15a and 4.15b respectively. In this case five missed detections and five false alarms occur as shown in Fig.4.16a because the SSVA is no longer able to separate the scatterers on the aircraft turbines which are merged by the support reduction stage.

However, the CLEAN is able to detect something. This is because "it may happen that spurious low-power targets can be created near the main scatterer to compensate for

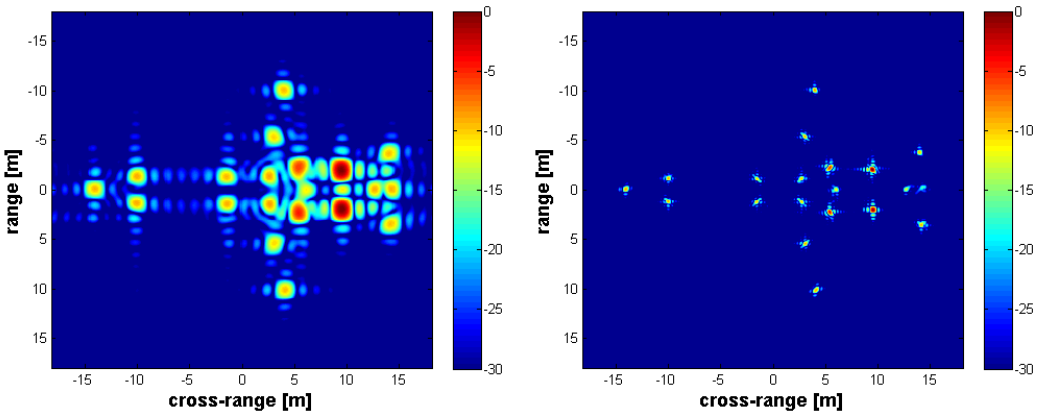

(a) (b)

FIGURE 4.15: Low-resolution (a) and SSVA super-resolved (b) images for $K_f = K_t = 4$.

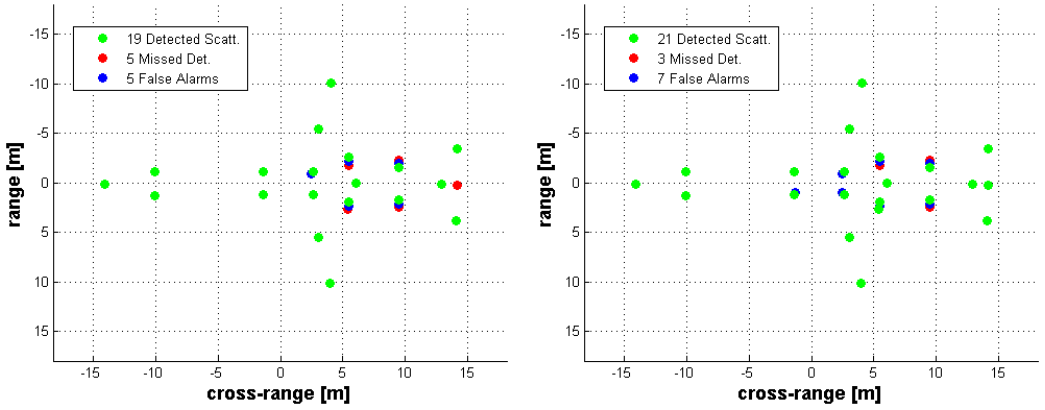

(a) (b)

FIGURE 4.16: Association result for scatterers for $K_f = K_t = 4$ and the CLEAN set to stop when 24 scatterers are found in both the images (a) or the residual energy is less than the 12% of the original energy (b).

estimation errors" (see Section 3.1.1), but such spurious low-power targets are detected not close enough to the actual turbine scatterers in Fig.4.6a. Moreover, another spurious peak is detected in the center of the ISAR and labeled as false alarm. Therefore, since the same number of scatterers has been chosen for both high-resolution and super-resolved images, CLEAN stops before the weakest peak on the aircraft tail can be spotted.

However, it is not necessary to set the same number of detected scatterers for both the images. For example, if the CLEAN is set to stop when the residual energy is less than the 12% of the original image energy, 24 scatterers are detected in the high-resolution image and 28 in the super-resolved one. In this case the peak on the tail is detected, but more false alarms occur. Moreover, the scatterers on the turbines are still missing. Such a result is depicted in Fig.4.16b.

	RRMSE
$K_f = K_t = 2$	0.1964
$K_f = K_t = 4$, CLEAN setting 1	0.3514
$K_f = K_t = 4$, CLEAN setting 2	0.3851

TABLE 4.2: Association results: RRMSE for the three cases in Fig.4.14, Fig.4.16a and Fig.4.16b.

Once correct detections, missed detections and false alarms are defined, the "amplitude estimation error evaluation" step can be performed. In particular the "Relative Root Mean Square Error" (RRMSE) is calculated on the amplitude estimations by considering only those scatterers labeled as "correct detections". By defining $\hat{\mathbf{A}}_H$ and $\hat{\mathbf{A}}_S$ as the vectors containing the estimated complex amplitudes $\hat{A}_k$ (see Section 4.1) for $k \in \Lambda_{\text{CD}}$, where Λ_{CD} is the set of indexes from 1 to N_s referring to correct detections, for the high-resolution and super-resolved images respectively, the RRMSE is calculated as

$$\text{RRMSE} = \sqrt{\frac{1}{N_{\text{CD}}} \sum_{i}^{N_{\text{CD}}} \text{RSE}(i)} \tag{4.37}$$

where N_{CD} denotes the number of correct detections and

$$\text{RSE} = \left(\frac{\left|\hat{\mathbf{A}}_H\right| - \left|\hat{\mathbf{A}}_S\right|}{\left|\hat{\mathbf{A}}_H\right|} \right)^2 \tag{4.38}$$

denotes the "Relative Square Errors" (RSE). The RRMSE results are summarized for the examples above in Table 4.2, where "CLEAN setting 1" refers to the CLEAN performed to have the same number of detected scatterers and peaks ($N_p = N_s$), whereas "CLEAN setting 2" refers to the CLEAN set to stop when the residual energy threshold is exceeded (see Fig.4.16a and 4.16b respectively). Higher values of K_f and K_t result in higher RRMSE because a smaller portion of the original complex signal is retained. If $K_f = K_t = 4$, "CLEAN setting 1" return lower RRMSE than "CLEAN setting 2".

To validate these results the RSE values for $K_f = K_t = 2$, $K_f = K_t = 4$ with "CLEAN setting 1" and $K_f = K_t = 4$ with "CLEAN setting 2" are plotted in Fig.4.17. It appears that "CLEAN setting 2" allows to detect two scatterers more with respect to "CLEAN setting 1". However, these scatterers are not well modeled by the SSVA and their Relative Square Error index is quite high. This is why "CLEAN setting 2" returns higher RRMSE with respect to "CLEAN setting 1".

It is worth pointing out that high-resolution and super-resolved images have to be normalized before the CLEAN performing as in (4.24) and (4.25). However, this is not

necessary if there is no interest in the RRMSE and only the knowledge of correct detections, missed detections and false alarms is desired.

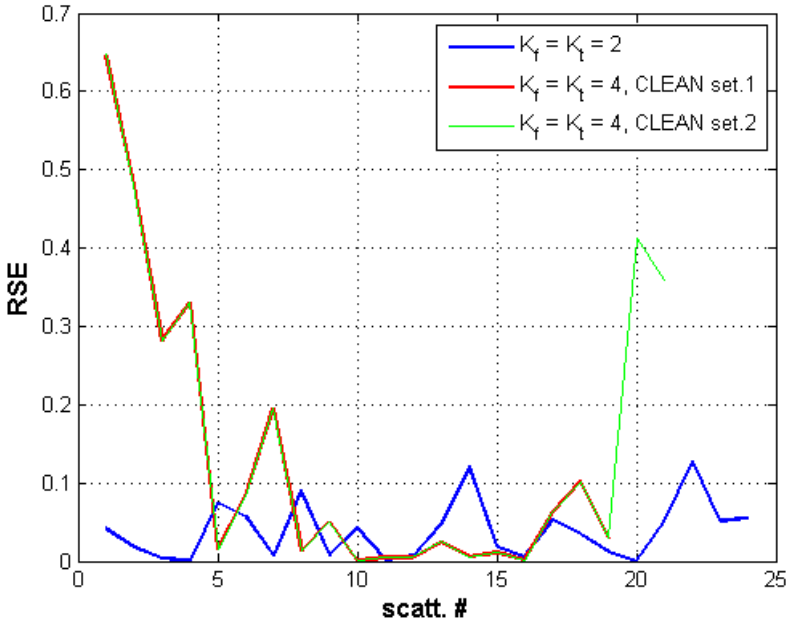

FIGURE 4.17: Relative Square Errors for $K_f = K_t = 2$ (blue), $K_f = K_t = 4$ with "CLEAN setting 1" (red) and $K_f = K_t = 4$ with "CLEAN setting 2" (green).

This comparison approach allows to quantify the distortion introduced by a certain super-resolution technique on a certain image in terms of lost scatterers (missed detections) and artifacts (false alarms). If applied on a large dataset of images, it allows to statistically describe the super-resolution technique in terms of Estimated False Alarm Probability and Estimated Missed Detection Probability. However, this approach has some disadvantages:

1. High-resolution and super-resolved images must be well aligned.

2. The result is strictly dependent on the scattering extraction method. The CLEAN technique is used in the example above because SSVA produces (theoretically) a known PSF which can be approximated as a sinc function. For other super-resolution techniques, which do not produce a known PSF, it would be appropriate to define a different scattering extraction method. Moreover, different settings for the CLEAN can produce different performance outputs.

3. Even if a peak appears in the same position in both the images, the scatterer extraction technique could not detect both of them. As a consequence, "false missed detections" and "false false alarms" may occur.

4. Scatterers in SAR/ISAR images are often not well defined and some image portions can look like as a "flat cloud" without thin peaks emerging.

5. Sometimes it happens that a missed detection and a false alarm are detected close to each other. This can be interpreted as "the super-resolution technique reconstructs the scatterer but in a different position". This is the peak shift issue. It may happen if range migration occurs in the high-resolution image.

6. Sometimes distortions introduced by a super-resolution technique generate a large number of peaks where in the truth there is a large blurred scatterer. A lot of false alarms are then detected.

Moreover, it seems that this approach needs the knowledge of cross-range resolution to calculate distances. However, also the Doppler resolution can be used for the calculation of `near_peaks_P` and `near_peaks_S`, but a different approach for distances evaluation must be used in (4.30) and (4.34).

4.2.2 Mobile Cross-Correlation based comparison algorithm

The Mobile Cross-Correlation approach aims is to give an index of how well the high-resolution image is reconstructed in different areas. The expected final result is a map of values between 0 and 1. Higher values indicate those image regions that have been well reconstructed. The Mobile Cross-Correlation comparison algorithm is implemented by calculating the normalized cross-correlation between small portions of the two images, i.e., within a mobile window. For a better comprehension see the drawing in Fig.4.18.

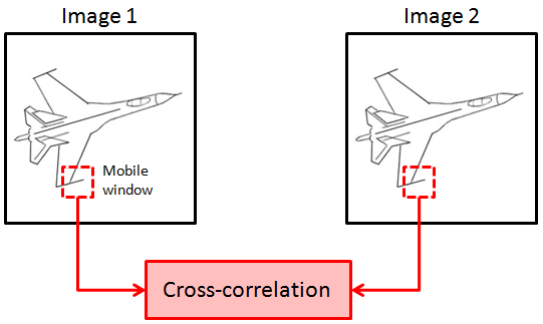

FIGURE 4.18: Mobile cross-correlation: concept sketch.

The cross-correlation index is calculated within such areas, but, for small mobile windows, high values could also be obtained in those areas where only background noise is present. A threshold is then applied to the high-resolution and super-resolved images as in the

following

$$I_{H,\lambda}(p,q) = \begin{cases} I_H(p,q) & \text{if} \quad |I_H(p,q)| > \lambda_H \\ 0 & \text{otherwise} \end{cases} \tag{4.39}$$

$$I_{S,\lambda}(p,q) = \begin{cases} I_S(p,q) & \text{if} \quad |I_S(p,q)| > \lambda_S \\ 0 & \text{otherwise} \end{cases} \tag{4.40}$$

where I_H and I_S denote the high-resolution and super-resolved images as in (4.22) and the thresholds λ_H and λ_S are calculated as

$$\begin{aligned} \lambda_H &= \mu_H + \delta_H \, \sigma_H \\ \lambda_S &= \mu_S + \delta_S \, \sigma_S \end{aligned} \tag{4.41}$$

where μ_H, σ_H, μ_S and σ_S are the high-resolution image amplitude mean value and standard deviation and the super-resolved image amplitude mean value and standard deviation respectively. δ_H and δ_S are settable parameters to control the thresholds. The mobile cross-correlation map is then calculated as follows

$$\mathbf{R}_{M,C}(p,q) = \frac{\sum\limits_{i,j \in \mathcal{B}(p,q)} I_{H,\lambda}(i,j) \, I^*_{S,\lambda}(i,j)}{\sqrt{\sum\limits_{i,j \in \mathcal{B}(p,q)} |I_{H,\lambda}(i,j)|^2 \sum\limits_{i,j \in \mathcal{B}(p,q)} |I_{S,\lambda}(i,j)|^2}} \tag{4.42}$$

where $\mathcal{B}(p,q)$ is a square box centered on (p,q), i.e., the mobile window which size can be arbitrarily set. The normalized cross-correlation between the two complex images within the moving square box is calculated, but, if the phase information is not needed to be reconstructed, only the image intensity can be considered

$$\mathbf{R}_{M,I}(p,q) = \frac{\sum\limits_{i,j \in \mathcal{B}(p,q)} |I_{H,\lambda}(i,j)| \, |I_{S,\lambda}(i,j)|}{\sqrt{\sum\limits_{i,j \in \mathcal{B}(p,q)} |I_{H,\lambda}(i,j)|^2 \sum\limits_{i,j \in \mathcal{B}(p,q)} |I_{S,\lambda}(i,j)|^2}} \tag{4.43}$$

$\mathbf{R}_{M,C}$ is the complex mobile cross-correlation map and $\mathbf{R}_{M,I}$ is the intensity mobile cross-correlation map. In order to have more efficient implementation, $\mathbf{R}_{M,C}$ and $\mathbf{R}_{M,I}$ can also be calculated as follows

$$\mathbf{R}_{M,C} = \frac{\left(\mathbf{I}_{H,\lambda} \circ \mathbf{I}^*_{S,\lambda}\right) \otimes \mathbf{O}_{W_\mathcal{B}}}{\sqrt{\left(|\mathbf{I}_{H,\lambda}|^2 \otimes \mathbf{O}_{W_\mathcal{B}}\right)\left(|\mathbf{I}_{S,\lambda}|^2 \otimes \mathbf{O}_{W_\mathcal{B}}\right)}} \tag{4.44}$$

$$\mathbf{R}_{M,I} = \frac{\left(|\mathbf{I}_{H,\lambda}| \circ |\mathbf{I}_{S,\lambda}|\right) \otimes \mathbf{O}_{W_\mathcal{B}}}{\sqrt{\left(|\mathbf{I}_{H,\lambda}|^2 \otimes \mathbf{O}_{W_\mathcal{B}}\right)\left(|\mathbf{I}_{S,\lambda}|^2 \otimes \mathbf{O}_{W_\mathcal{B}}\right)}} \tag{4.45}$$

where $\mathbf{I}_{H,\lambda}$ and $\mathbf{I}_{S,\lambda}$ denote the thresholded high-resolution and super-resolved images in matrix notation, the symbol $\circ$ denotes the Hadamard point wise product and $\otimes$ the convolutional operator. For a generic positive integer P, $\mathbf{O}_P$ is a $P \times P$ matrix of ones. $W_{\mathcal{B}}$ is the side length of the square box $\mathcal{B}$.

$\mathbf{R}_{M,C}$ is composed of complex values with modulus within $[0, 1]$ and phase within $[0, 2\pi)$, whereas $\mathbf{R}_{M,I}$ presents real values between 0 and 1. Once $\mathbf{R}_{M,C}$ (or $\mathbf{R}_{M,I}$) is computed, a "mean mobile cross-correlation" index can be calculated in order to give a scalar performance indicator as in (4.46) for the complex mobile cross-correlation map and (4.47) for the intensity map.

$$r_{M,C} = \frac{1}{N_\lambda} \sum_{p=1}^{P} \sum_{q=1}^{Q} \{\mathbf{R}_{M,C}\}_{p,q} \tag{4.46}$$

$$r_{M,I} = \frac{1}{N_\lambda} \sum_{p=1}^{P} \sum_{q=1}^{Q} \{\mathbf{R}_{M,I}\}_{p,q} \tag{4.47}$$

where N_λ is the number of elements in the complex and intensity mobile cross-correlation maps which are > 0. Such a number of elements depends on the selected threshold and is the same for both the complex and intensity maps.

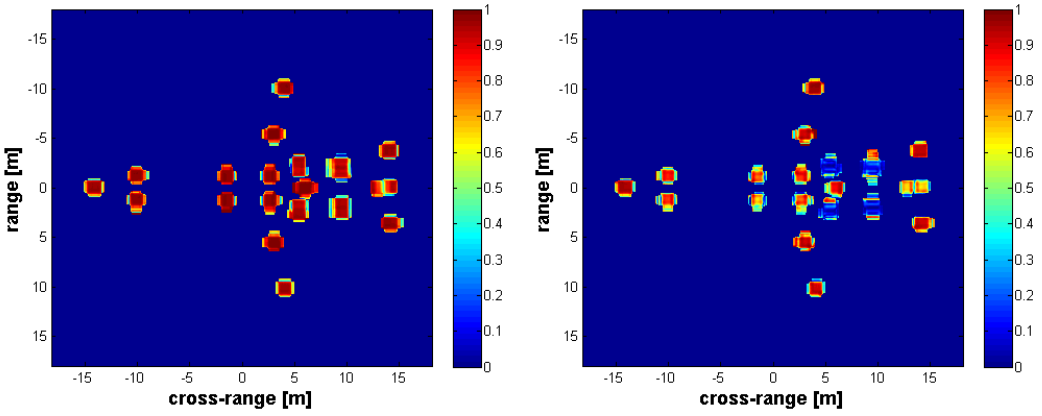

(a) (b)

FIGURE 4.19: Complex mobile cross-correlation maps magnitude for $K_f = K_t = 2$ (a) and $K_f = K_t = 4$ (b) as in the example above.

$r_{M,C}$ is a scalar complex performance index with magnitude within $[0, 1]$, whereas $r_{M,I}$ is a real number within $[0, 1]$. In general $\mathbf{R}_{M,I}$ contains higher values with respect to $\mathbf{R}_{M,C}$ and $r_{M,I} \geq |r_{M,C}|$. However, this approach does not allow to identify those high intensity areas (or peaks) which appear in only one of the two compared images, i.e., does not allow to detect "false alarms" and "missed detections", but gives a distributed similarity index and a description of "what the two images have in common".

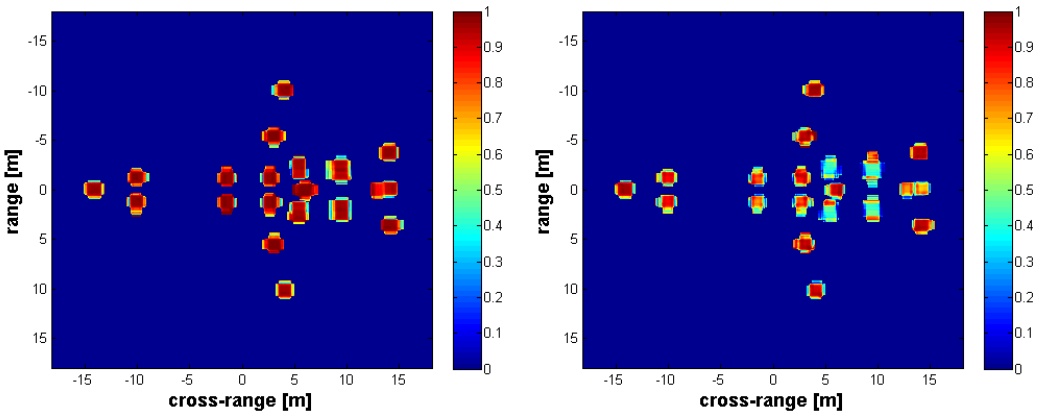

(a) (b)

FIGURE 4.20: Intensity mobile cross-correlation maps for $K_f = K_t = 2$ (a) and $K_f = K_t = 4$ (b) as in the example above.

	$K_f = K_t = 2$	$K_f = K_t = 4$
r_G	0.9467	0.5843
$r_{M,C}$	$0.7928 - 0.0138j$	$0.4059 + 0.0308j$
$r_{M,I}$	0.8127	0.6290
RMSE	0.1955	0.6893

TABLE 4.3: Global Correlation Index (4.22), Mean Mobile Cross-Correlation indexes (4.46) and (4.47) and RMSE index (4.23) for the two simulation cases.

By considering the high-resolution image in Fig.4.3a and the super-resolved in Fig.4.5a and Fig.4.15b, the $\mathbf{R}_{M,C}$ maps for the two cases $K_f = K_t = 2$ and $K_f = K_t = 4$ are shown in Fig.4.19 ((a) and (b) respectively). By comparing Fig.4.19a with 4.19b, it appears that in the first case with $K_f = K_t = 2$ the image is much more well reconstructed, especially in the area or the aircraft turbines and tail. The same can be said by looking at Fig.4.20 where the $\mathbf{R}_{M,I}$ maps are depicted. Such maps are obtained by setting $\lambda_H = \lambda_S = 2$ and $\mathcal{B}$ as a 3×3 box with respect to a $3\times$ zero-padding, i.e., $\mathbf{I}_H$ and $\mathbf{I}_S$ are built 3 times larger than the original images by means of zero-padding and $W_{\mathcal{B}} = 9$.

By comparing Fig.4.19 with Fig.4.20, it also appears that the intensity maps contain higher values with respect to the complex ones. The complex and intensity mean mobile cross-correlation indexes for the two cases, the Global Correlation Index as in (4.22) and the RMSE as in (4.23) are shown in Table 4.3.

4.3 Quality Index Based performance analysis methods

Quality Index Based methods for performance analysis are in principle simpler than Truth Based and consist of measuring standard quality metrics on the super-resolved image. There is no need to compare different images and the super-resolved can be arbitrarily produced with or without preliminary support reduction.

In the following, four Quality Index Based performance indexes are proposed:

1. Image Contrast (IC);
2. Image Entropy (IE);
3. Signal to Noise/Clutter Ratio (SNR);
4. -3dB Resolution.

Image Contrast is used in several applications such as ISAR autofocusing [22] and cross-range scaling [81] and is often used as an index for image quality.

Image Contrast can be considered as a measurement of the degree of image focus because allows one to emphasize the difference in the intensity of the scene. In photography, contrast is the difference between the reflectance or transmittance photographic density of subject and surrounding. In optics, it is defined as the ratio between maximum and minimum of the luminance in the scene. In Radar imaging a high contrast value is expected in focused images because of great differences in the intensity. In case of unfocused image the contrast value is instead lower because the amplitude is concentrated around its mean value [82].

In this Thesis, Image Contrast is considered as the ratio between standard deviation and mean value of the image intensity and is calculated as follows

$$\mathrm{IC} = \frac{\hat{\sigma}_I}{\hat{\mu}_I} = \frac{\sqrt{\mathbb{A}\left\{\left[I^2(p,q) - \mathbb{A}\left\{I^2(p,q)\right\}\right]^2\right\}}}{\mathbb{A}\left\{I^2(p,q)\right\}} \tag{4.48}$$

where I is the image amplitude, $\hat{\sigma}_I$ and $\hat{\mu}_I$ are the image amplitude estimated standard deviation and mean value and the operator $\mathbb{A}\{\cdot\}$ denotes the spatial mean over the image discrete coordinates (p, q).

Image Entropy is a statistical measure of randomness that can be used to characterize the image texture. In information theory, entropy (more specifically, Shannon entropy) is a measure of unpredictability of information content and can be interpreted as the

expected value of the information contained in a message/image/signal (flow of information). Low entropy is synonymous of low quantity of information and high redundancy. Mathematically, for a discrete random variable X with possible values $\{x_1, x_2, \ldots, x_N\}$ and probability mass function $P(X)$, the Shannon entropy is defined as

$$H(X) = -\sum_{i=1}^{N} P(x_i)\, \log_b\left(P(x_i)\right) \tag{4.49}$$

where b is the logarithm base used (usually 2, 10 or Euler's number e).

In Radar imaging, Image Entropy is used for autofocusing [83, 84] and is calculated as

$$\mathrm{IE} = -\sum_{p=1}^{P}\sum_{q=1}^{Q} \bar{I}(p,q)\, \ln\left(\bar{I}(p,q)\right) \tag{4.50}$$

where

$$\bar{I}(p,q) = \frac{|I(p,q)|^2}{\mathbb{A}\left\{|I(p,q)|^2\right\}} \tag{4.51}$$

denotes the power normalized image. Low entropy images have low contrast and large runs of pixels with the same or similar amplitude concentrated around the mean value. High entropy images is instead synonymous of high quantity of information and contrast.

Signal to Noise/Clutter/Interference Ratio is another very common quality metric used in several applications in several definitions. For example, in [85] the Target-to-Clutter ratio is defined as the ratio between the image maximum peak within the target region and the image mean value within a clutter patch. Such target and background regions are separated by performing adaptive thresholding. In [86] SNR is measured as ratio between the variance of the true magnitude image and a Mean Square Error between a noise-free and a filtered noisy image. In this Thesis, SNR is estimated by applying an adaptive threshold defined as in Section 4.2 for the Mobile Cross-Correlation:

$$\lambda_{\mathcal{T}} = \hat{\mu}_I + \delta_{\mathcal{T}}\, \hat{\sigma}_I \tag{4.52}$$

where $\hat{\sigma}_I$ and $\hat{\mu}_I$ are defined as in (4.48) and $\delta_{\mathcal{T}}$ is a settable parameter as in (4.41). The image of interest is then segmented in "target area" and "background area" and the SNR calculated as

$$\mathrm{SNR} = 20\log_{10}\left(\frac{\frac{1}{N_{\mathcal{T}}}\sum_{(p,q)\in\mathcal{T}}|I(p,q)|^2}{\frac{1}{N_{\mathcal{B}}}\sum_{(p,q)\in\mathcal{B}}|I(p,q)|^2}\right) \tag{4.53}$$

where $\mathcal{T}$ denotes the "target area" where $|I(p,q)| \geq \lambda_{\mathcal{T}}$, $\mathcal{B}$ the "background area" where $|I(p,q)| < \lambda_{\mathcal{T}}$, $N_{\mathcal{T}}$ is the number of pixels in the target area and $N_{\mathcal{B}}$ is the number of pixels in the background area.

For a measurement of the effective image resolution, the -3dB mainlobe width is estimated by exploiting the CLEAN. At the k^{th} CLEAN iteration the residual image $I_k(p,q)$ is thresholded and a black/white mask is calculated as

$$M_{\text{BW},k}(p,q) = 20\log_{10}\left(\frac{|I_k(p,q)|}{|I_k(p_k^*,q_k^*)|}\right) > -3 \tag{4.54}$$

where p_k^* and q_k^* are the discrete indexes relative to the brightest spot. The mask portion around (p_k^*,q_k^*) is then analyzed and the -3dB resolution for the k^{th} detected scatterer is measured in both range and cross-range as follows

$$\delta_{rng,k} = \delta_{rng}\frac{N_{rng}}{K_{zp}} \tag{4.55}$$

$$\delta_{crg,k} = \delta_{crg}\frac{N_{crg}}{K_{zp}} \tag{4.56}$$

where δ_{rng} and δ_{crg} are the theoretical range and cross-range resolution, N_{rng} and N_{crg} are the number of "true" pixels in M_{BW} around (p_k^*,q_k^*) along the range and cross-range direction respectively and K_{zp} is the zero-padding factor. The greater the zero-padding factor, the most accurate the resolution estimation.

Consider for example the super-resolved ISAR image in Fig.4.5a and assume $K_{zp}=5$. At first CLEAN step $I_1(p,q)=I(p,q)$ and the brightest spot is found at coordinates $(p_1^*,q_1^*)=(329,457)$. $I_1(p,q)$ and the mask $M_{\text{BW},1}(p,q)$ are zoomed and depicted in Fig.4.21a and 4.21b respectively. In this case, the connected component relative to the selected peak can be contained in a 4×5 box, which means that $N_{rng}=4$ and $N_{crg}=5$. As a result $\delta_{rng,1}=0.2400$m and $\delta_{crg,1}=0.3030$m.

After the first CLEAN iteration, the residual $I_2(p,q)$ is obtained as in (4.15). Such a residual is depicted in Fig.4.22a and the new mask $M_{\text{BW},2}(p,q)$ in Fig.4.22b. The new brightest spot is in position $(p_2^*,q_2^*)=(276,458)$ and, also in this case, $N_{rng}=4$, $N_{crg}=5$, $\delta_{rng,1}=0.2400$m and $\delta_{crg,1}=0.3030$m.

Finally, all the calculated resolution values in cross-range and range are plotted in blue in Fig.4.23a and 4.23b respectively. The red dotted lines in Fig.4.23 represent the mean measured range and cross-range resolution values:

$$\begin{aligned}\hat{\delta}_{rng} &= 0.2650 \text{ m}\\ \hat{\delta}_{crg} &= 0.3050 \text{ m}\end{aligned} \tag{4.57}$$

If the cross-range resolution is unknown, the -3dB Doppler resolution can be calculated by replacing δ_{crg} with δ_ν in (4.55).

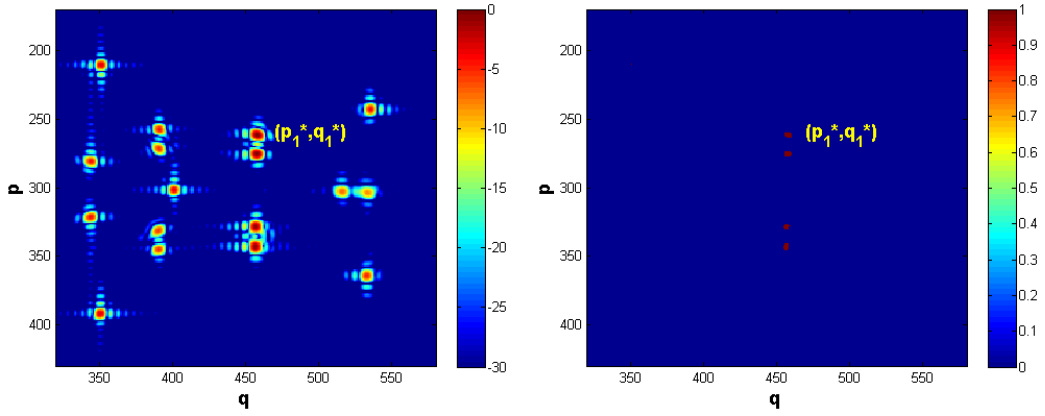

(a) (b)

FIGURE 4.21: Zoomed SSVA image in dB scale (a) and −3dB black/white mask with respect to the brightest peak (b).

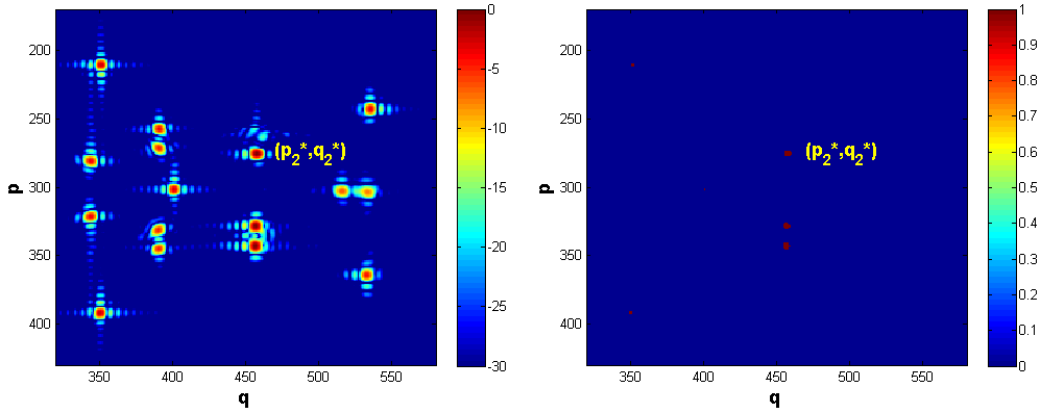

(a) (b)

FIGURE 4.22: Zoomed CLEAN residual $I_2(p,q)$ in dB scale (a) and relative −3dB black/white mask (b).

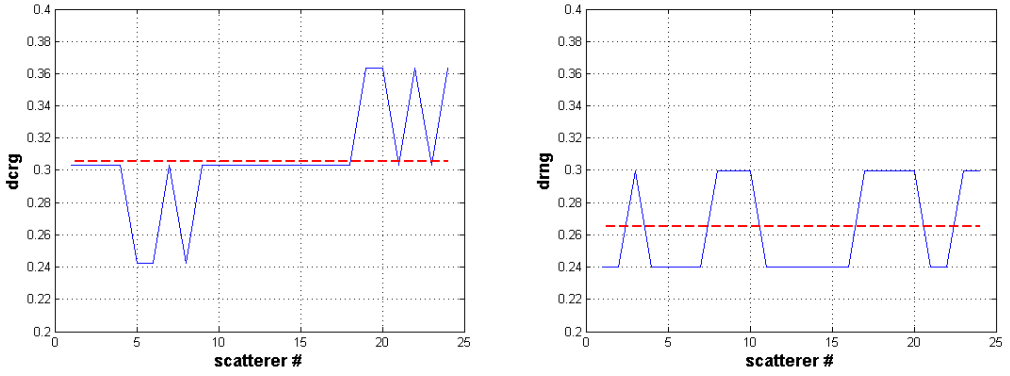

(a) (b)

FIGURE 4.23: Measured −3dB resolution for the detected scatterers in cross-range (a) and range (b) in blue and relative mean values plotted in red.

4.4 Performance analysis results using real data

In this Section the above proposed super-resolution techniques are tested on real ISAR data and the proposed "Truth Based" and "Quality Index Based" performance analysis methods are applied to compare the super-resolution results.

4.4.1 Scenario and data description

The real ISAR data under test has been obtained from a SAR subcrop of the COSMO-SkyMed (CSK) product named

`CSKS1_SCS_U_S2_11_HH_RD_SF_20080415162051_20080415162056.h5`

The CSK-SAR image, after despeckling, is depicted in Fig.4.24a, whereas the subcrop under test is in Fig.4.24b. The SAR/ISAR images in Fig.4.24 and all the following are shown in dB scale for illustration purposes.

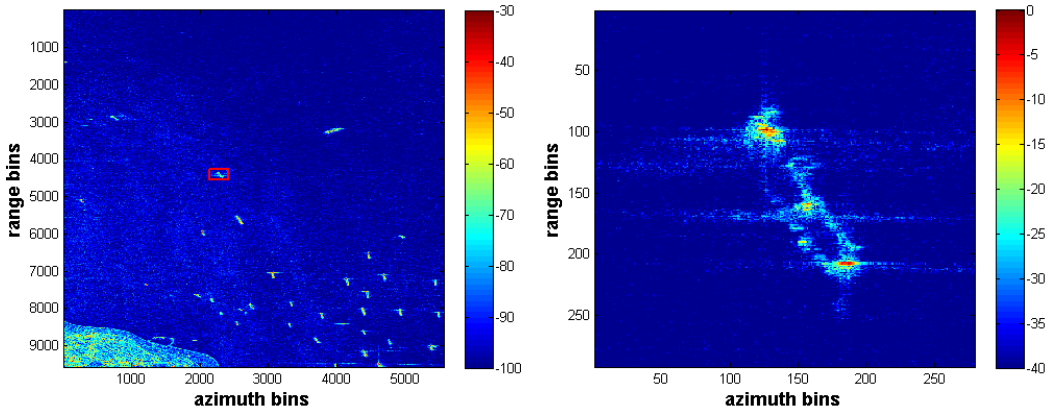

(a) (b)

FIGURE 4.24: WCOR despeckled CSK-SAR with target of interest highlighted in red (a) and SAR subcrop under test (b).

The SAR image in Fig.4.24a is taken from the city of Istanbul in April 2008 by the Satellite 1 of the COSMO-SkyMed constellation in spotlight mode and HH polarization. Some parameters of interest are summarized in Table 4.4.

For illustration purposes, the SAR image in Fig.4.24a is a result of the Wavelet Correlator (WCOR) despeckling algorithm proposed in [87] which takes advantage of the Wavelet theory in order to suppress noise and magnify edge structures that could belong to targets or land area.

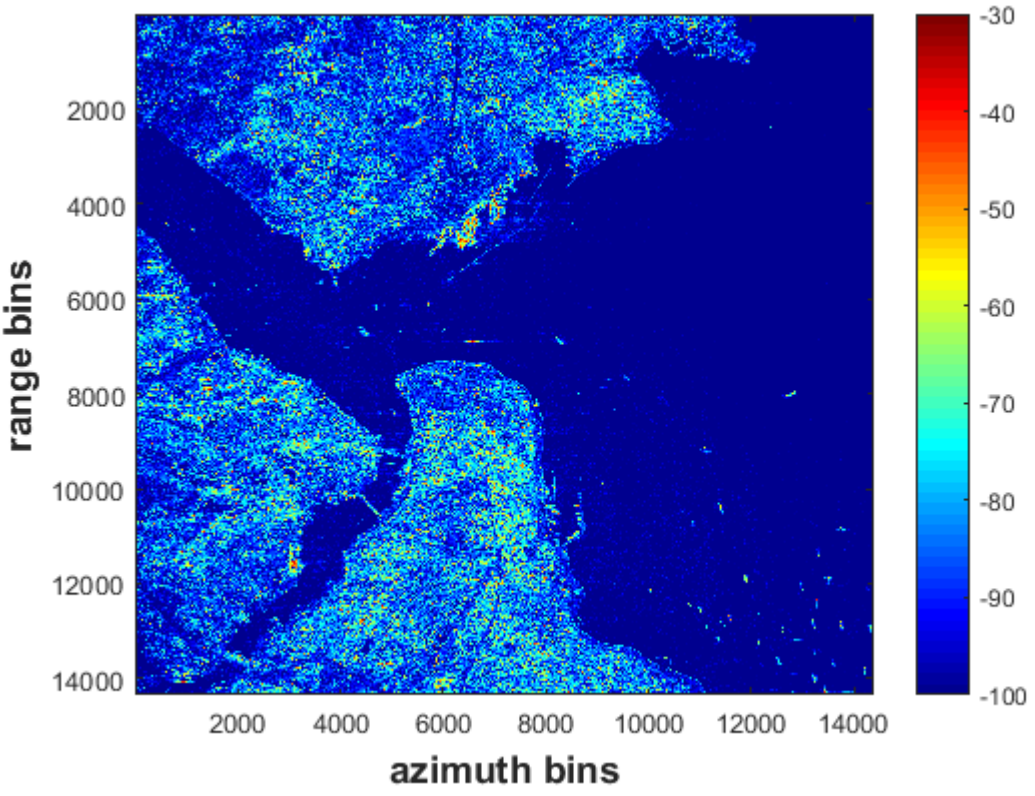

FIGURE 4.25: WCOR despeckled whole CSK-SAR image.

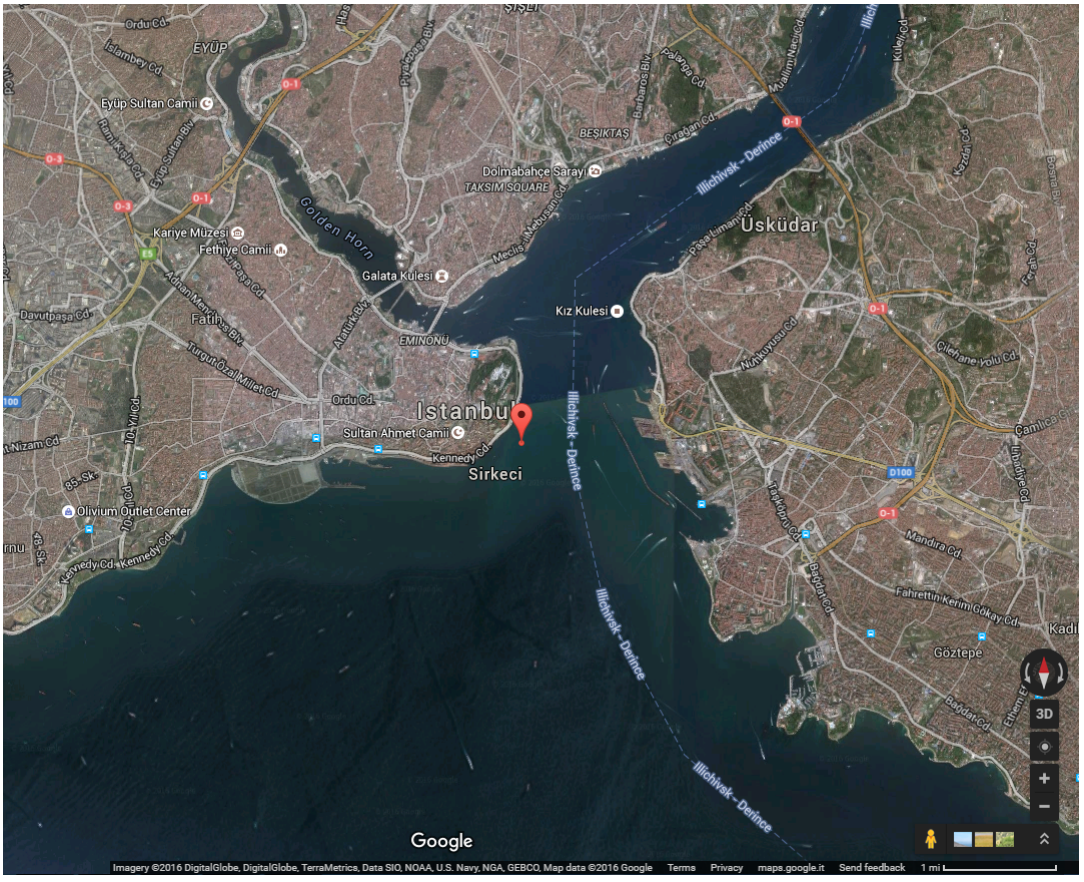

FIGURE 4.26: Scenario representation (Google Maps©).

Image Processing Algorithm	OMEGA-KEY
Sample Type	Complex
Radar Frequency	9.6 GHz
Frequency Bandwidth	277.5146 MHz
Pulse Repetition Frequency	3.575 kHz
Azimuth Looks	1
Range Looks	1
Azimuth Spacing	0.7022 m
Range Spacing	0.4349 m
Near Incidence Angle	37.4479°
Far Incidence Angle	38.1344°
Scene Centre Geodetic Coordinates (latitude)	41.0040°
Scene Centre Geodetic Coordinates (longitude)	28.9878°

TABLE 4.4: Parameters of interest about the CSK SAR under test.

The whole despeckled SAR image provided by COSMO-SkyMed is shown in Fig.4.25. In Fig.4.26 the scenario is represented by exploiting the "Scene Centre Geodetic Coordinates" information provided in the CSK product files (image taken from Google Maps©).

The SAR subcrop in Fig.4.24b is obtained by means of the WCOR based Constant False Alarm Rate (W-CFAR) automatic ship detection algorithm [88], which exploits the WCOR despeckle filter. Such a subcrop is also highlighted in a red box in Fig.4.24a. Such despeckling and automatic CFAR-based detection algorithms are not argument of this Thesis and are not further treated. For details the reader is referred to [87, 88].

The selected one is a non-cooperative moving target in SAR scenario and, as a consequence, it appears defocused. Therefore, a refocused image must be obtained by means of ISAR processing before any super-resolution can be applied.

The main steps of the refocusing method to obtain the refocused ISAR image are summarized below:

1. Target detection [88] and selection of the area around the defocused target image (sub-image);
2. Sub-image projection onto the data domain by means of 2D Fourier Transform;
3. ISAR processing for image refocalization.

Details about the "ISAR from SAR" for target refocusing can be found in [89].

The refocused ISAR image is shown in Fig.4.27a, whereas the relative complex signal in the frequency/slow-time domain is depicted in Fig.4.27b. As appears in Fig.4.27b, the

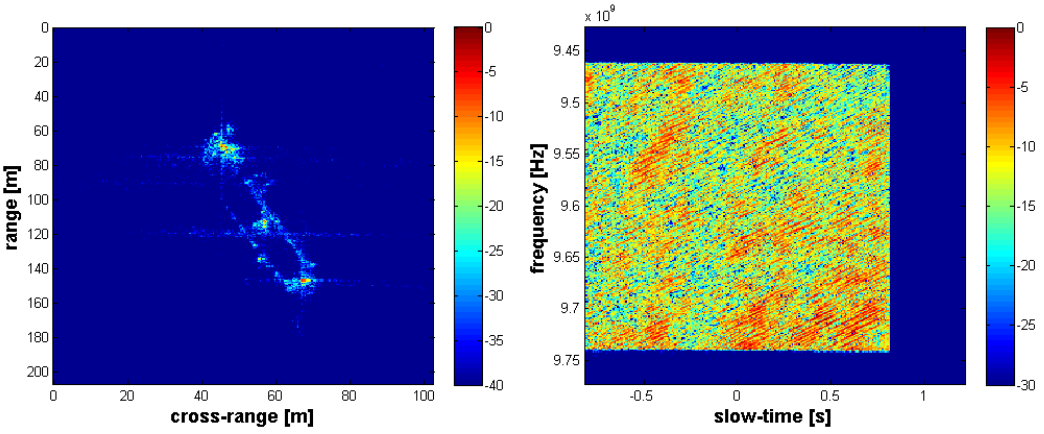

(a) (b)

FIGURE 4.27: Refocused ISAR under test (a) and relative frequency/slow-time raw signal (b).

raw signal is zero-padded. So, to apply the Truth Based performance analysis methods, such a zero-padding have to be removed first (see Fig.4.1). The zero-padding factor along the range direction can be easily estimated by comparing the Range Spacing ($\bar{\delta}_{rng}$) and Bandwidth (B) parameters in Table 4.4 as follows

$$K_{zp,rng} = \frac{c}{2B}\frac{1}{\bar{\delta}_{rng}} = 1.2428 \tag{4.58}$$

The zero-padding factor along the azimuth direction $K_{zp,crg}$ is instead roughly estimated by analyzing the raw signal amplitude and appears to be equal to $K_{zp,rng}$. Therefore, since the raw signal in Fig.4.27b is a $M_{zp} \times N_{zp} = 292 \times 279$ matrix, the zero-padding is removed by extracting the $M \times N$ portion by the following MatLab code

```
m = floor((Mzp-M)/2);
sig = sig_zp(m+1:m+M,1:N);
```

where

$$\begin{aligned} M &= \left\lfloor \frac{M_{zp}}{K_{zp,rng}} \right\rfloor = 234 \\ N &= \left\lfloor \frac{N_{zp}}{K_{zp,crg}} \right\rfloor = 224 \end{aligned} \tag{4.59}$$

The slant-range resolution δ_{srg} is calculated by using the Bandwidth parameter and the ground-range δ_{rng} by considering the mean value between the nearest and furthest Incidence Angle $\bar{\Theta}_{el}$ (see Table 4.4).

$$\delta_{rng} = \frac{\delta_{srg}}{\sin\left(\bar{\Theta}_{el}\right)} = \frac{c}{2B\sin\left(\bar{\Theta}_{el}\right)} = 0.8821 \text{ [m]} \tag{4.60}$$

The cross-range resolution must be instead estimated by means of the Cross-Range Scaling (CRS) algorithm in [81]. This is because in ISAR the cross-range resolution depends on the target effective rotation vector $\mathbf{\Omega}_{eff}$ (assumed constant in time). In this case, the Azimuth Spacing information in Table 4.4 cannot be used because the target is not stationary. The cross-range resolution is then estimated by means of the CRS algorithm

$$\delta_{crg} = 0.4594 \text{ [m]} \tag{4.61}$$

The non-zero-padded ISAR image is depicted in Fig.4.28a in the range/cross-range domain with together its relative frequency/slow-time complex signal in Fig.4.28b. The ISAR image in Fig.4.28a can then be used for the "Resolution Decreasing" step of the performance analysis chain (see Fig.4.1).

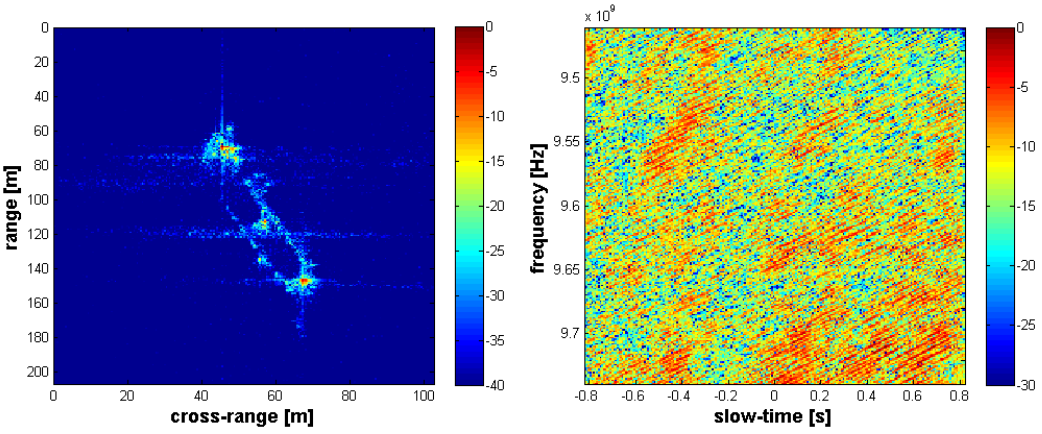

(a) (b)

FIGURE 4.28: Refocused ISAR image after zero-padding removing (a) and relative complex signal (b).

The "Resolution Decreasing" step is applied by setting $K_f = K_t = 2$, i.e., the frequency/slow-time signal support is halved and the image resolution doubled along both range and cross-range. The central $M_{low} \times N_{low}$ portion of the complex signal is then retained. The low-resolution ISAR image and relative complex signal are depicted in Fig.4.29a and 4.29b respectively. Such a low-resolution image is then given as input to the super-resolution algorithms under test.

The quality metrics proposed in Section 4.3 are measured on both the non-zero-padded high-resolution image in Fig.4.28a and low-resolution image in Fig.4.29a and reported in Table 4.5. It is worth comparing the measured range and cross-range resolution values with the theoretical δ_{rng} and δ_{crg} in (4.60) and (4.61): $\hat{\delta}_{rng}$ measured for the high-resolution image is quite lower than the theoretical resolution, whereas $\hat{\delta}_{crg}$ is almost equal. The same can be said for the low-resolution image with respect to the doubled

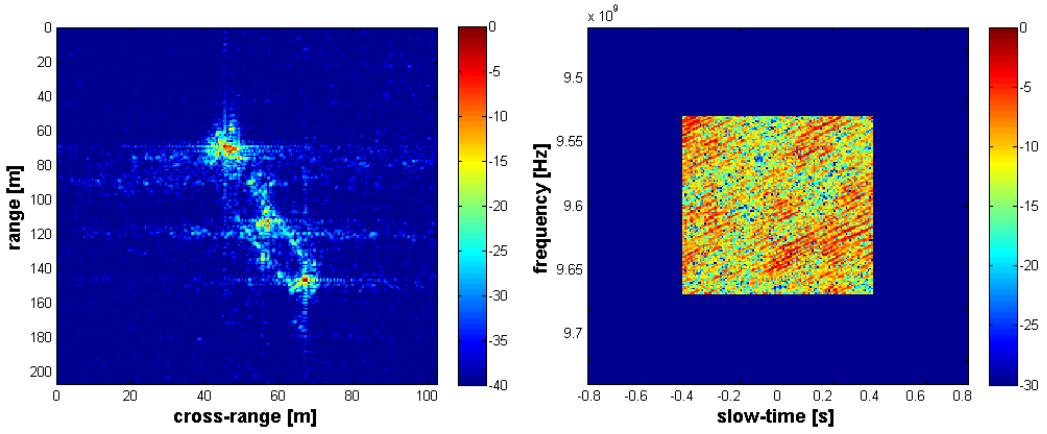

(a) (b)

FIGURE 4.29: Low-resolution ISAR image (a) and relative frequency/slow-time raw signal (b).

	High-res. ISAR (Fig.4.28a)	Low-res. ISAR (Fig.4.29a)
IC	2.1191	1.9698
IE $(\cdot 10^5)$	-2.3939	-2.1052
SNR [dB]	47.2843	45.1096
$\hat{\delta}_{rng}$ [m]	0.7755	1.4181
$\hat{\delta}_{crg}$ [m]	0.4526	0.8821

TABLE 4.5: Measured quality metrics for high and low-resolution ISARs.

resolution values. All the measured -3dB mean resolutions here and in the following are estimated by considering the first 20 scatterers detected by the CLEAN with zero-padding factor $K_{zp} = 10$. The SNR is calculated by setting $\delta_{\mathcal{T}} = 1.5$ (see (4.52)).

4.4.2 Super-resolution results

First, the Linear Prediction based Bandwidth Extrapolation (BWE) is performed. The complex signal in Fig.4.29b is first extrapolated along the frequency direction ("Frequency bandwidth extrapolation") and then along the slow-time ("Aperture extrapolation") separately. The model order p_{AR} is set as $M_{low}/3$ for the vertical (frequency) extrapolation and $N_{low}/3$ for the horizontal (slow-time) and the standard Burg's algorithm is used for the linear-prediction model coefficients estimation.

The resultant super-resolved image and extrapolated complex signal are shown in Fig.4.30a and 4.30b respectively. The super-resolved ISAR image in Fig.4.30a must be compared with the "truth" in Fig.4.28a, whereas the extrapolated complex signal in Fig.4.30b with the complete original signal in Fig.4.28b.

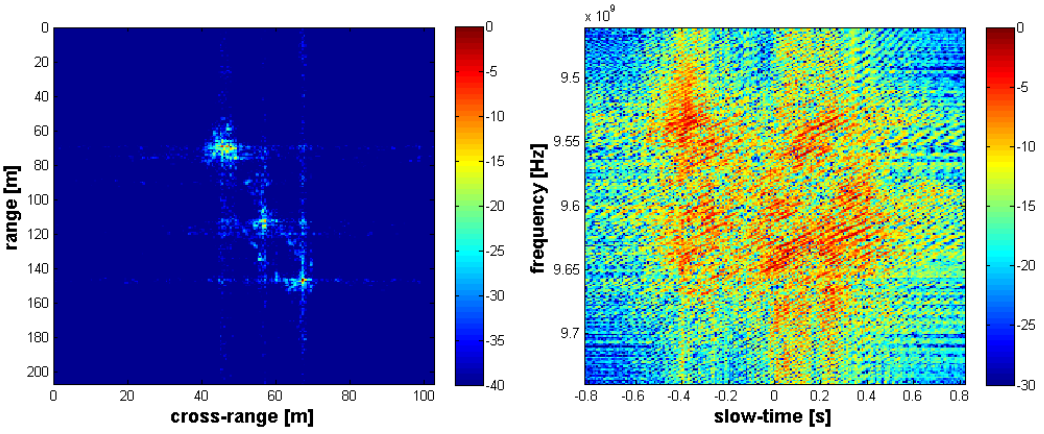

(a) (b)

FIGURE 4.30: BWE super-resolved ISAR image (a) and relative frequency/slow-time raw signal (b).

The second applied super-resolution technique is the Capon's MVM. The signal covariance matrix is estimated by means of the forward-backward method without diagonal loading or other regularization methods. Different subaperture sizes have been used to test and compare different results as shown in Fig.4.31, where MVM outputs for subaperture sizes from 30% to 55% are depicted. As appears in Fig.4.31, larger subapertures cause progressive SNR deterioration caused by a progressive statistical instability of the spectral estimates. As in Section 3.3, the larger the subaperture, the smaller the number of averages for the covariance matrix estimation. However, larger subapertures allow for the spectral resolution to be increased as shown in Fig.4.33, where MVM results for 30% (a) and 45% (b) subapertures are shown. By comparing Fig.4.33a with 4.33b, such a resolution enhancement for larger subapertures is evident. Such considerations are validated by the numerical results summarized in Table 4.6, where the quality indexes proposed in Section 4.3 are reported for different subapertures.

As predictable by observing the ISAR images in Fig.4.31, larger subapertures produce lower image contrast, higher image entropy and lower signal to noise ratio values. By comparing the results in Table 4.6 with Table 4.5, it appears that Capon's MVM allows to enhance the resolution along both range and cross-range with respect to the low-resolution ISAR image, but the high-resolution values are not reached. Moreover, the image quality in terms of contrast, entropy and SNR is strongly deteriorated.

Then the APES is applied. Even in this case the super-resolution algorithm is tested for six subaperture sizes for the covariance matrix estimation. In Fig.4.32 the resultant images are shown for subapertures from 30% to 55%, whereas the measured quality metrics are summarized in Table 4.7.

By comparing Fig.4.32 with Fig.4.31 and Table 4.7 with Table 4.6, it appears that APES has better performance in terms of image contrast, image entropy and SNR and is much less sensitive to the subaperture size, but does not allow a better resolution enhancement. $\hat{\delta}_{rng}$ and $\hat{\delta}_{crg}$ for MVM and APES are comparable. In Fig.4.34 the APES results for 30% (a) and 45% (b) subapertures are shown after 10× zero-padding and zooming. Even in this case the resolution enhancement for larger subapertures is evident but not as enhanced as in Fig.4.33. In Table 4.8 the estimated covariance matrix condition number and the total elapsed time for performing MVM and APES are summarized. Such results prove that smaller subapertures imply better conditioned covariance matrix and, as a consequence, higher image contrast, entropy and SNR.

Subap.	IC	IE $(\cdot 10^5)$	SNR [dB]	$\hat{\delta}_{rng}$ [m]	$\hat{\delta}_{crg}$ [m]
30%	1.4770	−1.6046	38.5389	1.2586	0.8890
35%	1.3639	−1.4552	36.4335	1.2408	0.8431
40%	1.2535	−1.2975	34.2467	1.3560	0.8661
45%	1.1388	−1.1172	31.6993	1.1478	0.7880
50%	1.0135	−0.9001	28.3726	1.0636	0.7121
55%	0.9148	−0.7156	25.0021	1.1212	0.6111

TABLE 4.6: Capon's MVM performance numerical results for different subaperture sizes.

Subap.	IC	IE $(\cdot 10^5)$	SNR [dB]	$\hat{\delta}_{rng}$ [m]	$\hat{\delta}_{crg}$ [m]
30%	1.6946	−1.8992	42.1230	1.1034	0.8500
35%	1.6399	−1.8445	41.2600	1.0680	0.8454
40%	1.5862	−1.7903	40.3788	1.1300	0.8615
45%	1.5351	−1.7349	39.5367	0.9749	0.7374
50%	1.4980	−1.6966	38.9481	1.0148	0.6639
55%	1.5099	−1.7374	39.0449	1.0458	0.6340

TABLE 4.7: APES performance numerical results for different subaperture sizes.

Furthermore, larger subapertures cause the computational load to increase and APES appears to be quite slower than Capon's MVM. Elapsed times reported in Table 4.8 are measured by applying MVM and APES on a personal computer with Intel Core2 Duo

Subap.	Cond. Number $(\cdot 10^5)$	MVM Elap. Time	APES Elap. Time
30%	0.1222	25.4602	44.0077
35%	0.2007	41.7264	65.7991
40%	0.3253	65.8975	96.8666
45%	0.6032	109.1426	176.8413
50%	1.4586	179.5790	6320.7421
55%	5.0059	408.7956	31744.4014

TABLE 4.8: Covariance matrix condition number and elapsed times for Capon's MVM and APES in seconds.

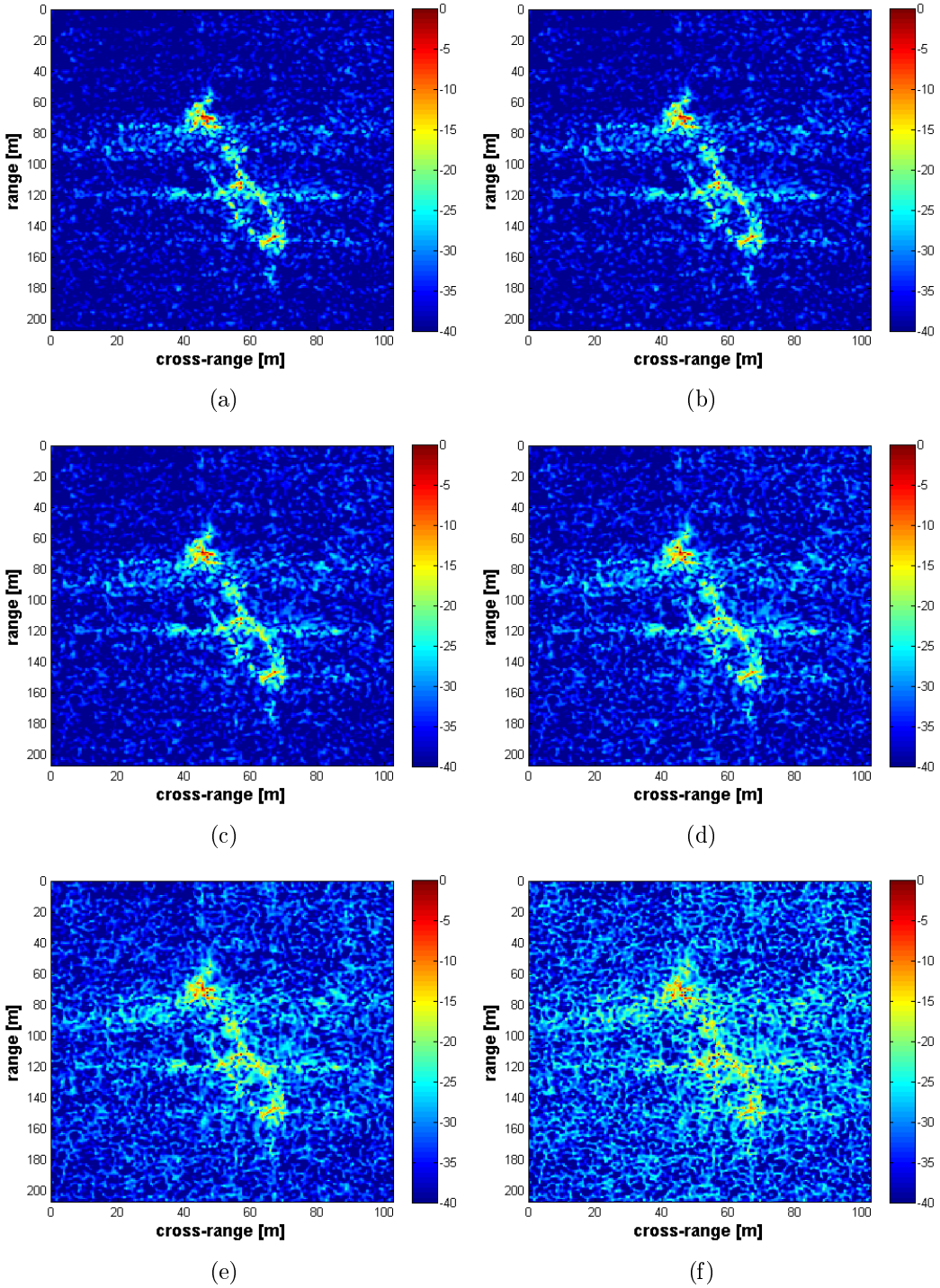

FIGURE 4.31: Capon's MVM results for subaperture sizes of 30% (a), 35% (b), 40% (c), 45% (d), 50% (e) and 55% (f).

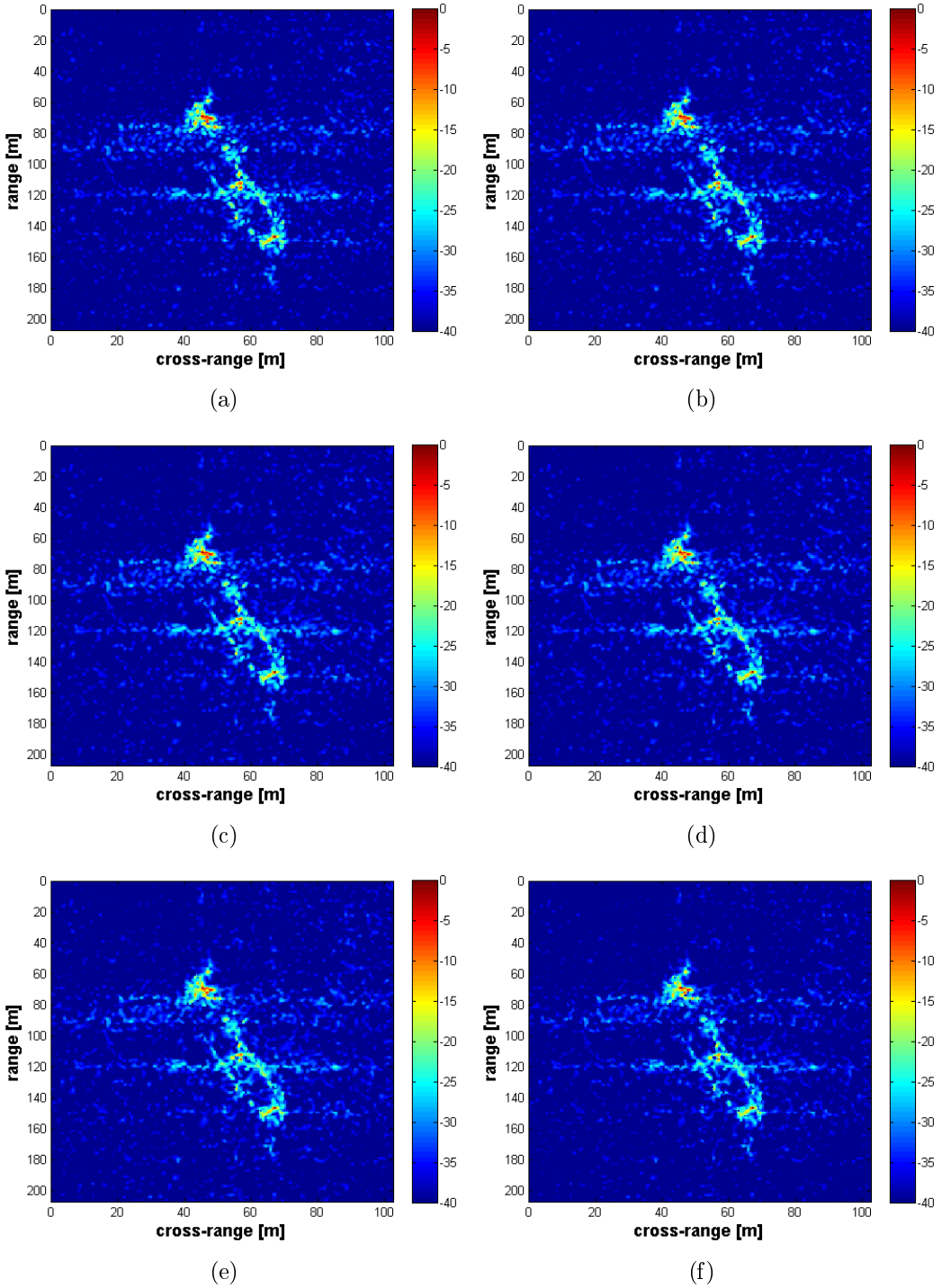

(a) (b)

(c) (d)

(e) (f)

FIGURE 4.32: APES results for subaperture sizes of 30% (a), 35% (b), 40% (c), 45% (d), 50% (e) and 55% (f).

E8400 3.00GHz CPU and 8.00GB RAM. In this case, the efficient method proposed in [53] is used for both MVM and APES faster implementation. If the standard MVM and APES implementations were used, the final results would be exactly the same, but the used method offers advantages in terms of computational load and elapsed time.

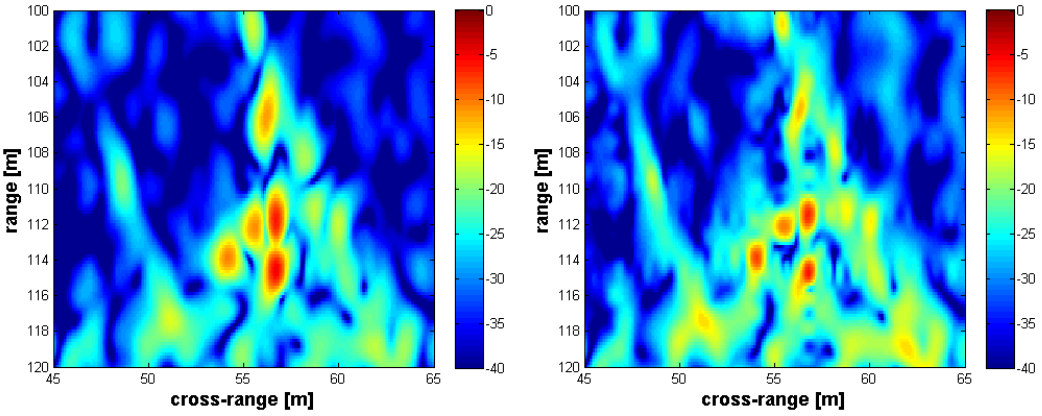

(a) (b)

FIGURE 4.33: Zoomed Capon's MVM results for subaperture sizes of 30% (a) and 45% (b) after 10× zero padding.

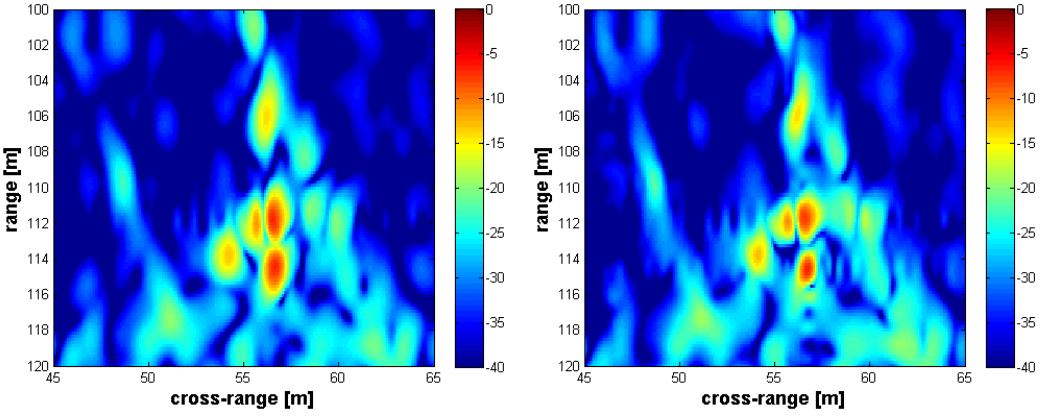

(a) (b)

FIGURE 4.34: Zoomed APES results for subaperture sizes of 30% (a) and 45% (b) after 10× zero padding.

Then Super-SVA is applied. SVA is iteratively exploited in "I and Q Separately - Two Dimensions Simultaneously" mode to extrapolate the complex signal. The SVA is implemented as in Section 3.5 and applied on both the ISAR image and a bidimensional sinc function to create the inverse filter by means of the following MatLab code

```
w = zeros(M,N);
w(1:floor(M/Ky),1:floor(N/Kx)) = 1;     % Rect function in the signal domain
w = circshift(w,-floor(M/(2*Ky)));
```

```
w = circshift(w.',-floor(N/(2*Kx))).'; % Shift around the 0 frequency
W = fft2(w);                           % Sinc function in the image domain
W = W/abs(W(1,1));                     % Normalization
W = SVA_2D(W,Ky,Kx);                   % Inverse filter in the image domain
w = ifft2(W);                          % Inverse filter in the signal domain
```

where `M` and `N` denote the ISAR image size, `Ky` and `Kx` the zero-padding factors along the vertical and horizontal directions, which must be updated at each SSVA iteration depending on the BEF η and decrease down to 1, `SVA_2D` is the MatLab function that performs the spatially variant apodization and the final `w` is the inverse filter $\mathbf{w}_{\mathrm{BE}}(m,n)$ as in (3.81). `w` is shifted in order to center the complex signal around the 0 frequency. Then the inverse filter is applied by meas of the following code

```
F = SVA_2D(G,Ky,Kx);
f = ifft2(F);
g = f./abs(w)
```

where `G` is the $\mathbf{I}_{\mathrm{SSVA}}$ at the previous iteration and `F` is $\mathbf{I}_{\mathrm{SVA}}$ at the current one. Then the $\mathcal{R}$ domain is calculated in order to perform the (3.82), `g` is set to zero outside such a domain and the original complex signal is replaced in the central portion of `g` to perform the (3.83). Then `G = fft2(g)` and the SSVA goes on to the following iteration. When the final iteration is performed, `G` represents the final SSVA output.

In this case, Super-SVA is performed by setting the bandwidth extrapolation factor $\eta = 2^{1/8}$, i.e., in 8 loops. The final super-resolved ISAR image is shown in Fig.4.35a, whereas its relative extrapolated complex signal is in Fig.4.35b.

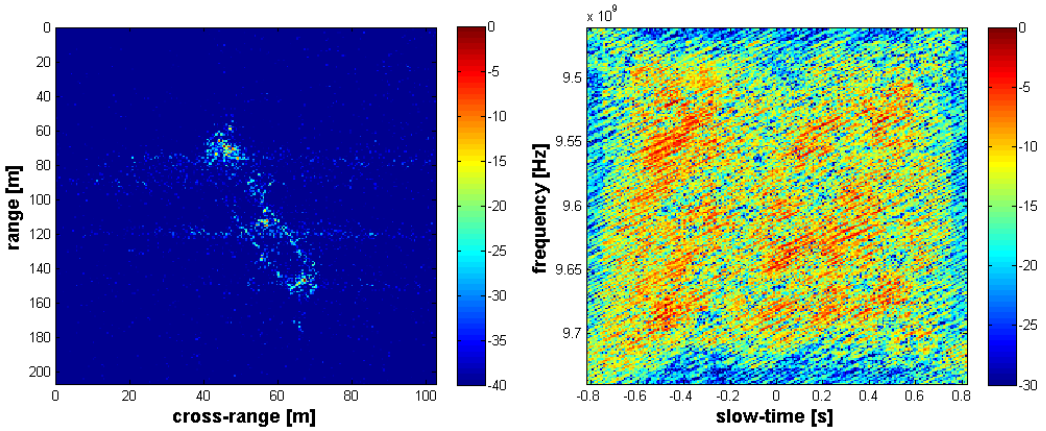

(a) (b)

FIGURE 4.35: SSVA super-resolved ISAR image (a) and relative frequency/slow-time raw signal (b).

Finally, Compressed Sensing is applied. By referring to the notation introduced in Section 3.6, the "recorded signal matrix" $\mathbf{S}$ is the low-resolution complex signal in Fig.4.29b and the undercomplete Fourier matrices $\mathbf{\Theta}_y$ and $\mathbf{\Theta}_x$ are defined as

$$\begin{aligned} \{\mathbf{\Theta}_y\}_{m,p} &= e^{-j2\pi\frac{mp}{P}} \in \mathbb{C}^{M\times P} \\ \{\mathbf{\Theta}_x\}_{n,q} &= e^{-j2\pi\frac{nq}{Q}} \in \mathbb{C}^{N\times Q} \end{aligned} \tag{4.62}$$

where $P = 3M$ and $Q = 3N$. The pseudo-inverse matrices are then calculated and $\hat{\mathbf{I}}_0$ is initialized. The next step is the σ vector definition. In this case σ_1 is set as in (4.63), the last element of the sequence is set equal to the estimated noise standard deviation as in (4.64) and the decreasing factor c_σ is set equal to 0.6.

$$\sigma_1 = 2\max\left\{\hat{\mathbf{I}}_0\right\} \tag{4.63}$$

$$\sigma_J = \sqrt{\frac{1}{N_{\mathcal{B}}}\sum_{(p,q)\in\mathcal{B}}\left(\hat{\mathbf{I}}_0(p,q) - \mu_{\mathcal{B}}\right)^2} \tag{4.64}$$

where $\mathcal{B}$ denotes the "background area" as in (4.53) in Section 4.3, $N_{\mathcal{B}}$ is the number of background elements in the matrix and $\mu_{\mathcal{B}}$ their mean value. In this case $\sigma_1 = 0.0055$, $\sigma_J = 1.1973\cdot 10^{-5}$ and $J = 12$. Then the "approximate maximization of $F_\sigma(\mathbf{x})$" is performed in $N_L = 50$ iterations and setting the constant $\mu = 2$.

In the end, the super-resolved complex signal (depicted in Fig.4.36b) is calculated as

$$\mathbf{S}_{\text{CS}} = \mathbf{\Theta}_y\hat{\mathbf{I}}_J\mathbf{\Theta}_x \tag{4.65}$$

and the super-resolved ISAR image via 2D Fourier Transform as in Fig.4.36a.

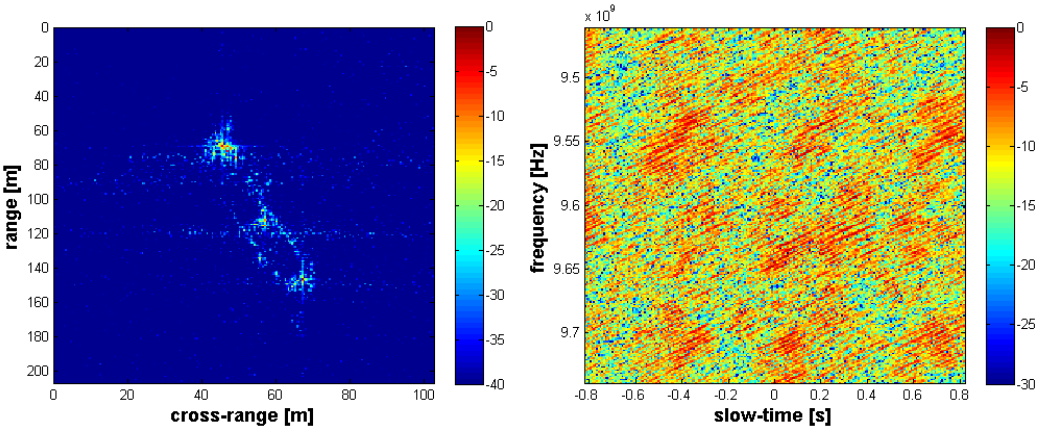

(a) (b)

FIGURE 4.36: CS super-resolved ISAR image (a) and relative frequency/slow-time raw signal (b).

4.4.3 Performance analysis

In the following, the results of the five tested super-resolution methods are summarized and evaluated by means of the performance analysis methods proposed in this Chapter. Such results are shown in Fig.4.37 and Fig.4.38.

The original ISAR image before zero-padding removing is depicted in Fig.4.37a and its relative frequency/slow-time complex signal in Fig.4.38a. Such images are the same shown in Fig.4.27a and 4.27b respectively. In Fig.4.37b, 4.37c, 4.37d, 4.37e and 4.37f the results of BWE, Capon's MVM, APES, SSVA and CS are shown respectively. Such super-resolution outputs are zero-padded by the same original zero-padding factor $K_{zp,rng} = K_{zp,crg} = 1.2428$ (see (4.58)) as can be seen in their relative complex signals in Fig.4.38. A 45% subaperture is used for Capon's MVM and APES.

By visual inspection, it appears that SSVA and CS allow for the original high-resolution image to be better reconstructed and the super-resolved image to have higher SNR and better resolution enhancement with respect to the other techniques. The worst one appears to be the Capon's MVM result. Such considerations are confirmed in Table 4.9 where the measured quality indexes proposed in Section 4.3 are summarized with the measured elapsed times. The same parameters are reported for the original high-resolution and low-resolution images for comparison purposes. Image contrast, entropy and SNR are measured on the zero-padded images shown in Fig.4.37, whereas the mean range and cross-range resolutions $\hat{\delta}_{rng}$ and $\hat{\delta}_{crg}$ are measured on the high-resolution, low-resolution and super-resolved images without zero-padding. This is why IC, IE and SNR for the high-resolution and low-resolution images in Table 4.9 are different from the values in Table 4.5, whereas $\hat{\delta}_{rng}$ and $\hat{\delta}_{crg}$ are the same.

The image quality indexes in Table 4.9 confirm better performance for Compressed Sensing with respect to the other tested super-resolution techniques in terms of image contrast, entropy and SNR. IC, IE and SNR for Capon's MVM and APES are even lower than the measured values for the low-resolution ISAR image. Such techniques provoke a quality deterioration with respect to the RD imaging technique. However, IC, IE and SNR could be enhanced by applying some regularization method or diagonal loading on the estimated covariance matrix. As observed above, there is a resolution enhancement with respect to the low-resolution image, i.e., MVM and APES allow a better resolved spectral estimation than the RD in the same frequency/slow-time support.

BWE has better performance than MVM and APES. IC, IE and SNR appear to be enhanced with respect to the low-resolution image, but the quality indexes of the original high-resolution ISAR image are not reached. The measured resolution values are smaller than $\hat{\delta}_{rng}$ and $\hat{\delta}_{crg}$ for the low-resolution image, MVM and APES, but still higher than

	IC	IE ($\cdot 10^5$)	SNR [dB]	$\hat{\delta}_{rng}$ [m]	$\hat{\delta}_{crg}$ [m]	Elap. Time
High-Res.	2.1365	−3.8556	47.5423	0.7755	0.4526	-
Low-Res.	1.9692	−3.2703	45.0984	1.4181	0.8821	-
BWE	2.0626	−3.8156	45.4553	0.7534	0.6157	0.9280
MVM	1.1353	−1.7035	31.6344	1.1478	0.7857	105.2336
APES	1.5290	−2.6539	39.4569	0.9749	0.7351	176.8413
SSVA	2.4283	−4.0470	48.8868	0.7977	0.4824	0.8836
CS	2.5830	−4.1958	49.0874	0.7711	0.4204	103.4969

TABLE 4.9: Performance numerical results summary (quality index based) and elapsed times in seconds.

the resolution of the original image. On the other hand, both SSVA and CS images have higher image contrast, entropy and SNR than the high-resolution image and the measured resolution is comparable with the original values.

Furthermore, by analyzing the extrapolated signals in Fig.4.38, it appears that MVM and APES do not allow to extrapolate the complex signal within the whole available support, i.e., do not allow a controlled extrapolation. For this reason, MVM and APES are not suited for gap filling. This is why the measured mean resolutions $\hat{\delta}_{rng}$ and $\hat{\delta}_{crg}$ for such techniques are not as enhanced as in the BWE, SSVA and CS images. Moreover, by looking at the shape of the complex signals in Fig.4.38c and 4.38d, the image PSF will not likely have a sinc-like shape. As a consequence, the CLEAN technique is likely not suited for both scatterers detection and resolution estimation. Therefore, the resolution measurements in Table 4.6, 4.7 and 4.9 for MVM and APES are probably not reliable.

For further analysis, consider the high-resolution ISAR image in Fig.4.39a and its portion zoomed in Fig.4.39b, where the target part highlighted in the red box is depicted. Such images are obtained by applying 10× zero-padding to the "truth" in Fig.4.28a. Then, consider the red segment in Fig.4.39b. The image profiles along such a segment are plotted in Fig.4.40 for the high-resolution and the super-resolved images. The "truth" profile is plotted in blue on both Fig.4.40a and 4.40b, the image profiles for BWE, SSVA and CS are plotted in Fig.4.40a in cyan, green and red respectively. MVM and APES profiles are plotted in Fig.4.40b in red and black respectively. By analyzing such results, it is clearly visible that Compressed Sensing allows for the best estimation and is the only one that allows to reconstruct the small peak at cross-range equal to 46m.

In the following, the truth based performance analysis methods are exploited to further analyze the super-resolution results. The "truth" to be estimated is the high-resolution ISAR image after zero-padding removing in Fig.4.28a. The "estimations" to be analyzed and compared are the super-resolved images in Fig.4.30a (BWE), Fig.4.31d (Capon's MVM), Fig.4.32d (APES), Fig.4.35a (SSVA) and Fig.4.36a (CS). The Scatterer Position based comparison algorithm (Section 4.2.1) is applied first.

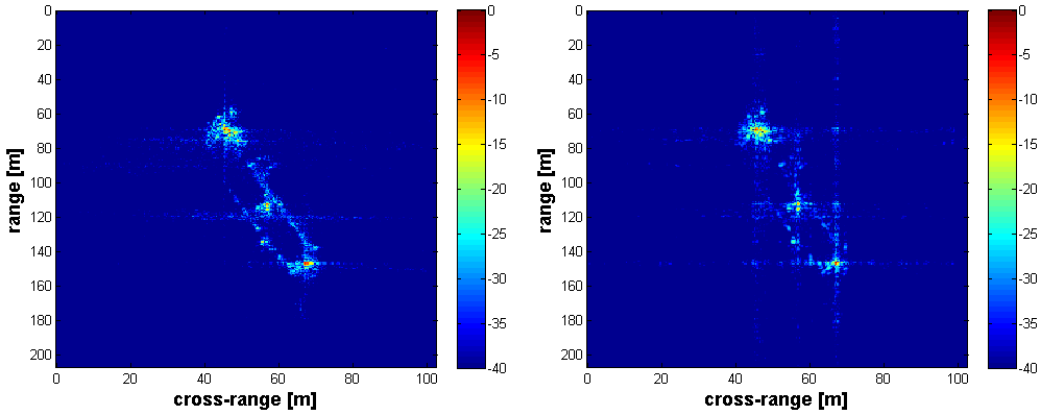

(a)

(b)

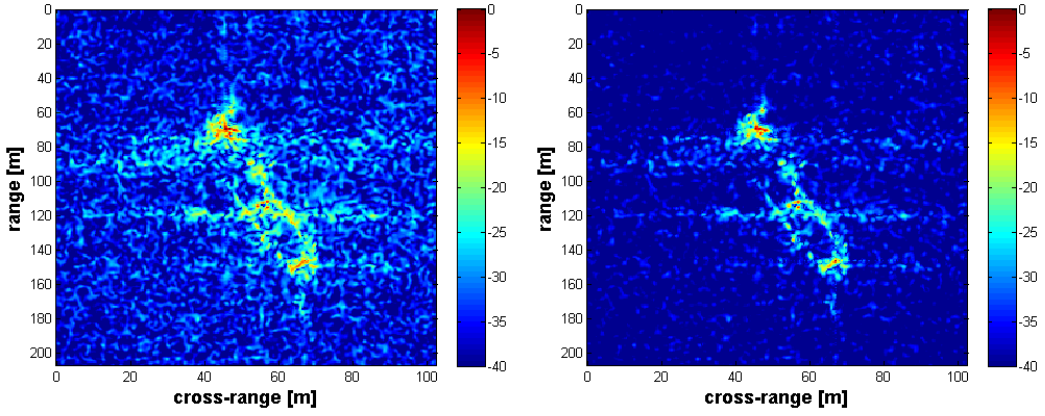

(c)

(d)

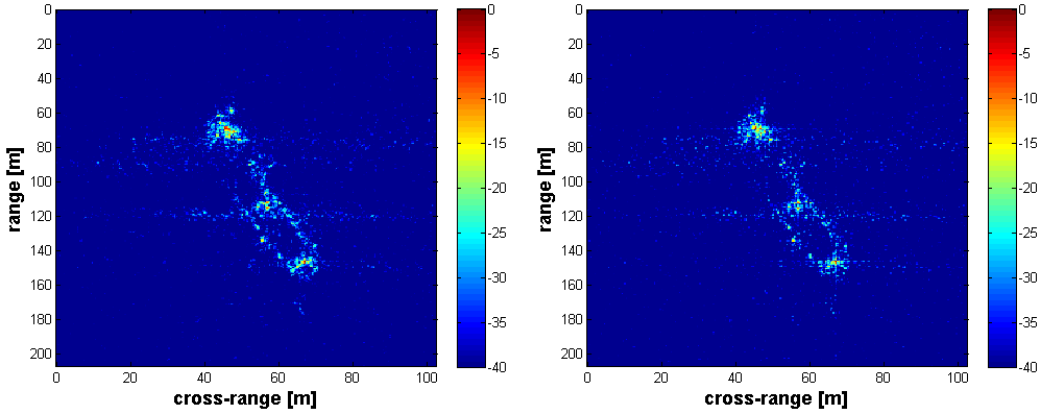

(e)

(f)

FIGURE 4.37: Zero-padded original high-resolution ISAR image (a) and super-resolved by BWE (b), Capon's MVM (c), APES (d), SSVA (e) and Compressed Sensing (f).

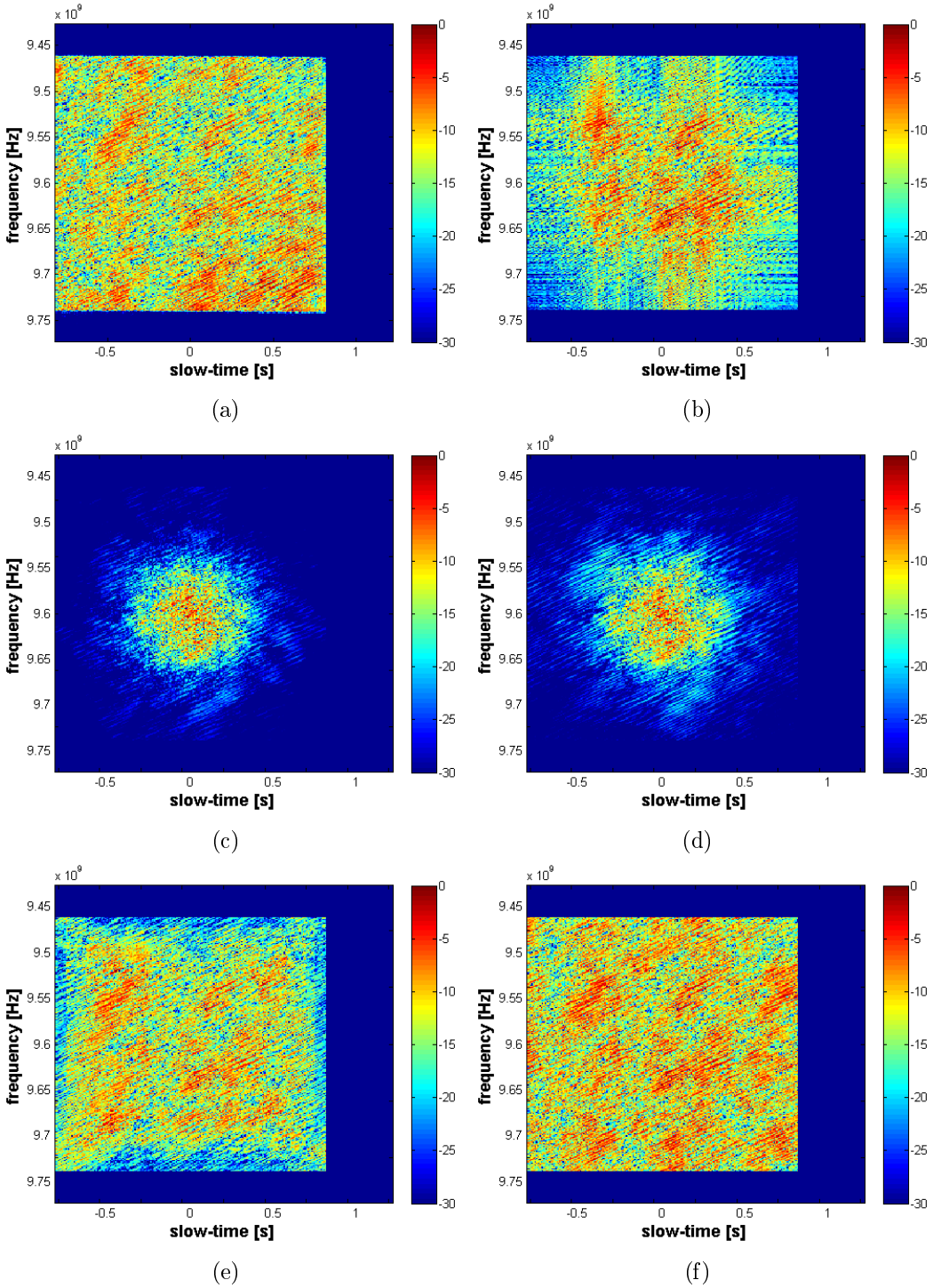

FIGURE 4.38: Zero-padded original frequency/slow-time signal (a) and reconstructed by BWE (b), Capon's MVM (c), APES (d), SSVA (e) and Compressed Sensing (f).

As written above, CLEAN is not suited for scattering detection in case of Capon's MVM and APES super-resolution. However, it is used anyway. CLEAN is first performed on the "truth" by setting the stop condition as a function of the residual energy. By stopping the CLEAN when the residual energy is less than the 15% of the original image energy, 68 scatterers are detected. After that, CLEAN is performed on the super-resolved ISAR images by setting the stop condition as a function of the detected peaks amplitude: when the measured peak amplitude is lower than the 95% of the weakest detected scatterer in the "truth", the CLEAN is stopped. Therefore, a different number of scatterers/peaks are detected in different images, but a fair peaks detection strategy is guaranteed. It is worth pointing out that every image is normalized with respect to its own norm before the CLEAN is performed.

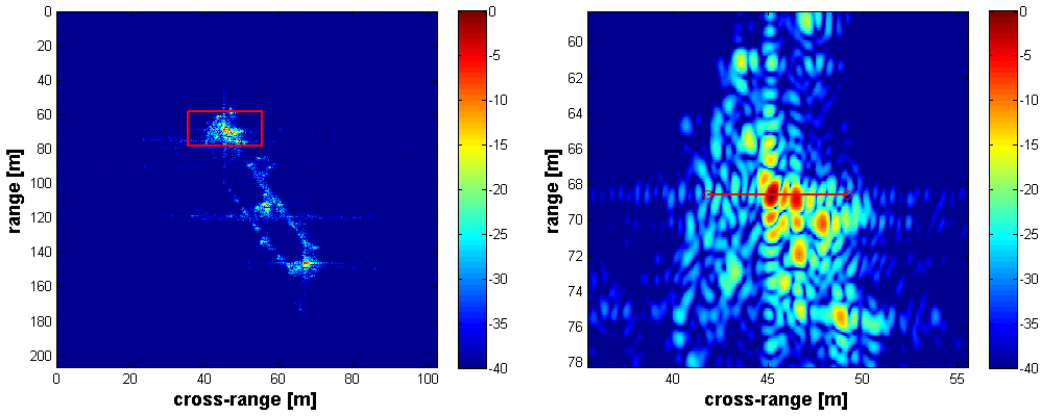

(a) (b)

FIGURE 4.39: 10× zero-padded high-resolution ISAR image (a) and highlighted portion with profile segment in red (b).

The Scatterer Position based comparison algorithm is applied for every "estimation" as depicted in Fig.4.41. Numerical performance analysis results are reported in Table 4.10 where "NoS" denotes the number of detected scatterers. Such results highlight that the CLEAN detects more scatterers in the super-resolved images than in the original high-resolution, except in the BWE result. In this case, 67 peaks are detected, but about the half are classified as false alarms (artifacts) and only 35 scatterers are correctly detected. In the MVM image the number of correct detections is quite larger, but it is just because a very large number of peaks is detected. This is probably because of the low SNR and the large number of artifacts. Moreover, as written above, the CLEAN is not suited for Capon's MVM and a lot of detections are probably spurious low-power peaks detected near the main targets. The same can be written for the APES. SSVA produces a lot of artifacts too and the half of the detected peaks are false alarms. A lot of peaks are detected in the CS result too, but in this case the RRMSE value (see (4.37)) is lower with respect to the other super-resolution techniques. Therefore, the Scatterer Position based

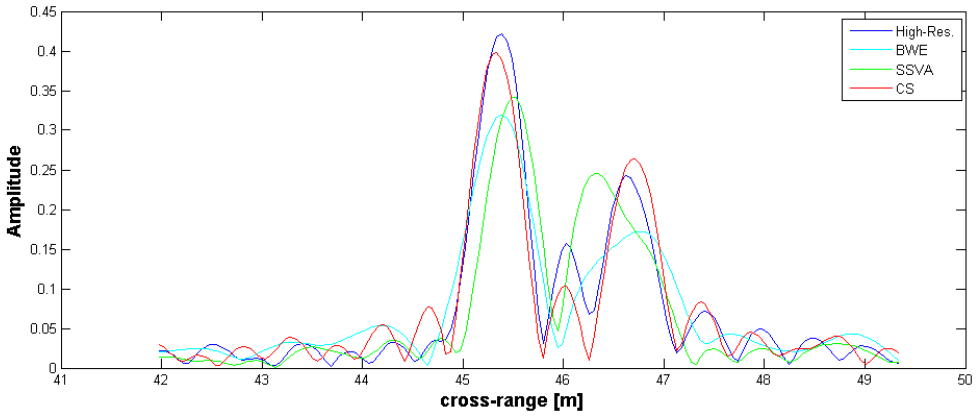

(a)

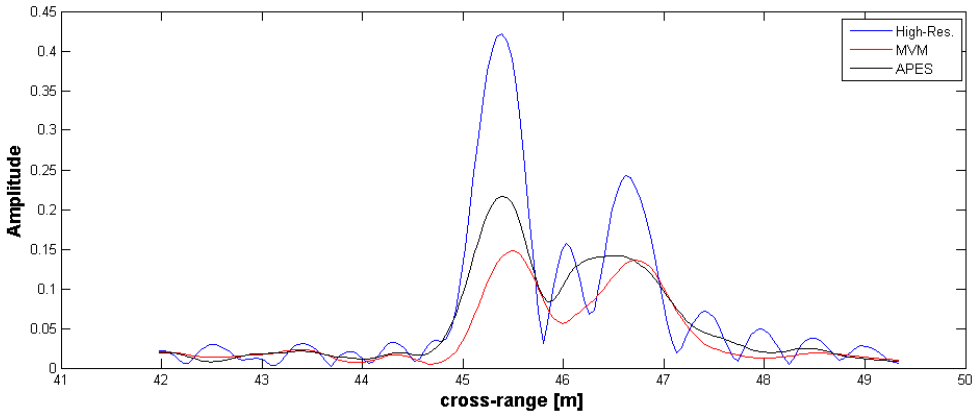

(b)

FIGURE 4.40: Amplitude profiles for High-res. ISAR image (both (a) and (b)), BWE, SSVA and CS in (a) and MVM and APES in (b).

comparison approach returns better performance for CS with respect to the others in terms of RRMSE, but the Correct Detection, Missed Detection and False Alarms indexes appear to be not very significative in this case.

Finally, the Mobile Cross-Correlation based comparison algorithm is performed. The intensity mobile cross-correlation maps $\mathbf{R}_{M,I}$ for all the tested super-resolution techniques are calculated by setting $\delta_H = \delta_S = 0.5$ (see (4.41)) and $W_{\mathcal{B}} = 15$. The resultant maps are depicted in Fig.4.42. A preliminary $5\times$ zero-padding is performed before the $\mathbf{R}_{M,I}$ maps calculation. The mean mobile cross-correlations $r_{M,I}$, the r_G and Root Mean Square Error values, as in (4.22) and (4.23), respectively are reported in Table 4.11. In this case, BWE, APES and CS return similar values of r_G correlation, whereas MVM and SSVA return lower values. However, CS has the greatest $r_{M,I}$ value. $r_{M,I}$ for APES is quite high too and the lowest value is given by SSVA. The best result in terms of RMSE is instead given by APES.

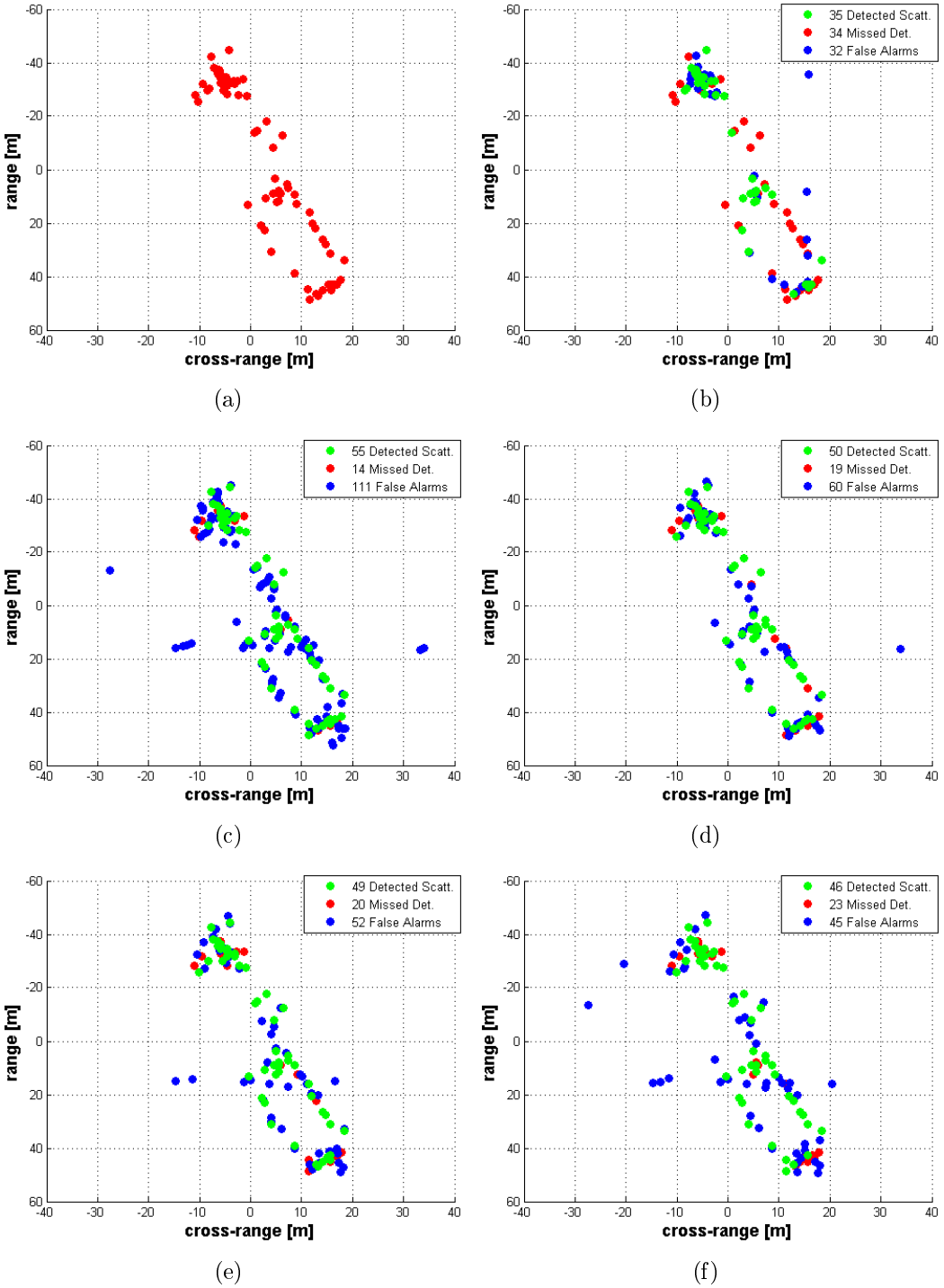

FIGURE 4.41: Detected scatterers in the "truth" in Fig.4.28a (a) and Scatterer Position based comparison results for BWE (b), Capon's MVM (c), APES (d), SSVA (e) and Compressed Sensing (f).

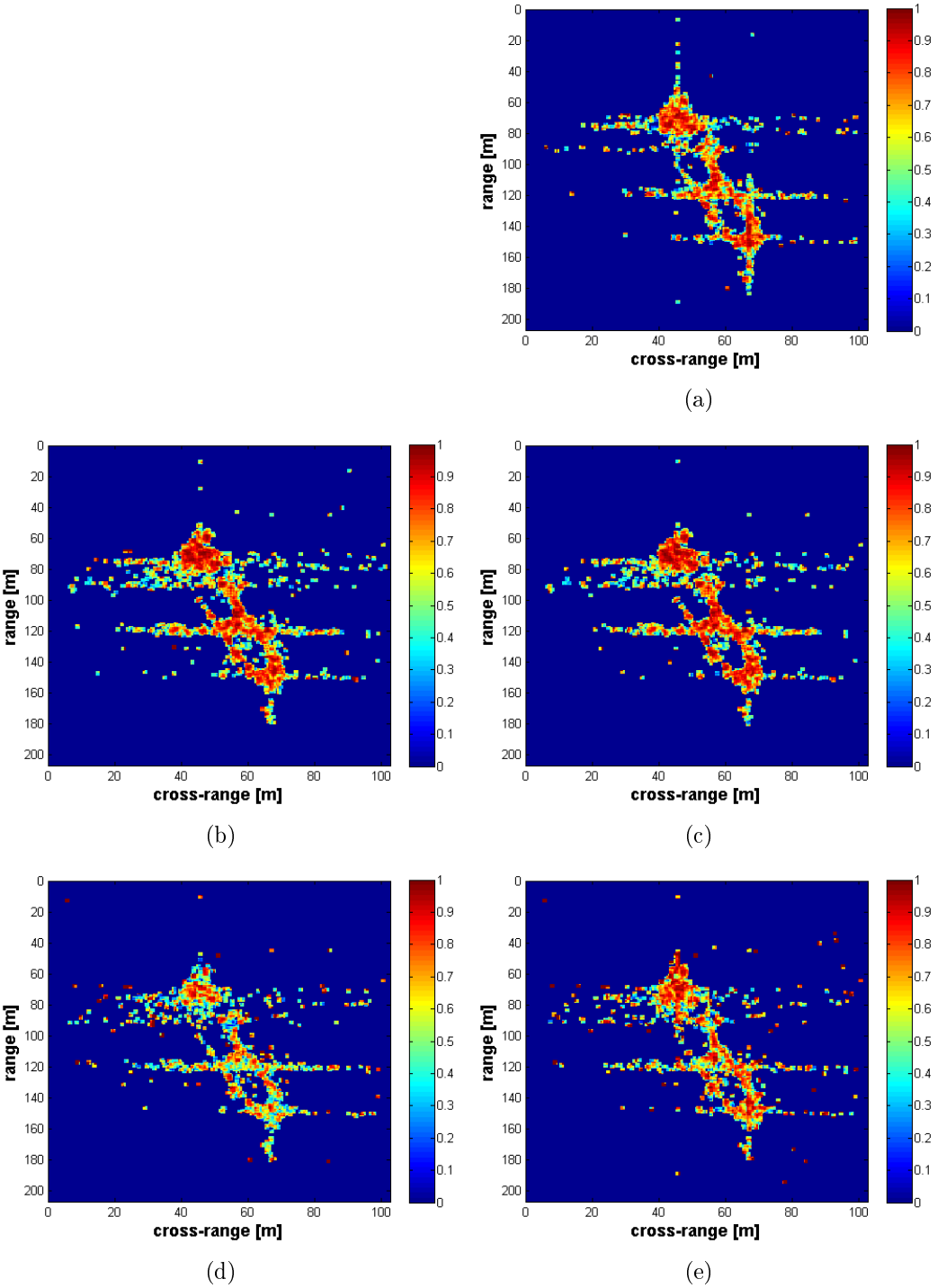

FIGURE 4.42: Mobile Cross-Correlation intensity maps for BWE (a), Capon's MVM (b), APES (c), SSVA (d) and Compressed Sensing (e).

	NoS	Correct Det.	Missed Det.	False Alarms	RRMSE
High-Res.	68	-	-	-	-
BWE	67	35	35	32	0.8131
MVM	167	54	14	113	0.6786
APES	110	50	18	60	0.6160
SSVA	101	50	19	51	0.8658
CS	91	46	22	45	0.5685

TABLE 4.10: Scatterer Position based comparison numerical results.

	r_G	$r_{M,I}$	RMSE
BWE	0.7695	0.6368	0.3018
MVM	0.6883	0.6382	0.3244
APES	0.7711	0.6541	0.2657
SSVA	0.6956	0.5965	0.3211
CS	0.7503	0.6627	0.3024

TABLE 4.11: Global Correlation Index, Mean Mobile Correlation Index and RMSE results.

In conclusion, as reported in Table 4.9, the proposed quality index based analysis methods return better results for the Compressed Sensing based super-resolution with respect to the other techniques. The worst case is given by Capon's MVM, whereas SSVA returns worse but still comparable values with respect to CS. In particular, CS has better performance than SSVA in terms of image contrast, image entropy and signal to noise ratio, but almost equal in terms of effective -3dB measured resolution.

Truth based methods do not return very clear results. By referring to Table 4.10, the scatterer position based comparison algorithm detects a large number of artifacts in the Capon's MVM and APES images, but such a result is not likely reliable because the used scatterers detection method seems to be not suitable for MVM and APES. On the other hand, BWE, SSVA and CS return very similar results in terms of number of correct detections relative to the number of detected peaks. However, both amplitude estimation RRMSE and mean mobile cross-correlation seem to confirm better performance for Compressed Sensing, but good results for APES too.

By considering the global cross-correlation r_G and RMSE (see Table 4.11), APES and BWE seem to have better performance with respect to MVM, SSVA and CS, even though the relative images in Fig.4.37 do not seem to be so similar to the truth.

Chapter 5

Bistatic radar imaging super-resolution

In this Chapter super-resolution radar imaging is treated in case of bistatic radar configuration. In Section 5.1 the super-resolution techniques treated in Chapter 3 are theoretically analyzed by considering the bistatic received signal model introduced in Section 2.3 and their validity for bistatic radar imaging is analytically demonstrated. In Section 5.2 super-resolution is exploited for bistatic distortion mitigation when range and/or Doppler migration occur. Linear prediction BWE, Super-SVA and Compressed Sensing are applied and the results are analyzed and compared by means of the performance analysis methods proposed in Chapter 4. Finally, in Section 5.3 the super-resolution techniques are applied on real bistatic data with further performance evaluation.

5.1 Bistatic super-resolution: theoretical analysis

In this Section the super-resolution techniques treated in Sections 3.2 to 3.6 are analyzed in case of bistatic configuration. The BEM signal model in (2.48) is exploited to theoretically validate BWE, Capon's MVM, APES, SSVA and CS when the received signal phase term is affected by the bistatic distortion term $K(n)$.

5.1.1 Linear Prediction based Bandwidth Extrapolation

As stated in Section 3.2, BWE super-resolution exploits an autoregressive modeling of the received radar signal. BWE is a parametric super-resolution technique, which means that the received signal is modeled as a sum of a finite number of complex exponential contributions as in (3.18).

Unfortunately, there is no analytical proof for validating for such a modeling in literature. In general, it is assumed that the target radar signature can be modeled as a stochastic process. Radar target fluctuation models were first introduced by Swerling in the 1950s and they proved to be very useful to describe the statistical properties of the radar cross-section of complex objects [90]. The Swerling models are based on the concept of scan-to-scan and pulse-to-pulse fluctuation.

In the scan-to-scan fluctuation case, "the returned signal power is assumed to be constant for the time on target during a single scan, but to fluctuate independently from scan to scan" [90]. In statistical terms, for the time in which the target of interest is in the antenna beam, the target radar cross-section is assumed as a stochastic process with normalized autocorrelation function approximately one.

In the pulse-to-pulse fluctuation case, the normalized autocorrelation function of the radar cross-section through consecutive pulses is instead assumed zero, i.e., the returned signal power through consecutive pulses is totally independent.

An intermediate case consists of modeling the target radar cross-section as fluctuating as a stochastic process with a certain dependence on the signal power in the previous pulses, i.e., with a certain normalized autocorrelation function with values between zero and one. Then, if it can be assumed that the stochastic process of the radar cross-section depends linearly on its own previous values, thus the signal model can be written in the form of a stochastic difference equation, i.e., an autoregressive process.

In the ISAR case, the consecutive pulses refer to the slow-time dimension. If such a fluctuation modeling can also be used for the spatial domain, i.e., the radar cross-section of a certain part of the target body can be assumed linearly depending on the cross-sections of the adjacent parts, the autoregressive model can be used for the slant-range dimension too. As a consequence, the discrete radar signal $S(m,n)$ can be modeled as an autoregressive stochastic process along both the vertical and horizontal directions. This is independently of the monostatic or bistatic radar geometry.

The "Frequency bandwidth extrapolation" step of the BWE algorithm is not affected by the bistatic geometry, because the presence of $K(n)$ in the bistatic signal model in (2.48) does not affect the linear dependence of the signal phase on the frequency variable. On the other hand, $K(n)$ affects the signal phase dependence on the slow-time variable and, as a consequence, the "Aperture extrapolation" step of the BWE algorithm. In fact, as stated in Section 3.2, "the aperture extrapolation can be efficaciously applied if the angle change is small enough to approximate the sine and cosine functions with a first order Taylor-Maclaurin polynomial and no range/cross-range migration effects occur", i.e., if "the phase dependence on n is linear".

To guarantee such a linear dependence on the slow-time variable, it is important to have the quadratic term $R_{B,2}$ of the BEM effective range in (2.54) negligible with respect to $R_{B,0}$ and the first order term $R_{B,1}$, i.e., satisfy the constraint in (2.64) for the Doppler migration. If Doppler migration does not occur, then the BWE algorithm can be efficaciously applied in bistatic configuration too.

5.1.2 Capon's MVM and APES

Capon's MVM and APES are signal processing techniques that aim to estimate the Power Spectral Density (PSD) of a signal. Both MVM and APES consists of modeling the signal of interest as a complex sinusoid plus an unmodeled noise/interference term as in (3.33) and (3.49) for the 1-D and 2-D cases respectively.

In the monostatic case, by considering the signal model in (2.18) and approximating the effective range in (2.20) by its first order Taylor-Maclaurin polynomial, the received signal in case of single scatterer target can be written as follows

$$\begin{aligned} S(f,n) &= W(f,t_n)\, A\, e^{-j2\pi \frac{2f}{c}\left(z_{1,0}\Omega_{eff} t_n + z_{2,0}\right)} \\ &\simeq W(f,n)\, A\, e^{-j2\pi\left(\frac{2z_{2,0}}{c} f + \frac{2f_0\Omega_{eff} z_{1,0}}{c} t_n\right)} \\ &= W(f,n)\, A\, e^{-j2\pi(\tau_0 f + \nu_0 t_n)} \end{aligned} \tag{5.1}$$

where ν_0 and τ_0 are defined in (2.39) and (2.40) respectively and $2f\Omega_{eff} z_{1,0}$ is approximated with $2f_0\Omega_{eff} z_{1,0}$ for the rectangular Fourier domain approximation. Then, by discretizing the frequency variable as $f = f_0 + m\delta_f$

$$S(m,n) = A\, e^{-j2\pi\tau_0 f_0}\, e^{-j2\pi\left(\tau_0\delta_f m + \nu_0 T_R n\right)} \tag{5.2}$$

where $m = 1, \ldots, M$, $n = 1, \ldots, N$ and the window function W is omitted since it is always defined equal to 1 within such a discrete domain. Therefore, by defining

$$\omega_{M,1} = \tau_0\delta_f \tag{5.3}$$

$$\omega_{M,2} = \nu_0 T_R \tag{5.4}$$

the result in (5.2) is compatible with the signal model in (3.49). On the other hand, by considering the received signal expression in bistatic configuration in (2.52) and approximating $R'_B(t_n, z_{1,0}, z_{2,0})$ by its first order Taylor-Maclaurin polynomial, (5.1) becomes

$$\begin{aligned} S(f,n) &= W(f,n)\, A\, e^{-j2\pi \frac{2f}{c}\left(R_{B,0} + R_{B,1} t_n\right)} \\ &\simeq W(f,n)\, A\, e^{-j2\pi\left(\frac{2R_{B,0}}{c} f + \frac{2f_0 R_{B,1}}{c} t_n\right)} \end{aligned} \tag{5.5}$$

Then, by discretizing the frequency variable and considering $t_n = nT_R$

$$\begin{aligned} S(m,n) &= A\, e^{-j2\pi \frac{2R_{B,0} f_0}{c}}\, e^{-j2\pi\left(\frac{2R_{B,0}\delta_f}{c} m + \frac{2f_0 R_{B,1} T_R}{c} n\right)} \\ &= A\, e^{-j2\pi \frac{2R_{B,0} f_0}{c}}\, e^{-j2\pi(\omega_{B,1} m + \omega_{B,2} n)} \end{aligned} \tag{5.6}$$

where

$$\omega_{B,1} = \frac{2R_{B,0}\delta_f}{c} = \frac{2K_0 z_{2,0}\delta_f}{c} = K_0\, \tau_0 \delta_f = K_0\, \omega_{M,1} \tag{5.7}$$

$$\begin{aligned} \omega_{B,2} &= \frac{2f_0 R_{B,1} T_R}{c} = \frac{2f_0\left(K_1 z_{2,0} + K_0 z_{1,0}\Omega_{eff}\right) T_R}{c} \\ &= \frac{2f_0 K_0 z_{1,0}\Omega_{eff} T_R}{c} + \frac{2f_0 K_1 z_{2,0} T_R}{c} = K_0\, \omega_{M,2} + \Delta_\nu T_R \end{aligned} \tag{5.8}$$

where Δ_ν is the linear distortion term defined in (2.73). The result in (5.6) is also compatible with the signal model in (3.49). As a consequence, Capon's MVM and APES techniques can be indifferently used in both monostatic and bistatic configurations.

5.1.3 Super Spatially Variant Apodization

SSVA iteratively applies and inverts SVA in order to make a controlled extrapolation of the received complex signal beyond the available frequency/slow-time support. The only constraint is that SVA must be applicable. As mentioned in Section 3.5, SVA needs the knowledge of the image sampling rate, i.e., any zero-padding in the signal domain must be known, and the imaging PSF must have a sinc-like shape. As a consequence, any weighting by means of Hamming, Hanning, Kaiser, or other window functions in the signal domain must be known and inverted.

By considering the bistatic image model in (2.80), it appears that the image scaling caused by K_0 and the linear distortions due to Δ_ν only affect the position of the scatterers in the time-delay/Doppler (or range/cross-range) domain and does not modify the imaging PSF represented by $w(\tau,\nu)$. On the other hand, the imaging PSF could be altered by the quadratic distortion term $D_{2,B}(\nu, z_{1,0}, z_{2,0})$, which causes a blurring of the PSF along the Doppler (or cross-range) coordinate. Such a blurring effect occurs if the constraint in (2.64) is not satisfied, i.e., if there is Doppler migration. However, even if Doppler migration occurs, (2.64) is not satisfied and $D_{2,B}(\nu, z_{1,0}, z_{2,0})$ cannot be neglected, such a distortion affects the PSF shape only along the Doppler direction (see Fig.2.9a). On the other hand, range migration affects the PSF shape along both range and cross-range.

SSVA can be applied in any case, but if $\Delta_{rng} > \delta_{rng}$ and/or $\Delta_{crg} > \delta_{crg}$, i.e., (2.57) and/or (2.64) are not satisfied, resolution will be eventually enhanced, but the final result will not have sinc-like shape. Such considerations are validated in Fig.5.1.

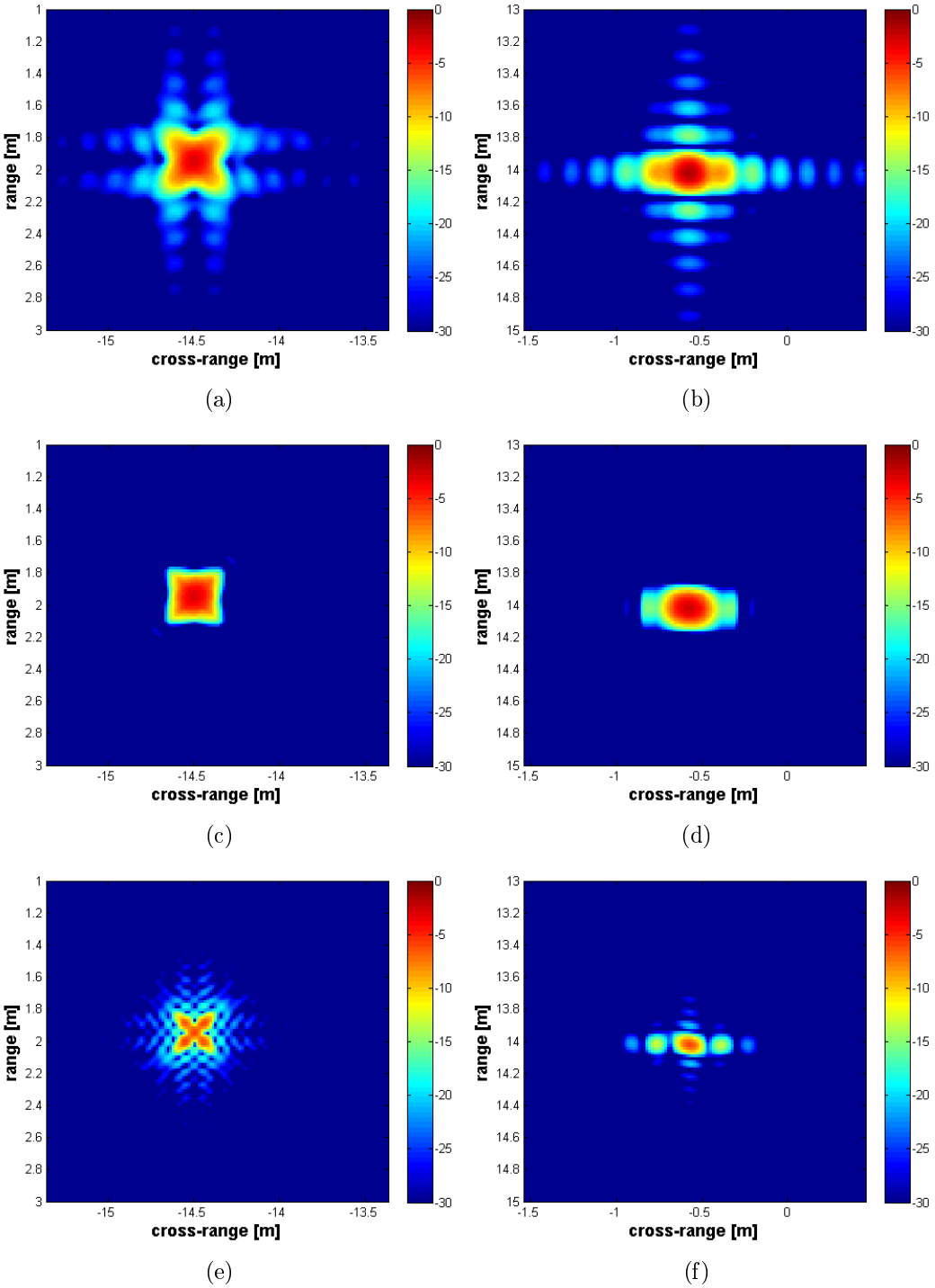

FIGURE 5.1: Original ISAR images in case of range migration (a) and Doppler migration (b), results of SVA in case of range migration (c) and Doppler migration (d) and results of SSVA in case of range migration (e) and Doppler migration (f).

Simulated ISAR images in Fig.5.1 are produced as in Section 2.4 but with the target

speed reduced to 20m/s and different target size. The ISAR image in Fig.5.1a is a zoom on scatterer #3 in case of $z_{1,3} = 14$m and $z_{2,3} = 2$m. In this case $\Delta_{rng} = 0.2316$m, $\Delta_{crg} = 0.0312$m and only range migration occurs ($\delta_{rng} = 0.15$m and $\delta_{crg} = 0.1432$m).

As in Fig.5.1c, SVA successfully suppresses sidelobes and the SSVA result in Fig.5.1e appears to have a similar shape with respect to the original low-resolution image and the resolution is successfully enhanced. However, the super-resolved image in Fig.5.1e cannot be stated to be a good result. This is because five prominent peaks appear where only one scatterer is simulated to be in such a position. Such artifacts are caused by the non-sinc-like shape of the image in Fig.5.1a.

The same can be stated if only Doppler migration occurs as in Fig.5.1b, 5.1d and 5.1f. Fig.5.1b shows the original image zoomed on scatterer #2 in case of $z_{1,2} = 2$m and $z_{2,2} = 14$m with $\Delta_{rng} = 0.0088$m and $\Delta_{crg} = 0.3677$m, whereas SVA and SSVA results are shown in Fig.5.1d and 5.1f respectively. In this case, three prominent peaks appear in the super-resolved image aligned along the cross-range direction. This is because when Doppler migration occurs, the image PSF is still sinc-like along the range direction.

In all cases described above, SSVA is applied by setting $\eta = 2^{1/4}$ and in 4 loops to halve the image resolution along both range and cross-range. All images in Fig.5.1 are 10× zero-padded and shown in dB scale.

Therefore, it can be stated that SSVA can be successfully applied if both (2.57) and (2.64) are satisfied, i.e., if both range and Doppler migration do not occur. However, it can still be applied to enhance range resolution if only (2.57) is satisfied.

However, such considerations can be stated also for the monostatic case. In monostatic configuration, if (2.25) is not satisfied, range migration occurs and SSVA behaves as described above for the bistatic configuration, whereas if (2.34) is not satisfied, Doppler migration occurs and SSVA can be only applied along the range direction.

5.1.4 Super-Resolution via Compressed Sensing

In this Section, the signal model with the Fourier dictionaries in matrix representation in (3.104), i.e., the applicability of the Compressed Sensing theory for signal reconstruction/extrapolation, is validated for the bistatic configuration.

By considering the signal model in (2.48), the effective range expression in (2.54) and the target/scene reflectivity function modeled as a set of point-like scatterers as in (3.90), if $R'_B(t_n, z_{1,0}, z_{2,0})$ is approximated by its first order Taylor-Maclaurin polynomial, the bistatic received signal can be written as follows

$$
\begin{aligned}
S(f,n) &= W(f,n)\int_{z_1}\int_{z_2}\gamma(z_1,z_2)\,e^{-j\frac{4\pi f}{c}[K_0 z_{2,i}+(K_1 z_{2,i}+K_0 z_{1,j}\Omega)t_n]}dz_1 dz_2 \qquad (5.9)\\
&= W(f,n)\sum_{i=1}^{P}\sum_{j=1}^{Q}\sigma_{i,j}\,e^{-j\frac{4\pi f}{c}[K_0 z_{2,i}+(K_1 z_{2,i}+K_0 z_{1,j}\Omega)t_n]}\\
&= W(f,n)\sum_{i=1}^{P}\sum_{j=1}^{Q}\sigma_{i,j}\,e^{-j2\pi(K_0\tau_i f+K_0\nu_j t_n+\Delta_{\nu,i}t_n)}
\end{aligned}
$$

where τ_i and ν_j are the delay-time and the Doppler frequency for the $(i,j)^{\text{th}}$ scatterer defined in (3.92) and (3.93) respectively, whereas

$$\Delta_{\nu,i}=\frac{2f}{c}K_1 z_{2,i}\simeq\frac{2f_0}{c}K_1 z_{2,i}=K_1 f_0\tau_i \qquad (5.10)$$

is the linear distortion term defined as in (2.73). Such a signal representation is equivalent to (3.91) if $K_0\to 1$ and $K_1\to 0$, i.e., when the bistatic angle tends to zero. In (5.10), the frequency variable f is approximated with f_0 for the rectangular domain approximation as in (3.93). Therefore, by considering the products in (3.100) and (3.101) for the delay-time and Doppler variables discretization and

$$
\begin{aligned}
\Delta_{\nu,i}\,t_n &= K_1 f_0\frac{p_i}{P\delta_f}\,nT_R\,\frac{Q}{Q} \qquad (5.11)\\
&= \frac{n}{Q}\left[K_1 f_0\frac{QT_R}{P\delta_f}\,p_i\right]\\
&= \frac{n}{Q}\left[K_1 f_0\frac{T_{ob}}{B}\,p_i\right]=\frac{n}{Q}\Delta_q(i)
\end{aligned}
$$

where $\tau_i=\frac{p_i}{P\delta_f}$, $t_n=nT_R$ and

$$\Delta_q(i)=K_1 f_0\frac{T_{ob}}{B}\,p_i \qquad (5.12)$$

the signal model in (5.9) can be written as

$$S(m,n)=W(m,n)\sum_{i=1}^{P}\sum_{j=1}^{Q}\sigma_{i,j}\,e^{-j2\pi\frac{f_0}{B}K_0 p_i}\,e^{-j2\pi\frac{m(K_0 p_i)}{P}}\,e^{-j2\pi\frac{n\left(K_0 q_j+\Delta_q(i)\right)}{Q}} \qquad (5.13)$$

Compare (5.13) with (3.102) for the monostatic case. By using the same matrix notation as in Section 3.6, the received signal matrix $\mathbf{S}_C$ can then be written as follows

$$\mathbf{S}_C=\mathbf{\Psi}_y\mathbf{I}_B\mathbf{\Psi}_x^T \qquad (5.14)$$

where $\mathbf{\Psi}_y$ and $\mathbf{\Psi}_x$ are the Fourier dictionaries defined in (3.105) and (3.106) respectively and $\mathbf{I}_B$ is the matrix representation of

$$I_B(p,q) = \sum_{i=1}^{P}\sum_{j=1}^{Q} \sigma_{i,j}\, w\left(p - K_0 p_i\ ,\ q - K_0 q_j - \Delta_q(i)\right)\ e^{-j2\pi \frac{f_0}{B} K_0 p_i} \tag{5.15}$$

Compare (5.15) with (3.103). As a result, CS can be applied also in case of bistatic configuration to reconstruct the acquired signal beyond the available frequency/slow-time support and enhance image resolution. The SL0 algorithm described in Section 3.6 can be used without any modification.

5.2 Bistatic distortion mitigation

In this Section linear prediction BWE (Section 3.2), Super-SVA (Section 3.5) and Compressed Sensing (Section 3.6) are applied for bistatic distortion mitigation. The basic idea has been introduced in Section 2.4 and consists of reducing the CPI by a factor K_T (see (2.86)) in order to mitigate the bistatic range/Doppler distortion and then apply super-resolution to restore the cross-range resolution loss caused by the signal support reduction.

As in Section 2.4, the range and Doppler migration parameters Δ_{rng} and Δ_{crg}, defined in (2.57) and (2.64) respectively, are directly proportional to the CPI. Range and Doppler migration are stated to occur when $\Delta_{rng} > \delta_{rng}$ and $\Delta_{crg} > \delta_{crg}$ respectively.

The CPI reduction parameter K_T must satisfy the constraints in (2.87) and (2.88) for range and Doppler respectively. Such constraints can then be merged as follows

$$K_T < \min\left\{K_{T,rng}\ ,\ K_{T,crg}\right\} \tag{5.16}$$

where

$$K_{T,rng} \doteq \min_{i=1,\dots,N_s}\left\{\frac{c}{2B\left|K_1 z_{2,i} + K_0 z_{1,i}\Omega\right| T_{ob}}\right\} \tag{5.17}$$

$$K_{T,crg} \doteq \min_{i=1,\dots,N_s}\left\{\sqrt{\frac{c}{2f_0\left|K_2 z_{2,i} + 2K_1 z_{1,i}\Omega - K_0 z_{2,i}\Omega^2\right| T_{ob}^2}}\right\} \tag{5.18}$$

$K_{T,rng}$ can be estimated by estimating the product $z_{1,i}\Omega = \frac{c}{2f_0}\nu_i$ (see 2.38) and the target path for the bistatic angle and $K(t)$. On the other hand, $K_{T,crg}$ needs the effective rotation vector to be estimated. However, also the image focusing center needs to be evaluated to estimate the scatterers position in range $z_{2,i}$ and Doppler ν_i.

	Scatterer #2	Scatterer #3
$z_{1,i}$[m]	4	-4
$z_{2,i}$[m]	8	8
δ_{rng}[m]	0.15	0.15
δ_{crg}[m]	0.1432	0.1432
Δ_{rng}[m]	0.0059	0.1231
Δ_{crg}[m]	0.6535	0.5362
$K_{T,rng}$	25.4237	1.2185
$K_{T,crg}$	0.4682	0.5168

TABLE 5.1: Bistatic distortion parameters for the simulated example in Section 2.4.

By referring to the simulation example in Section 2.4, the calculated distortion parameters for scatterers #2 and #3 are summarized in Table 5.1 and the zoomed ISAR images are shown in Fig.5.3a and 5.3b respectively.

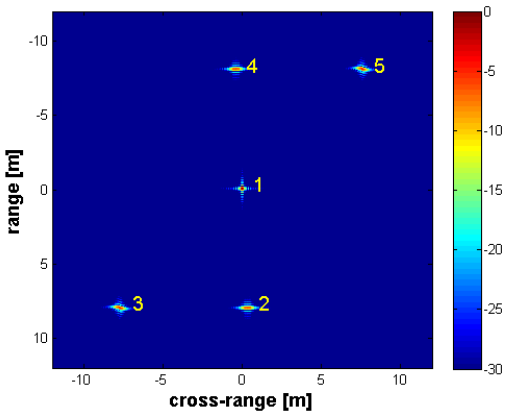

FIGURE 5.2: High-resolution distorted bistatic ISAR image with the five scatterers labeled.

The whole ISAR image under test is shown in Fig.5.2. As in Section 2.4, all the ISAR images in the following are 10× zero-padded and shown in dB scale for illustration purposes.

As in Table 5.1, $\Delta_{rng} < \delta_{rng}$ for both scatterers #2 and #3, but range migration can be observed in Fig.5.3b. This is because Δ_{rng} for scatterer #3 is lower but still comparable with δ_{rng}, whereas for scatterer #2 Δ_{rng} is much smaller than δ_{rng}. Range migration occurs, but does not exceed the range resolution cell. Δ_{crg} is instead considerably greater than δ_{crg} for both scatterers #2 and #3 and strong Doppler migration is evident in Fig.5.3.

Therefore, in order to mitigate Doppler migration and enclose the Doppler bandwidth within the Doppler resolution cell, the CPI reduction factor K_T must be chosen as follows

$$K_T < K_{T,crg} = \min\{0.4682\,,\ 0.5168\} = 0.4682 \tag{5.19}$$

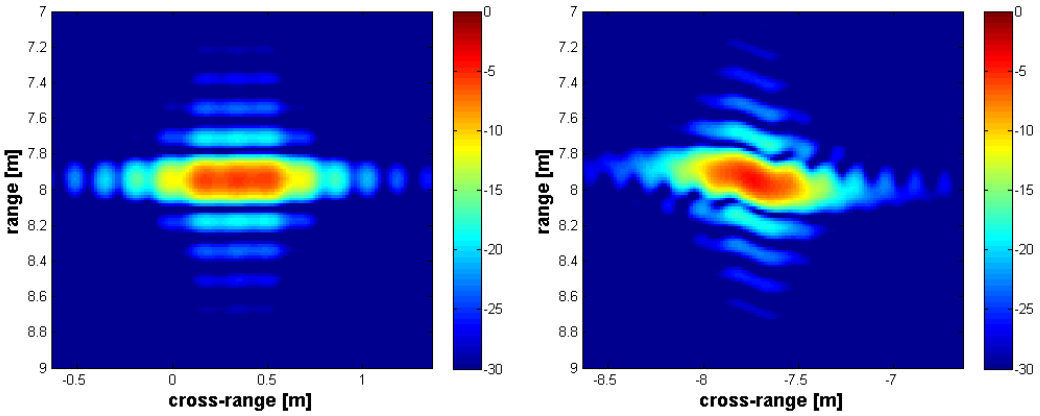

(a) (b)

FIGURE 5.3: High-resolution distorted bistatic ISAR image zoomed on the scatterer #2 (a) and #3 (b) before CPI reduction.

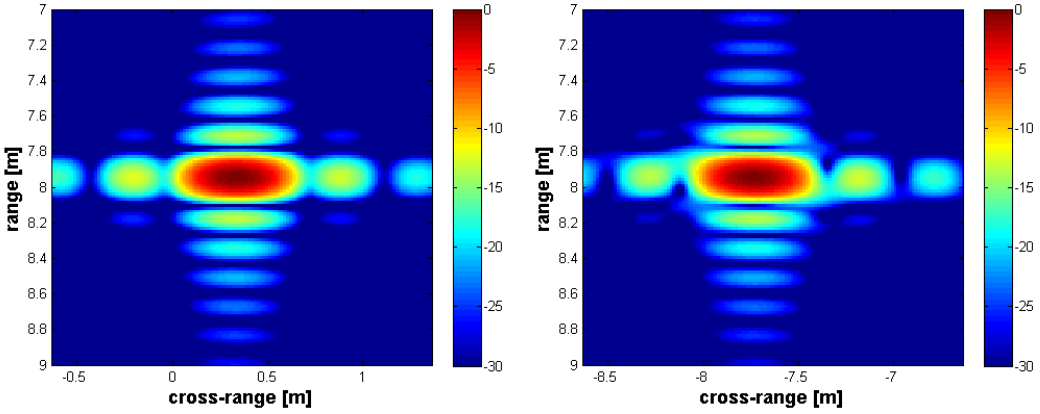

(a) (b)

FIGURE 5.4: High-resolution distorted bistatic ISAR image zoomed on the scatterer #2 (a) and #3 (b) after CPI reduction.

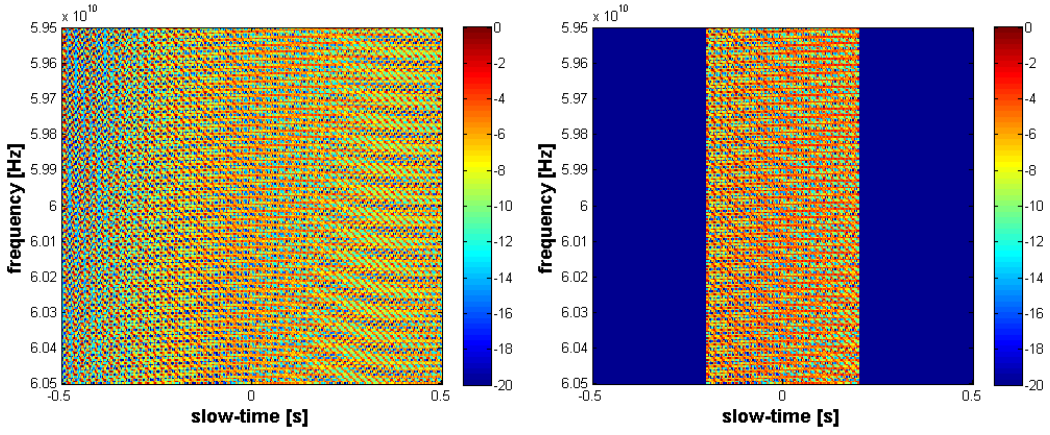

(a) (b)

FIGURE 5.5: Frequency/slow-time complex signal before (a) and after (b) CPI reduction.

By using $K_T = 0.4$, the result of the CPI reduction on the ISAR images in Fig.5.3a and 5.3b are depicted in Fig.5.4a and 5.4b respectively (see Fig.2.13a and 2.13b too). The complex signal in the frequency/slow-time domain before and after CPI reduction is shown in Fig.5.5a and 5.5b respectively.

In Section 2.4, such results are commented and compared with the case $K_T = 0.6$, i.e., when the CPI is not reduced enough to mitigate the bistatic distortion. Images in Fig.5.4 show a sinc-like shape which is not visible in Fig.5.3, but the resolution loss along the cross-range is evident. By considering the super-resolution techniques tested in Chapter 4, only BWE, SSVA and CS are applied to restore the Doppler/cross-range resolution, because Capon's MVM and APES are not able to arbitrarily extrapolate the retained complex signal as highlighted in Section 4.4.

BWE:	p_{AR}	$N_{low}/3$
SSVA:	η	$2^{1/4}$
	N_{loop}	4
CS:	c_σ	0.6
	N_L	50
	μ	2

TABLE 5.2: Parameter setting for the used super-resolution techniques.

Such techniques are applied with the parameter settings summarized in Table 5.2 where p_{AR} is the AR model order for the linear prediction BWE (see Section 3.2), $N_{low} = K_T T_{ob}/T_R$, η is the BEF for the SSVA, N_{loop} is the number of SSVA loops (see Section 3.5), c_σ is the σ-decreasing factor for the σ sequence, N_L is the number of iterations of the steepest ascend algorithm and μ is the constant parameter for the SL0 algorithm (see Section 3.6). Super-resolution results are shown in Fig.5.6 ordered as follows.

1. Fig.5.6a: result of BWE zoomed on scatterer #2;
2. Fig.5.6b: result of BWE zoomed on scatterer #3;
3. Fig.5.6c: result of SSVA zoomed on scatterer #2;
4. Fig.5.6d: result of SSVA zoomed on scatterer #3;
5. Fig.5.6e: result of CS zoomed on scatterer #2;
6. Fig.5.6f: result of CS zoomed on scatterer #3;

By observing the results in Fig.5.6, it appears that Compressed Sensing allows for a better sinc-like result when only Doppler migration occurs, whereas SSVA allows for a sidelobe suppression in addition to the cross-range resolution reinstatement (compare Fig.5.6c with 5.6e).

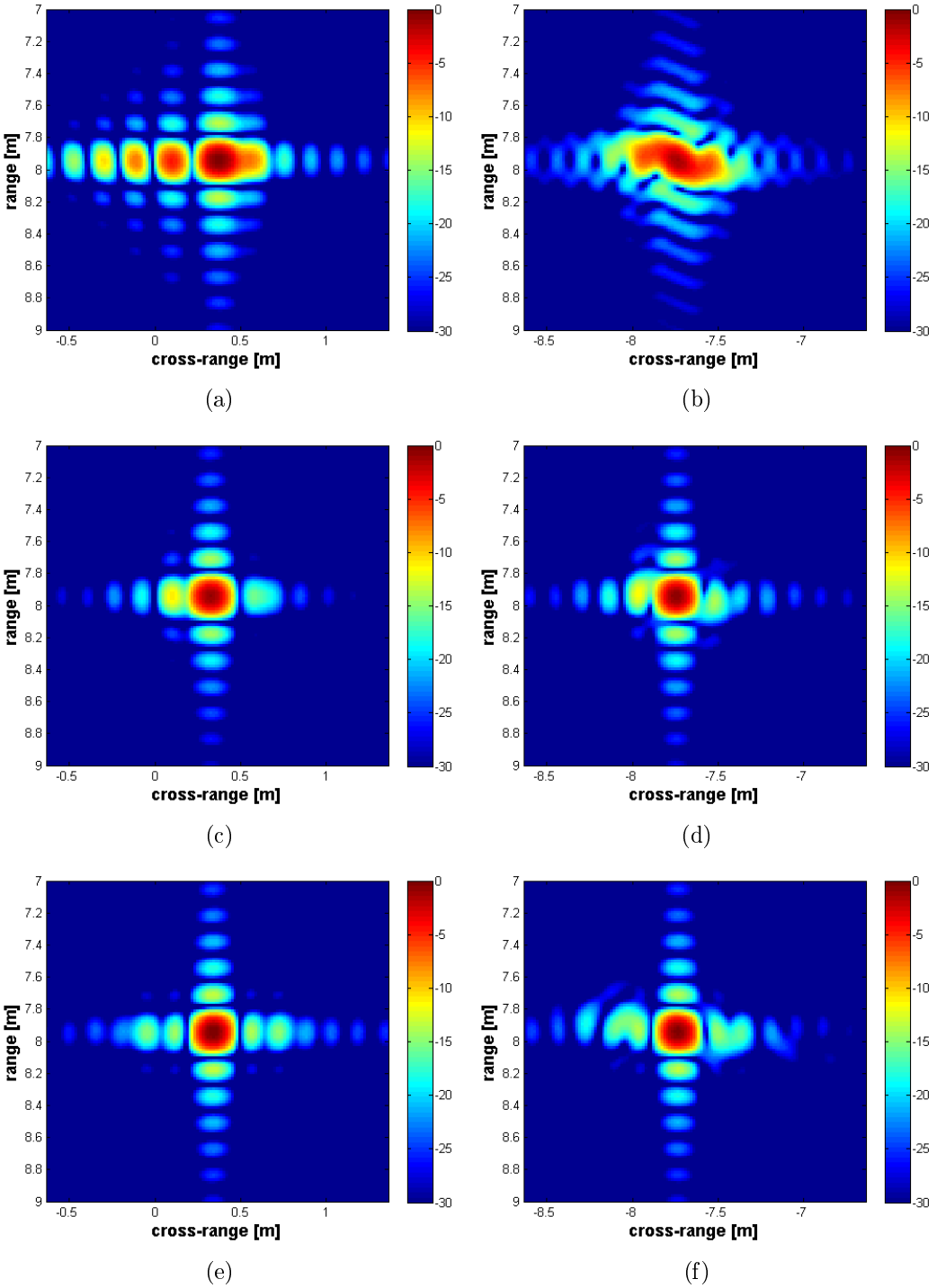

FIGURE 5.6: Results of BWE, SSVA and CS zoomed on scatterer #2 ((a), (c) and (e) respectively) and #3 ((b), (d) and (f) respectively).

BWE appears instead to reconstruct the range migration on scatterer #3. This is probably because the signal model exploited by the BWE super-resolution in (3.15) is the same as in (2.82) which is used to generate the simulated ISAR image under test (compare Fig.5.6b with Fig.2.9b). However, Doppler distortion on scatterer #2 is not reconstructed and BWE is able to restore the cross-range resolution even if the final result is definitely not sinc-like (compare Fig.5.6a with Fig.2.9a). This is because, as stated in Section 5.1.1, BWE can be successfully applied in bistatic configuration if the signal phase term is linearly dependent on the slow-time variable, i.e., if Doppler migration does not occur.

For a better performance evaluation, in the following the performance analysis methods proposed in Chapter 4 are applied. However, in this case the original high-resolution image is not suitable for being used as "truth" because super-resolution is not applied in order to reconstruct it, but to mitigate quadratic distortions. In order to apply truth based performance analysis methods another "truth" must be used.

Since in this Section simulated data is used, all the scatterers position in the range/-Doppler (or range/cross-range) domain are known. Therefore, another "truth" can be built by placing ideal 2D sinc functions in the same positions where the scatterers are theoretically located as shown in Fig.5.7. In Fig.5.7a the whole "truth" image is depicted, whereas Fig.5.7b shows the image zoomed on scatterer #3. The other four scatterers have the same 2D sinc shape. The "truth" in Fig.5.7 is used to compare the original distorted ISAR image in Fig.5.2 and 5.3 with the super-resolution images in Fig.5.6.

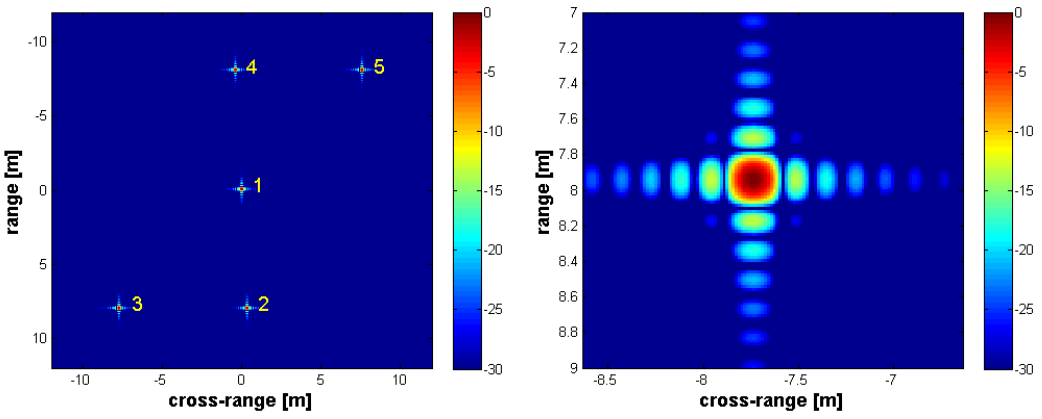

(a) (b)

FIGURE 5.7: "Truth" for performance analysis (a) and zoom on scatterer #3 (b).

Results of the proposed "truth based" and "quality index based" performance analysis methods are shown in Table 5.3. By considering the quality indexes Image Contrast (IC), Image Entropy (IE) and SNR in Table 5.3, SSVA appears to give better results with respect to BWE and CS. This is because SSVA allows to restore the cross-range resolution but does not generate an output image with sinc-like shape as in the truth,

	Original	**BWE**	**SSVA**	**CS**
IC	10.2975	8.7994	12.9652	12.1943
IE ($\cdot 10^5$)	−445.4773	−447.4476	−492.7380	−489.538
SNR [dB]	75.4708	72.2198	80.3709	78.8742
$\hat{\delta}_{rng}$ [m]	0.1470	0.1410	0.1350	0.1350
$\hat{\delta}_{crg}$ [m]	0.3295	0.1576	0.1432	0.1289
NoS	5	5	5	5
Correct Det.	5	5	5	5
Missed Det.	0	0	0	0
False Alarms	0	0	0	0
RRMSE	0.3721	0.2108	0.0915	0.0400
r_G	0.8344	0.8599	0.9840	0.9857
$r_{M,I}$	0.7652	0.6553	0.8014	0.8743
RMSE	0.4180	0.3624	0.1363	0.1013

TABLE 5.3: Truth based and quality index based performance analysis results for the original distorted ISAR image and the super-resolved by BWE, SSVA and CS.

but produce a further sidelobe suppression as in Fig.5.6c and 5.6d. However, CS results are quite similar, whereas BWE returns the worst performance even with respect to the original distorted image.

It is worth noting that $\hat{\delta}_{crg}$ for the original distorted image is quite high because of the Doppler migration, but the measured value for BWE is similar to the theoretical cross-range resolution in Table 5.1 even though the BWE result on scatterer #3 is similar to the original image (compare Fig.5.3b with Fig.5.6b). This is because the BWE result on scatterers #2 and #4 has a sinc-like mainlobe (see Fig.5.6a), whereas scatterers #3 and #5 spread below the −3dB threshold.

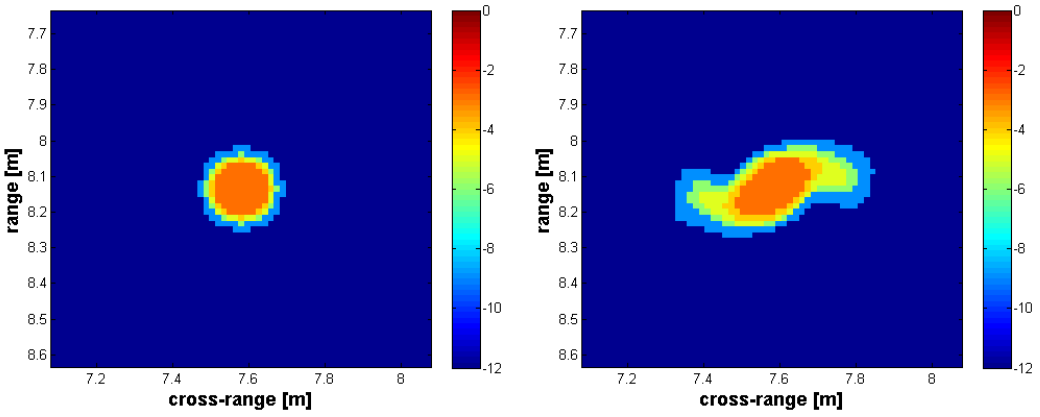

(a) (b)

FIGURE 5.8: Resolution maps for "Truth" (a) and BWE result (b) for amplitude levels −3dB, −4dB, −5dB, −6dB and −9dB.

	TRUTH	**BWE**
$\delta_{crg,3}\vert_{-3\text{dB}}$ [m]	0.1289	0.1862
$\delta_{crg,3}\vert_{-4\text{dB}}$ [m]	0.1576	0.2722
$\delta_{crg,3}\vert_{-5\text{dB}}$ [m]	0.1576	0.3581
$\delta_{crg,3}\vert_{-6\text{dB}}$ [m]	0.1862	0.4154
$\delta_{crg,3}\vert_{-9\text{dB}}$ [m]	0.2149	0.4870

TABLE 5.4: Measured cross-range resolution for scatterer #3 in both "truth" and BWE for different thresholds.

To confirm this, consider the "resolution map" for the "truth" in Fig.5.8a and BWE in Fig.5.8b where the image amplitude levels at -3dB, -4dB, -5dB, -6dB and -9dB with respect to the maximum image peak are shown zoomed on scatterer #3. $\hat{\delta}_{rng}$ and $\hat{\delta}_{crg}$ in Table 5.3 are calculated by measuring the -3dB map width and height for each scatterer and then calculating the mean value. By considering only scatterer #3 and the resolution maps depicted in Fig.5.8, the measured cross-range resolution values for both "truth" and BWE are shown in Table 5.4, which highlights that the cross-range resolution in the BWE image increases much faster than the cross-range resolution in the "truth" as the threshold decreases.

In the BWE image, the same values of cross-range resolution are measured for scatterer #5, whereas scatterers #2 and #4 return lower resolution and have more sinc-like shape (see Fig.5.6a). Furthermore, scatterer #1 is located on the image focusing center and is about sinc-like for all the images. In particular

$$\underline{\delta}_{crg}\big|_{-3\text{dB}} = [0.1289\,,\ 0.1432\,,\ 0.1862\,,\ 0.1432\,,\ 0.1862] \tag{5.20}$$

This is why the measured mean cross-range resolution for BWE is comparable with the theoretical resolution even if the super-resolved image is distorted. The measured mean range resolution is instead almost the same in all cases. SSVA and CS return slightly better results.

Scatterer position based comparison algorithm (Section 4.2.1) does not return significant results in terms of missed detection and false alarms, but the RRMSE index is considerably lower when using CS rather than the other techniques. RRMSE results are validated in Fig.5.9, where the estimated amplitudes in the original image and in the super-resolution results are plotted and compared with the "truth" amplitude (the dotted black plot). The Relative Square Error plots for the original high-resolution image, BWE, SSVA and CS are instead plotted in blue, cyan, green and red respectively in Fig.5.9b. Results in Fig.5.9 highlight that BWE, SSVA and CS progressively correct the amplitude errors caused by the bistatic distortion and Compressed Sensing allows for the best distortion mitigation in terms of amplitude correction.

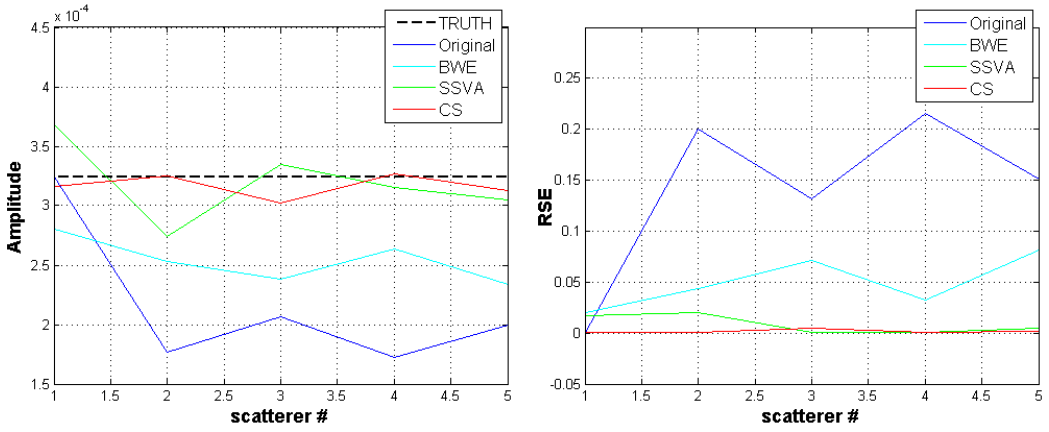

(a) (b)

FIGURE 5.9: Estimated scatterer amplitude in the original high-resolution image, BWE, SSVA and CS compared with the "truth" (a) and relative RSE plots (b).

Global cross-correlation (r_G in (4.22)), Root Mean Square Error (RMSE in (4.23)) and intensity mean mobile cross-correlation ($r_{M,I}$ in (4.47)) in Table 5.3 give better results for Compressed Sensing too with respect to the other images.

The results shown above are obtained in the case of images only affected by bistatic distortion. In the following, super-resolution performance is further evaluated after corrupting the simulated signal with additive white Gaussian noise and the images under test are compared by varying the signal to noise ratio from -40 to 40dB. Image contrast, image entropy, global and mean mobile cross-correlation, RMSE and amplitude estimation Relative Root Mean Square Error results are plotted in Fig.5.10.

The IC and IE trends in Fig.5.10a and 5.10b respectively are not so significant. From -40 up to 20dB SNR, IC and IE in the four images under test are quite similar. When SNR $>$ 20dB, IC and IE for SSVA and CS increase with respect to the original distorted image and BWE. Global cross-correlation for the original image, BWE, SSVA and CS in Fig.5.10c are similar up to -10dB SNR. Then, the values for SSVA and CS depart from the others. r_G for the original high-resolution image saturates at about 0.8 for values of the SNR above 10dB, whereas it approaches 1 for SSVA and CS. BWE returns intermediate results up to 0.9 for SNR $=$ 40dB. r_M for low SNR (Fig.5.10d) is about the same for all the images. However, for high SNR, r_M for CS increases with respect to the others, whereas r_M for BWE is always the smallest one.

RMSE for SSVA and CS in Fig.5.10e are always lower with respect to BWE and the original image. If SNR $>$ 10dB, the original image RMSE saturates at about 0.4, whereas for BWE, SSVA and CS keeps decreasing as the SNR increases. RMSE for SSVA is almost always the smallest one, but it saturates at about 0.15 for SNR $>$ 20dB, whereas RMSE for CS continues decreasing. BWE returns similar RMSE values with respect to the

original distorted image up to SNR = 20dB. The RMSE decreases also for high values of the SNR but does not reach the values obtained with SSVA and CS. The amplitude estimation error in Fig.5.10f decrease for SNR from −40 up to −10dB, then saturate at about 0.4 for the original image, 0.1 for SSVA and 0.04 for CS, whereas keeps decreasing for BWE.

In general, BWE, SSVA and CS results are almost the same in terms of image contrast, image entropy, global and mean mobile cross-correlation for low SNR. As SNR increase, CS and SSVA performance increase with respect to BWE. RMSE performance indicators for SSVA and CS are instead comparable and better than BWE for all the tested SNR levels. SSVA returns even better performance with respect to CS for SNR $\leq$ 20dB. Amplitude estimation RRMSE returns better performance for CS for every SNR value. SSVA is still comparable, whereas BWE has the worst performance index but still improved with respect to the original distorted image.

In conclusion, without considering additive noise, in this simulated case BWE allows to mitigate quadratic distortions due to Doppler migration (compare Fig.5.3a with Fig.5.6a), but range migration is almost restored even though the image PSF after CPI reduction in Fig.5.4b is almost sinc-like (compare Fig.5.3b with Fig.5.6b). As a confirmation, it is worth comparing the results in Fig.5.9a where the estimated amplitudes for BWE (in cyan) approach the blue line of the original image in correspondence of scatterers #3 and #5 where range migration occurs, and depart for scatterers #2 and #4 where only Doppler migration occurs.

In general, SSVA has better performance with respect to BWE and is comparable with CS. Both SSVA and CS allow for the cross-range resolution to be restored and mitigate both range and Doppler distortions. SSVA allows for a further sidelobe suppression and, as a consequence, higher image contrast, entropy and SNR. Compressed Sensing allows for better image reconstruction and distortion mitigation, especially in terms of amplitude estimation in both noisy and non-noisy cases as in Fig.5.9a and 5.10f. Furthermore, CS allows to have a sinc-like output PSF and much better amplitude estimation if only Doppler migration occurs (compare Fig.5.6e with Fig.5.6f). Such a consideration is validated in Fig.5.11 where the RSE is plotted for only Compressed Sensing and much lower Relative Square Error values are highlighted for scatterers #2 and #4, where only Doppler migration occurs, with respect to #3 and #5.

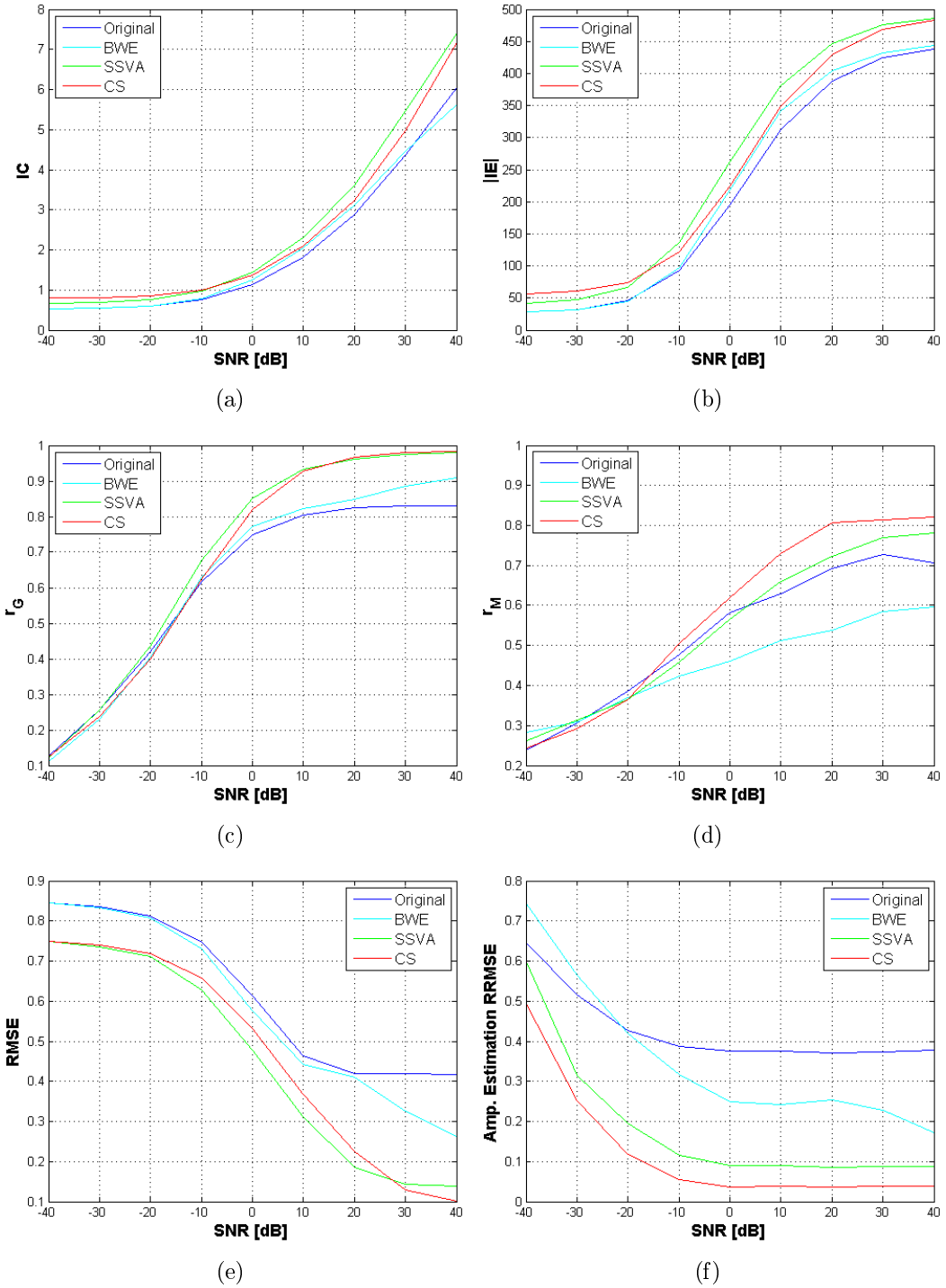

FIGURE 5.10: Performance analysis results for SNR from −40 to 40dB: image contrast (a), image entropy (b), global cross-correlation (c), mean mobile cross-correlation (d), RMSE (e) and amplitude estimation RRMSE (f).

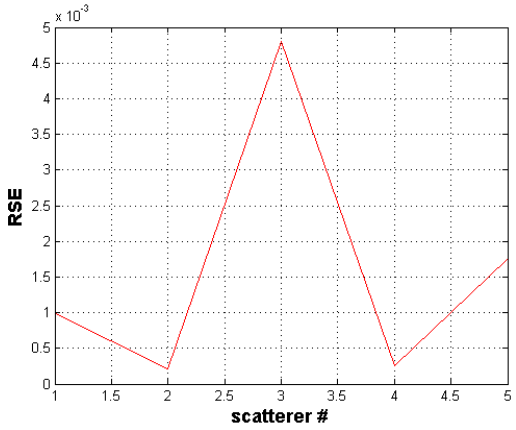

FIGURE 5.11: RSE for Compressed Sensing.

5.3 Super-resolution on bistatic real data

In this Section the super-resolution techniques mentioned in this Chapter are applied on real bistatic data and successively analyzed by means of the performance analysis approaches proposed in Chapter 4. Such real data were acquired during the NATO SET-196 trials from September 29th to October 3rd, 2014. The trials were hosted by the Istituto Vallauri of the Italian Navy located in Livorno, which provided the logistic supports. During the trials, cooperative vessels and small boats where navigating in front of the Naval Academy and ultralight aircrafts were flying above them, while active and passive radar sensors, operating in different frequency bands, were simultaneously illuminating the scene from different locations. Real data used in this Thesis have been acquired by means of two HABRA Radar systems jointly designed by Metasensing BV and CNIT (the HABRA1 Radar as receiver and HABRA2 as transmitter) during the second trials day. In order to provide external data for system performance evaluation, two differential Global Positioning System (GPS) receivers were installed on-board two cooperative targets. The Radar system and the acquisition scenario are described in Section 5.3.1. In Section 5.3.3 the resultant Range-Doppler map and ISAR image are shown and the measured data is analyzed in order to estimate the effective rotation vector and evaluate bistatic distortions. Super-resolution results are shown in Section 5.3.4, whereas in Section 5.3.5 such results are analyzed and compared by means of the performance analysis methods proposed in Chapter 4.

5.3.1 Scenario description

The acquisition scenario is depicted in Fig.5.12 and 5.13 where transmitter (HABRA 2) and receiver (HABRA 1) position, radar antenna beams and target trajectory are shown. Radars are placed in two different sites in the Naval Academy of Livorno at coordinates 43.5248° latitude, 10.3091° longitude, 12m altitude (HABRA 1) and 43.5265° latitude, 10.3093° longitude, 22m altitude (HABRA 2). The bistatic baseline is 183m.

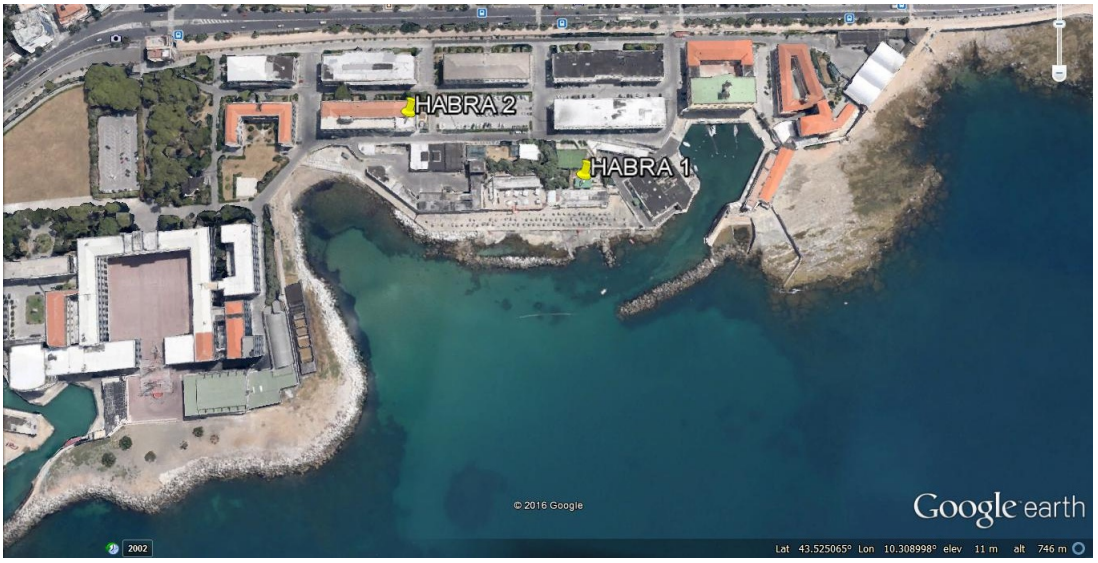

FIGURE 5.12: NATO SET-196 trials scenario (picture 1).

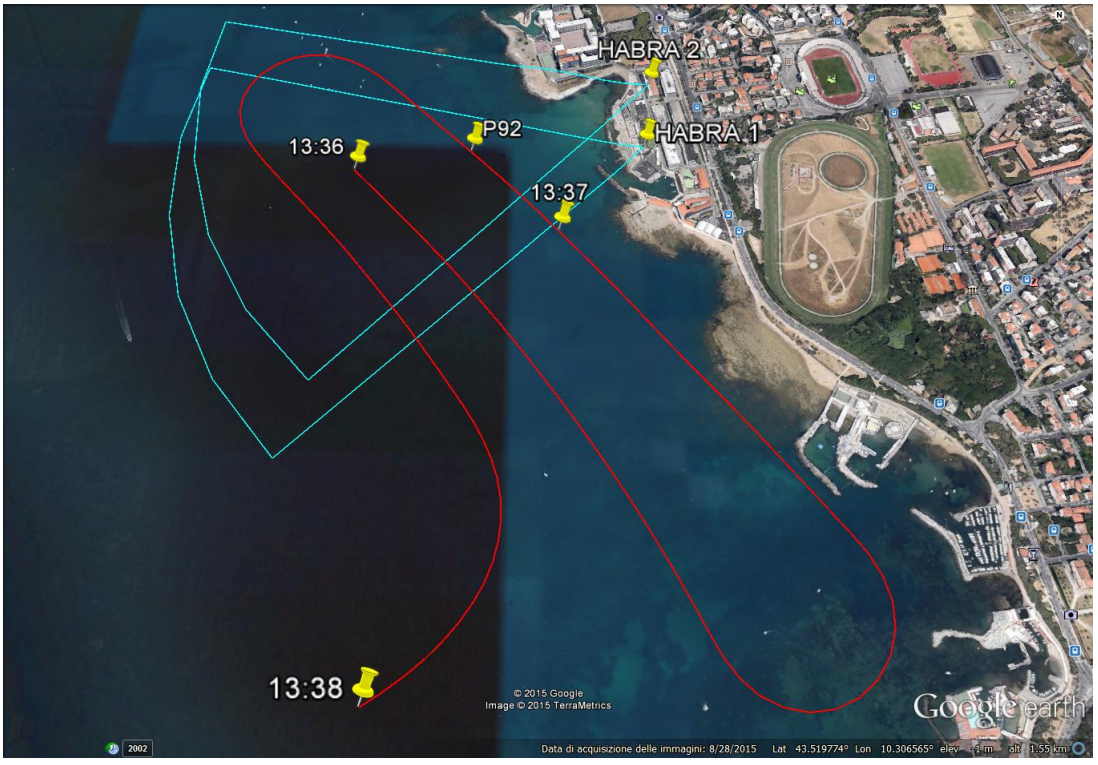

FIGURE 5.13: NATO SET-196 trials scenario (picture 2).

Transmitted Signal Waveform	Linear-FMCW
Image Processing Algorithm	RD
Sample Type (ADC output)	Real
Transmitted Power	37 dBm
Radar Frequency	9.6 GHz
Frequency Bandwidth	300 MHz
Pulse Repetition Frequency	1.223 kHz
ADC Sampling Frequency	10 MHz
Samples per Sweep	8176
Antenna Type	Microstrip
Polarization	V-Linear
Antenna Gain	13 dB
Azimuth −3dB antenna beamwidth	60 deg
Elevation −3dB antenna beamwidth	20 deg
Side Lobe Level	−13 dB

TABLE 5.5: HABRA Radar system settings.

The HABRA system is a X-band multichannel ground-based coherent FMCW radar that transmits a vertically polarized waveform. The system consists of a cabinet containing the radar transceiver hardware and four antennas that can be moved along a rectangular frame. This frame is composed of three receiving and one transmitting flat panels. The receivers lie on a horizontal and a vertical baseline as shown in Fig.5.14. The antenna on the top right corner is used as transmitter, whereas the ones forming the L-shape on the left bottom corner are receivers. Such a transmitter/receivers configuration is set-up for 3D-InISAR purposes which is not treated in this Thesis. Details about 3D-InISAR can be found in [13, 70]. In this Thesis only the receiver 0 (on the left bottom corner in Fig.5.14a) is exploited and the received signal is used to produce Range-Doppler maps by means of the RD imaging technique. Radar settings are summarized in Table 5.5.

5.3.2 Position and attitude system

During the trials, some cooperative vessels and aircrafts were equipped with two GPS and Inertial Measurement Unit (IMU) systems provided by the Defence Science and Technology Organisation (DSTO), Australia, and the Council for Scientific and Industrial Research (CSIR), South Africa. Such system is the Advanced Navigation Spatial Dual shown in Fig.5.15. The Spatial Dual system combines temperature calibrated accelerometers, gyroscopes, magnetometers and a pressure sensor with a dual antenna Real Time Kinematic (RTK) GNSS receiver. It allows to measure GPS position, velocity, acceleration, Euler angles and angular velocity and can be exploited to estimate the target effective rotation vector. Latitude, longitude and height are measured with respect to the WGS84 reference ellipsoid. Velocities and relative positions are provided with respect to

(a)

(b)

FIGURE 5.14: HABRA system: (a) frame of the antennas; (b) cabinet and frame installed on a lifting structure.

the NED (North East Down) co-ordinate frame. When a GNSS fix is available Spatial Dual's time is accurate to within 50 nanoseconds.

FIGURE 5.15: Advanced Navigation Spatial Dual system.

5.3.3 Acquired data and distortion analysis

The radar data was acquired starting at 13:36:23 (UTC time) the September 30th, 2014 and the measured data is organized in frames of 1223 sweeps (CPI = $1s$) without time skip or overlap between frames. In this case, the 43th frame between 42 and 43 seconds after the acquisition start is considered (from 13:37:05 to 13:37:06). The measured data is then processed by means of the RD imaging technique and the resultant Range-Doppler map is shown in Fig.5.16. In particular, the Range-Doppler map in Fig.5.16 is range gated from 200 to 1600m when the maximum available range distance is

$$R_{\max} = \frac{cf_s}{4B\,\mathrm{PRF}} = 2044 \text{ [m]} \tag{5.21}$$

where f_s is the ADC sampling frequency (see Table 5.5). This is because, in case of Linear-FMCW signal, the beat frequency

$$f_b = \frac{B}{T_{\mathrm{SW}}}\tau \simeq B\,\mathrm{PRF}\,\tau \tag{5.22}$$

where T_{SW} is the FMCW waveform duration and its maximum is

$$f_{b,\max} = B\,\mathrm{PRF}\,\frac{2R_{\max}}{c} \tag{5.23}$$

For the Nyquist sampling theorem, the maximum measurable beat frequency must be not greater than the half of the sampling frequency, i.e., $f_{b,\max} = f_s/2$ and the (5.23) implies the (5.21). On the other hand, the maximum non-ambiguous radial speed is

$$v_{R,\max} = \frac{c}{2f_0}f_{d,\max} = \frac{c}{2f_0}\frac{\mathrm{PRF}}{2} = 9.56 \text{ [m/s]} \tag{5.24}$$

where $f_{d,\max} = \mathrm{PRF}/2 = 611.5460\mathrm{Hz}$ is the maximum non-ambiguous Doppler frequency. A lot of targets can be observed in the Range-Doppler map in Fig.5.16, but they appear strongly defocused because of the too long CPI. The target highlighted in the red box in Fig.5.16 is then chosen and cropped from the whole Range-Doppler map. Such a crop is shown in Fig.5.17a and its relative range profile in the range/slow-time domain in Fig.5.17b where the slow-time axis is expressed in seconds of the UTC time. After preliminary data analysis, it has been decided to reduce the CPI and retain the portion of the range profile from $t = 5.6$ to 6s as highlighted in Fig.5.17b. The cropped portion is then given as input to the Image Contrast Based Autofocusing (ICBA) algorithm in order to obtain a well focused ISAR image. ICBA is a parametric autofocusing technique which aims to estimate the target radial velocity and acceleration and approximate the radial Radar-Target distance $R_0(n)$ by its second order Taylor-Maclaurin polynomial in order to compensate it. ICBA is not argument of this Thesis and not further treated. For details the reader is referred to [22].

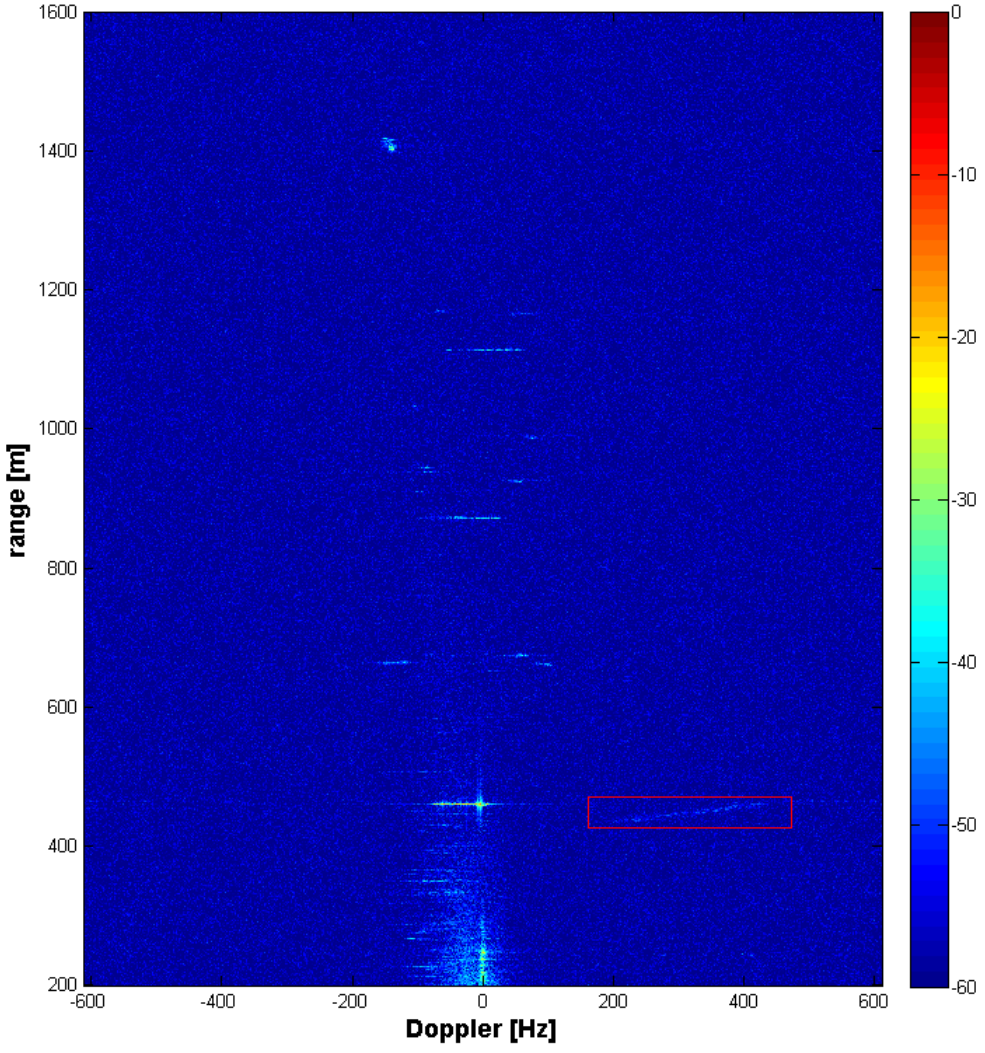

FIGURE 5.16: 43th frame Range-Doppler map (from 13:37:05 to 13:37:06 UTC).

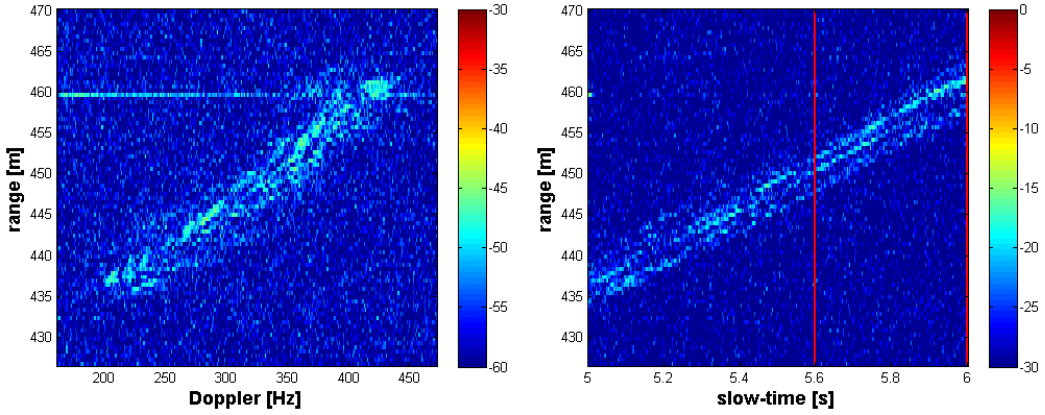

(a) (b)

FIGURE 5.17: Cropped Range-Doppler map (a) and relative range profile (b).

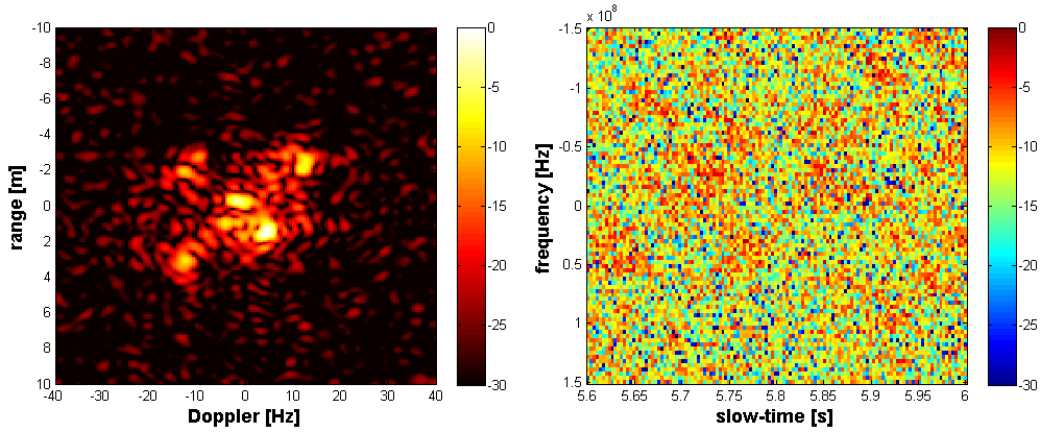

(a) (b)

FIGURE 5.18: Refocused ISAR image (a) and relative frequency/slow-time complex signal (b).

FIGURE 5.19: Tecnam P92 picture.

The result of the ICBA algorithm is shown in Fig.5.18a and is clearly the ISAR image of a small aircraft. The relative complex signal in the frequency/slow-time domain is shown in Fig.5.18b. The ISAR image in Fig.5.18a and all the following in this Section are shown after a 5x zero-padding and in dB scale for illustration purposes.

The target of interest is the Tecnam P92 provided by the Pisa Aero Club and depicted in Fig.5.19. The measured trajectory from 13:36:00 till 13:38:00 UTC is shown in Fig.5.13. Such a trajectory was acquired by means of the Spatial Dual system provided by the CSIR and installed on the aircraft. The aircraft position at 13:37:05.8, which is the UTC time relative to the central sweep of the time window highlighted in Fig.5.17b, is pointed by the "P92" yellow pin in Fig.5.13.

Some geometrical parameters calculated by means of the GPS installed on the aircraft are plotted in Fig.5.21. The GPS allows to measure the target position expressed in latitude, longitude and altitude every 0.05 seconds. Such results can be converted in meters in a Cartesian reference system centered on the transmitter (HABRA2) where the y-axis points the north direction. The target flightpath is plotted in red in Fig.5.21a from 13:37:00 to 13:37:10 UTC, whereas its position during the CPI is drawn in blue. Transmitter, receiver and BEM positions are highlighted too in blue, red and green respectively. The knowledge of transmitter, receiver and target position allows the calculation of the bistatic angle and the bistatic distortion term $K(n)$. Bistatic angle $\beta(n)$ and $K(n)$ are plotted in Fig.5.21c and 5.21d respectively from 13:37:00 to 13:37:10 UTC with the measured values within the CPI highlighted in blue. Such a results allow for the distortion parameters to be calculated as in (2.51) with the following results

$$K_0 = 9.8096 \cdot 10^{-1} \tag{5.25}$$

$$K_1 = -5.6149 \cdot 10^{-4} \tag{5.26}$$

$$K_2 = 1.0541 \cdot 10^{-3} \tag{5.27}$$

In order to evaluate range e Doppler migration, the CLEAN technique is applied to the ISAR image in Fig.5.18a and the scatter-plot of the detected scatterers is shown in Fig.5.20. By analyzing the CLEAN result in Fig.5.20, it appears that the maximum range distance from the focusing center $z_{2,\max} = 3.814$m, whereas the maximum Doppler frequency $\nu_{\max} = 13.75$Hz. The range migration parameter can then be calculated as follows (see (2.85))

$$\Delta_{rng} = \left| K_1 z_{2,\max} + K_0 \frac{c}{2f_0} \nu_{\max} \right| T_{ob} = 0.0834 < \delta_{rng} = 0.5 \tag{5.28}$$

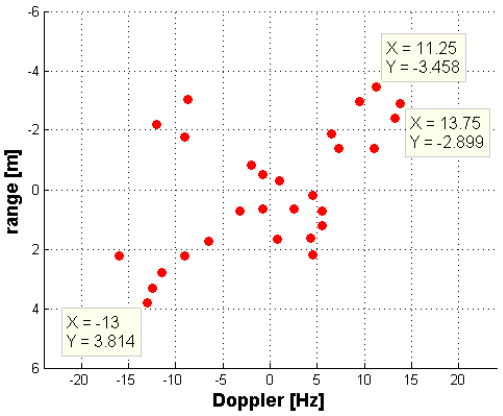

FIGURE 5.20: CLEAN output on the focused ISAR image.

Therefore, it can be stated that there is not range migration in the produced ISAR image. Furthermore, by considering the Doppler linear distortion term Δ_ν defined in (2.73)

$$|\Delta_\nu| = \frac{2f_0}{c} K_1 z_{2,\max} = 0.1371 \text{ Hz} < \delta_\nu = \frac{1}{T_{ob}} = 2.5 \text{ Hz} \tag{5.29}$$

it can also be stated that linear distortion does not occur either.

Measured target speed is plotted in meters per second in Fig.5.21e, whereas Fig.5.21f shows the calculated effective bistatic rotation vector module. The bistatic effective rotation vector is calculated as follows

$$\mathbf{\Omega}_{Bi,eff}(n) = \frac{(\mathbf{i}_{LoSTX}(n) \times \mathbf{\Omega}_{TX}(n)) + (\mathbf{i}_{LoSRX}(n) \times \mathbf{\Omega}_{RX}(n))}{2K(n)} \times \mathbf{i}_{LoSBi}(n) \tag{5.30}$$

where

$$\mathbf{\Omega}_{TX}(n) = \mathbf{\Omega}_A(n) + \mathbf{\Omega}_{t,TX}(n) \tag{5.31}$$

$$\mathbf{\Omega}_{RX}(n) = \mathbf{\Omega}_A(n) + \mathbf{\Omega}_{t,RX}(n) \tag{5.32}$$

$$\mathbf{\Omega}_{t,TX}(n) = \frac{\mathbf{v}(n) \times \mathbf{i}_{LoSTX}(n)}{R_{TxTg,0}(n)} \tag{5.33}$$

$$\mathbf{\Omega}_{t,RX}(n) = \frac{\mathbf{v}(n) \times \mathbf{i}_{LoSRX}(n)}{R_{RxTg,0}(n)} \tag{5.34}$$

$\mathbf{\Omega}_A(n)$ in (5.31) and (5.32) is the rotation vector caused by the target angular velocity measured by the GPS, $\mathbf{\Omega}_{t,TX}$ is the rotation vector due to the target translation with respect to the transmitter and $\mathbf{\Omega}_{t,TX}$ with respect to the receiver. By calculating the mean effective rotation vector within the CPI, the following result is obtained

$$\Omega_{Bi,eff,1} = 0.0758 \text{ [rad/s]} \tag{5.35}$$

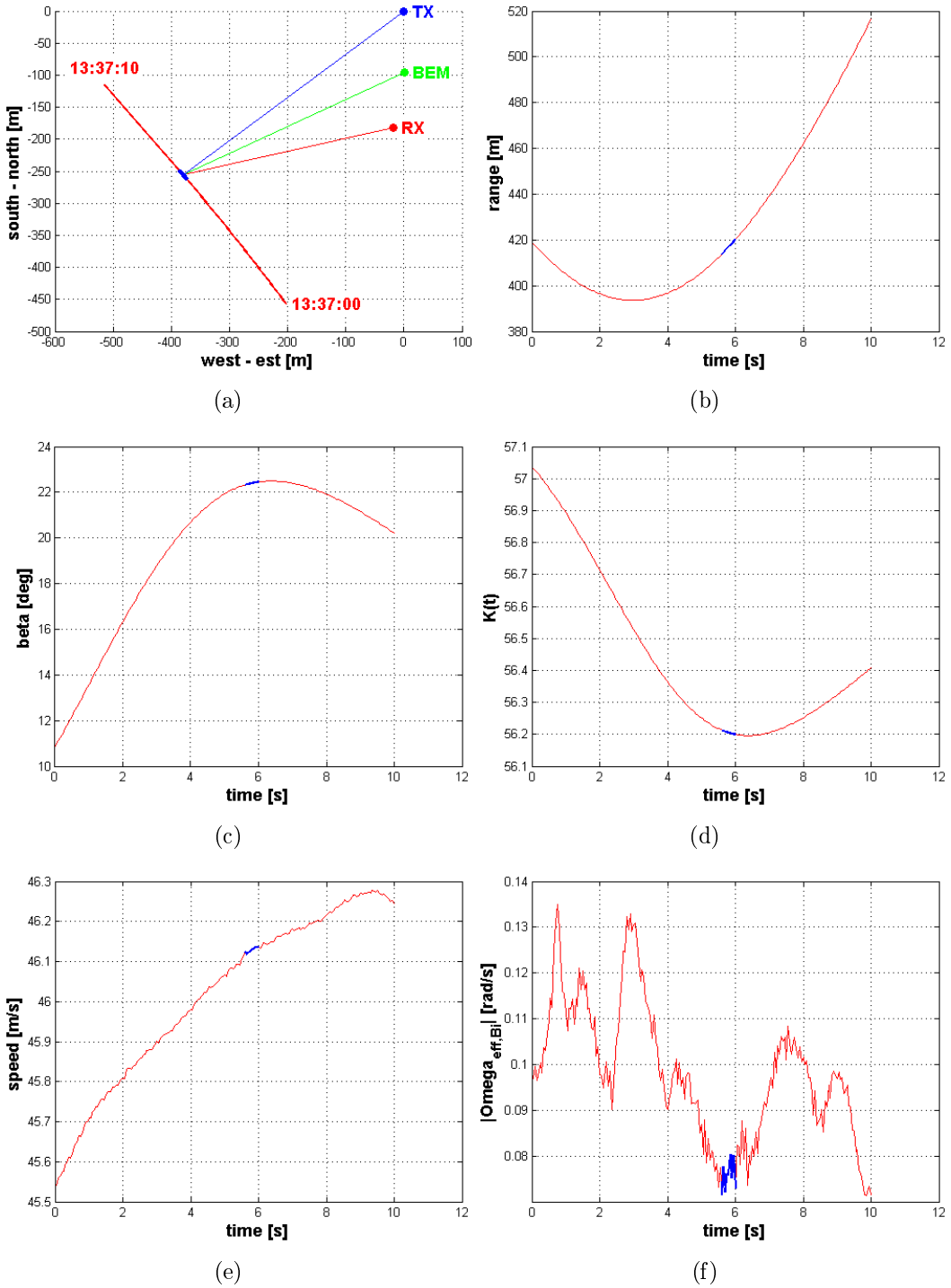

(a) (b) (c) (d) (e) (f)

FIGURE 5.21: P92 experiment: scenario in cartesian reference system (a), equivalent target range (b), bistatic angle (c), bistatic distortion parameter $K(t)$ (d), target speed (e), measured bistatic effective rotation angular speed (f).

Ω [rad/s]	$z_{1,\max}$ [m]	Δ_{crg} [m]	δ_{crg} [m]
$\Omega_{Bi,eff,1} = 0.0758$	2.8344	0.0935	0.5153
$\Omega_{Bi,eff,2} = 0.0823$	2.6105	0.1048	0.4746
$\Omega_{Bi,eff,3} = 0.0875$	2.4554	0.1137	0.4464

TABLE 5.6: Maximum cross-range distance, Doppler migration parameter and cross-range resolution for all the calculated $\Omega_{Bi,eff}$.

If the 3D-InISAR is applied, the estimated effective rotation vector is

$$\Omega_{Bi,eff,2} = 0.0823 \text{ [rad/s]} \tag{5.36}$$

whereas, if we suppose the ISAR image in Fig.5.18a as a top view and exploit the knowledge of the aircraft wingspan equal to 8.70m[1], if $\Delta_{z_2} = 3.814 + 3.458 = 7.272$m (see Fig.5.20) is the range distance between the wings extremity, then the distance in cross-range will be

$$\Delta_{z_1} = \sqrt{\text{Wingspan}^2 - \Delta_{z_2}^2} = 4.7758 \text{ [m]} \tag{5.37}$$

and

$$\Omega_{Bi,eff,3} = \frac{c}{2f_0}\frac{\Delta_{f_d}}{\Delta_{z_1}} = 0.0875 \text{ [rad/s]} \tag{5.38}$$

where $\Delta_{f_d} = 13.75 + 13 = 26.75$Hz (see Fig.5.20) is the Doppler distance between the wings extremity. Therefore, by considering the definition in (2.64), the Doppler migration parameter is calculated as follows

$$\Delta_{crg} = \left| \frac{K_2 z_{2,\max}}{\Omega} + 2K_1 z_{1,\max} - K_0 z_{2,\max}\Omega \right| T_{ob} \tag{5.39}$$

where $z_{1,\max}$ is the maximum cross-range distance from the focusing center. The values of Δ_{crg} and δ_{crg} for the three effective rotation vector modules in (5.35), (5.36) and (5.38) are reported in Table 5.6. As shown in Table 5.6, $\Delta_{crg} < \delta_{crg}$ for all the three cases and Doppler migration does not occur.

In general, the distance between the scatterers at the wings extremities in the ISAR image is less than or equal to the aircraft wingspan, because it cannot be stated whether the image is or is not a top view. The target orientation is measured by the GPS system, but the IPP depends on the effective rotation vector which is wanted to be estimated. As a consequence

$$\Delta_{z_1} = \frac{c}{2f_0\Omega_{Bi,eff}}\Delta_{f_d} \leq \sqrt{\text{Wingspan}^2 - \Delta_{z_2}^2} \Rightarrow \Omega_{Bi,eff} \geq \frac{c}{2f_0}\frac{\Delta_{f_d}}{\sqrt{\text{Wingspan}^2 - \Delta_{z_2}^2}} \tag{5.40}$$

and $\Omega_{Bi,eff,3}$ is actually a lower bound for the effective rotation vector.

[1] By https://en.wikipedia.org/wiki/Tecnam_P92

5.3.4 Super-resolution results

As in Section 4.4, the frequency/slow-time support of the full resolution ISAR image in Fig.5.18 is reduced in order to generate the low-resolution image. By setting $K_f = K_t = 2$, the central

$$M_{low} = \left\lfloor \frac{M}{K_f} \right\rfloor \quad \times \quad N_{low} = \left\lfloor \frac{N}{K_t} \right\rfloor$$

portion of the complex signal in Fig.5.18b is retained as shown in Fig.5.22b and the obtained low-resolution image is shown in Fig.5.22a.

The low-resolution ISAR image in Fig.5.22a is given as input to the super-resolution techniques under test. The results of BWE, Capon's MVM, APES, SSVA and CS are shown in Fig.5.23 (ISAR images) and 5.24 (complex signals).

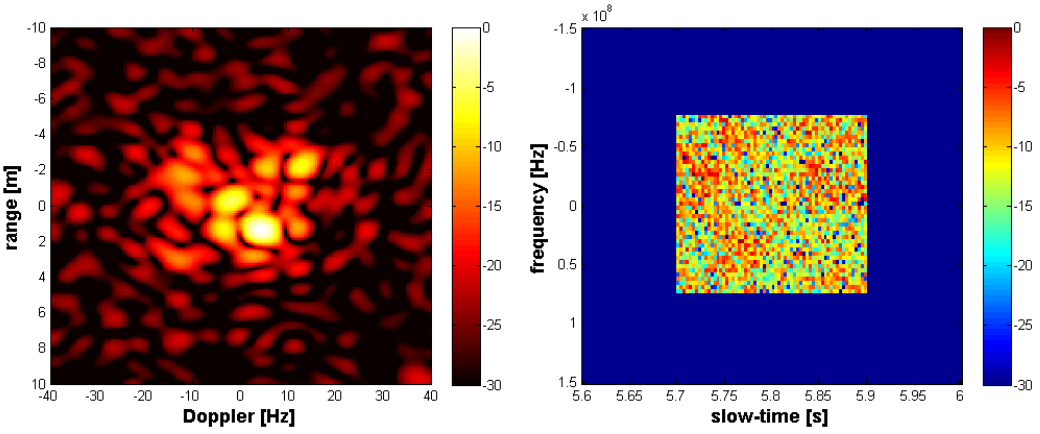

(a) (b)

FIGURE 5.22: Low-resolution ISAR image (a) and relative frequency/slow-time complex signal (b).

As in Section 4.4, Linear Prediction based Bandwidth Extrapolation (BWE) is the first technique performed. Frequency bandwidth extrapolation and Aperture extrapolation are performed separately on the complex signal in Fig.5.22b and the AR model order p_{AR} is set as $M_{low}/3$ for the vertical (frequency) extrapolation and $N_{low}/3$ for the horizontal (slow-time). The linear-prediction model coefficients are estimated by means of the Burg's algorithm and the obtained ISAR image in shown in Fig.5.23b. In this case, BWE does not return a good result: the shape of the aircraft in the ISAR image is not visible and the complex signal is clearly not well extrapolated (compare Fig.5.24b with Fig.5.24a).

For Capon's MVM and APES, the covariance matrix is estimated by means of the forward-backward method without diagonal loading or other regularization methods as in Section 4.4 for the monostatic case. The covariance matrix is estimated by using a 35% subaperture size and the output images are shown in Fig.5.23c and 5.23d respectively.

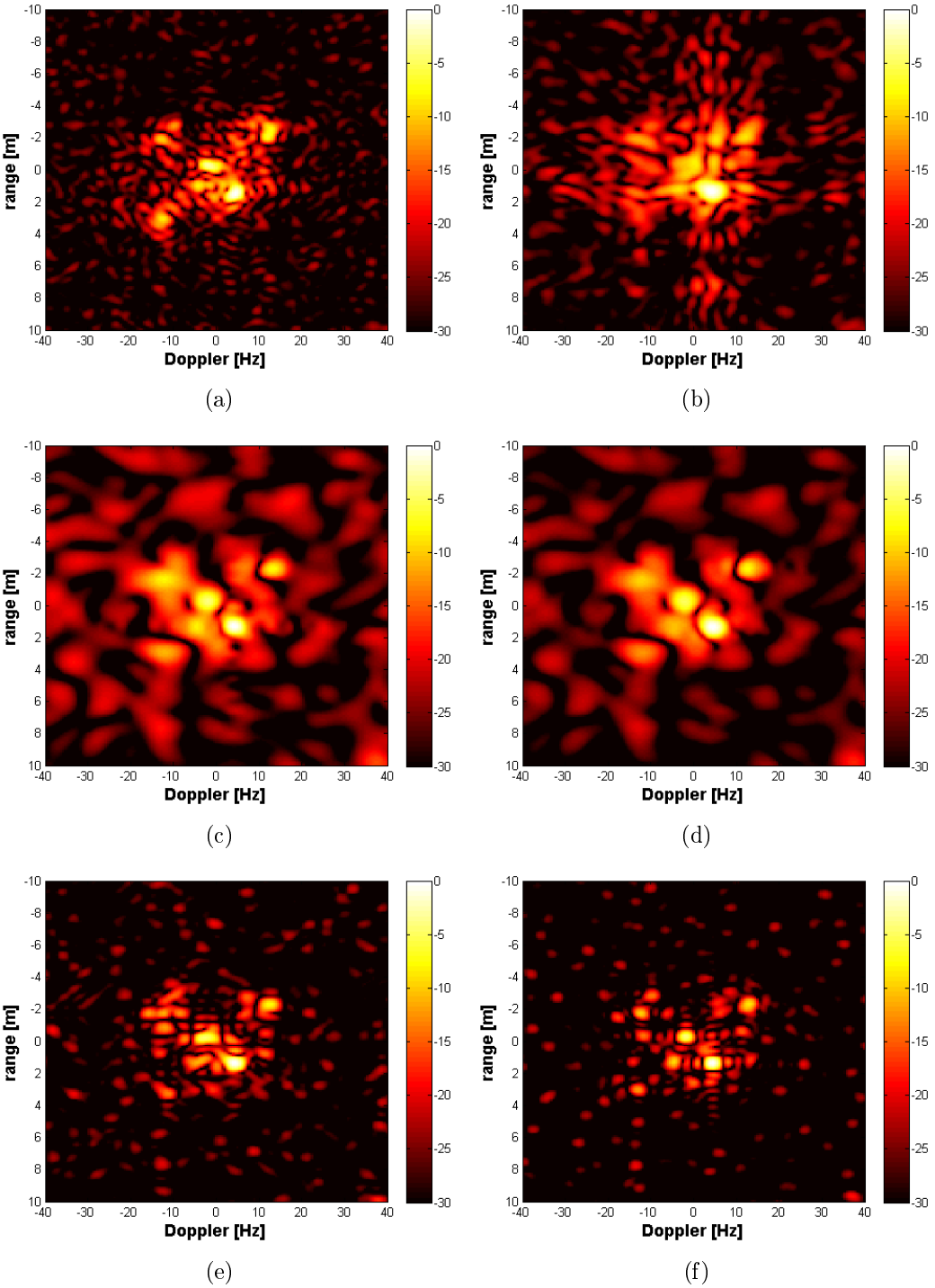

FIGURE 5.23: P92 experiment: original high-resolution ISAR image (a) and super-resolved images by means of BWE (b), Capon's MVM (c), APES (d), SSVA (e) and CS (f).

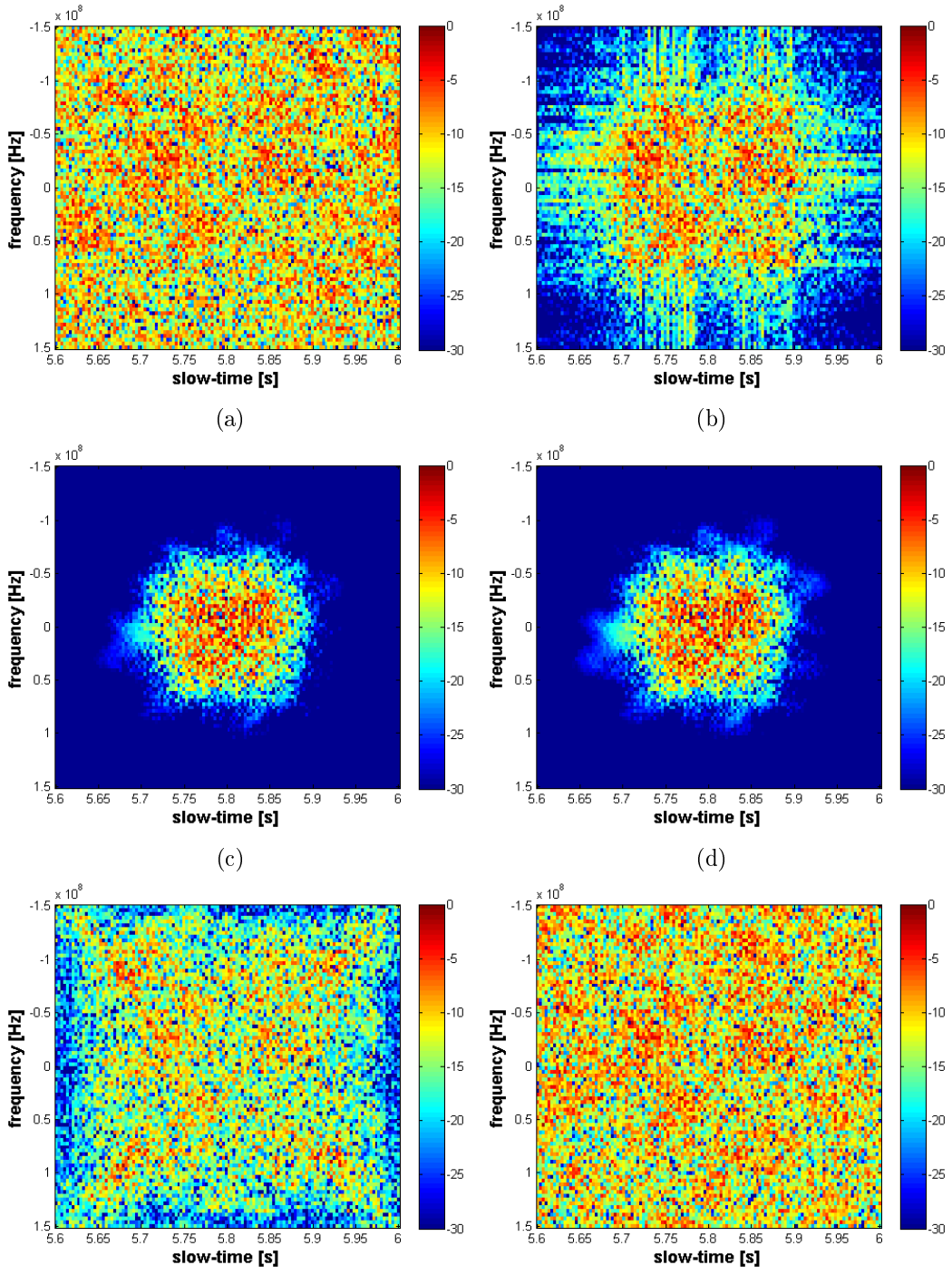

FIGURE 5.24: P92 experiment: original high-resolution complex signal (b) and super-resolution signals by means of BWE (b), Capon's MVM (c), APES (d), SSVA (e) and CS (f).

Such a subaperture size is chosen as a compromise between resolution enhancement and SNR. In these cases the shape of the aircraft in the resultant images can be observed, especially in the APES result in Fig.5.23d. The APES output appears to have higher SNR with respect to MVM, but both techniques are not able to perform a significant resolution enhancement with respect to the input image in Fig.5.22a. Furthermore, as in the monostatic case in Section 4.4, by observing the relative frequency/slow-time complex signals in Fig.5.24c and 5.24d, it appears that MVM and APES does not allow to arbitrarily extrapolate the low-resolution signal.

SSVA is performed as described in Section 3.5 and 4.4. The bandwidth extrapolation factor η is set equal to $2^{1/8}$ (8 SSVA loops) and SVA is performed in "I and Q Separately - Two Dimensions Simultaneously" mode. The result in Fig.5.23e appears to have higher SNR with respect to the BWE, MVM and APES and is comparable with the high-resolution image in Fig.5.23a. Rather than BWE, MVM and APES, range and Doppler resolution are successfully enhanced.

Finally, the SL0 algorithm is performed to obtain the Compressed Sensing super-resolution image in Fig.5.23f. Implementation details can be found in Section 3.6 and 4.4. The σ vector is defined by setting σ_1 as in (4.63), σ_J equal to the noise standard deviation as in (4.64) and the decreasing factor $c_\sigma = 0.6$. In particular, $\sigma_1 = 12.0186$, $\sigma_J = 0.1135$ and $J = 10$. Then the "approximate maximization of $F_\sigma(\mathbf{x})$" is performed in $N_L = 50$ iterations by setting the constant $\mu = 2$. By visual assessment, Compressed Sensing appears to return the "best" result with respect to the other techniques. Image resolution is successfully restored and Image Contrast and SNR are considerably enhanced even with respect to the original high-resolution image. Furthermore, by comparing Fig.5.24f with the other sub-figures in Fig.5.24, it appears that CS allows to reconstruct the original complex signal in Fig.5.24a much better than BWE and SSVA.

The above mentioned super-resolution techniques are then tested when directly applied on the original image too with the same parameters setting described above. The refocused image in Fig.5.18a is given as input to BWE, Capon's MVM, APES, SSVA and CS in order to double both range and Doppler resolution and the resultant super-resolved images are shown in Fig.5.25. In this case, the superiority of Compressed Sensing with respect to the other techniques in terms of resolution enhancement, Image Contrast and SNR is even more evident with respect to the previous case. However, SSVA appears to have a good result too. The SSVA super-resolved image in Fig.5.25e has higher Image Contrast and SNR with respect to BWE, MVM and APES and is comparable with the CS image in Fig.5.25f. The result of APES in Fig.5.25d is similar to the MVM image in Fig.5.25c, but with higher IC and SNR.

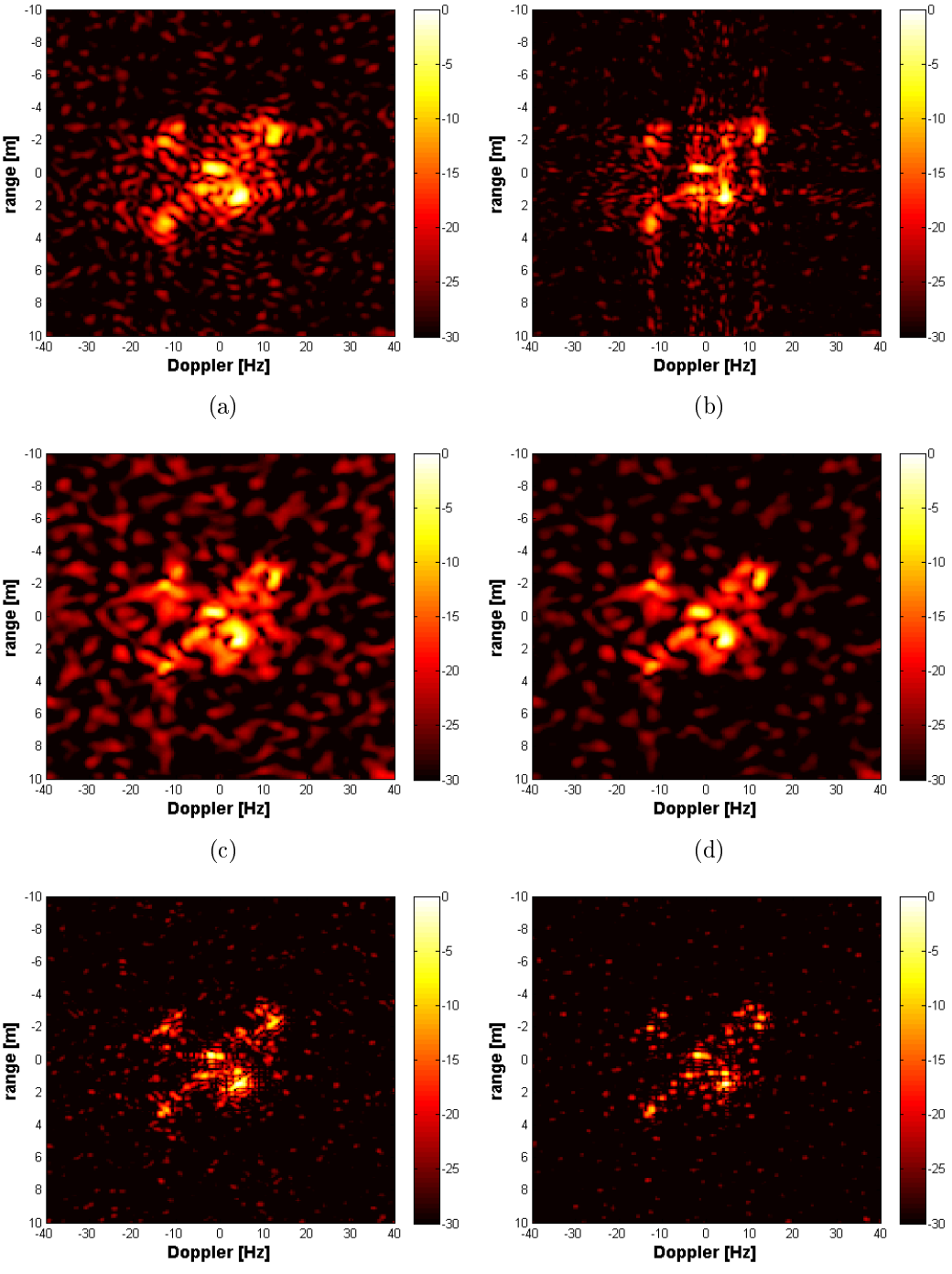

FIGURE 5.25: P92 experiment: original ISAR image (a) and 2x super-resolved images by means of BWE (b), Capon's MVM (c), APES (d), SSVA (e) and CS (f).

5.3.5 Performance analysis

In this Section the performance analysis methods proposed in Chapter 4 are exploited to evaluate and compare the super-resolution results shown above. Truth based algorithms are applied to analyze the results in Fig.5.23 where the reference "truth" is the ISAR image in Fig.5.23a. They cannot be applied to the 2x super-resolved images in Fig.5.25 because there is not any available "truth" they can be compared with. 2x super-resolved images are only analyzed by means of the quality metrics proposed in Section 4.3.

"Truth" and "estimations" in Fig.5.23 are first compared by means of the position based comparison algorithm as in Section 4.2.1 and the resultant scatter-plots with correct detections, missed detections and false alarms marked in green, red and blue respectively are shown in Fig.5.27. As in Section 4.4, the scatterers in the ISAR images under test are detected by means of the CLEAN. The "truth" scatter-plot in Fig.5.27a is obtained by stopping the CLEAN when the residual energy is less than the 50% of the original image energy. The threshold for the monostatic dataset in Section 4.4 is set equal to the 15% of the image energy because of the much higher SNR. Such a high threshold is justified by considering the ISAR image and the scatter-plot shown in Fig.5.26. The ISAR image in Fig.5.26a is the whole refocused high-resolution ISAR image. All the other ISAR images shown in this Section are actually zoomed for illustration purposes. The scatter-plot in Fig.5.26b is the result of the CLEAN on the image in Fig.5.26a and a lot of scatterers outside the actual target can be observed. If a lower threshold were used, much more noise peaks would be detected by the CLEAN but the number of actual target scatterers would not substantially increase. The detected scatterers outside a 12m $\times$ 40Hz box around the zero-range and zero-Doppler are then discarded for all the images under test.

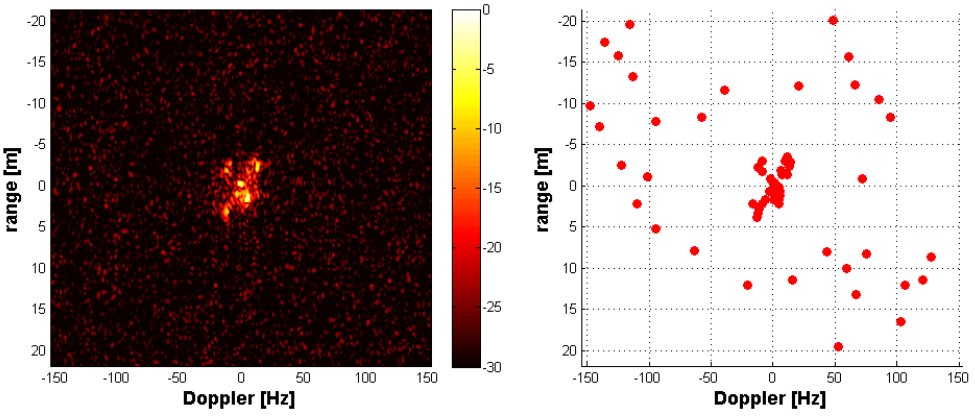

(a) (b)

FIGURE 5.26: Non-zoomed original high-resolution ISAR image (a) and detected scatterers (b).

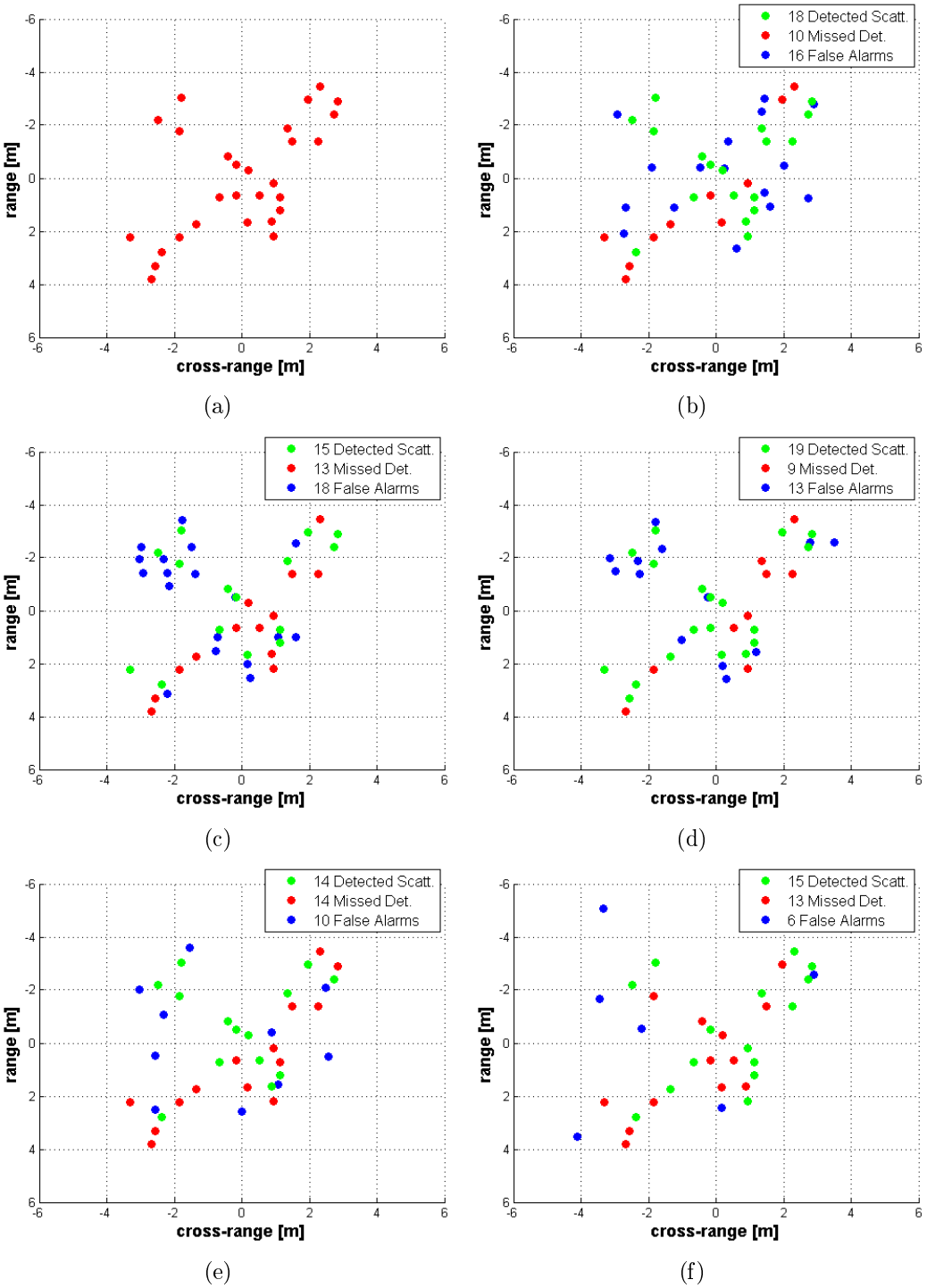

FIGURE 5.27: P92 experiment: detected scatterers in the original high-resolution ISAR image (a) and results of the scatterer position based comparison algorithm for BWE (b), Capon's MVM (c), APES (d), SSVA (e) and CS (f).

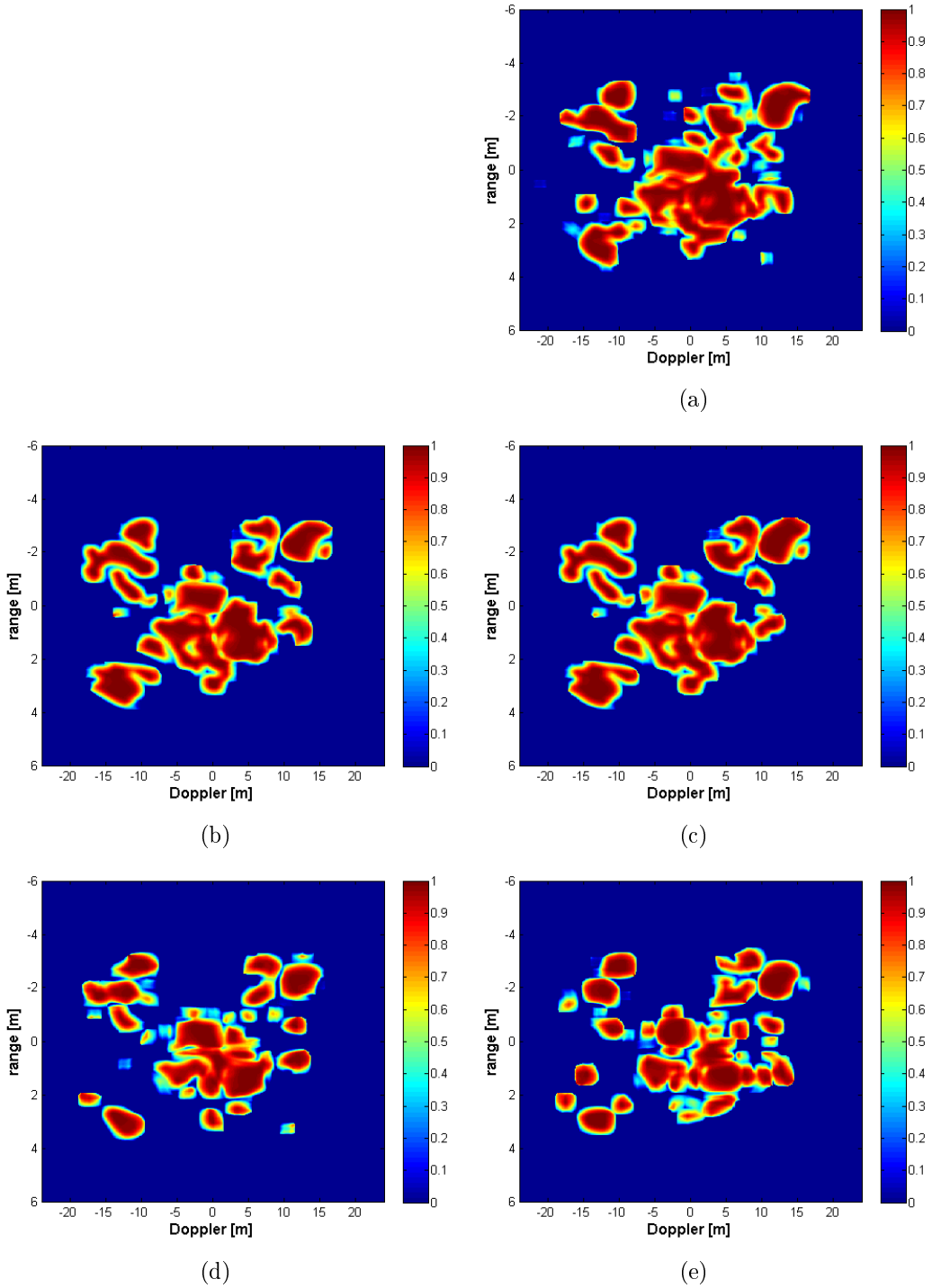

FIGURE 5.28: P92 experiment: results of the mobile cross-correlation based comparison algorithm for BWE (a), Capon's MVM (b), APES (c), SSVA (d) and CS (e).

	NoS	Correct Det.	Missed Det.	False Alarms	RRMSE
High-Res.	28	-	-	-	-
BWE	34	18	10	16	0.4356
MVM	33	15	13	18	0.5508
APES	32	19	9	13	0.5994
SSVA	24	14	14	10	0.5271
CS	21	15	13	6	0.4297

TABLE 5.7: P92 experiment: numerical results of the Scatterer Position based comparison method.

As in Section 4.4, the CLEAN is performed after applying a 10× zero-padding on the images under test and set to stop when the measured peak amplitude is lower than the 95% of the weakest detected scatterer in the "truth" when applied on the super-resolved images in Fig.5.23b to 5.23f. The comparison algorithm is performed by setting $\Omega_{Bi,eff} = \Omega_{Bi,eff,1}$, which implies $\delta_{crg} = 0.5153$m (see Table 5.6). Furthermore, every image is preliminarily normalized with respect to its own norm.

By observing the results in Fig.5.27, it appears that APES has the best performance in terms of correctly detected scatterers, whereas the worst case is the SSVA result where the half of the scatterers are missed. In terms of artifacts introduced, the worst case is the Capon's MVM where a lot of scatterers are lost too. Compressed Sensing returns the smallest number of false alarms, but a lot of scatterers are missing. This is also because a small number of peaks are detected with respect to the other cases. On the contrary, BWE returns good results in terms of correct detections, but a lot of artifacts are introduced because of a large number of detected peaks.

The RRMSE for the scatterers amplitude estimation (see (4.37)) are summarized in Table 5.7 with together the number of detected scatterers (NoS), correct detections, missed detections and false alarms. By comparing the results in Table 5.7 with the results for the monostatic dataset in Table 4.10, the RRMSE values are quite lower. This means that the scatterers detected in the "truth" are in general better reconstructed with respect to the monostatic case in Section 4.4. The best results are given by BWE and CS, whereas the worst case is the APES. It is also worth noting the high number of detected peaks in the BWE, MVM and APES cases, whereas the number detected of peaks in the CS image is very low.

Results in Fig.5.28 seem to be not very significant. The mobile cross-correlation maps are calculated as in (4.45) after a preliminary 5x zero-padding by setting the parameters $\delta_H = \delta_S = 2.5$ and $W_{\mathcal{B}} = 15$. By observing the maps in Fig.5.28, a larger number of pixels exceed the threshold in the BWE, MVM and APES cases with respect to SSVA and CS, which return super-resolved images with narrower peaks.

	r_G	$r_{M,I}$	RMSE
BWE	0.5801	0.6866	0.1987
MVM	0.5004	0.7083	0.1829
APES	0.5550	0.7189	0.1648
SSVA	0.4896	0.6416	0.2270
CS	0.5341	0.6558	0.2256

TABLE 5.8: P92 experiment: global cross-correlation, mean mobile cross-correlation and RMSE performance indexes.

Intensity Mean Mobile Cross-correlation indexes ($r_{M,I}$ in (4.47)) are reported in Table 5.8 with together the r_G (see (4.22)) and RMSE (see (4.23)) values for all the tested super-resolution techniques. For all the indexes reported in Table 5.8, APES returns good results with respect the other techniques, whereas the SSVA returns the worst performance indexes. In this case correlation and RMSE indexes are not very reliable because CS and SSVA seem to have very low performance, whereas BWE have the highest r_G. Global correlation r_G, $r_{M,I}$ and RMSE basically say that the ISAR image in Fig.5.23b is a better result than the images in Fig.5.23e and 5.23f.

The quality index parameters calculated as in Section 4.3 are instead summarized in Table 5.9 with together the elapsed times for the super-resolution techniques performing. By observing such results, the BWE image has Image Contrast and Entropy slightly higher with respect to the original image and comparable SNR. Both the range and cross-range measured resolution are considerably higher with respect to the original image. However, the measured cross-range resolution of the original image is comparable with the theoretical cross-range resolution $\delta_{crg} = 0.5153$m, but $\hat{\delta}_{rng}$ is quite lower than $\delta_{rng} = \frac{c}{2B} = 0.5$m. MVM appears to have the worst performance, but both range and cross-range resolution are enhanced with respect to the low-resolution image anyway. APES gives better results with respect to the MVM in terms of IC, IE and SNR, whereas the measured resolution is basically the same. SSVA and CS allows instead for the image quality to be enhanced. Both CS and SSVA allow to successfully restore the range and cross-range resolution, but CS has the best results in terms of image quality. All the measured -3dB mean resolutions are estimated as in Section 4.3 by considering the first 20 scatterers detected by the CLEAN with a zero-padding factor $K_{zp} = 10$. The SNR parameters are instead calculated by setting $\delta_{\mathcal{T}} = 2.5$.

However, as in Section 4.4, by observing the complex signal shape for the MVM and APES in Fig.5.24c and 5.24d respectively, the image PSF for such techniques is likely not a sinc function and the CLEAN is likely not suited for both scatterers detection and resolution estimation. Therefore, the resolution measurements in Table 5.9 may be not reliable.

	IC	IE ($\cdot 10^5$)	SNR [dB]	$\hat{\delta}_{rng}$ [m]	$\hat{\delta}_{crg}$ [m]	Elap. Time
High-Res.	0.8108	−3.7462	34.8445	0.3865	0.5360	-
Low-Res.	0.8556	−1.0041	34.6979	0.9155	0.9998	-
BWE	0.8652	−3.9664	34.1991	0.6001	0.7395	0.2141
MVM	0.6774	−2.3206	28.4372	0.7959	1.0281	1.2344
APES	0.7400	−2.9419	31.2630	0.8010	1.0023	2.4072
SSVA	1.0687	−4.9437	37.4680	0.3433	0.5617	0.2139
CS	1.2326	−5.9009	38.4294	0.3636	0.4896	13.7302

TABLE 5.9: P92 experiment: quality indexes and elapsed times in seconds.

	IC	IE ($\cdot 10^5$)	SNR [dB]	$\hat{\delta}_{rng}$ [m]	$\hat{\delta}_{crg}$ [m]	Elap. Time
BWE	0.8137	−3.8332	34.8947	0.3191	0.4007	0.8333
MVM	0.6909	−2.5924	30.3663	0.3738	0.4922	27.3276
APES	0.7387	−3.1241	32.6625	0.3789	0.4922	44.8787
SSVA	1.0827	−5.2645	38.3491	0.2136	0.2706	0.4747
CS	1.2154	−5.8396	38.9371	0.2251	0.2551	97.8105

TABLE 5.10: P92 experiment: quality indexes for 2x super-resolution and elapsed times in seconds.

In this case, IC and SNR are generally lower with respect to the results in Section 4.4 for the monostatic case, because the image under test in this Section is significantly noisier (compare Fig.5.26a with Fig.4.28a). However, the results for the tested super-resolution techniques with respect to the "truth" image are coherent with the ones in Section 4.4.

The quality index parameters for the 2x super-resolution images in Fig.5.25 are instead shown in Table 5.10. IC, IE and SNR are not so different with respect to the previous case. Both range and cross-range resolution is successfully doubled by the SSVA and CS, whereas in the MVM and APES images the measured values are slightly lower with respect to the original image. BWE gives intermediate resolution results.

Regarding the elapsed times, BWE and SSVA are much faster than MVM, APES and CS. APES takes about twice the time needed by the MVM, but they are both faster than CS. However, as the image size is doubled, the elapsed time increases by a factor of about 20 for MVM and APES and 7 for CS. In this case, the input image is 43×62 pixels in the first case (see Fig.5.22a) and 86×124 in the 2x super-resolution case (the original image in Fig.5.18a). In the monostatic case in Section 4.4, the input image is 117×112 pixels (see Fig.4.29a) and the elapsed time for CS is about the same (compare Table 5.10 with Table 4.9). MVM and APES take instead more time because of a larger subaperture size used for the covariance matrix estimation. The elapsed times for MVM and APES in the 2x super-resolution bistatic case in Table 5.10 are comparable with the elapsed times in the monostatic case when a 30% subaperture is used (see Table 4.8).

Chapter 6

Conclusions

In this Thesis the topic of super-resolution applied for monostatic and bistatic radar imaging is treated. The B-ISAR and super-resolution radar imaging topics are firstly treated separately. Then, super-resolution is theoretically validated in case of bistatic configuration by exploiting the bistatic received signal model and the BEM approximation. Different super-resolution techniques are tested on both monostatic and bistatic real data with comprehensive performance analysis and comparison.

6.1 Conclusive summary

In Chapter 2 the B-ISAR theory has been recalled. The received signal model has been defined that extended the monostatic case to the more generic bistatic configuration. The applicability of the standard range-Doppler ISAR imaging technique in case of bistatic configuration has been theoretically demonstrated. The differences in the received signal model between the monostatic and bistatic cases have been analytically analyzed and a theoretical foundation has been laid that introduces the concept of "Bistatically Equivalent Monostatic" configuration, which allows approximating a bistatic geometry with a monostatic one. This greatly simplifies the geometrical understanding and allows using monostatic ISAR processors to form B-ISAR images. However, the BEM approximation has some limitations due to the distortions introduced by the bistatic geometry. Such distortions have been thoroughly investigated and cataloged in terms of

1. Image scaling due to the bistatic angle width;
2. Linear distortions due to the bistatic angle variation speed;
3. Quadratic distortions expressed in terms of range/Doppler migration.

Constraints for the bistatic distortions due to range and Doppler migration have been analytically derived and validated by means of simulated data. It is worth pointing out that the exploiting of the second order approximation of the bistatic distortion term $K(t)$ is an innovative aspect of this Thesis. Such a second order approximation has been demonstrated to be fundamental to the analytical study of the bistatic distortions.

In Chapter 3 the concept of super-resolution for SAR/ISAR imagery has been recalled and the most common super-resolution techniques have been reviewed by differentiating between parametric and non-parametric methods. Particular attention has been paid on linear prediction based super-resolution, Capon's MVM and APES spectral estimation, Super-SVA and super-resolution based on the CS theory. Such techniques have been discussed and theoretically analyzed by referring to the monostatic received signal model.

In Chapter 4 novel performance analysis methods have been proposed in order to test the effectiveness of a generic super-resolution technique. This is in order to give measurable parameters and provide comparable indexes of performance. In particular, two different approaches have been proposed:

1. Truth based analysis methods which consider the super-resolution result as an "estimation" of a reference "truth";
2. Quality index based methods which consists of directly calculate standard image quality metrics on the super-resolution output, e.g., IC, SNR and -3dB resolution.

Truth based analysis methods consist of consider a source SAR/ISAR image as a high-resolution truth. The signal support of such a truth is reduced in order to create a low-resolution image, which is given as input to the super-resolution technique under test. The super-resolution output is considered as an estimation of the original high-resolution image. Super-resolution performance is evaluated by comparing truth and estimation. Two comparison methods have been proposed in order to evaluate the estimation validity:

1. Scatterer position based comparison: the dominant scatterers in both the original image and the super-resolution output are detected. The super-resolution performance is expressed in terms of correct detections, missed detections, i.e., number of scatterers which are lost during the performance analysis chain, and artifacts introduced by the super-resolution technique or false alarms.
2. Mobile cross-correlation based comparison: truth and estimation are compared by means of a cross-correlation index calculated within a mobile window. As a result, a "cross-correlation map" is obtained. Such a map highlights those areas where the high-resolution image has been well or badly estimated.

Furthermore, the scatterer position based comparison method allows to estimate the amplitude estimation RRMSE by considering only those scatterers labeled as "correctly detected". The quality metrics proposed in this Thesis are instead the Image Contrast, Image Entropy, SNR and the -3dB resolution calculated by exploiting the CLEAN technique. Such performance analysis methods are used to evaluate and compare the super-resolution techniques described in Chapter 3 applied on real monostatic data.

The real data under test is a spaceborne SAR image in maritime scenario taken from the city of Istanbul in the April 2008 and provided by COSMO-SkyMed. A subcrop of the whole SAR image is taken around a randomly chosen detected vessel. Such a vessel is classified as "moving" and appears defocused in the original SAR image. It is then refocused by means of ISAR processing and the ICBA technique. In this case, the scatterer position based comparison method detects the largest number of artifacts in the MVM result and the largest number of missed detections in the BWE. Better results are obtained by APES, SSVA and CS, but CS returns much better performance in terms of scatterers amplitude estimation. The best performance in terms of mobile cross-correlation are given by CS and APES, whereas the worst case is the SSVA. Quality index based methods return the best performance indexes for CS and the worst for MVM.

In Chapter 5 super-resolution is treated in case of bistatic radar configuration. The super-resolution techniques examined in Chapter 3 have been theoretically validated by considering the bistatic received signal model. A novel super-resolution based approach for bistatic distortion mitigation has been proposed and results for three different super-resolution techniques, i.e., BWE, SSVA and CS, have been produced and evaluated. Results on both noisy and non-noisy simulated data highlighted better performance for CS with respect to the others in terms of scatterer amplitude estimation, whereas SSVA and CS appear almost equivalent in terms of image contrast and correlation. Then, super-resolution has been tested also on real bistatic data.

Real data used to test the super-resolution techniques in Chapter 5 were acquired during the NATO SET-196 trials from the September 29th to the October 3rd, 2014. The trials were hosted by the Istituto Vallauri of the Italian Navy located in Livorno where real data have been acquired by means of two HABRA Radar systems designed and provided by Metasensing BV. The target of interest is a cooperative Tecnam P92 ultralight aircraft. The refocused ISAR image has been obtained by means of the ICBA technique, whereas target trajectory, effective rotation vector and bistatic angle have been measured by means of a differential GPS receiver and IMU provided by the CSIR, South Africa. By exploiting the GPS data, the range and Doppler migration parameters have been estimated and the absence of both linear and quadratic bistatic distortions has been proven. Then, the super-resolution techniques BWE, Capon's MVM, APES, SSVA

and CS have been tested on the refocused ISAR image and compared by means of the performance analysis methods proposed in Chapter 4. The best performance in terms of number of correctly detected scatterers is given by the APES, whereas CS has the lowest number of artifacts and the best performance in terms of amplitude estimation error. CS also gives the best performance in terms of image contrast, entropy, SNR and measured resolution. On the other hand, the mobile cross-correlation comparison method does not provide significative results.

In general, Compressed Sensing appears to give the best performance results over the other tested super-resolution techniques in both monostatic and bistatic cases.

6.2 Future work

Future work will aim to further examine the super-resolution topic. Real data collected during the visiting period at the Ohio State University will be exploited for monostatic/bistatic phenomenology studies and super-resolution radar imaging application for ATR purposes.

Such real data has been collected at the ElectroScience Laboratory of the Ohio State University under the supervision of Dr. Christopher Baker. A W-band multistatic radar system has been used to obtain a set of ISAR images of seven similar targets. Such targets have been built with aluminum foil and several metallic pieces and placed on a controlled rotating table. ISAR data has then been collected by means of three transmitters in Time Division Multiplexing (TDM) configuration and three independent receivers. Received signals have been range gated in order to make the first receiver to sense the radar echo only from the first transmitter and so on. Transmitters and receivers have been placed on order to build a monostatic radar system and two bistatic systems with 30° and 90° bistatic angles. The monostatic system has been placed in the BEM position.

For illustration purposes, the experiment scenario in shown in Fig.6.1 with transmitters and receivers labeled. The target #3 is depicted in Fig.6.2 and the ISAR results for azimuth angle 30° and receivers #1, #2 and #3 are shown in Fig.6.3. Similar ISAR images have been collected for seven targets and 360 azimuth angles and will be used for phenomenology studies and super-resolution applied for ATR purposes.

Experiments described above took place in collaboration with Dr. Seung Ho Doo, Dr. Adam Mitchell and Dr. Landon Garry from the Ohio State University.

FIGURE 6.1: Monostatic/bistatic experiment: scenario.

FIGURE 6.2: Monostatic/bistatic experiment: target #3 picture.

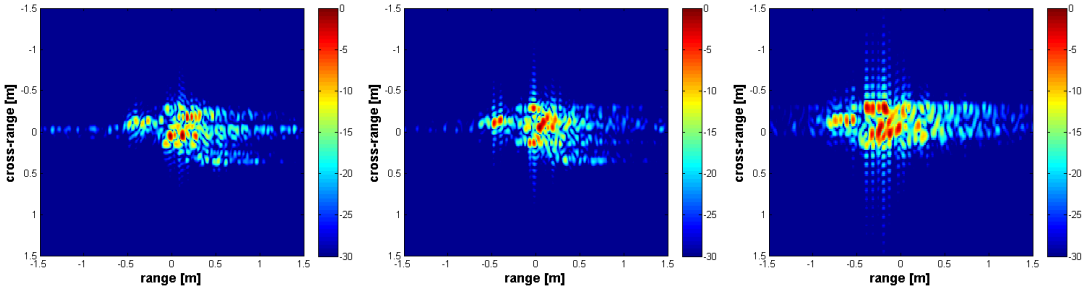

(a) (b) (c)

FIGURE 6.3: Monostatic/bistatic experiment: ISAR results for target #3, azimuth angle 30°, bistatic angle 0° (a), 30° (b) and 90° (c).

Bibliography

[1] C. Hülsmeyer. Hertzian-wave projecting and receiving apparatus adapted to indicate or give warning of the presence of a metallic body, such as a ship or a train, in the line of projection of such waves, 09 1904.

[2] J. Ender. 98 years of the RADAR principle: the inventor Christian Hülsmeyer. *EUSAR2002*, June 2002.

[3] Radar in the twentieth century. *Aerospace and Electronic Systems Magazine, IEEE*, 15(10):27–46, Oct 2000. ISSN 0885-8985. doi: 10.1109/62.879403.

[4] A. Love. In memory of carl a. wiley. *Antennas and Propagation Society Newsletter, IEEE*, 27(3):17–18, June 1985. ISSN 2168-0329. doi: 10.1109/MAP.1985.27810.

[5] Jack L. Walker. Range-doppler imaging of rotating objects. *Aerospace and Electronic Systems, IEEE Transactions on*, AES-16(1):23–52, Jan 1980. ISSN 0018-9251. doi: 10.1109/TAES.1980.308875.

[6] Chung-Ching Chen and H.C. Andrews. Target-motion-induced radar imaging. *Aerospace and Electronic Systems, IEEE Transactions on*, AES-16(1):2–14, Jan 1980. ISSN 0018-9251. doi: 10.1109/TAES.1980.308873.

[7] Chung-Ching Chen and H.C. Andrews. Multifrequency imaging of radar turntable data. *Aerospace and Electronic Systems, IEEE Transactions on*, AES-16(1):15–22, Jan 1980. ISSN 0018-9251. doi: 10.1109/TAES.1980.308874.

[8] Dale A. Ausherman, Adam Kozma, Jack L. Walker, Harrison M. Jones, and Enrico C. Poggio. Developments in radar imaging. *Aerospace and Electronic Systems, IEEE Transactions on*, AES-20(4):363–400, July 1984. ISSN 0018-9251. doi: 10.1109/TAES.1984.4502060.

[9] Mark T Crockett and David Long. An introduction to synthetic aperture radar: a high-resolution alternative to optical imaging. *19th Annual Fellowship Symposium, Utah Space Grant Consortium*, May 2013.

[10] Steven J. Ostro, R. Scott Hudson, Michael C. Nolan, Jean-Luc Margot, Daniel J. Scheeres, Donald B. Campbell, Christopher Magri, Jon D. Giorgini, and Donald K. Yeomans. Radar observations of asteroid 216 kleopatra. *Science*, 288(5467):836–839, 2000. ISSN 0036-8075. doi: 10.1126/science.288.5467.836. URL http://science.sciencemag.org/content/288/5467/836.

[11] D. Olivadese, E. Giusti, D. Petri, M. Martorella, A. Capria, and F. Berizzi. Passive ISAR with DVB-T signals. *Geoscience and Remote Sensing, IEEE Transactions on*, 51(8):4508–4517, Aug 2013. ISSN 0196-2892. doi: 10.1109/TGRS.2012.2236339.

[12] D. Pastina, M. Bucciarelli, and P. Lombardo. Multistatic and mimo distributed isar for enhanced cross-range resolution of rotating targets. *Geoscience and Remote Sensing, IEEE Transactions on*, 48(8):3300–3317, Aug 2010. ISSN 0196-2892. doi: 10.1109/TGRS.2010.2043740.

[13] D. Stagliano, E. Giusti, S. Lischi, and M. Martorella. Bistatic three-dimensional interferometric isar. *IET Radar, Sonar and Navigation*, September 2015. ISSN 1751-8784. URL http://digital-library.theiet.org/content/journals/10.1049/iet-rsn.2015.0131.

[14] A.M. Mishra and M. Bernard. Automatic target recognition using multipolar bistatic synthetic aperture radar images. *Aerospace and Electronic Systems, IEEE Transactions on*, 46(4):1906–1920, Oct 2010. ISSN 0018-9251. doi: 10.1109/TAES.2010.5595603.

[15] M. Martorella, J. Palmer, F. Berizzi, and B. Bates. Advances in bistatic inverse synthetic aperture radar. In *Radar Conference - Surveillance for a Safer World, 2009. RADAR. International*, pages 1–6, Oct 2009.

[16] M. Martorella, J. Palmer, J. Homer, B. Littleton, and I.D. Longstaff. On bistatic inverse synthetic aperture radar. *Aerospace and Electronic Systems, IEEE Transactions on*, 43(3):1125–1134, 2007. ISSN 0018-9251. doi: 10.1109/TAES.2007.4383602.

[17] M. Martorella, D. Cataldo, and S. Brisken. Bistatically equivalent monostatic approximation for bistatic isar. In *Radar Conference (RADAR), 2013 IEEE*, pages 1–5, April 2013. doi: 10.1109/RADAR.2013.6586074.

[18] M. Martorella. Analysis of the robustness of bistatic inverse synthetic aperture radar in the presence of phase synchronisation errors. *Aerospace and Electronic Systems, IEEE Transactions on*, 47(4):2673–2689, October 2011. ISSN 0018-9251. doi: 10.1109/TAES.2011.6034658.

[19] J.H.G. Ender and A.R. Brenner. Pamir - a wideband phased array sar/mti system. *Radar, Sonar and Navigation, IEE Proceedings* -, 150(3):165–172, June 2003. ISSN 1350-2395. doi: 10.1049/ip-rsn:20030445.

[20] K. Nakamura, H. Wakabayashi, K. Naoki, F. Nishio, T. Moriyama, and S. Uratsuka. Observation of sea-ice thickness in the sea of okhotsk by using dual-frequency and fully polarimetric airborne sar (pi-sar) data. *Geoscience and Remote Sensing, IEEE Transactions on*, 43(11):2460–2469, Nov 2005. ISSN 0196-2892. doi: 10.1109/TGRS.2005.853928.

[21] E. Giusti, S. Tomei, A. Bacci, M. Martorella, and F. Berizzi. Autofocus for CS based ISAR imaging in the presence of gapped data. In *2nd International Workshop on Compressive Sensing applied to Radar (CoSeRa2013)*, Sept 2013.

[22] M. Martorella, F. Berizzi, and B. Haywood. Contrast maximisation based technique for 2-D ISAR autofocusing. *Radar, Sonar and Navigation, IEE Proceedings* -, 152 (4):253–262, Aug 2005. ISSN 1350-2395. doi: 10.1049/ip-rsn:20045123.

[23] Richard Oliver Lane. *Bayesian super-resolution with application to radar target recognition.* PhD thesis, The University of London, February 2008.

[24] R.O. Schmidt. Multiple emitter location and signal parameter estimation. *Antennas and Propagation, IEEE Transactions on*, 34(3):276–280, Mar 1986. ISSN 0018-926X. doi: 10.1109/TAP.1986.1143830.

[25] J.W. Odendaal, E. Barnard, and C.W.I. Pistorius. Two-dimensional superresolution radar imaging using the music algorithm. *Antennas and Propagation, IEEE Transactions on*, 42(10):1386–1391, Oct 1994. ISSN 0018-926X. doi: 10.1109/8.320744.

[26] R. Roy and T. Kailath. Esprit-estimation of signal parameters via rotational invariance techniques. *Acoustics, Speech and Signal Processing, IEEE Transactions on*, 37(7):984–995, Jul 1989. ISSN 0096-3518. doi: 10.1109/29.32276.

[27] J. A. Högbom. Aperture synthesis with a non-regular distribution of interferometer baselines. *Astronomy and Astrophysics Supplement*, 15:417, June 1974.

[28] Jenho Tsao and B.D. Steinberg. Reduction of sidelobe and speckle artifacts in microwave imaging: the clean technique. *Antennas and Propagation, IEEE Transactions on*, 36(4):543–556, Apr 1988. ISSN 0018-926X. doi: 10.1109/8.1144.

[29] Jian Li and Petre Stoica. Efficient mixed-spectrum estimation with applications to target feature extraction. In *Signals, Systems and Computers, 1995. 1995 Conference Record of the Twenty-Ninth Asilomar Conference on*, volume 1, pages 428–432 vol.1, Oct 1995. doi: 10.1109/ACSSC.1995.540585.

[30] J. Mather. The incremental multi-parameter algorithm. In *Signals, Systems and Computers, 1990 Conference Record Twenty-Fourth Asilomar Conference on*, volume 1, pages 368–, Nov 1990. doi: 10.1109/ACSSC.1990.523362.

[31] S.P. Luttrell. Prior knowledge and object reconstruction using the best linear estimate technique. *Optica Acta: International Journal of Optics*, 32(6):703–716, 1985. doi: 10.1080/713821785. URL http://dx.doi.org/10.1080/713821785.

[32] L M Delves, G C Pryde, and S P Luttrell. A super-resolution algorithm for sar images. *Inverse Problems*, 4(3):681, 1988. URL http://stacks.iop.org/0266-5611/4/i=3/a=010.

[33] H. Nasir, V. Stankovic, and S. Marshall. Singular value decomposition based fusion for super-resolution image reconstruction. In *Signal and Image Processing Applications (ICSIPA), 2011 IEEE International Conference on*, pages 393–398, Nov 2011. doi: 10.1109/ICSIPA.2011.6144138.

[34] J. Capon. High-resolution frequency-wavenumber spectrum analysis. *Proceedings of the IEEE*, 57(8):1408–1418, Aug 1969. ISSN 0018-9219. doi: 10.1109/PROC.1969.7278.

[35] Jian Li and Petre Stoica. An adaptive filtering approach to spectral estimation and sar imaging. *Signal Processing, IEEE Transactions on*, 44(6):1469–1484, Jun 1996. ISSN 1053-587X. doi: 10.1109/78.506612.

[36] H.C. Stankwitz and M.R. Kosek. Super-resolution for sar/isar rcs measurement using spatiall variant apodization. In *Proceedings of Antenna Measurement Techniques Association (AMTA) 17th Annual Meeting and Symposium, Williamsburg, VA*, November 1995.

[37] H.C. Stankwitz, R.J. Dallaire, and J.R. Fienup. Nonlinear apodization for sidelobe control in sar imagery. *Aerospace and Electronic Systems, IEEE Transactions on*, 31(1):267–279, Jan 1995. ISSN 0018-9251. doi: 10.1109/7.366309.

[38] D. Pastina, A. Farina, J. Gunning, and P. Lombardo. Two-dimensional super-resolution spectral analysis applied to sar images. *Radar, Sonar and Navigation, IEE Proceedings* -, 145(5):281–290, Oct 1998. ISSN 1350-2395. doi: 10.1049/ip-rsn:19982225.

[39] S.R. DeGraaf. Sar imaging via modern 2-d spectral estimation methods. *Image Processing, IEEE Transactions on*, 7(5):729–761, May 1998. ISSN 1057-7149. doi: 10.1109/83.668029.

[40] S.B. Bowling. Linear prediction and maximum entropy spectral analysis for radar applications. *NASA STI/Recon Technical Report N*, 78:10362, May 1977.

[41] K. M. Cuomo. A bandwidth extrapolation technique for improved range resolution of coherent radar data, revision 1. *NASA STI/Recon Technical Report N*, 93:18262, December 1992.

[42] Thomas G. Moore, Brian W. Zuerndorfer, and Earl C. Burt. Enhanced imagery using spectral-estimation-based techniques. *Lincoln Laboratory Journal*, 10(2), 1997.

[43] J.P. Burg. *Maximum entropy spectral analysis*. Stanford Exploration project. Stanford University, 1975. URL https://books.google.it/books?id=Xug_AAAAIAAJ.

[44] Koen Vos. A fast implementation of burg's method. *www.arxiv.org*, August 2013.

[45] Robert D. Palmer, Sridhar Gopalam, Tian-You Yu, and Shoichiro Fukao. Coherent radar imaging using capon's method. *Radio Science*, 33(6):1585–1598, 1998. ISSN 1944-799X. doi: 10.1029/98RS02200. URL http://dx.doi.org/10.1029/98RS02200.

[46] F. Lombardini and A. Reigber. Adaptive spectral estimation for multibaseline sar tomography with airborne l-band data. In *Geoscience and Remote Sensing Symposium, 2003. IGARSS '03. Proceedings. 2003 IEEE International*, volume 3, pages 2014–2016, July 2003. doi: 10.1109/IGARSS.2003.1294324.

[47] Jong-Sen Lee and M.R. Grunes. Classification of multi-look polarimetric sar data based on complex wishart distribution. In *Telesystems Conference, 1992. NTC-92., National*, pages 7/21–7/24, May 1992. doi: 10.1109/NTC.1992.267879.

[48] M. Jansson and Petre Stoica. Analysis of forward-only and forward-backward sample covariances. In *Acoustics, Speech, and Signal Processing, 1999. Proceedings., 1999 IEEE International Conference on*, volume 5, pages 2825–2828 vol.5, 1999. doi: 10.1109/ICASSP.1999.761350.

[49] P. Lopez-Dekker and J.J. Mallorqui. Capon- and apes-based sar processing: Performance and practical considerations. *Geoscience and Remote Sensing, IEEE Transactions on*, 48(5):2388–2402, May 2010. ISSN 0196-2892. doi: 10.1109/TGRS.2009.2038902.

[50] Yanwei Wang, Jian Li, and Petre Stoica. Rank-deficient robust capon filter bank approach to complex spectral estimation. *Signal Processing, IEEE Transactions on*, 53(8):2713–2726, Aug 2005. ISSN 1053-587X. doi: 10.1109/TSP.2005.850365.

[51] W. Featherstone, H.J. Strangeways, M.A. Zatman, and H. Mewes. A novel method to improve the performance of capon's minimum variance estimator. In *Antennas and Propagation, Tenth International Conference on (Conf. Publ. No. 436)*, volume 1, pages 322–325 vol.1, Apr 1997. doi: 10.1049/cp:19970264.

[52] E.G. Larsson and Petre Stoica. Fast implementation of two-dimensional apes and capon spectral estimators. In *Acoustics, Speech, and Signal Processing, 2001. Proceedings. (ICASSP '01). 2001 IEEE International Conference on*, volume 5, pages 3069–3072 vol.5, 2001. doi: 10.1109/ICASSP.2001.940306.

[53] Z.-S. Liu, Hongbin Li, and Jian Li. Efficient implementation of capon and apes for spectral estimation. *Aerospace and Electronic Systems, IEEE Transactions on*, 34 (4):1314–1319, Oct 1998. ISSN 0018-9251. doi: 10.1109/7.722716.

[54] E. Hecht. *Optics*. Pearson education. Addison-Wesley, 2002. ISBN 9780321188786. URL https://books.google.it/books?id=T3ofAQAAMAAJ.

[55] F.J. Harris. On the use of windows for harmonic analysis with the discrete fourier transform. *Proceedings of the IEEE*, 66(1):51–83, Jan 1978. ISSN 0018-9219. doi: 10.1109/PROC.1978.10837.

[56] S.R. DeGraaf. Sidelobe reduction via adaptive fir filtering in sar imagery. *Image Processing, IEEE Transactions on*, 3(3):292–301, May 1994. ISSN 1057-7149. doi: 10.1109/83.287022.

[57] C.F. Castillo-Rubio, S. Llorente-Romano, and M. Burgos-Garcia. Spatially variant apodization for squinted synthetic aperture radar images. *Image Processing, IEEE Transactions on*, 16(8):2023–2027, Aug 2007. ISSN 1057-7149. doi: 10.1109/TIP.2007.899603.

[58] B.H. Smith. Generalization of spatially variant apodization to noninteger nyquist sampling rates. *Image Processing, IEEE Transactions on*, 9(6):1088–1093, Jun 2000. ISSN 1057-7149. doi: 10.1109/83.846250.

[59] G. Thomas, B.C. Flores, and Jae Sok-Son. Sar sidelobe apodization using the kaiser window. In *Image Processing, 2000. Proceedings. 2000 International Conference on*, volume 1, pages 709–712 vol.1, 2000. doi: 10.1109/ICIP.2000.901057.

[60] D. Pastina, F. Colone, and P. Lombardo. Effect of apodization on sar image understanding. *Geoscience and Remote Sensing, IEEE Transactions on*, 45(11):3533–3551, Nov 2007. ISSN 0196-2892. doi: 10.1109/TGRS.2007.905309.

[61] H.C. Stankwitz and M.R. Kosek. Sparse aperture fill for sar using super-sva. In *Radar Conference, 1996., Proceedings of the 1996 IEEE National*, pages 70–75, May 1996. doi: 10.1109/NRC.1996.510659.

[62] Chong Ni, YanFei Wang, XiangHui Xu, ChangYi Zhou, and PengFei Cui. A super-resolution algorithm for synthetic aperture radar based on modified spatially variant apodization. *Science China Physics, Mechanics and Astronomy*, 54(2):355–364, 2011. ISSN 1674-7348. doi: 10.1007/s11433-010-4186-8. URL http://dx.doi.org/10.1007/s11433-010-4186-8.

[63] H. Chinmay, R. Baraniuk, M. A. Davenport, and M. F. Duarte. *An Introduction to Compressive Sensing*. OpenStax CNX., August 2014. URL http://cnx.org/contents/f70b6ba0-b9f0-460f-8828-e8fc6179e65f@5.12@5.12.

[64] R. Baraniuk and P. Steeghs. Compressive radar imaging. In *Radar Conference, 2007 IEEE*, pages 128–133, April 2007. doi: 10.1109/RADAR.2007.374203.

[65] Lei Zhang, Mengdao Xing, Cheng-Wei Qiu, Jun Li, Jialian Sheng, Yachao Li, and Zheng Bao. Resolution enhancement for Inversed Synthetic Aperture Radar imaging under low snr via improved compressive sensing. *Geoscience and Remote Sensing, IEEE Transactions on*, 48(10):3824–3838, 2010. ISSN 0196-2892. doi: 10.1109/TGRS.2010.2048575.

[66] Lei Zhang, Mengdao Xing, Cheng-Wei Qiu, Jun Li, Jialian Sheng, Yachao Li, and Zheng Bao. Resolution enhancement for inversed synthetic aperture radar imaging under low snr via improved compressive sensing. *Geoscience and Remote Sensing, IEEE Transactions on*, 48(10):3824–3838, Oct 2010. ISSN 0196-2892. doi: 10.1109/TGRS.2010.2048575.

[67] H. Mohimani, Massoud Babaie-Zadeh, and C. Jutten. A fast approach for overcomplete sparse decomposition based on smoothed l0 norm. *Signal Processing, IEEE Transactions on*, 57(1):289–301, Jan 2009. ISSN 1053-587X. doi: 10.1109/TSP.2008.2007606.

[68] A. Ghaffari, M. Babaie-Zadeh, and C. Jutten. Sparse decomposition of two dimensional signals. In *Acoustics, Speech and Signal Processing, 2009. ICASSP 2009. IEEE International Conference on*, pages 3157–3160, 2009. doi: 10.1109/ICASSP.2009.4960294.

[69] Elisa Giusti, Qiu Wei, Alessio Bacci, Sonia Tomei, and Marco Martorella. Super resolution ISAR imaging via compressing sensing. In *EUSAR 2014; 10th European Conference on Synthetic Aperture Radar; Proceedings of*, pages 1–4, June 2014.

[70] A. Bacci, D. Stagliano, E. Giusti, S. Tomei, F. Berizzi, and M. Martorella. 3D interferometric ISAR via compressive sensing. In *European Radar Conference (EuRAD), 2014 11th*, pages 233–236, Oct 2014. doi: 10.1109/EuRAD.2014.6991250.

[71] W. Qiu, E. Giusti, A. Bacci, M. Martorella, F. Berizzi, H.Z. Zhao, and Q. Fu. Compressive sensing for passive ISAR with DVB-T signal. In *Radar Symposium (IRS), 2013 14th International*, volume 1, pages 113–118, June 2013.

[72] P. Maechler, N. Felber, and H. Kaeslin. Compressive sensing for wifi-based passive bistatic radar. In *Signal Processing Conference (EUSIPCO), 2012 Proceedings of the 20th European*, pages 1444–1448, Aug 2012.

[73] Ali Cafer Gurbuz, J.H. McClellan, and W.R. Scott. Compressive sensing for gpr imaging. In *Signals, Systems and Computers, 2007. ACSSC 2007. Conference Record of the Forty-First Asilomar Conference on*, pages 2223–2227, Nov 2007. doi: 10.1109/ACSSC.2007.4487636.

[74] A.C. Gurbuz, J.H. McClellan, and W.R. Scott. A compressive sensing data acquisition and imaging method for stepped frequency gprs. *Signal Processing, IEEE Transactions on*, 57(7):2640–2650, July 2009. ISSN 1053-587X. doi: 10.1109/TSP.2009.2016270.

[75] A.B. Suksmono, E. Bharata, A.A. Lestari, A.G. Yarovoy, and L.P. Ligthart. Compressive stepped-frequency continuous-wave ground-penetrating radar. *Geoscience and Remote Sensing Letters, IEEE*, 7(4):665–669, Oct 2010. ISSN 1545-598X. doi: 10.1109/LGRS.2010.2045340.

[76] A. Bacci, E. Giusti, S. Tomei, M. Martorella, and F. Berizzi. Time-slotted FMCW MIMO ISAR with compressive sensing image reconstruction. In *3rd International Workshop on Compressive Sensing applied to Radar (CoSeRa2015)*, Sept 2013.

[77] A.P. Petropulu, Yao Yu, and H.V. Poor. Distributed mimo radar using compressive sampling. In *Signals, Systems and Computers, 2008 42nd Asilomar Conference on*, pages 203–207, Oct 2008. doi: 10.1109/ACSSC.2008.5074392.

[78] Yao Yu, A.P. Petropulu, and H.V. Poor. Mimo radar using compressive sampling. *Selected Topics in Signal Processing, IEEE Journal of*, 4(1):146–163, Feb 2010. ISSN 1932-4553. doi: 10.1109/JSTSP.2009.2038973.

[79] M. Lustig, D.L. Donoho, J.M. Santos, and J.M. Pauly. Compressed sensing MRI. *Signal Processing Magazine, IEEE*, 25(2):72–82, March 2008. ISSN 1053-5888. doi: 10.1109/MSP.2007.914728.

[80] M. Martorella, N. Acito, and F. Berizzi. Statistical clean technique for isar imaging. *Geoscience and Remote Sensing, IEEE Transactions on*, 45(11):3552–3560, Nov 2007. ISSN 0196-2892. doi: 10.1109/TGRS.2007.897440.

[81] M. Martorella. Novel approach for isar image cross-range scaling. *Aerospace and Electronic Systems, IEEE Transactions on*, 44(1):281–294, January 2008. ISSN 0018-9251. doi: 10.1109/TAES.2008.4517004.

[82] F. Berizzi and G. Corsini. Autofocusing of inverse synthetic aperture radar images using contrast optimization. *Aerospace and Electronic Systems, IEEE Transactions on*, 32(3):1185–1191, July 1996. ISSN 0018-9251. doi: 10.1109/7.532282.

[83] F. Berizzi, M. Martorella, B. Haywood, E. Dalle Mese, and S. Bruscoli. A survey on isar autofocusing techniques. In *Image Processing, 2004. ICIP '04. 2004 International Conference on*, volume 1, pages 9–12 Vol. 1, Oct 2004. doi: 10.1109/ICIP.2004.1418676.

[84] Li Xi, Liu Guosui, and JinLin Ni. Autofocusing of isar images based on entropy minimization. *Aerospace and Electronic Systems, IEEE Transactions on*, 35(4): 1240–1252, Oct 1999. ISSN 0018-9251. doi: 10.1109/7.805442.

[85] M. Cetin, W.C. Karl, and D.A. Castanon. Feature enhancement and atr performance using nonquadratic optimization-based sar imaging. *Aerospace and Electronic Systems, IEEE Transactions on*, 39(4):1375–1395, Oct 2003. ISSN 0018-9251. doi: 10.1109/TAES.2003.1261134.

[86] F. Argenti and L. Alparone. Speckle removal from sar images in the undecimated wavelet domain. *Geoscience and Remote Sensing, IEEE Transactions on*, 40(11): 2363–2374, Nov 2002. ISSN 0196-2892. doi: 10.1109/TGRS.2002.805083.

[87] D. Stagliano, A. Lupidi, and F. Berizzi. Ship detection from sar images based on cfar and wavelet transform. In *Advances in Radar and Remote Sensing (TyWRRS), 2012 Tyrrhenian Workshop on*, pages 53–58, Sept 2012. doi: 10.1109/TyWRRS.2012.6381102.

[88] D. Stagliano, L. Musetti, D. Cataldo, A. Baruzzi, and M. Martorella. Fast detection of maritime targets in high resolution sar images. In *Radar Conference, 2014 IEEE*, pages 0522–0527, May 2014. doi: 10.1109/RADAR.2014.6875647.

[89] Marco Martorella, Elisa Giusti, Alessio Bacci, Fabrizio Berizzi, and Adriano Meta. Non-cooperative maritime target imaging with an fmcw sar system. In *Synthetic Aperture Radar, 2012. EUSAR. 9th European Conference on*, pages 127–130, April 2012.

[90] P. Swerling. Probability of detection for fluctuating targets. *Information Theory, IRE Transactions on*, 6(2):269–308, April 1960. ISSN 0096-1000. doi: 10.1109/TIT.1960.1057561.